Dissertation

submitted to the

Combined Faculties of Mathematics, Engineering and Natural Sciences
of Heidelberg University, Germany

for the degree of
Doctor of Natural Sciences

Put forward by
M.Sc. Andrey Alekseevich Butkevich
born in Sankt-Petersburg, Russian Federation

Oral examination date: 20.10.2025

Effects of structural disorder on electrical properties of molecular organic ferroelectrics and semiconductors

Andrey Alekseevich Butkevich

2025

Department of Physics and Astronomy
Ruprecht Karl University of Heidelberg

Referees:
Prof. Dr. Martijn Kemerink
Prof. Dr. Peer Fischer

Effects of structural disorder on electrical properties of molecular organic ferroelectrics and semiconductors: Structural disorder plays a significant role in organic materials because it influences many of their properties. The electrical properties of structurally disordered organic thin films of several molecular ferroelectric materials and one semiconducting polymer were investigated. Supramolecular ferroelectric discotic trialkylbenzene-1,3,5-tricarboxamide (BTA) was pre-aligned by dip coating, which improved ferroelectric switching similarly to field annealing. Furthermore, Barkhausen noise in BTA was simulated using kinetic Monte Carlo method to gain insight into the switching mechanisms of organic ferroelectric materials. Self-organized critical behavior was established in the BTA system with varying degrees of disorder. Additionally, Barkhausen noise in the ferroelectric copolymer poly(vinylidene fluoride-co-trifluoroethylene) (P(VDF:TrFE)) was measured experimentally. The experimental behavior of the P(VDF:TrFE) system differed slightly from the anticipated self-organized critical behavior. Three non-planar, C3-symmetric triphenylamine (TPA) derivatives were investigated for their ferroelectric behavior. Although no direct evidence of ferroelectricity was observed, considerable electrical conductivity with temperature hysteretic behavior originating from structural reordering at elevated temperatures was established for all three TPAs. Finally, experiments provided evidence that the thermoelectric properties of dip-coated and doped semiconducting π-conjugated polymer poly(3-hexylthiophene) (P3HT) thin films generally improve due to less disorder associated with a better overall packing in the P3HT system, despite the absence of aligned P3HT morphologies.

Effekte der strukturellen Unordnung auf die elektrischen Eigenschaften molekularer organischer Ferroelektriker und Halbleiter: Strukturelle Unordnung ist für organische Materialien von großer Bedeutung, da sie mehrere ihrer Eigenschaften beeinflusst. Die elektrischen Eigenschaften strukturell ungeordneter organischer Dünnschichten mehrerer molekularer ferroelektrischer Materialien und eines halbleitenden Polymers wurden untersucht. Das supramolekulare, ferroelektrische, diskotische BTA wurde durch Tauchbeschichtung ausgerichtet, wodurch sich eine Verbesserung des ferroelektrischen Schaltens, ähnlich wie bei Feldausrichtung, nachweisen ließ. Des Weiteren wurde das Barkhausenrauschen in BTA mittels kinetischer Monte-Carlo-Methode simuliert, wodurch sich weitere Einblicke in die Schaltmechanismen organischer ferroelektrischer Materialien ergaben. Dabei wurde im System ein selbstorganisiertes kritisches Verhalten für unterschiedliche Unordnungsgrade festgestellt. Zusätzlich wurde das Barkhausenrauschen im ferroelektrischen Copolymer P(VDF:TrFE) experimentell gemessen. Das experimentelle Verhalten des P(VDF:TrFE)-Systems wich geringfügig vom erwarteten selbstorganisierten kritischen Verhalten ab. Darüber hinaus wurde das ferroelektrische Verhalten dreier nicht-planarer, C3-symmetrischer TPAs untersucht. Obwohl keine direkten Hinweise auf Ferroelektrizität vorlagen, zeigte sich eine hohe elektrische Leitfähigkeit mit temperaturhysteretischen Verhalten für alle drei TPAs, die auf struktureller Umordnung bei höheren Temperaturen beruht. Schließlich belegten Experimente, dass sich die thermoelektrischen Eigenschaften von tauchbeschichteten und dotierten Dünnschichten aus dem halbleitenden, π-konjugierten Polymer P3HT aufgrund geringerer Unordnung und einer insgesamt besseren Materialpackung im P3HT-System generell verbessern, obwohl keine ausgerichteten P3HT-Morphologien beobachtet wurden.

Contents

Chapter 1

Introduction

Structural disorder is an inherent characteristic of organic materials that significantly impacts device performance and, in certain instances, is crucial for their functionality. This is due to the relatively weak intermolecular forces in these materials. In contrast, structural disorder in inorganic materials is generally considered undesirable because it impairs device performance. Consequently, numerous techniques have been developed to minimize its occurrence. Conversely, research in organic materials aims to understand the underlying mechanisms of structural disorder and its influence on material properties and devices. The goal is to manipulate structural disorder parameters to improve device performance. This dissertation investigates the influence of structural disorder on the electrical properties of several organic systems.

In the face of today's many challenges, such as the ongoing digitalization of society, climate change, and the pursuit of renewable energy and sustainable development, organic materials have emerged as a competitive alternative to inorganic materials in certain areas. While inorganic materials generally outperform organic materials in terms of pure performance metrics due to their higher efficiency, thus dominating the corresponding market, organic materials offer significant advantages. These advantages include low-cost production due to the abundance of their constituent materials in nature, ease of processing and scalability, high flexibility, environmental friendliness, and relative ease of recycling or biodegradability [1–3]. Research on organic materials, including small molecules and polymers, dates back more than a century [4]. However, academic interest in organic materials did not increase significantly until the end of the last century, when Heeger et al. discovered electrical transport in doped simple organic polymer polyacetylene [5, 6]. Industrial interest followed with the successful implementation of organic solar cells and light-emitting diodes [1], which demonstrated the wide range of potential and significant technological promise of this class of materials [7]. Consequently, organic electronics has emerged as a vibrant field of fundamental research, development, and applications, combining physics, chemistry, materials science, and engineering [8]. This is partly due to their

electronic flexibility, which allows them to be tailored to different designs and offers significant potential in diverse applications [7]. Currently, however, their poorer performance compared to inorganic materials prevents their widespread use beyond foldable and semi-transparent solar cells [9], displays [3], and specific medical applications, such as highly flexible bioelectronic implants [10].

In general, the (opto)electronic applications of a material depend on its ability to facilitate charge transport [11], which can be ionic, semiconducting, or metallic. However, materials do not need to conduct charges to be of interest in research and applications. For example, ferroelectric organic materials possess a spontaneous electric polarization that can be reversed by an applied electric field, making them a particularly intriguing class of materials. When this polarization is reversed by an applied electric field, hysteresis behavior arises, making these materials promising candidates for memory devices [3]. Furthermore, all ferroelectric materials exhibit pyroelectricity and piezoelectricity, expanding their potential applications.
Although research on ferroelectrics dates back more than a century, to the discovery of Rochelle salt, an organic material, in 1920 [12], the research field has historically focused on inorganic materials. The most prominent examples are barium titanate oxide (BTO) and lead zirconium titanate (PZT), which form the basis of most commercially available applications today [13–16]. In the realm of organic ferroelectric materials, both small molecules and polymers have garnered academic interest. Notable examples include the liquid crystalline supramolecular organic ferroelectric of the columnar discotic type trialkylbenzene-1,3,5-tricarboxamide (BTA) and the polymer polyvinylidene fluoride (PVDF). The latter has found commercial use due to its piezoelectric properties [2, 17–22]. However, no organic materials have yet been commercialized for their ferroelectric properties. This is due to their inferior performance metrics compared to inorganic materials. Organic materials have less ordered morphologies by nature, which limits their performance in terms of power, stability, and endurance. Nevertheless, organic ferroelectric materials are feasible for certain applications due to their advantages, such as flexibility, softness, and biocompatibility. Therefore, these materials are used in areas such as wearable electronics [23–25] and body implants [26] where there are no alternatives.
Besides coercivity, the primary performance metric of ferroelectric materials is saturation polarization, which is achieved by aligning all dipoles with an applied electric field. This dipolar alignment is usually accomplished through extensive post-deposition treatments, such as field annealing. Although the deposition of a ferroelectric material theoretically plays a minor role because it can be aligned either way, the process can be complicated depending on the material's structure, size, and the device geometry. Therefore, pre-alignment of ferroelectric materials through processing is of interest for certain applications.

Organic semiconductors are a stable class of materials for electronic applications. One goal of organic semiconductor research is to study the physics of doped organic semiconductors and

increase the efficiency of various devices. Organic semiconductors are of particular interest for thermoelectric applications since they typically exhibit low thermal conductivities and high Seebeck coefficients. One of the most representative organic semiconductor materials is the π-conjugated polymer poly(3-hexylthiophene) (P3HT). P3HT is used in field-effect transistors, organic thermoelectrics, and solar cells due to its low-cost fabrication [27], solution processability [28, 29], and high charge carrier mobility [30–32].
These polymer materials exhibit interesting electrical transport properties due to the formation of long polymer chains. It is widely accepted that charge transport along these polymer chains is significantly better than transport between them. Consequently, much of the academic research on P3HT focuses on optimizing the device morphology to achieve optimal thermoelectric properties.

When considering organic materials, structural disorder is a common concern. Since device performance is generally dictated by film morphology, any effects that negatively impact it are undesirable [33, 34]. Because most organic materials are amorphous or polycrystalline, structural disorder is a critical factor in device fabrication. Controlling structural disorder is important, as evidenced by the large amount of research devoted to this topic in different classes of organic materials. This work investigates the effects of structural disorder on organic ferroelectric and semiconducting systems. Three well-established systems were chosen for investigation: the ferroelectric liquid crystal BTA, the semicrystalline copolymer poly(vinylidene fluoride-trifluoroethylene) (P(VDF:TrFE)), and the π-conjugated polymer P3HT. These systems are representative of their respective material classes and share properties with other compounds, so the results can be applied to a wide variety of materials. This work focuses on how structural disorder affects the electrical properties of these materials.

This dissertation investigates the potential enhancement of ferroelectric switching properties through pre-alignment using dip coating as an alignment technique for BTA. Dip coating was found to improve ferroelectric switching, achieving performance comparable to field annealing without the need for additional alignment through an applied electric field.
Additionally, crackling (or Barkhausen) noise simulations and experiments were performed to study the switching mechanisms, the corresponding dipole cooperativity, and the disorder in BTA and P(VDF:TrFE). Barkhausen noise in BTA was simulated using kinetic Monte Carlo (kMC) method and examined at various temperatures, frequencies, and disorder parameters. The system was found to exhibit self-organized critical behavior at lower temperatures and higher frequencies when sufficient structural disorder is present.
Although Barkhausen noise has not been successfully measured experimentally in BTA, it has been observed in P(VDF:TrFE) with different electric fields and rise times. The obtained power-law exponents tend to increase with the applied electric field and shift to lower values with longer rise times. However, a definitive statement about the self-organized critical behavior of polarization

reversal avalanches in P(VDF:TrFE) could not be made.
The ferroelectric properties of three triphenylamine (TPA) derivatives, which are non-planar, C3-symmetric compounds that were speculated to be ferroelectric, were also investigated. Although no direct evidence of ferroelectricity was obtained for any of the molecules, varying degrees of molecular alignment resembling that of ferroelectric materials were observed, which enabled considerable electrical conductivity with temperature hysteretic behavior.
Finally, dip coating was used to fabricate P3HT devices. Typically, different deposition techniques are employed to induce polymer alignment and enhance thermoelectric properties. For this project, P3HT polymers were deposited on substrates using both dip and spin coating at various speeds. Although no observable aligned P3HT morphologies were detected using various structural resolution techniques, a general improvement in the resulting thermoelectric properties was observed for dip-coated samples, depending on the dip coating speed. This improvement is attributed to dip coating providing better overall packing and thus less disorder in the system. The resulting thermoelectric performance is comparable to that of other deposition methods that provide uniaxial alignment.

This dissertation consists of ten main chapters, including the introductory chapter, Chapter 1. Chapter 2 provides the main concepts relevant to the subsequent discussions. Chapter 3 presents the experimental setups, corresponding instrumentation, methods, and sample preparations. Chapter 4 characterizes the materials used. Chapters 5, 6, 7, 8, and 9 discuss the results of the project. Chapter 5 presents an investigation into improving the ferroelectric switching properties of BTA through dip coating. Chapter 6 deals with the Barkhausen noise simulated using kMC method in a BTA system and the influence of disorder on it. Chapter 7 continues the topic of Barkhausen noise, presenting its experimental observation in PVDF samples. Chapter 8 provides insight into the structural alignment and the resulting electrical conductivity of three TPA derivatives. Chapter 9 summarizes the dip coating of the polymer P3HT, which was used to study how the deposition technique affects the thermoelectric properties of P3HT devices. Each chapter begins with an explanation of the project's purpose and scope, followed by a discussion of the results and a summary. Since these results have been published, the corresponding manuscripts are referenced and the author's contributions are described in detail. Finally, Chapter 10 reflects on, discusses, and summarizes the overall findings.

Chapter 2

Theoretical background

This chapter aims to provide the necessary physical background for understanding the underlying theory of the research topics presented in this dissertation. It emphasizes how structural disorder affects the functional properties of organic ferroelectric and semiconductor materials.

2.1 Overview of structural disorder in organic materials

Although modeling perfectly ordered, periodic material structures can provide detailed information about band structures and orbital overlaps that can be used to predict transport properties, these structures are not an accurate representation of real materials. This section provides an overview of the different types of structural disorder generally present in molecular organic materials. More details on the influence of disorder on the ferroelectric and semiconducting materials are provided in Sections 2.2.6 and 2.3.3, respectively.

In general, solid-state materials inevitably contain structural disorder of various kinds, whereas in bulk or thin-film forms [35]. Even a perfect crystalline material with a regular, ordered crystal lattice structure is constantly disordered by the thermal motion of its atoms at finite temperatures. While thermal disorder can be well understood within the framework of statistical thermodynamics, additional structural disorder includes, but is not limited to, point defects, dislocations, grain boundaries, and grain surfaces, as shown in Figure 2.1.1. The concentration, spatial distribution, and interactions of these defects strongly influence the material's physical properties, such as electronic band structures, electrical and thermal transport properties, and density of states (DOS). These properties have been intensively studied in condensed matter and solid-state physics [33, 34, 36–38]. Although defects were historically believed to negatively impact the material properties, recent research demonstrates that desirable material performance can be achieved through proper defect engineering [39, 40].
Unlike perfect crystals, amorphous or "glassy" materials have a random and disordered atomic ar-

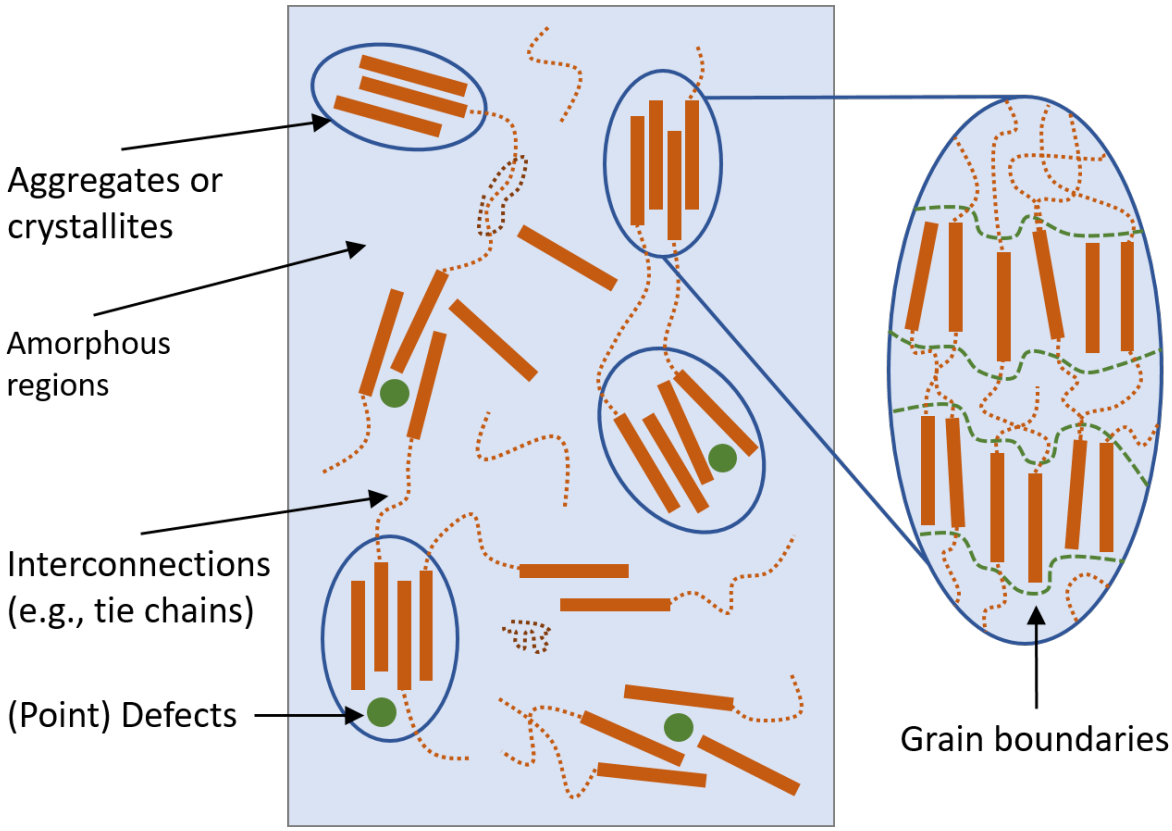

Figure 2.1.1: A schematic of a disordered polycrystalline material consisting of crystalline (ordered) and amorphous (disordered) regions with various interconnections and structural defects. The crystalline phase is represented by brown rectangles, and the larger ordered regions are marked by blue ovals. The interconnections are indicated by dotted brown lines. The amorphous phase is represented by light blue and is everywhere else. The (point) defects or grain boundaries are indicated by green circles or dotted lines, respectively. The schematic is not to scale.

rangement, resembling a liquid. They lack conventional long-range translational and orientational order. These materials are so structurally disordered that they cannot be considered perturbed or defective states of otherwise perfect crystals [41, 42]. The types of structural disorder generally depend on the specific material. Nevertheless, developing a comprehensive theory of amorphous materials and describing structural disorder is crucial to understanding its effect on different material properties. Various stochastic morphological models have been developed to provide rigorous mathematical descriptions of such disorder [43]. Furthermore, percolation models have been widely used to study the structural and transport properties of amorphous materials [44]. Because of their ordered or unordered structure, crystalline and amorphous materials typically respond differently to external factors, such as temperature or pressure. For instance, crystalline materials remain solid until they reach their specific melting point when heated, whereas amor-

phous materials gradually soften. However, most materials are neither perfectly crystalline nor fully amorphous. In addition to crystalline and amorphous materials, there are also polycrystalline and semicrystalline materials. These materials consist of crystallites (crystals or grains) separated by disordered regions, or grain boundaries [45], as shown in Figure 2.1.1. Nevertheless, categorizing materials solely by their type and degree of order is insufficient for characterizing all system's structures. Liquid crystals, for example, are a unique category discussed in more detail in Section 4.1.2.1.

Until now, only static disorder has been introduced. However, it is important to distinguish between dynamic and static structural disorder. As mentioned above, the energy levels within a material fluctuate over time due to the thermal vibrations of its molecules. These fluctuations lead to time-dependent variations in microscopic transport parameters, such as site energies, transfer integrals, and electronic couplings [46]. This fluctuation is referred to as dynamic disorder and is related to electron-phonon interactions that alter energy levels [46–48]. If all molecules had the same equilibrium conformation, as in a perfectly ordered crystalline system, then all time-averaged energy levels would be equal and only dynamic disorder would be present [46, 49]. However, in less-than-perfectly crystalline structures, such as most real materials, molecules are constrained to individual equilibrium conformations. This leads to a spread of time-independent site energies and transfer integrals. This spread is referred to as energetical and positional static disorder, or diagonal and off-diagonal disorder, respectively [46, 50]. Static disorder depends on the size, polarizability, and flexibility of the molecules; the response of energy levels to conformational charges; the degree of crystallinity; and dopants. The latter are especially important for organic semiconductors and their charge transport [51]. This dissertation only investigates static disorder.

In general, the above applies to both organic and inorganic materials. The main difference is the amount of disorder in the corresponding systems. Typically, the stronger the intermolecular forces, the more stable the bulk or lattice and the fewer defects present. In particular, the cohesive forces among molecules in organic molecular materials are relatively weak. This is evident when comparing the low melting points of most organic materials to the high melting points of typical inorganic salts, metals, semiconductors, and ferroelectrics [52]. Additionally, unlike in inorganic materials, non-bonded interactions, also known as steric effects, arise from the spatial arrangement of atoms in organic materials. These effects influence the variability in inter-atomic distances and angles of organic molecular conformations. While steric effects are not directly related to structural disorder, disorder in organic materials can exacerbate them. This affects a material's structure, particularly its ability to adapt to external perturbations [52, 53].

2.2 Ferroelectricity in organic materials

This section is based on various textbooks [54–56] and review articles [57–60] on the topic.

2.2.1 Overview of the ferroelectric phenomena

When an external electric field is applied to an insulator material, charges do not conduct throughout its bulk. However, the valence electrons shift from their equilibrium position due to the applied field. This leads to a macroscopic electric polarization of the material, which is referred to as a dielectric in this context [61]. Dielectric materials fall into two categories: polarizable and polar. Polarizable materials can be polarized by an external field, inducing polarization due to a change in electron positions. The polarization $\boldsymbol{P}$ is defined as the normalized volumetric dipole density

$$\boldsymbol{P} = \frac{\boldsymbol{M}}{V}, \tag{2.2.1}$$

where $\boldsymbol{M}$ is the total dipole moment of the material given by $\boldsymbol{M} = \sum_{\mathrm{i}} \boldsymbol{\mu_{\mathrm{i}}}$ with the individual dipole moments of the domains $\boldsymbol{\mu_{\mathrm{i}}}$, and V is the corresponding volume. For weaker fields and linear dielectrics, Equation 2.2.1 can be approximated as a linear dependence, given by

$$\boldsymbol{P} = \epsilon_0 \chi_{\mathrm{e}} \boldsymbol{E}, \tag{2.2.2}$$

with the vacuum permittivity ϵ_0, electric susceptibility χ_{e} and applied electric field $\boldsymbol{E}$. Electric susceptibility is a measure of how much a material becomes polarized in an applied electric field. It is defined by $\chi_{\mathrm{e}} = 1 - \epsilon_{\mathrm{r}}$ where ϵ_{r} is the relative permittivity or dielectric constant. Dielectrics are typically characterized by their dielectric constant ϵ, which is given as $\epsilon = \epsilon_0 \epsilon_{\mathrm{r}}$ for isotropic materials [2, 62]. In general, $\boldsymbol{\epsilon}$ is commonly referred to as the dielectric tensor, and χ_{e} is a complex number with frequency dependency, which is also a tensor in case of anisotropic materials [3]. Figure 2.2.1a shows a typical dielectric polarization as a function of an applied electric field.
Polar materials contain permanent dipoles that are inherent to their molecular structure. This generally occurs in heteronuclear diatomic molecules where there is a significant difference in electron negativity between the constituent atoms, which results in an asymmetric charge distribution. Examples include ionic species and water. The dipoles in these materials usually have random orientations that cancel each other out. However, when an external electric field is applied, the dipoles align with it. This creates macroscopic bulk polarization through the microscopic reordering of dipolar units and provides an additional contribution to the material's total polarization. Such materials are called paraelectrics. Once all dipoles are oriented, polarization saturates. Increasing the electric field further merely leads to more induced electronic polarization, as shown in Figure 2.2.1b. When the electric field is no longer applied, a paraelectric material typically depolarizes completely, reverts to its neutral, disordered state, and the polarization vanishes at zero field.

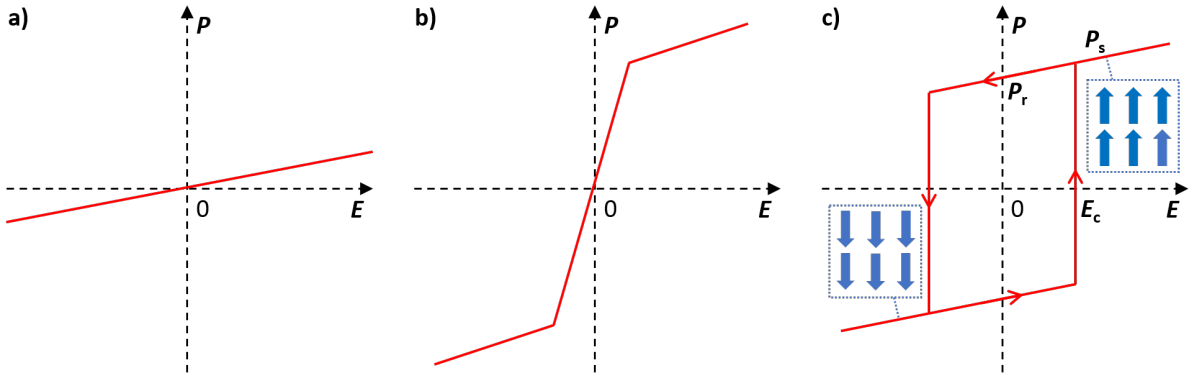

Figure 2.2.1: A schematic of the ideal polarization P as a function of the applied electric field E (red) for **a)** a dielectric, **b)** a paraelectric, and **c)** a ferroelectric material. The latter includes the coercive field E_c, the remnant polarization P_r, the saturation polarization P_s, and the indicated flipped dipole moments (blue).

However, for some materials containing permanent dipoles, the polarization does not vanish at zero field. This is attributed to the material's structure; the intrinsic dipoles are thermodynamically stable and maintain their alignment after the applied electric field is removed. The corresponding polarization value is referred to as the remnant polarization P_r. Materials in this subgroup of dielectrics have non-centrosymmetric dipolar ordering and are called ferroelectric materials. Their dipoles can be reoriented again by increasing the external electric field above a material-dependent threshold called the coercive field E_c. The polarization value that emerges when all dipoles are aligned is known as the saturation polarization P_s. Similar to ferromagnetism, this leads to a characteristic hysteresis loop, as shown in Figure 2.2.1c. Ferroelectric materials typically have low conductivity, similar to dielectrics; however, some have been shown to exhibit proper semiconductivity [63].

Ferroelectricity was discovered in Rochelle salt by Valasek in 1920 [12]. Ferroelectric materials exhibit switchable spontaneous electric polarization and a hysteresis loop (see Figure 2.2.2a). Despite their unique properties, ferroelectrics can lose their ferroelectric characteristics and revert to being paraelectrics. Heating a ferroelectric eventually causes it to undergo a phase transition from the ferroelectric to the paraelectric phase, accompanied by the loss of its polarization at a certain threshold. This phenomenon is described by the Landau theory, which is discussed in Section 2.2.2. This phase transition is accompanied by a divergence of the susceptibility at the transition temperature. Similar to ferromagnetism, this transition temperature is referred to as the Curie temperature T_C, and the susceptibility in the paraelectric phase follows the Curie-Weiss relation

$$\chi_\mathrm{e} = \frac{C}{T - T_\mathrm{C}} = \frac{1}{a_0\,(T - T_\mathrm{C})}, \tag{2.2.3}$$

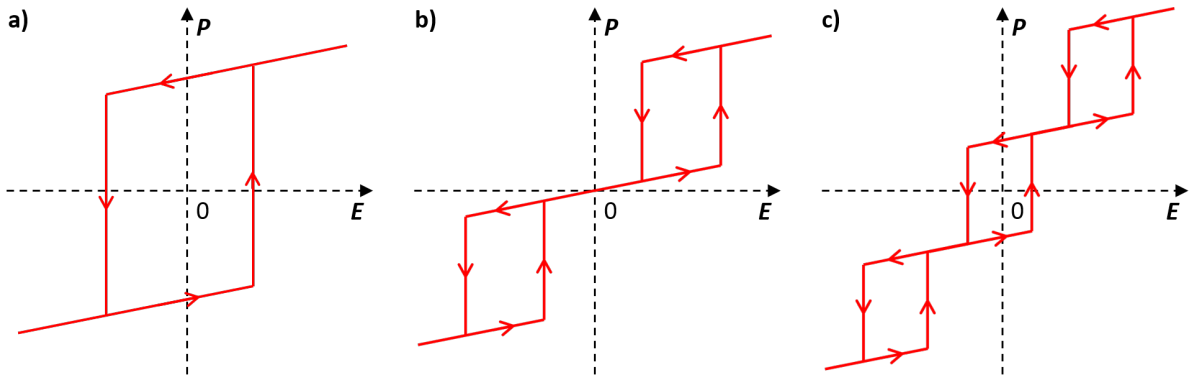

Figure 2.2.2: A schematic of the ideal polarization P as a function of applied electric field E (red) for **a)** a ferroelectric, **b)** an antiferroelectric, and **c)** a ferrielectric material.

where $C = a_0^{-1}$ is called the Curie constant. The parameter a_0 originates from the Landau theory, as discussed in Section 2.2.2. At the Curie temperature, the ferroelectric undergoes a phase transition accompanied by a change in its material structure and symmetry breaking. Thus, the former no longer satisfies the non-centrosymmetric condition [64]. Not only does the Curie temperature depend on the material, but it also increases with the applied electric field, which can complicate measurements near the Curie point [65, 66].

Ferroelectric materials can generally be separated into two categories: the displacive and order-disorder ferroelectrics [67, 68]. Displacive ferroelectrics, such as the prototypical ferroelectric barium titanate $BaTiO_3$, are characterized by a small ($\approx 1\%$ for $BaTiO_3$) net ionic displacement within the unit cell. This displacement forms spontaneously when the material transitions from the paraelectric phase to the ferroelectric phase. The polarization switching is accomplished by shifting ions in opposite directions from the cell center [69, 70]. Order-disorder ferroelectrics, on the other hand, are characterized by a transition from randomly oriented dipoles in the paraelectric phase to ordered dipoles in the ferroelectric phase [70]. These materials are the main focus of this dissertation.

When discussing ferroelectricity, it is usually assumed that all polarized dipoles point in the same direction. However, materials actually consist of multiple sublattices, some of which may have dipoles that are oriented antiparallel to each other, canceling out their total polarization. If all dipoles can still align in the presence of a large enough external electric field, the material is antiferroelectric. This leads to a characteristic double hysteresis loop, as shown in Fig 2.2.2b. Since an antiferroelectric has no polarization at zero applied field, it also loses its pyroelectric and piezoelectric properties in the absence of an external bias [71, 72]. Antiferroelectrics are assumed to have the same polarization for each sublattice. If this is not the case, then the antiparallel sublattices do not cancel out their polarization completely. These materials are called

ferrielectrics, which have a distinctive triple hysteresis loop, as presented in Fig 2.2.2c [73].

Furthermore, all ferroelectric materials are pyroelectric and, therefore, piezoelectric. This is because ferroelectricity requires a non-centrosymmetric structure. However, the reverse is not true [56, 57]. In summary, all ferroelectric materials are pyroelectric, all pyroelectric materials are piezoelectric, and all piezoelectric materials are dielectric. Antiferroelectric, pyroelectric, and piezoelectric properties are interesting on their own but are beyond the scope of this dissertation and will not be discussed further.

2.2.2 Landau-Devonshire theory

The two defining properties of a ferroelectric material are the polarization and bistable switching. The polarization is generally described by the dipole density; however, a different choice of the unit cell can result in different polarization directions in a bulk material. Therefore, changes in polarization are considered instead of absolute values [3]. The phenomenological Landau theory describes bistability and switching between the 'up' and 'down' states for bistable switching. Landau formulated it in 1937 to characterize generic continuous (second-order) phase transitions [74], and Devonshire adapted it to ferroelectrics in 1949 [75]. Landau theory uses a thermodynamic approach to express the Gibbs free energy density G of a given system as a power series expansion in the order parameter near an order-disorder phase transition. At this point, all strain effects are neglected. For ferroelectrics, the order parameter is the polarization P:

$$G - G_0 = \frac{1}{2}\alpha P^2 + \frac{1}{4}\beta P^4 - EP. \tag{2.2.4}$$

Here, the series goes to the fourth term. The coefficients α and β determine the nature of the phase transition. G_0 is the energy density of the unpoled ferroelectric state, which is typically considered zero. E is the external applied electric field. This truncated power series of the polarization yields a double-well free energy landscape for a continuous phase transition, as shown in Figure 2.2.3a in red.
It is usually assumed that $\alpha = \alpha_0 (T - T_C)$ is the only temperature-dependent parameter. In this definition, α_0 is a positive coefficient, and α changes sign at the Curie temperature T_C. Differentiating Equation 2.2.4 and setting it to zero minimizes the Gibbs free energy and yields the electric field E as a function of the polarization P at equilibrium:

$$\frac{\partial G}{\partial P} \stackrel{!}{=} 0 \Longrightarrow E = \alpha P + \beta P^3 = \alpha_0 (T - T_\mathrm{C}) P + \beta P^3. \tag{2.2.5}$$

The second derivative of Equation 2.2.4 provides the susceptibility χ_e when the polarization P is set to its equilibrium value at zero field. For $T > T_\mathrm{C}$, this yields $P_0 = 0$, indicating the paraelectric phase. Using the general relation from Equation 2.2.2 in Section 2.2.1, the Curie-Weiss relation $\chi_\mathrm{e}^{-1} = \alpha = \alpha_0 (T - T_\mathrm{C})$ is obtained, as shown for the paraelectric phase in Figure 2.2.3b.

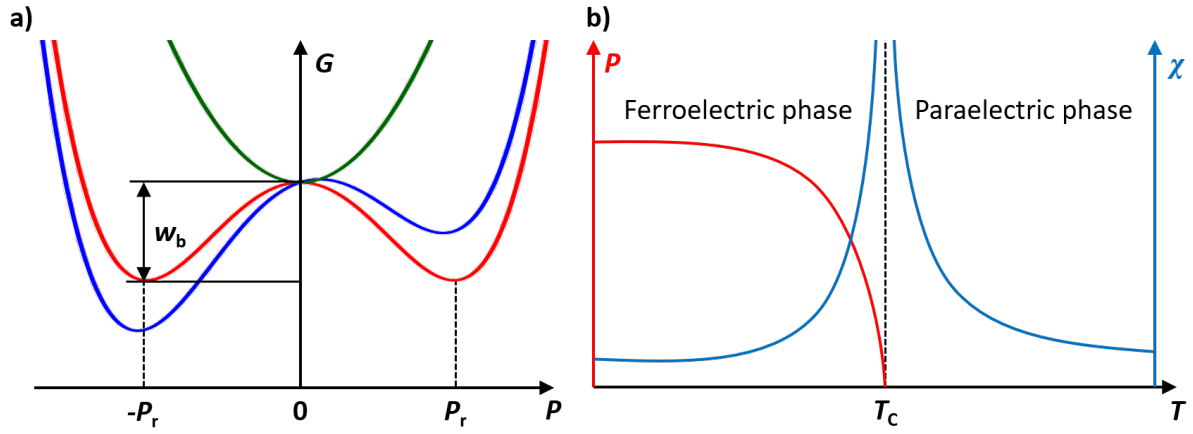

Figure 2.2.3: a) A schematic of the Gibbs free energy G as a function of polarization P according to Landau theory. The ferroelectric phase landscape changes with an applied negative electric field (blue) and without one (red). For the ferroelectric phase, the remnant polarization P_r and energy barrier w_b are indicated. The paraelectric landscape (green) is shown for comparison. **b)** A schematic of the polarization P and susceptibility χ as a function of temperature T illustrating the phase transition between the ferroelectric and paraelectric phases at the Curie temperature T_C. This phase transition is accompanied by a divergence of the susceptibility.

Below the Curie temperature, the nature of the phase transition is determined by the sign of β. When $\beta < 0$, a sixth-order term is required in Equation 2.2.4 to obtain a double-well potential below T_C. In this case, the transition is of first order, and both polarization and susceptibility are discontinuous at T_C. This case of first-order transitions has been investigated in detail [69, 76], but will not be discussed further here. The other simpler case of $\beta > 0$ is sufficient for understanding the mechanism, which yields two possible values for the spontaneous polarization at equilibrium at zero field:

$$P_0 = \pm\sqrt{\frac{\alpha_0}{\beta}\,(T - T_\mathrm{C})}, \tag{2.2.6}$$

and from that $\chi_\mathrm{e}^{-1} = 2\alpha = 2\alpha_0\,(T_\mathrm{C} - T)$ for the electric susceptibility. This corresponds to the ferroelectric phase curve shown in Figure 2.2.3b.
The free energy G landscape, as depicted in Equation 2.2.4, is shown in Figure 2.2.3a. Above the Curie temperature, the paraelectric phase is present. Below the Curie temperature and in the absence of an external electric field, two equivalent minima occur in the free energy landscape. This corresponds to the bistable polarization states of a ferroelectric material. These minima are separated by an energy barrier $w_\mathrm{b} = \alpha^2/\,(4\beta)$ obtained from Equations 2.2.4 and 2.2.6, which is typically significantly larger than the thermal energy of the system $k_\mathrm{B}T$, indicating the stability of the states. When an external electric field is applied, the two polarization states have different energies, and one becomes favored. In the energy landscape, applying an external electric field is

similar to a linear superposition, as of Equation 2.2.2 in Section 2.2.1. For weak electric fields, the ferroelectric system may remain in the unfavored state due to the energy barrier. Once a large enough electric field, corresponding to the intrinsic coercive field $E_c = \alpha\sqrt{\alpha/\beta}/4$, is applied, the polarization switches to the favored state [2, 3]. In reality, the experimentally observed intrinsic coercive field is typically significantly lower than the theoretical value [60, 77, 78]. This difference is attributed to a combination of thermal activation and nucleation processes - in other words, structural disorder dictates the nucleation growth process [3]. In most real organic materials, the polarization switches extrinsically rather than intrinsically. This means that multiple domains switch successively rather than simultaneously, as often happens in a nucleation process. This topic is discussed in more detail in Section 2.2.3.

2.2.3 Polarization switching

Ferroelectric materials typically exhibit a domain structure. Domains are macroscopic regions of aligned electric dipoles with spontaneous polarization. As previously mentioned, ferroelectric switching is characterized by a reversal of the spontaneous polarization that can be observed in a hysteresis loop, as depicted in Figure 2.2.1c in Section 2.2.1. Completely depolarized ferroelectric materials have randomly arranged dipoles and thus a zero bulk polarization. This is typically present in untreated ferroelectric materials because defects and depolarization tend to suppress the spontaneous polarization. Applying a steadily increasing electric field induces a linear energy offset, as shown in Figure 2.2.3a in Section 2.2.2. As the coercive field is approached, single dipolar domains begin to flip. This transfers into an avalanche of all remaining dipoles aligning with the applied electric field at the coercive field. This behavior is known as crackling or Barkhausen noise and is discussed in detail in Section 2.2.7. Once the applied electric field is large enough to switch all dipoles, the polarization saturates at the saturation polarization value P_s. However, in reality, polarization continues to increase with higher electric fields due to leakage and displacement currents. This topic is discussed further in Section 3.3.1.2. Decreasing the applied electric field toward zero typically causes the polarization to decrease slightly because real materials undergo a depolarization process in which the dipoles lose their alignment. At zero field, the remaining polarization value is the remnant polarization P_r.

The coercive field value E_c is not a universal material characteristic because it is influenced by the applied temperature, the sweeping rate of the applied field, the material's morphology, and device's structure [79, 80]. Therefore, direct comparisons of coercive field values should be made with caution. However, the polarization values are a valid metric for comparison as long as the material and device geometry are considered. Generally, every ferroelectric material has a unique hysteresis loop that can change depending on external factors such as temperature, the amplitude and frequency of the applied electric field, and chemical forces [58].

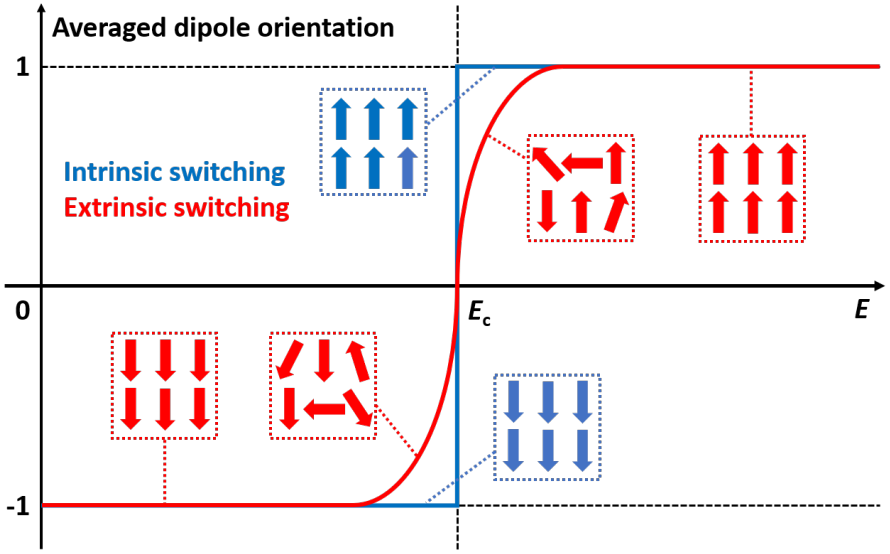

Figure 2.2.4: A schematic illustrating the difference between intrinsic (blue) and extrinsic (red) switching using the averaged dipole orientation - interchangeable with polarization - as a function of the applied electric field E. The colored arrows represent dipole domains and their orientations. Initially, a negative electric field poled all dipoles downwards, giving them a polarization value of $-P_s$. As a positive electric field is gradually increased, the domains flip direction at the coercive field E_c, reaching the saturation polarization value $+P_s$. However, the switching process differs for the two cases. Intrinsically, the domains switch instantaneously; extrinsically, switching occurs successively. Note that the x-axis is not representative of the timescale, and the coercive field value E_c is vastly different for the two switching mechanisms in a real material.

In idealized ferroelectric materials, polarization reversal occurs abruptly at the coercive field as most dipoles flip simultaneously. Thus, a single domain spanning the entire material is formed. However, in thin-film organic ferroelectric devices, polarization reversal is a nucleation-driven process in which many smaller domains are initially formed. These domains grow in response to the applied electric field, resulting in the consecutive switching of nearby domains over time. The former is known as intrinsic switching, and the latter is extrinsic switching. Note that the switching process does not inherently determine the timescale of the process. While intrinsic switching occurs almost simultaneously for all dipoles in the system, it can take time. The difference between the two switching processes is shown in Figure 2.2.4. For organic films, intrinsic switching can take seconds, whereas extrinsic switching typically takes microseconds and occurs at much lower fields [81, 82].

Furthermore, reversible and irreversible mechanisms of polarization switching can be distinguished [2]. The former includes the dielectric response and small polarization fluctuations around local energy minima, which are governed by intrinsic microscopic effects. Irreversible contributions

arise from switching between global polarization minima and are generally related to domain wall movements occurring on a macroscopic scale. According to the Landau model in Figure 2.2.3a in Section 2.2.2, reversible and irreversible switching correspond to fluctuations around a minimum and a transition from one minimum to another, respectively.

A key parameter to consider when evaluating ferroelectric materials for applications is the stability of the polarization state over time and in response to thermal variations. This stability is heavily dependent on the amount of disorder present in the system [2]. Polarization retention is typically considered the representative parameter that describes how quickly a poled ferroelectric material depolarizes or how much of the original remnant polarization remains after a certain amount of time. When a ferroelectric is polarized and the external electric field is switched off, the polarization in the bulk creates bound surface charges that generate a depolarization field of the opposite sign. As a surface effect, this is especially noticeable in thin films, while larger single crystals remain largely unaffected [83, 84]. The strength of the depolarization field F_{dep} depends on the remnant polarization and the dielectric screening properties of the material, i.e., its dielectric permittivity, and is given by $F_{\text{dep}} = -\frac{P_{\text{r}}}{\epsilon_0 \epsilon_{\text{r}}}$. If not compensated for, the depolarization field causes polarization loss in the material over time until full depolarization is reached, at which point all dipoles are randomly oriented and the bulk polarization value is zero. In real devices, charges on metal electrodes can compensate for the depolarization field. However, film inhomogeneities at interfaces, dead material layers, and a limited screening range diminish this compensation. Consequently, the depolarization field is typically significantly weaker than the uncompensated field [2, 3].

2.2.4 Analytical description of ferroelectric polarization switching

This subsection describes the macroscopic switching kinetics of ferroelectrics. It focuses on the analytical models relevant to this dissertation. For a more complete overview, see various textbooks, such as [85].

2.2.4.1 Kolmogorov-Avrami-Ishibashi model

The Kolmogorov-Avrami-Ishibashi (KAI) model is based on the crystallization theory work of Kolmogorov and Avrami [86, 87], which Ishibashi et al. further developed to describe ferroelectric domain switching in ferroic single crystals [88]. The model assumes a random nucleation throughout the material, followed by the growth of switched domains at a constant velocity under a constant applied electric field [85]. Furthermore, the nucleation growth velocity is considered the limiting factor in the switching process rather than the nucleation rate. This yields the following

expression for the polarization change ΔP as a function of time:

$$\Delta P\left(t\right) = 2P_{\mathrm{s}}\left(1 - \exp\left(-\left(\frac{t}{\tau}\right)^{d}\right)\right). \tag{2.2.7}$$

Here, ΔP saturates at the double saturation polarization $2P_{\mathrm{s}}$; τ is the characteristic switching time, which is inversely proportional to the domain wall speed; and d is the Avrami index, which is a dimensionality factor. There are two cases for the latter. In the case of simultaneous nucleation at the beginning of switching, d equals the dimensionality of the domain growth ($d = 1, 2, 3$). If nucleation continues throughout the switching process, the dimensionality of the growth is given by $d - 1$. Note that distinguishing between these two cases is not straightforward, so that d is often left as a fitting parameter [2, 85].
Ishibashi et al. further extended the KAI model to include frequency dependence on the probing signal frequency [89, 90]. This enabled the description of hysteresis loops and yielded a relationship between the coercive field E_{c} and the frequency of the applied electric field f:

$$E_{\mathrm{c}} \propto f^{d/\alpha}, \tag{2.2.8}$$

with the geometric factor α, which is empirical and depends on the waveform used.
While the KAI model successfully describes certain systems, primarily single crystals, it generally fails to explain switching in polycrystalline and semicrystalline thin films [85]. This is attributed to two assumptions of the model. First, it describes switching with a single switching time τ, second, it assumes that domain wall motion is the limiting factor in the switching process when it is often the nucleation process. Furthermore, the model does not consider how the applied electric field or temperature influence the switching process.

2.2.4.2 Du-Chen model

Du and Chen developed an alternative thermally activated nucleation-limited switching model [91], in which the nucleation rate was considered the polarization switching limiting factor rather than the domain wall propagation speed. The model assumes that domain walls are immobilized by a potential well in lower electric fields until a nucleus of sufficient size forms. After this occurs, the domain walls propagate. The model assumes $E_{\mathrm{c}} \propto f$, yielding a more physical expression that includes domain wall energy γ, the binding energy between structural defects and the wall γ_{b}, the change in polarization due to the domain wall passing ΔP, and a limiting domain switching frequency f_0, above which the nucleation rate is no longer the limiting factor:

$$E_{\mathrm{c}}\left(f, T\right) = B'/\sqrt{k_{\mathrm{B}}T \cdot \ln\left(f_0/f\right)} \quad \text{with} \quad B' = 2\sqrt{\pi}\gamma_{\mathrm{b}}\sqrt{\gamma}\Delta P. \tag{2.2.9}$$

Here, k_{B} is the Boltzmann constant, T is the absolute temperature, and the parameter B' is typically used as a fitting parameter. This model considers a temperature dependency in critical nucleus formation and significantly better describes coercive field versus frequency trends in polycrystalline thin-film ferroelectric materials compared to the KAI model [79, 92, 93].

2.2.4.3 Domain wall propagation models

The KAI model (see Section 2.2.4.1) provides an isotropic domain wall propagation for perfect crystalline materials. This can be extended by introducing defects, which are typically described as pinning centers. Encountering such a defect hinders the movement of the domain wall, reducing its speed and thus the polarization. Once the domain wall surpasses a pinning center, it encloses an unpolarized region, accelerating the polarization of the surrounding area. Therefore, the domain wall propagation becomes an irregular process described by the ABBM model, named after its authors, Alessandro, Beatrice, Bertotti, and Montorsi [94, 95]. While the ABBM models describes ferromagnetic materials, it is also applicable to ferroelectrics [96].
The ABBM model states that the domain wall propagation can be limited by various effects. These effects can be random or non-random. Random effects include pinning centers arising from defects in the material, while non-random effects include dipolar forces and demagnetization fields. The wall propagation velocity v is proportional to the first derivative of the magnetization M with the dampening factor Γ as the proportionality factor:

$$\Gamma \frac{\partial M}{\partial t} = H(t) - kM + W(M) = H(t) + H_\mathrm{d} + H_\mathrm{p}. \tag{2.2.10}$$

Here, $H(t)$ is the applied field, $-kM = H_\mathrm{d}$ is the demagnetization field with the demagnetization factor k, and $W(M) = H_\mathrm{p}$ is a function describing defects and impurities within the material. Typically, the latter is assumed to be Brownian correlated in the magnetization M [97].
The ABBM model is limited by its assumption of a singular domain wall throughout the entire material, which is rarely observed in reality due to materials typically exhibiting many domains. This leads to a switching process involving multiple nucleation centers that expand through domain wall motions after an initial spin flip. Furthermore, the ABBM model fails to reproduce non-universal features, such as the asymmetric shape of Barkhausen signals [97].

Cizeau et al. provided another description of the domain wall movement [98], comparing it to the movement of an elastic interface that strives to minimize its surface area while moving through the material. This movement is impeded by pinning sites present in the material. For ferroelectric materials, surface charges further obstruct the electrode/material interface, acting as an additional barrier that must be overcome to initiate domain wall movement. Assuming the critical force F_c is reached and thermal fluctuations are neglected ($T = 0$ K), the interface velocity v undergoes a second-order phase transition in external force F, representing the depinning regime:

$$v \propto (F - F_\mathrm{c})^\theta, \tag{2.2.11}$$

where θ is a fitting parameter. Assuming the pinning centers act as an energy barrier of magnitude ΔE leads to the domain wall propagation speed in the quasi-static regime:

$$v \propto \exp\left(-\frac{\Delta E}{k_\mathrm{B} T}\right) F. \tag{2.2.12}$$

As shown in Equation 2.2.12, the domain wall propagation speed increases linearly with driving force, but decreases exponentially with increasing temperature. When the driving force is very high, the system enters the linear flow regime, and the interface velocity scales linearly with the driving force.

2.2.4.4 Thermally-activated nucleation-limited switching model

Vopsaroiu et al. developed the thermally-activated nucleation-limited switching (TA-NLS) model, which combines the Landau-Devonshire theory and the KAI model [99, 100]. This nucleation-driven polarization switching model is more fundamental and describes the probability of nucleus formation while considering thermally-activated nucleation, the influence of an applied external electric field, and a depolarization field. It also assumes that a fixed number of nucleation sites are randomly distributed in the material at any given time. Starting from the Landau free energy landscape (see Section 2.2.2), the TA-NLS model considers switching between two states as overcoming the energy barrier w_b by combining temperature, the applied electric field, and the depolarization field. When an electric field is applied, the energy states shift by $\pm P_\mathrm{s} E_\mathrm{app} V$, where V is the volume of the nucleation site. Once the polarization reversal of a nucleation site reaches the critical volume $V = V^*$, which depends on the material and temperature, the nucleation domain rapidly expands until the bulk polarization is reversed. The time-limiting step is the time it takes a nucleation site to reach the critical volume, as opposed to the nucleation time or expansion rate. This time dependence is described by a non-equilibrium statistical model that is solved in terms of a master equation. The resulting polarization switching transient is equivalent to the KAI model result with $d = 1$ (see Equation 2.2.7 in Section 2.2.4.1). The corresponding switching time t_sw, which represents the time required for a nucleation site to reach the critical volume, is given by

$$t_\mathrm{sw}\left(E, T\right) = \nu_0^{-1} \exp\left(\frac{\left(w_\mathrm{b} - P_\mathrm{s} E\right) V^*}{k_\mathrm{B} T}\right), \tag{2.2.13}$$

with the Boltzmann factor k_B and the attempt frequency ν_0, which describes the number of attempts to overcome the energy barrier and is generally associated with the typical phonon frequency of the material [85]. From Equation 2.2.13, an expression for the coercive field can be derived:

$$E_c\left(\nu_\mathrm{exp}, T\right) = \frac{w_\mathrm{b}}{P_\mathrm{s}} - \frac{k_\mathrm{B} T}{V^* P_s} \log\left(\frac{\nu_0 t_\mathrm{exp}}{\log\left(2\right)}\right), \tag{2.2.14}$$

where $t_\mathrm{exp} = \nu_\mathrm{exp}^{-1}$ is the experiment duration, i.e., the inverse of the voltage sweeping frequency ν_exp. In Equation 2.2.14, the first term represents the intrinsic coercive field, and the second term equals the extrinsic reduction due to thermal activation of the nucleation process.
The TA-NLS model has generally been successfully applied to a wide variety of materials, including BTA [79, 101] and PVDF [2].

2.2.5 Preisach model

A simple description of disorder in ferroelectric materials originates from the corresponding description in magnetism, provided by Franz Preisach in 1935 [102], which has been shown to apply to most hysteretic systems, including ferroelectrics [103–105]. The Preisach model is primarily mathematical, but when combined with physical formalism, it can fully define the dynamic and static characteristics of disordered ferroelectric materials, taking into account a given material's morphology [2, 105]. Thus, it is a powerful tool that provides a physical explanation for the partial switching observed in real ferroelectric materials.

The Preisach model assumes that the macroscopic ferroelectric bulk consists of a distribution of small single units called hysterons. Hysterons are conceptual entities that can be seen as dipolar domains. They are independent microscopic polarization units with ideal rectangular polarization hysteresis loops. Each hysteron has its own local energy landscape representing a potentially asymmetric Landau-Devonshire double-well potential (see Section 2.2.2). This potential is characterized by discrete 'up' and 'down' switching field values, denoted as U and V, which define its position on the corresponding Preisach plane. By construction, a hysteron's polarization hysteresis loop has a polarization of unity. In real ferroelectric materials, hysterons differ in shape due to varying electrostatic environments, as depicted in Figure 2.2.5a. The distribution of switching field values provided by hysterons is usually assumed to be a statistical double Gaussian around the macroscopic coercive field. However, it can vary significantly based on morphology due to defects such as internal biases [106]. The sum of all hysterons yields the macroscopic polarization of the ferroelectric bulk. An average coercive field is obtained from $E_\mathrm{c} = \frac{U-V}{\sqrt{2}}$, and an imprint field that describes the deviation from the former is given by $E_\mathrm{i} = \frac{U+V}{\sqrt{2}}$. Together, these two field values provide an alternative description of the hysteron properties and correspond to a coordinate transformation of U and V, as shown in Figure 2.2.5b. While the shown distribution is spherical, it can also be ellipsoid and offset from the center, depending on the material [105]. Generally, the slope of a polarization hysteresis is determined by the width of the corresponding Preisach distribution in a ferroelectric; that is, intrinsic switching would have a delta-like Preisach distribution.

Furthermore, Urbanaviciute et al. unified the Preisach and TA-NLS models to describe the polarization switching process in disordered organic ferroelectrics [105]. They demonstrated that each hysteron can be described by the TA-NLS model, which has its own critical volume and switching time. This explains the dispersive switching kinetics observed in various organic ferroelectric materials, which can be traced back to a distribution of hysterons' switching times.

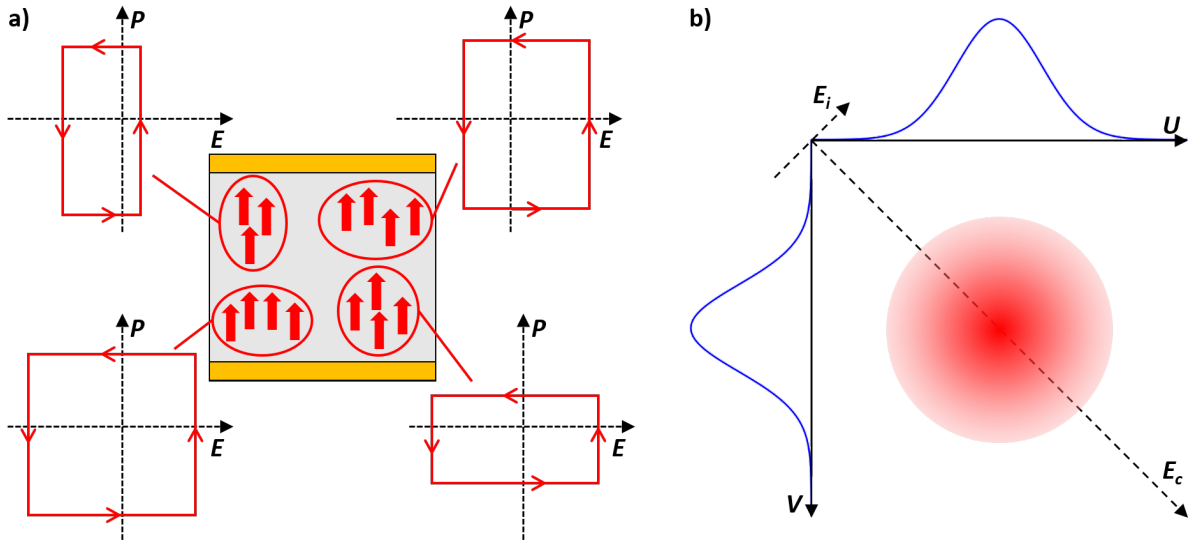

Figure 2.2.5: a) A schematic depiction of single hysterons (circled in red) that are randomly distributed in a switched ferroelectric bulk (gray area), which is located between electrodes (yellow areas), as well as the corresponding polarization hysteresis loops. The exact shapes of the hysteresis loops are merely examples and should not be directly related to the hysteron distributions shown. **b)** A schematic of the double Gaussian distribution N of the hysterons' switching field values (red circle) within the 'up' (U) and 'down' (V) switching fields, as well as the average macroscopic coercive field E_c and the imprint field E_i planes. The intensity of the color of the distribution represents the number of the hysterons in the $N(U,V) = N(E_\mathrm{i}, E_\mathrm{c})$ distribution for a given (U,V) or $(E_\mathrm{i}, E_\mathrm{c})$ pair, respectively.

2.2.6 Structural disorder in ferroelectrics

For ferroelectrics, the complete elimination of disorder results in an elusive ideal: immediate and fully defined intrinsic ferroelectric switching [107, 108]. Deviation from intrinsic switching originates from morphological issues caused by pores, grains, structural defects, crystal lattice defects, ionic impurities, vacancies, and other impurities and homogeneities [2]. These defects negatively affect ferroelectric characteristics such as switching speed, coercive fields, remnant and saturation polarization, and stability. Specifically, the influence of common positional disorder in the form of translational and orientational offsets has been demonstrated in BTA and P(VDF:TrFE) systems, both experimentally and via simulation [105, 109]. In general, hysteresis loops and macroscopic switching kinetics are influenced by device morphology and energetic disorder. It is well-established that introducing structural disorder broadens the Preisach distribution shape (see Section 2.2.5), which is directly related to the size of the ferroelectric domains and the electrostatic interactions between them. These interactions also influence the switching time. Structural disorder interrupts long-range interactions within materials, leading to

different nucleation processes and, consequently, switching kinetics, as nucleation typically tends to occur at defects. Furthermore, each ferroelectric domain may have its own coercive field, causing the hysteresis loop to become more slanted. Increased structural disorder results in weaker or shorter-ranged interactions, which widens the coercive field distribution and makes the hysteresis loop more slanted [109]. Furthermore, introducing more structural disorder significantly decreases polarization retention, which is generally undesirable, especially for applications. Nevertheless, disorder can provide new functionality in ferroelectric materials [2]. One possibility is to use partial poling by electrically treating different parts of the Preisach plane. While the stability of these intermediate states may be insufficient in some systems, others, such as P(VDF:TrFE), allow for long-lasting partial poling while providing sufficient polarization retention [110]. This has been used to create multi-bit ferroelectric memory devices [105, 111]. Additionally, the greater the disorder in a ferroelectric system, the more intermediate states are available for a multi-bit memory [105].

2.2.7 Barkhausen noise

Physical systems typically exhibit specific length scales that characterize the events occurring within them. In critical systems, the events occur on all possible length scales, and the corresponding critical behavior often exhibits a power-law distribution of the event sizes. While the presence of a power-law distribution is insufficient to conclude criticality, it is required for criticality to occur [112, 113]. A physical system driven by an external force may respond to a perturbation in multiple ways depending on its internal structure, the strength of the driving force, and especially the degree of structural disorder. Two possible responses are snapping and popping. The former is represented by a large, singular event that propagates throughout the entire system and can be considered an intrinsic case. The latter is represented by a large number of small events of similar amplitude and typically occurs in a disorder-dominated system. Based on the interactions within the system, the intermediate or crackling case represents transitional behavior between popping and snapping [114]. In this case, sudden, jerky events with a wide distribution of amplitudes, durations, and energies occur.

The mean field plasticity (MFP) model provides a theoretical description of Barkhausen noise. Originally applied to materials under shear stress that displayed step-like stress-strain curves with material-independent power-law event size distributions, this model has since been used to describe a variety of materials [115]. Similar to crackling, popping, and snapping noise, these materials exhibit different behaviors depending on how their parts are coupled. The MFP model assumes that slip initiation occurs once the local failure stress τ_f is overcome and continues until the local stress falls below the sticking stress τ_s. Due to structural disorder in real materials, however, both quantities vary depending on the location within the material. Initial slip alters the local stress, which can induce further slips in adjacent areas. This leads to an avalanche that

propagates through the material as an external force F slowly increases the stress and causes the medium to deform elastically. Using mean field theory, the evolution of the accumulated slip $u(r,t)$ can be described by

$$\eta \frac{\partial u(r,t)}{\partial t} = F + \sigma_{\text{int}}(r,t) - f_{\text{r}}\left(u, r, u\left(r, t' < t\right)\right), \tag{2.2.15}$$

with the friction coefficient η, the failure stress distribution f_{r}, and the shear stress σ_{int}. In accordance with the domain wall propagation models (see Section 2.2.4.3), the solution of Equation 2.2.15 predicts a power-law distribution of all sizes with an exponential cut-off [116].

In ferroelectric materials, crackling noise manifests as Barkhausen noise, which arises from the irregular movement of domain walls in response to an applied electric field and temperature [117]. Since ferroelectrics are critical systems that generally exhibit universality, the MFP model has been linked to switching processes in soft ferroic materials [118]. Thus, a step-like stress-strain curve is established, representing the step-like motion of a domain boundary (domain wall). This motion results from a competition between a driving force, such as an increasing electric field, and a stopping force associated with pinning at structural defects [115, 118]. This implies that data collected over the entire hysteresis loop aligns with stress-integrated exponents, while data taken solely around the coercive field corresponds to the non-stress-integrated values [119, 120]. The resulting events are discrete and vary widely in size; their distributions typically follow a power-law distribution on large scales [114, 121]. In our case, the critical behavior is observed near the coercive field, where a change in the external electric field causes dipoles to switch, thereby changing the polarization [96]. The critical exponents are stress-dependent. The critical exponents that typically result from the power-law describing the event size distribution τ, and energy distribution ϵ, are $3/2$ and $4/3$, respectively [115]. Although the exact exponents vary among different materials, their overall similarity suggests universality in systems exhibiting Barkhausen noise [96, 122–125], which is generally interpreted as a dynamical critical phenomenon [114, 121]. Thus, Barkhausen noise can be used to probe critical behavior in the presence of a power-law by checking the value of the exponent. Furthermore, noise spectroscopy via Barkhausen noise measurements allows one to investigate the internal structure and cooperativity of ferroic materials by examining the spectral distribution of events, which is determined by the (relative) strength of disorder. Thus, intrinsic switching in an ideal, fully ordered ferroelectric material would result in a single snapping event spanning the entire volume. In contrast, a ferroelectric material dominated by disorder would barely exhibit any correlations, leading to popping noise.

2.3 Organic semiconductors

The fundamentals provided in this section are a brief summary of the more detailed descriptions found in various textbooks, such as [126–129].

2.3.1 Carbon *sp*-hybridization

Since organic semiconductor materials are carbon-based, like all organics, their charge transport is based on the electronic structure of the carbon atom [127]. In its ground state, atomic carbon has six electrons, two of which occupy the 1s, 2s and 2p orbitals. The 2p orbitals are subdivided into $2p_x$, $2p_y$, and $2p_z$ orbitals. Depending on the configuration of their surroundings (i.e., the number and nature of neighboring atoms), carbon atoms can bind with other atoms. The concomitant external forces compensate for the energy difference between the 2s and 2p orbitals, rendering them degenerate. This process is referred to as orbital hybridization [127, 130]. This leads to the formation of new hybrid orbitals, which are a linear combination of the 2s with 2p orbitals. These hybrid orbitals are referred to as sp, sp^2, and sp^3 orbitals, depending on the number of p orbitals participating. The corresponding bond geometries are linear, planar, or tetrahedral, respectively. The initial slight decrease in energy due to the formation of molecular hybrid orbitals results in a large gain of negative binding energy after hybridization is complete, leading to a reduction in total energy due to hybrid orbital overlap. Materials with sp^3-hybridized carbon atoms form so-called σ-bonds via the overlap of all four sp^3 orbitals. These orbitals possess highly localized electrons and are strongly bound. These materials are usually insulators, as with diamond, for example [131].
Meanwhile, sp^2-hybridized carbon atoms lead to the formation of a partially delocalized electron system. The sp^2-hybridized orbitals form three highly stable σ-bonds in the xy-plane at 120° angles, while the non-hybridized p_z orbital is orthogonal to that plane. This orbital can form a bond with a neighboring p_z orbital, creating a significantly weaker π-bond. This form is found in the molecule ethylene [127], depicted in Figure 2.3.1a. Furthermore, the corresponding binding energies are energetically split into bonding and antibonding molecular orbitals, as shown in Figure 2.3.1b.
Each p_z orbital contains one electron and overlaps with two neighboring orbitals. Thus, the electron states are delocalized, a phenomenon referred to as π-conjugation. Therefore, when considering multiple carbon atoms within a molecule, it is not possible to localize the electrons of the π-orbitals exactly. This leads to a delocalized π-electron system, which is the basis for the semiconducting properties of organic materials [132].

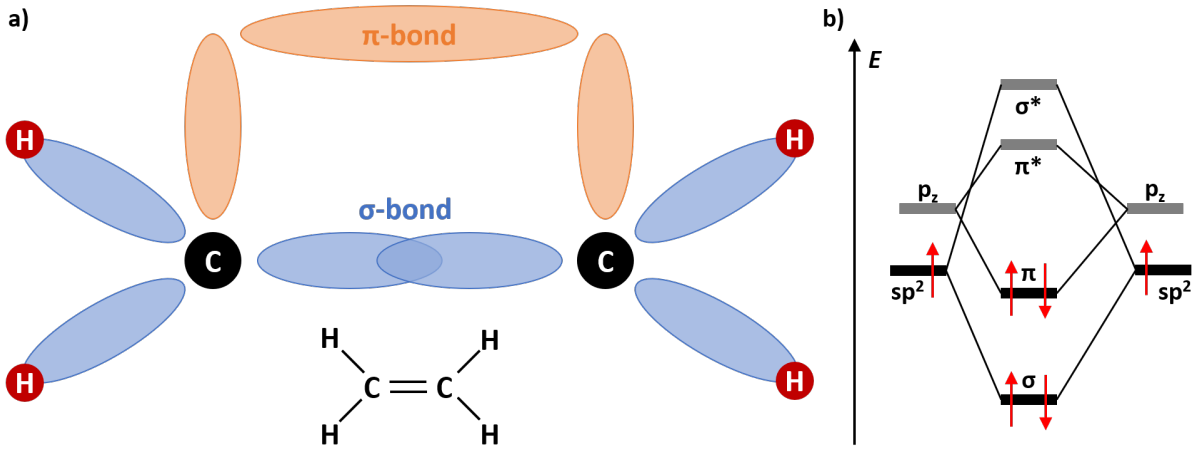

Figure 2.3.1: a) A schematic depiction of the sp^2-hybridization in ethylene, with the chemical structure shown in the inset. For easier representation, this depiction does not consider the 120° angle between the σ-bonds. The overlap of either two sp^2 orbitals (blue) or two p_z orbitals (orange) results in the formation of the σ- and π-bonds, respectively. **b)** The corresponding binding energies, with the occupied states symbolized by red arrows. Sp^2 orbital overlap leads to the formation of a binding σ and an anti-binding σ^* orbital, which are energetically separated. Similarly, the two electrons in the p_z orbitals create a binding π and an anti-binding π^* orbital. The latter are less separated due to smaller spatial overlap.

2.3.2 Charge transport

The electrical, optical, and thermal properties of organic devices are influenced by, among other factors, electronic charge transport in the organic materials [129]. The efficiency of charge transport depends on the energetic and spatial order of the molecules, as well as their interactions with each other and the interface. This is described by the DOS of the given material. In highly ordered or crystalline organic materials, charge carriers are typically delocalized across several neighboring molecules. This yields a delocalized band situated energetically at either the lowest unoccupied molecular orbital (LUMO) or the highest occupied molecular orbital (HOMO), depending on whether electron or hole transport is occurring. Charge transport occurs via charge carriers hopping between closely spaced molecules that form a crystalline stack [129]. In polycrystalline or amorphous organic semiconductors, charge transport is more related to the density of localized states. Depending on the degree of disorder and the position of the Fermi energy within an organic semiconductor, charge transport involves either the density of delocalized or localized states only, or both simultaneously [129]. These are described by different charge transport theories. In an undisturbed and fully ordered organic system or one with a Fermi energy level above the delocalized states (i.e., all trap states are filled), the charge carriers behave like free particles moving within the delocalized DOS, and the basic Drude model applies. For charge

transport in polycrystalline organic materials with a medium level of structural disorder, both localized and delocalized states must be considered. This is described by the multiple trapping and release (MTR) model. As neither of these cases is relevant to the organic materials included in this dissertation, a description of these models is omitted here.

The most relevant case for this dissertation is charge transport in fully disordered organic semiconducting material, which are common in organic devices. It is generally accepted that the charge transport occurs via incoherent tunneling or hopping of electrons and/or holes between strongly localized states that are randomly distributed spatially and energetically [133–135]. Charge hopping between two small molecules or subconjugated units of a polymer can be described as thermally assisted tunneling process with an equivalent energy site E_s and a corresponding position r_s. Initially, a charge carrier occupies a site i with energy E_i and position r_i, and site j is unoccupied. In theory, the charge carrier can hop to site j via quantum tunneling due to thermal fluctuations. After absorbing a phonon with energy ΔE, the carrier's energy increases to $E = E_\mathrm{i} + \Delta E$, thus increasing the probability of hopping from site i to site j. Ultimately, the charge carriers will be at energy E_j and position r_j. This process can be described by combining a tunneling term, which describes the wavefunction overlap of the two sites and can be approximated as $\exp\left(-2\alpha r_\mathrm{ij}\right)$, where α is the inverse of the localization length of charge carriers in localized states, r_ij is the hopping distance, and an exponential decay of the wavefunction tails occurs, with a thermal activation term. In the case of $E_\mathrm{i} < E_\mathrm{j}$, which corresponds to an energetically upward hop, the energetic difference between the two sites is provided by phonons. Thus, the total hopping probability depends on the number of phonons with energy $\Delta E = E_\mathrm{j} - E_\mathrm{i}$. Assuming a Boltzmann distribution for the phonons, the thermal activation term is given by $\exp\left(\Delta E / \left(k_\mathrm{B} T\right)\right)$. For energetically downward hops with $E_\mathrm{j} < E_\mathrm{i}$, no thermal activation is required, and hopping depends only on the tunneling term. Miller and Abrahams formulated the total hopping probability in 1960 [136], which is now referred to as the Miller-Abrahams hopping rate

$$\nu_\mathrm{ij} = \nu_0 \exp\left(2\alpha r_\mathrm{ij}\right) \times \begin{cases} \exp\left(-\frac{E_\mathrm{j} - E_\mathrm{i} + \left|E_\mathrm{j} - E_\mathrm{i}\right|}{2 k_\mathrm{B} T}\right), & \text{if } E_\mathrm{i} < E_\mathrm{j} \\ 1, & \text{if } E_\mathrm{i} \geq E_\mathrm{J} \end{cases}, \tag{2.3.1}$$

with the phonon vibration frequency ν_0, which is related to the interaction mechanism responsible for the hopping transition, and can be understood as the attempt-to-jump rate that is often set to a constant value [135–137], the Boltzmann factor k_B, and the temperature T. According to Equation 2.3.1, hopping does not have to be to the nearest neighbor. Rather, it is a process that depends on material parameters and temperature and balances between short hops (small spatial distances and large energetic differences) and far hops (large spatial distances and small energetic differences).

The expression in Equation 2.3.1 leads to the variable-range hopping (VRH) model for charge transport in disordered organic semiconductors, which is depicted in Figure 2.3.2 for a Gaussian

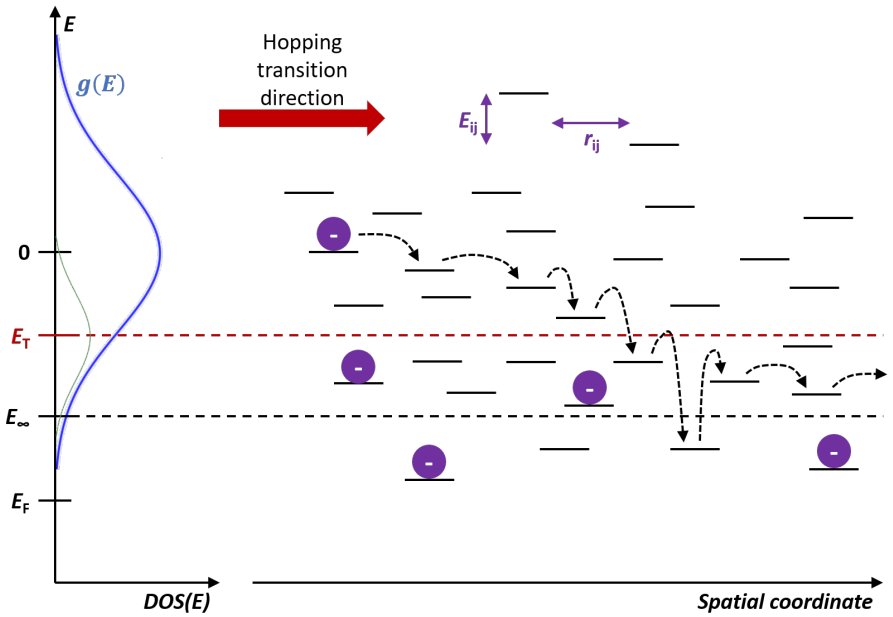

Figure 2.3.2: A schematic depiction of a downward charge carrier hopping process near the transport energy E_T within a Gaussian DOS in space and time. The charges, the Gaussian distribution of localized states, the carrier density, and the transport energy E_T are indicated in violet, blue, green, and red, respectively. The zero energy ($E = 0$) is chosen arbitrary. Over time, the charge carrier approaches the equilibrium energy $E_\infty = -\sigma^2/(k_\mathrm{B}T)$. During the hopping process, the charge carrier avoids occupied states, which are indicated in the schematic.

DOS. The VRH model assumes that the charge transport occurs through hops between localized states, which are predicted to occur via thermal activation. The model yields the following characteristic temperature dependence for conductivity σ in a disordered semiconductor:

$$\sigma = \sigma_0 \exp\left(-\left(\frac{T_0}{T}\right)^{\beta}\right), \tag{2.3.2}$$

where σ_0 and T_0 are constants and β is a parameter depending on the exact model. For the Mott VRH model, $\beta = 1/4$ is used for the three-dimensional conductance. While percolation theory may provide a better understanding of conductivity in disordered semiconductors, especially at lower temperatures, it goes beyond the scope of this dissertation and will not be described further.

2.3.3 Structural disorder in semiconductors

In general, organic thin-film electronic devices are susceptible to significant structural disorder and chemical defects [46]. Different packing densities and composite structures are expected to provide varying transport properties. In semiconducting polymers, variations in the polymer chain length and the presence of charged species, as well as conformational defects in the polymer

backbone (e.g., kinks and twists) and chemical defects, lead to significant variations in site energies because charge carrier delocalization is generally limited by defects [138]. This energetic disorder is essentially unavoidable and is generally considered a material property arising directly from the morphological or structural features of the organic semiconductor. Since structural defects occur randomly, they lead to a distribution of delocalization lengths of charge carriers. Since the energy of the charge carriers depends on both the degree of delocalization and the varying dielectric environment, there is usually a broad energy level distribution.

For organic semiconductors, both the static and dynamic disorders (see Section 2.1) affect charge transport properties, albeit differently. Static disorder is always detrimental to charge transport, while dynamic disorder can enhance transport properties by contributing to charge-carrier mobility via phonons in certain scenarios [8, 46]. When weak electronic couplings are considered, meaning charge transport can be described by a hopping mechanism, the Marcus electron transfer model is often assumed. In this model, static disorder is accounted for by site energies (energetic disorder) and transfer integrals (positional disorder). Dynamic disorder is characterized by reorganization energy [46, 139]. Static disorder describes how the energy and distance of individual carrier sites vary locally. This has already been considered in the discussion of charge transport in Section 2.3.2 and will be elaborated on further below. Dynamic disorder is associated with polaron propagation described by Marcus hopping [140] and will not be discussed further here.

In amorphous molecular solid materials, the distribution of orbital energies across all molecules in a given system is usually represented by a Gaussian distribution. This distribution results from the overlap of individual orbital energies. The most prominent model describing disordered charge transport is the Gaussian disorder (GD) model, introduced by Bässler [134] and subsequently expanded upon. The GD model assumes that charge carriers hop along sites with an energetic and spatial spacing described by a Gaussian distribution. The resulting distribution includes a material-dependent standard deviation σ, which is often referred to as (global) energy disorder in the GD model [49, 134]. The disorder parameter σ provides a measure for the disorder's strength. The corresponding Gaussian DOS of bulk organic semiconductors is then given by

$$g\left(E\right) = \frac{N_0}{\sqrt{2\pi}\sigma} \exp\left(-\frac{\left(E - E_0\right)^2}{2\sigma^2}\right), \tag{2.3.3}$$

with the energy of the site E, the mean energy E_0, and the concentration of the localized states N_0, as shown in Figure 2.3.2 in Section 2.3.2. Note that, although Equation 2.3.3 includes energy, it is different from the extended Gaussian disorder (eGD) model, which arises from the dependence of the charge carrier mobilities on temperature and provides a similar Gaussian shape for $\mu\left(T\right)$ for $\beta = 2$ in Equation 2.3.2 in Section 2.3.2.

Chapter 3

Experimental methods

This chapter provides an overview of the experimental aspects of the work presented in this dissertation. The sample preparation section details the fabrication of the samples used for measurements. The deposition method section describes the techniques employed for thin film device fabrication, with an emphasis on dip coating. Finally, the experimental methods are thoroughly explained by discussing the theory behind the measurements and introducing the setups used for them.

3.1 Sample preparation

This section describes the sample preparation processes for the various measurements. The substrate cleaning process is described separately in Section A.1.

3.1.1 Structural characterization on glass substrates

To determine the film thickness and obtain structural characterization, pure glass substrates without deposited electrode structures were used. The substrates were cut from commercially available 75 mm × 25 mm Corning plain microscope slides, which had a thickness ranging from 0.96 to 1.06 mm, using a glass cutter. The final dimensions of the glass substrates were either 10 mm × 25 mm or 15 mm × 25 mm. After cleaning the substrates, the material was deposited on top of them.

BTA-C_8 on glass samples were dip coated using solutions of 5, 10, and 40 mg ml^{-1} BTA-C_8 in chloroform (CF, solvent supplied by VWR Chemicals; $\geq$ 99.0% purity), which were annealed at 40 °C for 15 min after mixing and before deposition. The dip coating withdrawal speeds ranged from 0.1 to 150 mm min^{-1}. BTA-C_8 reference samples were typically drop cast $2 \cdot 5$ μl per sample from the same solutions.
P3HT pure glass samples were either dip coated or spin coated using 5 or 10 mg ml^{-1} P3HT

in CF or orthodichlorobenzene (ODCB, solvent supplied by VWR Chemicals; $\geq 99.0\%$ purity). The solutions were stirred at 70 °C for 24 h to ensure complete dissolution. Spin coating was performed dynamically using the same P3HT solutions inside a glovebox with a nitrogen atmosphere. Spin coating speeds ranged from 1000 to 10000 rpm for 60 s for both solvents to control the final thickness of the samples. For dip coating, the withdrawal speeds were $2 - 150$ and $0.1 - 3.5$ mm min^{-1} for CF and ODCB, respectively.

3.1.2 Ferroelectric characterization

3.1.2.1 Out-of-plane devices

The out-of-plane samples used for ferroelectric characterization consisted of crossbar electrode geometries, as depicted in Figure 3.1.1a and b for side and top views, respectively, as well as the material in between. The bottom electrodes were typically $3 - 5$ nm of chromium with $50 - 70$ nm of gold or aluminum on top. The top electrodes were evaporated onto the material film and were identical to the bottom electrodes, except without the chromium layer. The material evaporation process was carried out from evaporation boats in a thermal metallic evaporator (Mantis Deposition LTD Evaporator) at pressures lower than $5 \cdot 10^{-6}$ mbar using shadow masks. During evaporation, the substrates were rotated at 10 rpm to ensure homogeneous evaporated material deposition. Built-in software (Titanium Software) steered the evaporation rate, which was typically ≈ 0.1 and ≈ 0.5 Å for chromium and gold or aluminum, respectively. The substrate and evaporation mask sizes were 2.5 cm × 2.5 cm, and each sample consisted of nine devices. Three different electrode widths (0.2, 0.5, and 1.0 mm) were used for both the top and bottom contacts so that each sample included all nine possible combinations of top and bottom electrodes. To contact the bottom electrode, either the electrode was cleaned of material, or the material was pierced by the probe needles. Depending on the sample, silver paste was applied to the top electrode to ensure good contact.

BTA-C_8 was spin coated statically at 900 rpm for 45 s from a solution on top of the bottom electrodes. ≈ 150 μl of solution was deposited per sample at room temperature. The solution used was 40 mg ml^{-1} BTA-C_8 in CF and was annealed at 40 °C for 15 min after mixing. After deposition, the samples were annealed at 70 °C for 15 min to improve film quality. The typical film thickness was $\approx 350 - 450$ nm.
P(VDF:TrFE) thin films were statically spin coated on top of the bottom electrodes at 1000 rpm for 45 s and then at 4000 rpm for 15 s from a 60 mg ml^{-1} PVDF:TrFE in cyclohexanone (CHN, solvent supplied by VWR Chemicals; $\geq 99.0\%$ purity) solution. This solution was stirred overnight and filtered before spin coating. ≈ 150 μl of solution was deposited per sample at room temperature. The deposited films were annealed at 140 °C for two hours to promote crystallinity in the ferroelectric β-phase, yielding typical film thicknesses of $\approx 400 - 500$ nm.

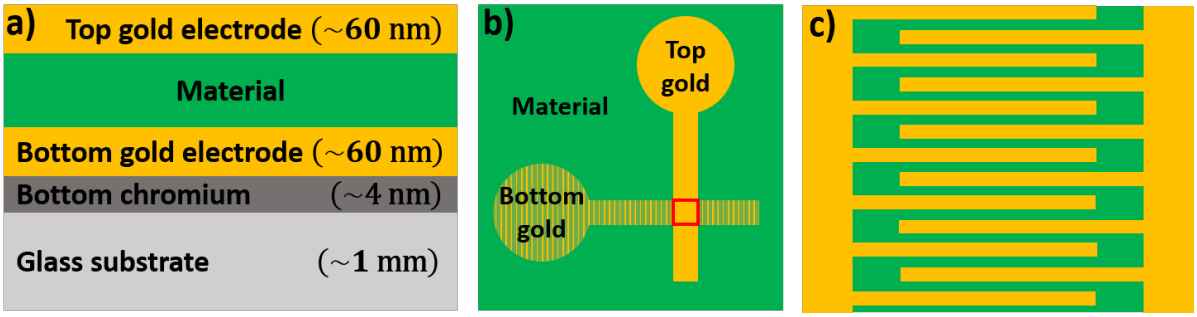

Figure 3.1.1: A schematic depiction of the device structures used for ferroelectric characterization. **a)** A side view and **b)** a top view of out-of-plane samples. The material film was spin coated on top of the bottom electrodes. **c)** A top view of the IDE structure without the contacting pads, which are connected directly to the electrodes shown. The electrodes (yellow) are deposited directly onto the substrates, and the material film (green) was either drop cast, spin coated, or dip coated on top of the electrodes. All IDE structures used had both the electrode widths and distances between electrodes of 5 μm.

3.1.2.2 In-plane devices

Most ferroelectric characterization measurements were carried out with thin films deposited on glass substrates patterned with in-plane interdigitated electrodes (IDEs). Two types of IDEs were used: commercially available IDEs from MicruX Technologies with an electrode width and spacing of 5 μm and a height of 150 nm gold on top of 50 nm titanium, and homemade IDEs produced by photolithography. The latter have an electrode width and spacing of 5 μm and a height of 25 nm gold on top of 5 nm chromium. The evaporation process was performed using an electron-beam evaporator (Winter Vakuumtechnik GbR HVB-130), which had an evaporation rate of ≈ 0.1 and ≈ 0.5 Å for chromium and gold, respectively. While the author of this dissertation contributed to developing the photolithography process, two other members of the research group produced the final devices: M.Sc. Anton Kompatscher and Dr. Heiko Mager. Figure 3.1.1c shows a schematic of an IDE structure. Due to the sample geometry of the in-plane devices, it is more difficult to determine the effective material area compared to out-of-plane electrode structures. Section A.2 discusses the effective electric field in in-plane electrode structures.

The in-plane BTA-C_8 samples were fabricated on top of MicruX Technologies IDEs, where the material was drop cast $2 \cdot 5$ μl or dip coated from solution. The solutions used contained 5, 10, or 40 mg ml^{-1} BTA-C_8 in CF. In all cases, the solutions were annealed at 40 °C for 15 min after mixing and before deposition. After deposition, the samples were annealed at 70 °C for 15 min to improve film quality.
For all in-plane TPA samples, the material was drop cast $2 \cdot 5$ μl on top of homemade IDEs from

the respective 10 mg ml^{-1} solution. O-TPA-N was dissolved in a 1:1 THF:DMC (tetrahydrofuran and dimethylcarbonat, solvents supplied by VWR Chemicals; both $\geq$ 99.0% purity) solution. Both p-TPA-N and p-TPA-C were dissolved in pure THF. No additional temperature treatment was used during the deposition process. All samples had full electrode coverage and film thicknesses that were typically inhomogeneous and ranged from 0.5 to 2 μm.

3.1.3 Thermoelectric samples

Both glass and silicon substrates were used for the AC Seebeck measurements. The silicon substrate was chosen for its high thermal conductivity, which allows to convection to be neglected. The glass substrate was chosen to demonstrate the applicability of the developed model to other materials. The silicon was cleaved into 15 mm $\times$ 25 mm substrates from a silicon wafer. The glass substrates were cut from commercially available 75 mm $\times$ 25 mm Corning plain microscope slides, which have a thickness ranging from 0.96 to 1.06 mm, using a glass cutter. The final dimensions of the glass substrates were 15 mm $\times$ 25 mm. Gold electrodes were thermally evaporated from evaporation boats in a thermal evaporator (Mantis Deposition LTD Evaporator) at pressures lower than $5 \cdot 10^{-6}$ mbar using shadow masks, which allowed for different distances between contacting electrodes. During evaporation, the substrates were rotated at 10 rpm to ensure homogeneous evaporated material deposition. The channel lengths were 0.5, 1.0, or 2.0 mm, which is small compared to the 12 mm electrode length. This enables precise Seebeck voltage measurement with minimal influence from the contacting geometry. All electrodes were $\approx$ 0.3 mm wide. The distance between the heating electrode and the closest contacting electrode was 2.4 mm in all samples. Both the bottom and top electrodes were used. First, a layer of chromium $\approx 3-5$ nm thick was evaporated for the former. Then, in both cases, a layer of gold $\approx 50-80$ nm thick was evaporated. After deposition, the active material film was removed from all substrate areas except between the contacting electrodes by wiping with a Q-tip soaked in solvent (either CF or ODCB) to define the active material area. Figure 3.1.2 shows a schematic of a typical device used for thermoelectric characterization.

The P3HT:F4TCNQ thin films were deposited using either spin coating or dip coating. First, the P3HT solution was prepared by dissolving P3HT in either CF or ODCB at the desired concentration. The solution was then stirred at 70 °C for $\approx$ 24 h to ensure complete dissolution. The dynamically spin-coated samples were deposited from the respective P3HT solution inside a glovebox with a nitrogen atmosphere at speeds ranging from 1000 to 10000 rpm for 60 s to control the final thickness of the samples. Dip coating was performed with withdrawal speeds of $2-150$ and $0.1-3.5$ mm min^{-1} for CF and ODCB, respectively. After P3HT deposition, the samples were doped with either F_4TCNQ or Magic Blue (MB) for thermoelectric characterization. All P3HT:F_4TCNQ samples were sequentially doped with F_4TCNQ in a 4:1 THF:DCM (dichloromethane, solvent supplied by VWR Chemicals; $\geq$ 99.0% purity) solution by dynamically

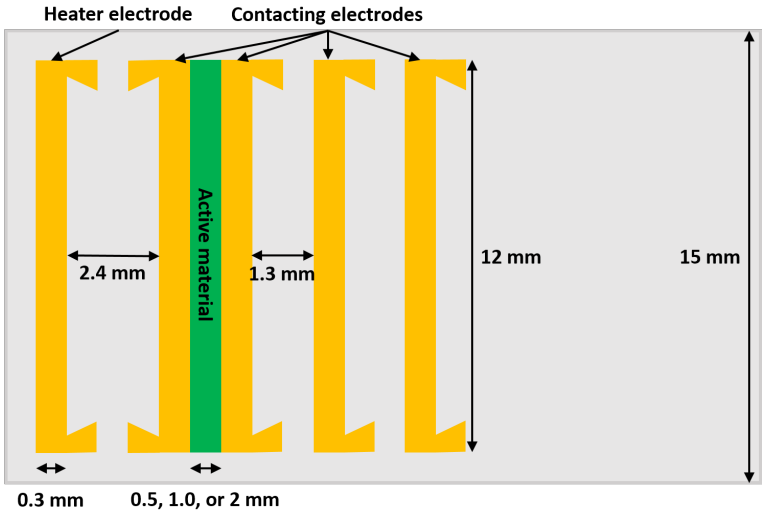

Figure 3.1.2: A schematic depiction of the device structures used for thermoelectric characterization from a top view. The electrode (yellow) on the far left is the heater electrode. The material (green) is located between the first and second contacting electrodes. The other contacting electrodes allow for measurements at different distances from the heater electrode and were used for testing and calibration.

spin coating 90 μl of the $0.1 - 10$ mg ml^{-1} F_4TCNQ in 4:1 THF:DCM solutions per sample at 3000 rpm for 30 s. The P3HT:MB samples were sequentially doped with a MB solution at different concentrations using a 3:1 AN:CF (acetonitrile, solvent supplied by VWR Chemicals; $\geq$ 98.0% purity) solvent mixture similar to the F_4TCNQ solution. Alternatively, the samples were doped via dip coating, whereby they were immersed in a MB solution in a 3:1 AN:CF solvent mixture.

3.2 Thin film deposition methods

To obtain high-quality thin films for use in devices, a large variety of deposition techniques has been thoroughly investigated and many successfully implemented. For example, many methods have been reported for inducing the alignment and orientation of π-conjugated polymers, such as P3HT, in thin films. In addition to scalable deposition techniques with different regimes that lead to different morphologies, such as dip coating [141] and blade coating [142, 143], less scalable methods that perform well, such as rubbing [144], tensile drawing [145], friction transfer [146], directional crystallization [147], ink-jet printing [148], substrate alignment [149], interfacial drawing [150] and slot-die coating [151], have been demonstrated to significantly improve the thermoelectric properties of devices. This section introduces the three deposition methods used in this dissertation.

3.2.1 Drop casting

Drop casting is the simplest method of depositing a material from a solution onto a substrate. In this method, the solution is dropped - typically from a pipette - onto the substrate, as shown in Figure 3.2.1a. The solution spreads across the substrate's surface and evaporates. This usually results in uneven films because the solvent evaporates anisotropically across the substrate. Although drop casting provides undesirable thin film properties, especially with regard to surface roughness and film thickness, it can be used in cases where these properties are not important and a simple coating technique is beneficial.

3.2.2 Spin coating

Spin coating is a straightforward process for quickly depositing thin, uniform coatings onto relatively flat substrates. The substrate is typically held by a rotatable fixture that uses vacuum suction to clamp it in place. The coating solution is dispensed onto the surface and spreads out uniformly due to the spinning of the substrate [152], as indicated in Figure 3.2.1b. The quality, and especially the thickness, of the resulting film can be controlled by varying solution properties such as material concentration, deposition volume, and substrate rotation speed. Furthermore, spin coating can be done statically or dynamically. In the static method, the solution is first deposited, and then the rotation begins. This allows for a uniform spread of the solution on the substrate. In the dynamic method, the solution is deposited on the already rotating substrate. In the latter case, the speed and precision of solution deposition play a larger role because off-center deposition, insufficient solution volume, or slow deposition can lead to defects. However, this technique can be beneficial, especially when working with volatile solvents that evaporate quickly, such as CF.

From a physical perspective, substrate rotation creates a fluid flow condition in which rotational accelerations are balanced by viscous drag within the solution [152]. This condition was first described by Emslie et al. in 1958 [153]. Meyerhofer followed in 1978 by considering solvent evaporation occurring simultaneously at the top of the solution. This led to the idea of spin coating happening in two stages: one controlled predominantly by viscous flow and the other by evaporation [154]. This model describes the characteristics of thin films by considering only centrifugal force, linear shear forces, and uniform solvent evaporation, yielding film thickness and drying times as functions of the various processing parameters. Furthermore, the film thickness is expected to be uniform and independent of substrate size if a large enough deposition volume is chosen. The model establishes the following dependency of film thickness h on spin speed f, initial solution viscosity ν_0, and evaporation rate Q_{ev}:

$$h \propto f^{-2/3} \nu_0^{1/3} Q_{\text{ev}}^{1/3} \propto f^{-1/2}, \tag{3.2.1}$$

with $Q_{\text{ev}} \propto f^{1/2}$ [154]. Equation 3.2.1 generally holds true for volatile solvents, although the exact exponent value may differ in experiments [152].

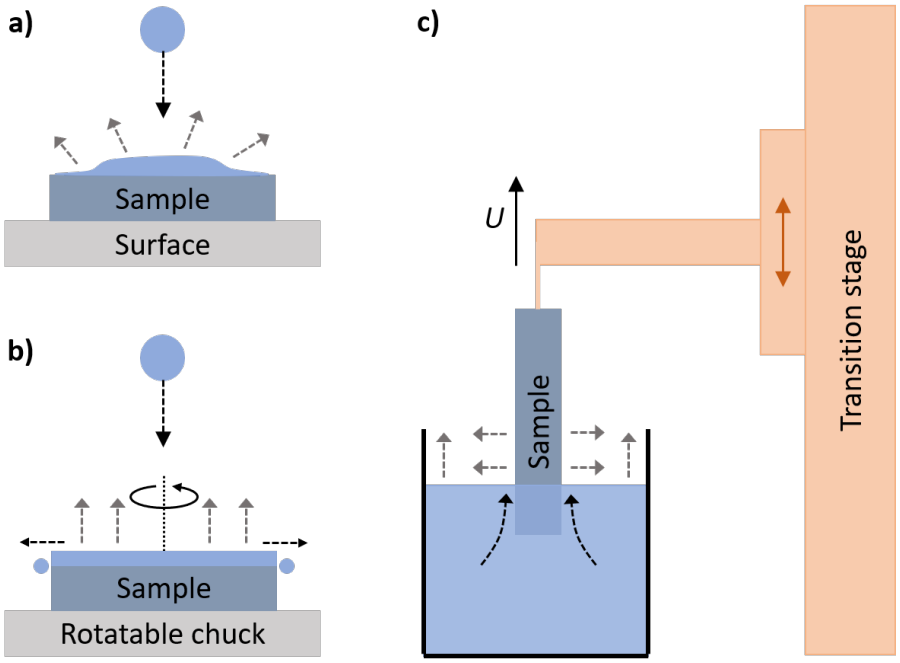

Figure 3.2.1: A schematic depiction of **a)** drop casting, **b)** spin coating, and **c)** dip coating. The deposited solution is shown in blue. Gray and black dashed arrows represent evaporation and decisive forces for the corresponding coating process, respectively.

3.2.3 Dip coating

This subsection is based on various textbooks and publications on dip coating, such as [155–157] and [158–160], respectively.

Dip coating is a deposition technique widely used in industrial and laboratory settings for fabricating thin, uniform films because it provides simple processing, low cost, and high coating quality [156, 161]. It is also well-known for its ability to produced aligned films in a controlled and reproducible manner [158]. Deposition takes place when a substrate is withdrawn from a liquid coating medium. When a substrate is immersed in a solution, a coherent liquid film forms on the substrate as it is withdrawn from the solution. This film consolidates by drying after withdrawal. A schematic depiction of the dip coating is shown in Figure 3.2.1c. In general, the dip coating process can be separated into five steps. First, the substrate is immersed in the solution. Next, a dwelling step typically follows, allowing the capillary force, and therefore the wetting zone (see below), to settle. This step also allows the substrate to reach thermal equilibrium with the solution and reduces the turbulent flow from the immersion step. Then, the substrate is withdrawn at a set speed. Next, the drying or consolidation step occurs, during which the solvent fully evaporates, leaving a dry film behind. This step represents a sol-gel transition

involving draining, evaporation, and hydrolysis processes [156]. Experimentally, this transition is observed via a receding drying line that moves downward during withdrawal, leaving behind the consolidated gel film. For volatile solvents, the complete transition process usually takes a few seconds. Due to solvent evaporation and the resulting cooling, a downward laminar flow of vapors forms at the surface of the wet film. This enhances the drying and maintains a nearly constant water content. However, during drying, turbulence or variations in the surrounding atmosphere can lead to inhomogeneities in the film properties. Finally, an optional curing step, i.e., a post-treatment, can be performed to achieve the desired properties of the final coating material, depending on the application [156].
The dip coating process has two critical stages that determine the resulting properties of the deposited films: withdrawal and drying. The final film thickness is defined by the interplay of entraining and draining forces during these stages. The drying process also plays a significant role because the liquid constantly evaporates from the solution layer as the substrate is lifted. The films formed during the process depend primarily on withdrawal speed and solution viscosity. These parameters allow us to distinguish three regimes: viscous flow, drainage, and capillary. These regimes are discussed in more detail further below.
Unlike drop casting or spin coating, which have two isotropic directions for film formation parallel to the substrate plane, dip coating has no equivalent directions. The first direction is the withdrawal direction, which is characterized by the evaporation of the liquid from the thin film. Second, the direction along the substrate is limited by the waterline. Third, the direction away from the substrate surface along the waterline is characterized by different physical processes, which are described in the following. This broken symmetry at the vapor-substrate-liquid interface results in aligned deposition of material, which is not present with drop casting or spin coating.

From a physical standpoint, the film formation process is based on fluid mechanical equilibrium between the entrained film and the receding coating liquid during the withdrawal stage [162, 163]. The two regimes are separated by a stagnation line. Above this line, the liquid is entrained by the substrate, and below it, the liquid is retained in the bath. This equilibrium is described by forces such as viscous drag, gravity, and surface tension [162], which can be categorized as draining or entraining. The former draw the liquid away from the substrate toward the solution; the latter retain the fluid on the substrate. Their balance determines the wet film thickness coated onto the substrate. Landau and Levich [164] and Deryaguin [165] derived a fundamental theoretical description of the final liquid film thickness h_∞ for pure, non-volatile liquids and homogeneous, flat, completely wettable substrate surfaces. This description is given by the Landau-Levich equation:

$$h_\infty = \mathrm{c}\frac{(\mu U)^{2/3}}{\sigma^{1/6}\,(\rho g)^{1/2}} \propto U^{2/3}, \tag{3.2.2}$$

with a constant c, typically around 0.946 for Newtonian fluids; the liquid or Newtonian viscosity μ; the withdrawal speed U; the surface tension of the liquid against air σ; and the liquid density ρ [163, 166]. Equation 3.2.2 can be rewritten using the capillary length $l_c = \sqrt{\sigma/(\rho g)}$ and the capillary number $\mathrm{Ca} = \mu U/\sigma$, which yields

$$h_\infty = c l_c \mathrm{Ca}^{2/3} \propto U^{2/3}. \tag{3.2.3}$$

This description is only valid when $\mathrm{Ca} \ll 1$, which occurs at sufficiently low withdrawal speeds. In reality, the exponent in withdrawal speed U varies for different coating liquids based on their chemical properties, typically ranging from 0.5 to 0.7. Davis and Troian [167] computed the maximum thickness of an entrained liquid film h_∞ for partially wettable surfaces, and Darhuber et al. [168] experimentally confirmed it to be

$$h_\infty = 0.356 w \mathrm{Ca}^{1/3} \propto U^{1/3}, \tag{3.2.4}$$

where w is the width of a hydrophobic stripe, which is the dominant length scale when $w \ll l_c$. It is necessary to distinguish between completely and partially wettable surfaces because they lead to drastic changes in the properties of the final films. Wettability is generally defined as the ability of a liquid to interact with other fluids and/or solid surfaces, and it is determined by the contact angle between the solid and liquid phases. A contact angle of less than 90° or greater than 90° indicates higher or lower wettability, respectively [169]. The former is typically observed with perfectly smooth and mostly flat substrates; however, a lower level of wetting may occur depending on the interaction between the solid and liquid phases, as well as defects in the substrate and coating processes. In this dissertation, fully wettable surfaces are similar to hydrophilic surfaces (contact angle $\leq 90°$), and partially wettable surfaces are similar to hydrophobic surfaces (contact angle $\geq 90°$) [170].
While the above approach provides basic dependencies, such as an increase in film thickness with withdrawal speed, it typically fails to describe real processeses, which are significantly more complex. This is because the approach assumes pure liquids and neglects evaporation [156, 163]. Additionally, exact descriptions are generally difficult because the underlying physical and chemical processes overlap in dip coating.

As mentioned above, the withdrawal stage significantly affects the properties of the wet film. The formation of the wet film can be divided into four distinct regions, as shown in Fig. 3.2.2a. Immersion of the substrate is accompanied by a static meniscus whose shape is determined by the balance of hydrostatic and capillary pressures. During the withdrawal process, a dynamic meniscus emerges and moves with the substrate near the stagnation point, where the entraining and draining forces are in equilibrium. The wet film thickness is determined by the dynamic meniscus and the balance of these forces. The film thickness h_∞ is reached and maintained in the constant thickness zone. The transition between the static and dynamic menisci occurs within

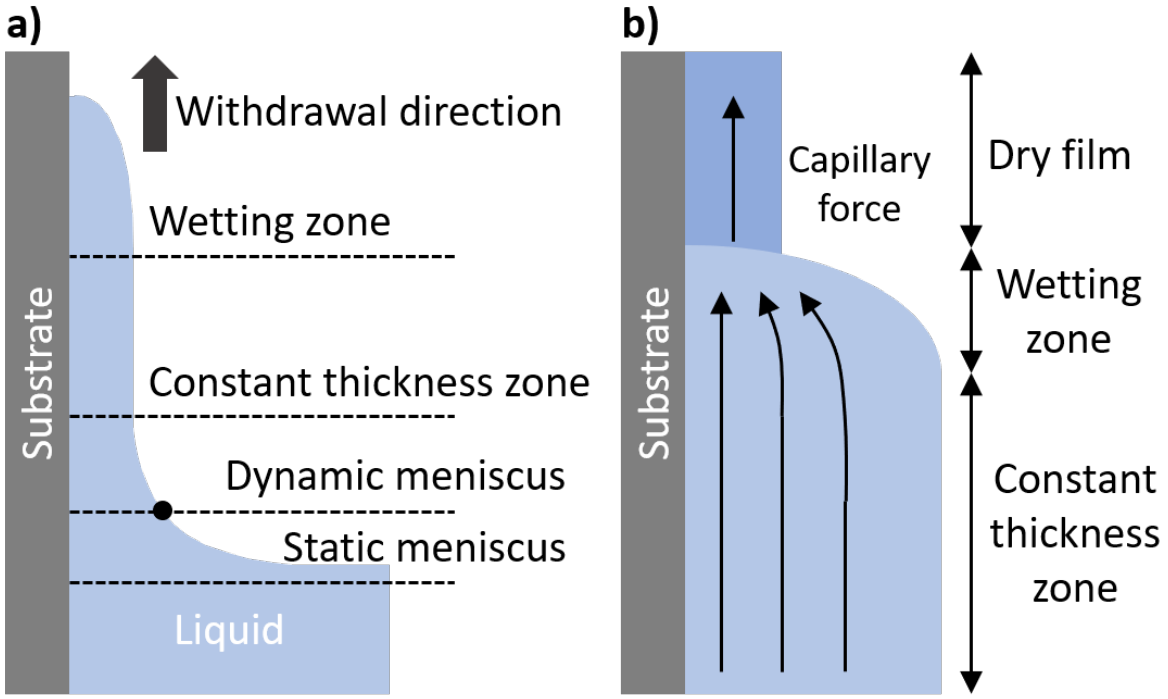

Figure 3.2.2: a) A schematic depiction of the four distinct regions of wet film formation. As shown, the substrate is withdrawn to the top. The stagnation point, where the entraining and draining forces are in equilibrium, is marked. **b)** A zoom-in on the area around the wetting zone depicting the dynamics of the wet film drying at the drying front.

a thin boundary layer, where viscous flow forces mainly determine the motion of the solution. Beyond the boundary layer, draining forces dominate viscous forces. Depending on which force dominates the behavior of the coating, three regimes can be distinguished: viscous flow, draining, and capillary or evaporation.

The viscous flow regime, dominated by viscous and gravitational forces, occurs at high withdrawal speeds and with viscous solutions. The entraining force consists of viscous forces acting on the solution during withdrawal, while the draining force results from gravity. This regime is typically not reached because it requires very high withdrawal speeds and viscosities. For lower viscosities, the balance between the entraining and draining forces depends on the surface tension-driven movement of the solution. In this case, the drainage regime occurs. It is typically considered a transition regime between the viscous flow and capillary regimes. The viscous flow and drainage regimes are often combined, resulting in the so-called Landau-Levich regime. The Landau-Levich regime is usually valid for most viscosity and withdrawal speed ranges, except for very high viscosity and very low withdrawal speeds. For the latter, the capillary or evaporation regime occurs. In this regime, it is assumed that the entrainment time is significantly shorter than the

drying time of the film. This results in uniform coverage of the entire length of the immersed substrate. The entraining rate through viscous flow is lower than the solvent evaporation rate; thus, the substrate begins to dry before complete withdrawal from the solution occurs. This creates a strong, evaporation-driven concentration gradient from the bulk of the solution toward the contact line. Thus, the drying dynamics are crucial for understanding the underlying process. The drying process can be divided into three stages: the constant rate period, the drying front, and the falling rate period. During the constant rate period, drying occurs within the constant thickness zone, both during and after coating. During this stage, solvent evaporation occurs uniformly across all surfaces of the wet film, except at the substrate edges where the drying front is present. The drying front is the most complex and is shown in Fig. 3.2.2b. The evaporation rate is highest in the wetting zone because the surface area-to-volume ratio is largest there. Thus, the wet film has a higher material concentration, resulting in the drawing of solution from the surroundings due to surface tension. Once a drying film forms at the drying front, capillary forces arise that 'pump' the solution into the drying film. This results in thickening of the deposited film. This occurs during the capillary regime of dip coating. In the Landau-Levich regime, the drying front recedes at a significantly lower rate than the formation of the constant thickness zone. Thus, the drying dynamics are dominated by the constant rate period, and the final film thickness depends on the initial wet film thickness. In the capillary regime, however, the drying front rate is higher than the withdrawal rate; therefore, the drying dynamics are dominated by the drying front. A constant thickness zone is never truly achieved, so the wet film thickness is no longer considered. Instead, the final film thickness depends on the withdrawal speed, the solution's properties, and the evaporation rate of the solvent. After dip coating finishes, most of the solvent is removed from the wet film, leaving merely a gel-like film. The falling rate period of drying then occurs, during which the small amount of remaining solvent becomes trapped within the gel. Evaporation is then determined by the diffusion of the solvent from the bulk to the surface.

As described above, dip coating can be separated into the Landau-Levich and the capillary or evaporation regimes, depending on the solution's viscosity and the withdrawal speed. According to Rogowski and Darhuber [158], the total deposited crystal mass m can be expressed as a function of the withdrawal speed U. In the Landau-Levich regime, which involves higher withdrawal speeds, the power-law relation $m = b_1 U^{\alpha}$ with $\alpha = 2/3$ is obtained by multiplying Equation 3.2.3 by the immersion surface area of the substrate S, the solution density ρ_{sol}, and the solute weight fraction C_0, yielding

$$m = b_1 U^{2/3} = \mathrm{c} l_{\mathrm{c}} \left(\mu U/\sigma\right)^{2/3} S C_0 \rho_{\mathrm{sol}} \propto U^{2/3}. \tag{3.2.5}$$

Similarly, the capillary regime yields the power-law relation $m \propto U^{-1}$ for lower withdrawal speeds, which can be derived from mass balances for the solvent and solute [158]. The main idea is to consider the flows that arise from the force balance at steady state. By applying the balance

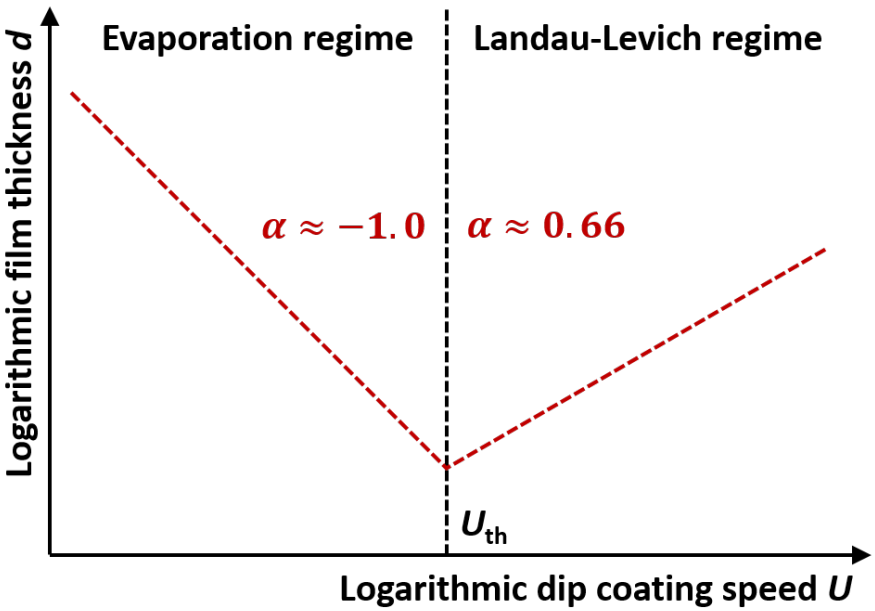

Figure 3.2.3: A schematic depiction of dip-coated film thickness d as a proxy for deposited mass m as a function of the withdrawal speed U in double-logarithmic representation. The dashed red and vertical black lines represent the functions $d \propto m \propto U^{\alpha}$ following Rogowski and Darhuber [158], as well as the threshold speed U_{th} that separates the evaporation and Landau-Levich regimes, respectively.

conditions and considering the boundary conditions, as well as using the mass conservation law at steady state, the following expression is obtained:

$$m = \rho_{\mathrm{cryst}} DS = \frac{Q_{\mathrm{ev}} C_0 S}{w_{\mathrm{sub}} U} \propto U^{-1}, \tag{3.2.6}$$

where Q_{ev} is the integral evaporation rate, C_0 is the bulk solute weight fraction, and w_{sub} is the width of the substrate. Fig. 3.2.3 schematically shows the total deposited mass m as a function of the withdrawal speed U in both the evaporation and Landau-Levich regimes. Note that the deposited film thickness can be taken as a proxy for the deposited mass.

In general, the theoretical prediction and experimental data generally agree well. Rogowski and Darhuber [158] obtained power-law exponents of $\alpha = -0.95$ for the evaporation regime and $\alpha = 0.66$ for the Landau-Levich regime. This values are consistent with other reported in similar investigations. For example, Le Berre et al. [171] found power-law exponents of $\alpha = -1.14$ and $\alpha = 0.76$, respectively.

As mentioned above, the Landau-Levich and evaporation regimes are clearly distinct, with no transition regime in between, and they possess different scaling exponents. This separation occurs at the well-defined threshold speed U_{th}, which can be obtained by setting Equations 3.2.5 and

3.2.6 equal (with $c = 0.946$):

$$U_{\mathrm{th}} = \left(Q_{\mathrm{ev}} \left(0.946 w_{\mathrm{sub}} l_{\mathrm{c}} \left(\frac{\mu}{\sigma} \right)^{2/3} \rho_{\mathrm{sol}} \right)^{-1} \right)^{3/5}. \tag{3.2.7}$$

As shown in Equation 3.2.7, the threshold speed depends on multiple solution parameters that change over time due to constant solvent evaporation. However, the amount of the solid material remains constant, leading to an increase in the solution's viscosity, density, and surface tension over time [158]. This influences the substrate coating process and threshold speed, regardless of whether the solution contains agglomerates or not, though the former is affected more. To counteract evaporation, all experiments were carried out with freshly prepared solutions and in a timely manner. The evaporated solution was refilled between substrate coatings to minimize the amount of solvent vapor in the saturated atmosphere above the vial because this also affects the coating result.

To roughly estimate the threshold speed using Equation 3.2.7, the evaporation rate Q_{ev} of the solution must be determined. First, a small droplet of the solution was deposited on a clean, flat glass substrate. Using a fine balance, the initial and final masses, m_1 and m_2, of the droplet after letting the solvent evaporate for a time Δt were determined. This leads to the mass evaporation rate

$$Q_{\mathrm{ev}} = \frac{m_1 - m_2}{f \cdot \Delta t}, \tag{3.2.8}$$

where $f = A_{\mathrm{ev}}/A_{\mathrm{sample}}$ accounts for the difference in size between the glass substrate surface area A_{ev} and the real sample area A_{sample}. Although this approach does not consider the significantly greater accumulation of solvent vapor in a saturated atmosphere above a vial, it still provides a sufficiently accurate estimate of the evaporation rate Q_{ev} [172].
For solution parameters such as density, viscosity, and surface tension, only the known values of the solvents were considered. While these values change (i.e., increase) when adding a solid material, the change is insignificant and is estimated to be less than the variation due to the evaporation's error margin. A more in-depth discussion of this topic can be found in Section A.3.

Furthermore, coating defects can occur during the dip coating process. These defects can be separated into two categories that can appear separately or simultaneously: instabilities in the dip coater (e.g., variation in withdrawal speed) and external factors (e.g., the atmosphere or the viscoelastic and chemical properties of the ink). The latter can lead to distinct structures in the dip coated film. Section A.4 provides a brief overview of the most common defects that occur during the dip coating process.

A dip coater (Nadetech Innovations ND-DC Dip Coater), which was located in a closeable box to isolate the coating process from external atmospheric changes, was used for substrate

coating. The cleaned substrates were placed between tweezers and positioned perpendicular to small vials. These vials were the bottom halves of 5 ml bottles, measuring ≈ 1.2 or ≈ 1.7 cm in width, and ≈ 1 cm in height. Due to the continuous evaporation of the solvents, the vials were filled to the top and refilled between substrate processing; otherwise, an atmosphere saturated with the evaporating solvent would form above the waterline, which would change the dip-coated film. The substrates were immersed for $\approx 7 - 8$ mm. This setup provides enough immersion depth while minimizing solution usage. A built-in software steers the dip coating process and the corresponding deposition parameters. The positioning and immersion speeds were typically set between 100 and 150 mm min^{-1}, with the exact values being unimportant as they barely influence the coating process. The down and up positions were chosen so that the substrate does barely touches the bottom of the vial and barely rises above of the solution, respectively. After full immersion, the process waited 20 s for the substrate to fully wet and for any turbulence to subside. Withdrawal was carried out at different speeds. After full withdrawal, the coated substrates were placed ≈ 7 cm above the vial, where they dried for $\approx 20 - 30$ s.

3.3 Measuring methods

3.3.1 Ferroelectric characterization

3.3.1.1 Measurement setup

The characterization of the ferroelectric samples, including the field annealing procedures and the hysteresis loop measurements, was mostly carried out in the air probe station (APS). These measurements were performed under normal atmospheric conditions at (possibly) elevated temperatures achieved by an included heating pad. Figure 3.3.1 shows a schematic overview of the setup. The entire setup is controlled via homemade software on a PC. The Python program for ferroelectric measurements, evaluation, and temperature control was written by the author of this dissertation, and the temperature PID control was provided by Dr. Clemens Göhler, a member of the research group. The setup consists of an arbitrary function generator (Tektronix Dual Channel Arbitrary/Function Generator AFG3052C, 1 GS/s and 50 MHz), short AFG, which applies the function signal. Since the AFG's amplitude is capped at 10 V, a high-voltage amplifier (TReK Piezo Driver/Amplifier Series MODEL PZD350A) with a 100x amplification factor is used. An analog to digital converter (ADC) monitors the non-amplified signal for comparison and setting the signal trigger. The amplified function signal is sent to a micropositioner with a contacting needle that touches the device under test (DUT), which is the ferroelectric sample (see Section 3.1.2). The sample's current response passes through a second micropositioner and is measured by an ADC (Tektronix TBS1102B-EDU digital oscilloscope). To protect the ADC in case of a short-circuit in the sample, a built-in resistance of $R = 1$ MΩ is used. The probe station has four micropositioners, which establish good contact with the electrodes (typically

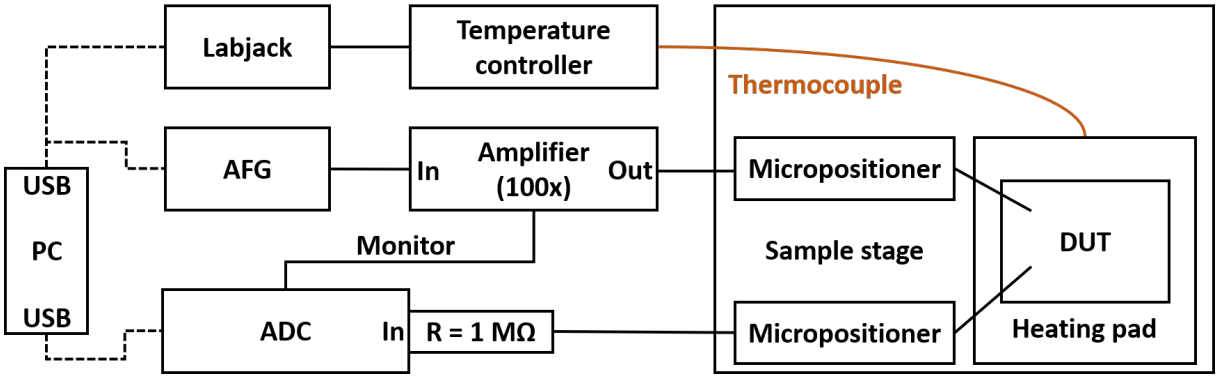

Figure 3.3.1: A schematic depiction of the APS setup for ferroelectric measurements.

$R < 10\ \Omega$). APS is also equipped with a light microscope (WILD EpiMakroScop M450). The devices in the measurement circuit are connected by BNC cables. Temperature control is achieved by applying power to the heating pad via a power supply (Delta Elektronika Power Supply ES 030-5), which is controlled by a LabJack. The LabJack reads out the temperature from the temperature controller, which provides voltage values based on the temperature of the connected thermocouple. These values are sent to the temperature PID. Once the set temperature is reached, temperature fluctuations amount to less than a degree. The heating pad's temperature range is between room temperature and 200 °C.

3.3.1.2 Double wave method

A triangular double wave (DW) was used as the pulse sequence for ferroelectric characterization, with the applied function signal generated by the AFG. Figure 3.3.2a shows a summary of the double wave method (DWM). The first pulse is a preparation pulse that fully polarizes the ferroelectric sample in one direction. The second pulse switches the polarization. However, in addition to the spontaneous polarization current, the second pulse contains non-switching current components, such as parasitic leakage, displacement, and conducting currents. The third pulse accounts for these non-switching currents by subtracting its currents from those of the second pulse, which should have fully polarized the sample. This compensation is necessary because non-ferroelectric materials, such as leaky dielectrics, can produce hysteresis curves similar to those of ferroelectrics, as demonstrated by J. F. Scott [173]. In a real measurement, the DW is applied over longer periods of time in both the positive and negative directions, so two 'up' signal and two 'down' signals are applied in sequence. This allows the material within the sample to be both polarized and aligned along the electric field, a process known as field annealing. This is necessary because otherwise, soft and disordered organic materials may not ferroelectrically switch, depending on the geometric configuration of the molecular dipoles relative to the direction of the applied electric field. A typical measurement performed on P(VDF:TrFE) at the APS is shown in Figure 3.3.1b. Although the DWM technique originates from the positive 'up' - negative

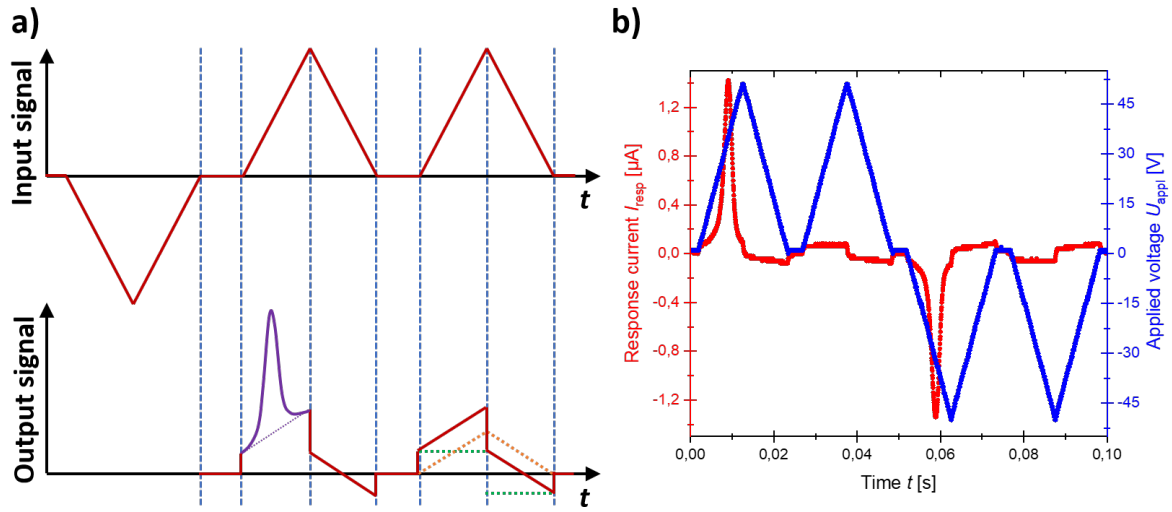

Figure 3.3.2: a) A schematic depiction of the DWM for ferroelectric measurements. The applied input signal consists of a downward preparation pulse followed by two upward probing pulses. The shape and length of both the preparation and probing parts of the complete DWM signal can be modified. The amplitude value of the preparation pulse is chosen to be significantly larger than the coercive voltage of the ferroelectric materials under investigation. The output signal represents the ferroelectric signal response to the probing pulses. The signal contribution from ferroelectric switching is depicted in purple, and the other contributions are shown in red. The non-switching currents consist of the leakage (orange) and displacement (green) currents. **b)** A typical DW measurement of P(VDF:TrFE) showing one full signal period. This measurement demonstrates a pronounced switching peak at the first peaks in both directions and barely shows any leakage current. There is some displacement current present. The measurement was conducted at 10 Hz, room temperature, and an applied voltage of 50 V.

'down' (PUND) approach, DWM typically uses continuous transients (a slow triangular ramp as opposed to a steep rectangular ramp). This quasi-static regime allows for small displacement currents and the accurate reconstruction of saturated and unsaturated ferroelectric hysteresis loops, as the coercive field is well-defined [174].
The DWM can be used to extract the polarization values from ferroelectric characterization measurements. Polarization P is given by the time integral of the measured current I:

$$P = \frac{Q}{A} = \frac{1}{A} \int I\,(t)\,\mathrm{d}t, \tag{3.3.1}$$

where Q is the total charge and A is the total area of the capacitor. The effective capacitor area is discussed separately in Section A.2. The applied voltage signal induces a current response from the capacitor device that is measured. Since oscilloscopes typically measure voltages across their

built-in resistances R, the outgoing current can be obtained from

$$I_{\text{out}} = \frac{U_{\text{out}}}{R}, \tag{3.3.2}$$

which can be further modified using the DWM:

$$I_{\text{out}} = \frac{U_{\text{out, signal}} - U_{\text{out, background}}}{R}. \tag{3.3.3}$$

The corresponding electric field is given by the capacitor relation

$$E = \frac{U_{\text{in}}}{d_{\text{sample}}}, \tag{3.3.4}$$

where d_{sample} is the thickness of the ferroelectric layer between the electrodes.

3.3.2 Dielectric spectroscopy

Dielectric spectroscopy (DS) is used to measure the dielectric properties of a material as a function of temperature and frequency. In this dissertation, DS was used to search for ferroelectric-to-paraelectric phase transitions. Measurements were performed using a Zurich Instruments MFIA impedance analyzer in four-probe geometry. The MFIA is a source measure unit (SMU) that contains a lock-in amplifier and a frequency sweeper. The sweeper allows us to measure capacitance over multiple orders of magnitude of frequency. An alternating current (AC) voltage signal with an amplitude of 300 mV was applied, and the resulting amplified current I and the corresponding phase shift $\Delta\phi$ relative to the applied voltage V were measured. This allowed us to obtain the impedance Z:

$$Z = Z^{'} + iZ^{''} = |Z| \exp(i\Delta\phi) = \frac{|V|}{|I|} \exp(i\Delta\phi) \tag{3.3.5}$$

For a capacitor with capacitance C, the impedance Z is given by

$$Z = \frac{1}{1\omega C}, \tag{3.3.6}$$

with the frequency $\omega = 2\pi f$. By applying an equivalent circuit model - here, a parallel RC circuit - to the measured data, the real and the complex impedances, as well as the capacitance can be obtained. The electric permittivity of the dielectric material ϵ_{r} can be obtained from $\epsilon_{\text{r}} = C/C_0$, where C_0 is the capacitance of the capacitor without the dielectric material (i.e., an empty device). Similar to polarization, calculating the capacitance C_0 for a parallel plate capacitor (i.e., an out-of-plane device) is straightforward using $C_0 = \epsilon_0 \epsilon_{\text{r}} A/d$. However, similar calculations for thin films on planar devices (i.e., IDEs) are more complicated. This is because the substrate permittivity and the effective penetration depth, as well as the curvature of the electric field lines must be considered (see Section A.2). Since the DS measurements were performed on IDEs, the investigation is qualitative only. However, this still allows us to identify the temperatures and frequency ranges at which phase transitions may occur. Capacitance is a sufficient proxy for the permittivity since the difference between the two is a geometric proportionality factor.

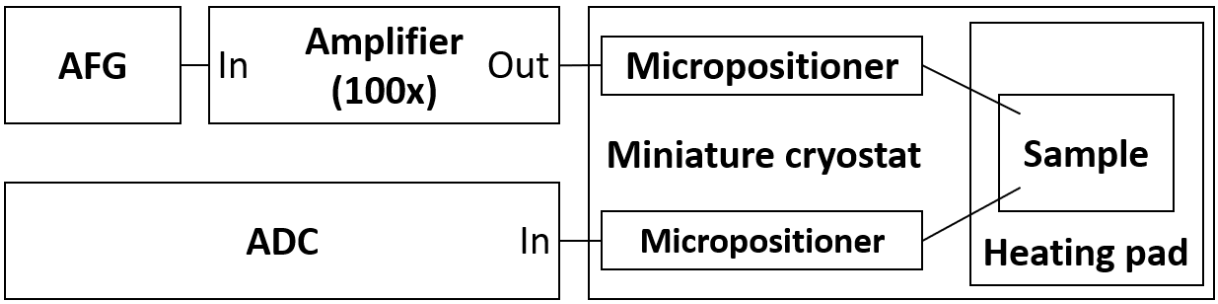

Figure 3.3.3: A schematic depiction of the Barkhausen noise measurement setup.

3.3.3 Barkhausen noise measurement

An AFG (Keysight 33600A), steered by a PC, supplied the input signal. The AFG applied a varying waveform signal, which an amplifier (TReK PZD350A high voltage amplifier) amplified to reach the required electric field strengths. The DUT was connected via contacting needles, and its response voltage and current were measured using an ADC, either a Zurich Instruments impedance analyzer (MFIA) or a lock-in amplifier (MFLI). The DUT was measured inside a Linkam miniature cryostat with electric contacts to reduce extrinsic noise and enable precise, temperature-dependent measurements. A schematic overview of the setup is shown in Figure 3.3.3. All Barkhausen noise measurements were performed at room temperature.

3.3.4 Thermoelectric characterization

3.3.4.1 Seebeck effect

In general, thermoelectricity refers to the direct conversion of heat into electricity, or vice versa, which typically occurs in a thermoelectric energy generator. The Seebeck effect is the phenomenon in which an electric voltage is directly generated by a temperature gradient in a material [175]. This temperature gradient causes a change in the energies of the charge carriers and thus a redistribution of the latter, creating a voltage. The magnitude of the Seebeck, or thermal, voltage ΔV generated, and thus the output of such generators, depends on the temperature gradient $\Delta T = T_2 - T_1$ and the temperature-dependent Seebeck coefficient $S = S_{\mathrm{ab}}(T)$:

$$\Delta V = -\int_{T_1}^{T_2} S_{\mathrm{ab}}(T)\,\mathrm{d}T, \tag{3.3.7}$$

where a and b represent the different materials [176, 177]. In thermoelectric energy generators, p-type and n-type semiconductors are connected between a heat source and a heat sink [178]. The Seebeck coefficient, also called thermopower, at the reference temperature T_0 is given by the slope of the temperature-dependent voltage at T_0:

$$S(T_0) = -\frac{\partial V}{\partial T}\bigg|_{T_0}. \tag{3.3.8}$$

For small temperature gradients, the Seebeck coefficient is assumed to be constant at the reference temperature $T_0 = (T_1 + T_2)/2$ [179]. This yields the following Seebeck voltage:

$$\Delta V = -S(T_0)\,\Delta T, \tag{3.3.9}$$

and the Seebeck coefficient can then be calculated as

$$S(T_0) = -\frac{\Delta V}{\Delta T}. \tag{3.3.10}$$

Setups that measure the Seebeck coefficient using either higher temperature gradients and Equation 3.3.8 or small temperature differences $\Delta T \ll T_0$ and Equation 3.3.10 are called integral or differential methods, respectively [178]. In this dissertation, the differential measurement method at the reference temperature $T_0 \approx 298$ K (room temperature) was applied.

3.3.4.2 Figure of merit

An efficient thermoelectric device should have a high electrical conductivity σ to allow charge carriers to diffuse easily within the material and reduce Joule heating, as well as a high Seebeck coefficient S to generate a large voltage from a temperature difference. Additionally, the material should be a good thermal insulator to maintain a large temperature gradient; thus, the thermal conductivity κ, which consists of electronic and lattice contributions, should be low. These parameters are typically quantified by the dimensionless figure of merit zT:

$$\mathrm{zT} = \frac{S^2\sigma}{\kappa}T. \tag{3.3.11}$$

Optimal values for inorganic materials are at or above 1, whereas those for organic materials are lower. The highest zT reported in organic materials at room temperature is 0.5 [180]. The main challenge in optimizing the figure of merit is that all parameters depend on temperature and interact with each other, i.e., S, σ, and κ are interdependent [181].
Since thermal conductivity κ is difficult to measure in thin-films, the power factor PF is often used as an accessible figure of merit to evaluate thermoelectric efficiency:

$$\mathrm{PF} = S^2\sigma. \tag{3.3.12}$$

3.3.4.3 Seebeck coefficient measurement

In general, there are two main methods for measuring the Seebeck coefficient: the integral method (large ΔT) and the differential method (small ΔT). The differential method is preferred and can be separated into three categories: steady-state (DC), quasi-steady-state (qDC), and transient (AC) Seebeck measurements. This dissertation used the transient Seebeck measurement method, which involves creating a periodically changing temperature gradient by oscillating the temperature difference via oscillating heating instead of applying constant heating power

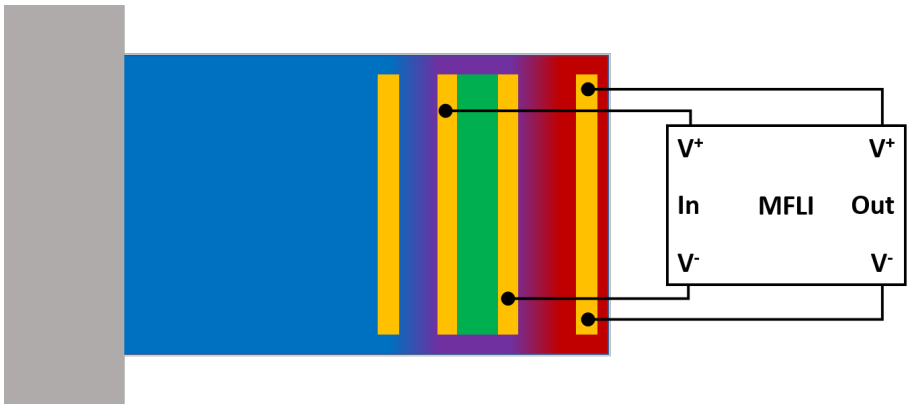

Figure 3.3.4: A schematic depiction of the thermal voltage measurement at the AC Seebeck measurement setup. The thermoelectric sample is clamped on one side, which is indicated by the gray area. The yellow and green areas represent the electrode structures and active material, respectively. The temperature gradient is represented by the red (hot), purple (intermediate), and blue (cold) color scheme.

to generate a stable gradient. The corresponding Seebeck voltage has the same periodicity as the temperature, and the Seebeck coefficient can be obtained in a manner similar to that in Equation 3.3.10 in Section 3.3.4.1:

$$S = -\frac{\Delta V_{\text{per}}}{\Delta T_{\text{per}}}. \tag{3.3.13}$$

The transient method has two main advantages: no offset correction is needed, and the measurements are quick and reliable.

The on-chip AC Seebeck measurement method was developed and performed by B.Sc. Clara Wiesner, B.Sc. Ejona Syla, and B.Sc. Andreas Waxweiler, under the supervision of M.Sc. Morteza Shokrani, all of whom are or were members of the research group. Figure 3.3.4 shows a schematic of the measurement. The sample containing the active material and electrode structures (see Section 3.1.3) is held by a clamp that establishes good thermal contact and has a significantly larger thermal mass than the sample. The heater and the two contacting electrodes are connected to the output of a lock-in amplifier (MFLI from Zurich Instruments) via contacting needles. The MFLI applies the heating current and measures the 2ω parts of the Seebeck voltage. The entire setup is contained within a glovebox with a nitrogen atmosphere to prevent the degradation of the organic materials used.
The MFLI applies an oscillating voltage $V(t) = V_0 \cos(\omega t)$ with an amplitude V_0 and a modulation frequency ω to the heater electrode. Due to Joule heating, this yields a periodic temperature wave with a frequency 2ω, which propagates through the sample and applies a 2ω temperature difference $\Delta T_{2\omega}$ between the measuring contacts. The thermoelectric active material between the electrodes then produces a Seebeck voltage $\Delta V_{2\omega}$ with a 2ω periodicity. This voltage can be di-

rectly measured by the electrodes, which allows us to obtain the corresponding Seebeck coefficient. To obtain the temperature of the active material and calibrate the sample, the temperatures of the two contacting electrodes must be measured. Thus, two additional probing needles are connected between the input of the MFLI and either of the contacting electrodes. A current source (Keithley 2636B) connected in parallel provides a constant current of $I_0 = 25$ mA for voltage readout. The MFLI measures the signal resulting from the heating $V_\mathrm{s} = A_\mathrm{s} \cos(2\omega_\mathrm{s} t - \phi_\mathrm{s})$, with the phase shift between the applied signal at the heater and the measured signal at the contact ϕ_s. Since the MFLI measures the root-mean-square values of the signals, the values must be multiplied by $\sqrt{2}$. To obtain $\Delta T_{2\omega}$, the analytical solution to the one-dimensional heat equation for the chip is required. Assuming the height of the chip h is small compared to its length l ($h \ll l$) and neglecting heat flow other than that which is orthogonal to the heater (x-direction), yields

$$\frac{\partial T}{\partial t} = \frac{\kappa}{\rho c_\mathrm{p}} \frac{\partial^2 T}{\partial x^2}, \tag{3.3.14}$$

with the thermal conductivity κ, density ρ, and specific heat capacity of the chip [182]. Considering the chip's geometry and applying boundary conditions allows us to calculate the 2ω temperature analytically. More information on the derivation and resulting expressions can be found in the corresponding works, primarily the bachelor's theses of B.Sc. Ejona Syla and B.Sc. Andreas Waxweiler.
The Seebeck coefficient measurement consisted of a voltage sweep from 1 to 20 V for frequencies of $\omega = 20$ mHz $-$ 5 Hz, performed by the MFLI. Using the setup and the corresponding calculations described above, the Seebeck coefficient can be obtained analytically.

3.3.4.4 Electrical conductivity measurement

The electrical conductance of the samples used for thermoelectric characterization was extracted from current-voltage (IV) measurements taken with a current source (Keithley 2636B). The samples were measured inside a glovebox with a nitrogen atmosphere. The thickness of the samples was obtained using a stylus profilometer (see Section 3.3.5.3). The electrical conductivity was calculated using the sample geometry and the measured resistance $R = U/I$:

$$\sigma = \rho^{-1} = \frac{l}{A}\frac{1}{R} = \frac{l}{A}\frac{I}{U}, \tag{3.3.15}$$

with the resistivity ρ, electrical resistance R, channel length l, and electrode cross-section A.

3.3.5 Structural resolving techniques

3.3.5.1 X-ray diffraction

X-ray diffraction (XRD) is a powerful, non-destructive tool used to analyze material structures at the microscopic and macroscopic levels. It is widely used to study crystal structures and atomic spacing. Measured X-ray diffraction peaks arise from the constructive interference of the X-ray beam at specific angles relative to the lattice planes of a sample. In this dissertation, XRD was used to investigate structural ordering in organic thin films.
X-rays are short-wavelength electromagnetic waves with wavelengths on the order of atomic sizes (i.e., $\lambda \approx 0.1$ nm). They are generated by a target (e.g., copper) bombarded by electrons extracted from a filament (e.g., tungsten) and accelerated by a high voltage. Two types of X-rays can be generated. First, white X-rays (also known as Bremsstrahlung X-rays) are produced when electrons collide with the target, reducing their speed and emitting white X-rays. These X-rays are typically present in the form of a wide background peak. Second, an inner electron is ejected by a high-speed electron. This causes an outer orbital electron to fall into the K-shell producing characteristic X-rays (K_α and K_β X-rays). These X-rays are measured as well-pronounced peaks. The X-rays generated are typically filtered to produce monochromatic radiation, which is then directed toward the sample. While X-rays interact with matter in multiple ways, this dissertation focuses on the scattered X-rays since only these have been measured. Both Compton (inelastic) and Thomson (elastic) scattering may occur. The former is present as a background contribution to the measured data, and the latter leads to the diffraction phenomenon. The interaction of the incident rays with the sample produces constructive interference (and thus a diffracted ray) when Bragg's law is satisfied:

$$n\lambda = 2d \sin\theta, \tag{3.3.16}$$

where n is an integer representing the diffraction order in the periodic lattice, λ is the X-ray wavelength, d is the interplanar spacing that generates the diffraction, and θ is the diffraction angle [183], as shown in Figure 3.3.5.

Both 1D $\theta/2\theta$ X-ray scattering and 2D grazing-incidence wide-angle X-ray scattering (GIWAXS) were used for structural measurements. The former allows scanning a wide range of angles along the height direction of a thin film, while the latter provides a 2D scan image and similar information to a $\theta/2\theta$ measurement. However, it only works at smaller angles with different measurement geometry, allowing higher resolution when measuring thin films. GIWAXS collects the wide-angle scattering, i.e., large momentum transfer values or small distances, by positioning the detector close to the sample stage. It is directly comparable to the small-angle X-ray scattering (SAXS). While there is no clear delineation between WAXS and SAXS, WAXS typically corresponds to angles between 1 and 45°, or q-values from 0.1 to 5 Å^{-1}, and therefore to real-space distances from 6 nm to Å. A schematic of the GIWAXS experimental geometry is shown in Figure 3.3.6a.

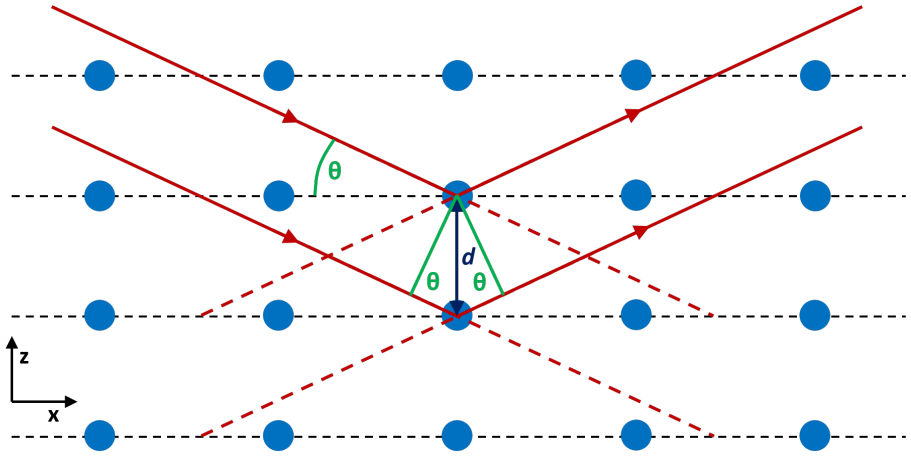

Figure 3.3.5: A schematic depiction of Bragg's law. The X-rays and lattice units are depicted in red and blue, respectively. The X-rays come in at an angle of incidence of θ and are reflected at the lattice with an interplanar spacing of d.

GIWAXS measures the elastic scattering in two dimensions (2D), so the corresponding wave vectors are located on the Ewald sphere. The Ewald sphere is the equivalent of Bragg's law in reciprocal space, as depicted in Figure 3.3.6b. The momentum transfer in the reciprocal space q can be obtained from the measured scattering angles θ_s as follows:

$$q = \frac{4\pi}{\lambda} \sin\left(\frac{\theta_s}{2}\right). \tag{3.3.17}$$

The mathematical derivation of Equation 3.3.17 is shown in Section A.5.

All XRD measurements in this dissertation were carried out using a Rigaku SmartLab setup with a copper source and a wavelength of 0.154 nm. The $\theta/2\theta$ measurements were performed on a flat substrate at $2\theta = 1 - 70°$ with a step size of 0.01° and a measuring speed of $1.5 - 2.0°$. The 2D GIWAXS measurements were performed in 2D measurement mode with an incident angle of 0.3° and a total exposure time of 3600 s per measurement. The substrate background was measured independently and manually subtracted from each measurement. The exact XRD setup configurations for the corresponding measurements are presented in Section A.6.

3.3.5.2 Atomic force microscopy

An atomic force microscope (AFM) can characterize the surface structure of relatively flat samples at the nanometer scale. The AFM uses a very fine tip positioned at a short distance from the sample. The position of the sample is controlled by piezoelectric elements. Surface information is obtained from the forces acting between the tip and the sample surface. Surface images are obtained by scanning the sample relative to the probing tip and measuring the deflection of the cantilever as a function of lateral position. The deflection height is obtained via optical techniques.

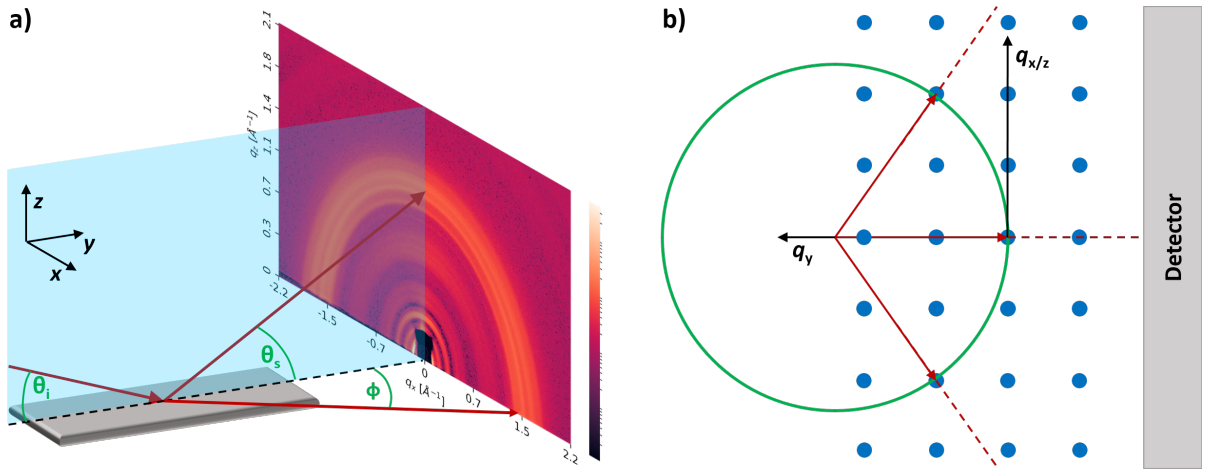

Figure 3.3.6: a) A schematic depiction of the scattering geometry in a 2D GIWAXS measurement. The incident X-ray beam is in the y-z-plane and scatters at the sample (in gray) in the x-z-plane. The intensity is measured at the detector as pixels and can be converted into scattering angles θ_s and ϕ or momentum transfer q_z and q_x, respectively. The y-z-plane is marked in blue and represents the $\theta/2\theta$ measurement direction. **b)** A simplified 2D representation of a scattering experiment in reciprocal space. The lattice and the Ewald sphere are represented in blue and green, respectively. Only the peaks that intersect the Ewald sphere are observed on the detector.

The applied force is obtained from a laser reflected from the cantilever and read by a two- or four-quadrant photodiode, as depicted schematically in Figure 3.3.7.
All measurements were performed in tapping mode of the AFM (Bruker AFM MultiMode 8-HR). In this intermittent-contact mode, the tip oscillates very close to the sample surface, tapping it at the end of each oscillation. Changes in resonance frequency or amplitude during oscillation are detected and used as input for the feedback circuit. Tapping mode is relatively sensitive, with minimal friction forces between the tip and the surface. The captured topography images were processed using built-in software (NanoScope Analysis), which applied a plane fit, flattened the image, and adjusted the color scale.

3.3.5.3 Stylus profilometer

To obtain thin film thicknesses, a stylus profilometer (Bruker DektakXT) was utilized. This device uses a diamond-tipped stylus that moves across the surface of the sample at various forces, velocities, and lengths. These factors influence the resolution and overall quality of the surface scans. During the scan, a linear variable differential transformer (LVDT) produces an electric signal that depends on the surface's roughness and is connected to the stylus. The software (Vision64) reads the electric signal and converts it to a height profile. To measure the

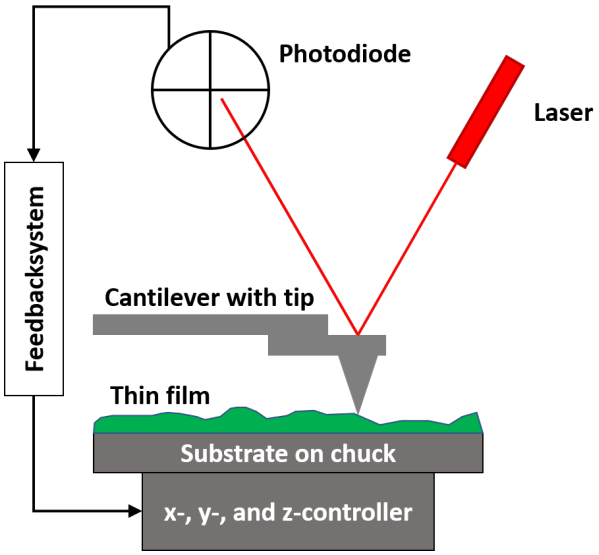

Figure 3.3.7: A schematic depiction of the AFM setup. A four-quadrant photodiode is shown. The image is not to scale.

film thickness, either the films were scratched until the substrates were reached or the films were locally removed by rubbing a cotton swab covered in the corresponding solvent. Since the stylus often scratches the surface during scanning, the provided film thicknesses are lower-limit estimates.

3.3.5.4 UV-vis spectroscopy

All UV-visible absorbance spectra were captured using a Jasco V-770 UV-vis/NIR spectrophotometer. Absorbance was measured for wavelengths between 300 and 2000 nm, and the data were corrected for background. Dichroic ratios were obtained by placing a Glan-Taylor polarizer in the beam path to polarize the light.

3.3.5.5 Polarized light microscopy

A light microscope (Zeiss Axio Imager 2) was used to characterize the dip-coated samples. The molecular alignment of the thin films was investigated using brightfield, as well as both the reflective and transmitted polarizations. When light passes through a birefringent material, its polarization changes, showing the transition between different cluster orientations. In polarized light microscopy (PLM), initially unpolarized light is first polarized in one direction by a polarizer. Then, it is focused on the specimen by a condenser and finally passes a second polarizer perpendicular to the first. If the specimen is birefringent, the polarization of the passing light changes. This provides observable light after the second polarizer and corresponds to light that passed through polarizing structures. All polarized light images were taken with crossed polarizers.

Chapter 4

Materials

This chapter introduces the organic materials investigated, focusing on the properties relevant to this dissertation.

4.1 Organic ferroelectric materials

4.1.1 Symmetry breaking

As described in Section 2.2.1, ferroelectricity is connected to symmetry breaking because an effective charge separation is necessary, which can be achieved through various molecular designs in organic materials [2]. The three main approaches to ferroelectric ordering in organic materials are proton transfer in hydrogen-bonded systems, the relative displacement of charged entities, and dipole reorientation. Proton transfer in hydrogen-bonded systems uses cooperative proton tautomerism [184], which typically results in ferroelectric materials with the highest recorded polarization in organics and relatively low coercive fields due to the moderate energy barrier for proton transfer, e.g., croconic acid [80, 185]. Relative displacement of charges is the most common type of ferroelectricity in inorganic materials and is caused by the relative movement of ions in unit cells. A conceptually similar effect arises in organic materials in dimerized charge-transfer complexes formed by small, planar, non-polar, conjugated molecules that are typically semiconducting. This effect is enabled by the molecular charge redistribution between paired donor and acceptor molecules [186, 187]. Permanent dipole reorientation is achieved by introducing field-switchable permanent dipoles into the material structure. The necessary molecular mobility for dipole flipping can be provided by freely rotatable single covalent bonds or weak van der Waals interactions. The collective dipole reorganization, or effective charge separation, is given by dipole-dipole coupling throughout the supramolecular structure [2]. Such systems typically have low remnant polarizations and high coercive fields but are easy to process and flexible; examples include BTA and PVDF. All ferroelectric materials investigated in this dissertation exhibit permanent dipole reorientation.

4.1.2 Liquid crystal BTA

Previous members of the research group, namely Dr. Indre Urbanaviciute [2] and Dr. Tim Cornelissen [3], have thoroughly investigated the structural and ferroelectric properties of the prototypical discotic N, N', N''-benzene-1,3,5-tricarboxamide (BTA) through experiments and simulations. This dissertation builds on their findings and further investigates how the structural properties of this liquid crystalline material affect its ferroelectric behavior.

4.1.2.1 Liquid crystals

When a solid or crystalline material is heated sufficiently, it usually transitions into an isotropic liquid state. However, some materials exhibit intermediate states lacking the order of solids but exhibiting more order than liquids. These ordered fluids are called liquid crystals, which typically have little to no positional order but have some orientational order and correlations between the directions of neighboring molecules. This ordering persists only within a certain temperature range, which is typically fairly narrow, and is related to the intrinsic molecular shape. Liquid crystalline molecules, called mesogens, are usually highly anisotropic in shape, thus predetermining the preferred orientation of nearby molecules. Rod-like mesogens are typically found in either the nematic or smectic phase. The nematic phase has orientational order but no positional order; thus, the averaged molecular orientation of all mesogens yields a preferred direction. In contrast, the smectic phase has both orientational and positional order [188, 189]. Liquid crystals possess a unique combination of properties found in both solids and liquids [85]. Their crystallinity provides polar order, and their liquidity provides good mechanical properties, sufficient molecular mobility, and processability [79, 85]. Liquid-crystalline molecules are soluble and typically exhibit spontaneous self-ordering [2, 85].
Ferroelectric liquid-crystalline mesogens typically have a similar structure: an aromatic (conjugated) core of different shapes is surrounded by hydrogen-bonding or dipolar moieties with permanent dipoles and flexible solubilizing tails [2]. These moieties can be located in the core, between the core and the tail, or on the tail. To achieve ferroelectricity, these materials must exhibit enough structural order to maintain the macroscopic alignment of the molecular dipoles. Due to the typical quasi-1D morphology typical of organic liquid-crystalline materials, a large influence on the switching process is expected in the case of suitable ferroelectric materials [174].

4.1.2.2 BTA properties

The molecular structure of the prototypical discotic BTA consists of a planar π-π stacking conjugated core, three strongly polar hydrogen-bonding groups, and three alkyl tails that act as spacers. The BTA structure is depicted in Figures 4.1.1a and b. BTA distinguishes itself from other small ferroelectric molecules due to its strong inherent self-assembly, which enables the discotics to form supramolecular columns [2, 79, 190]. This columnar stacking results in

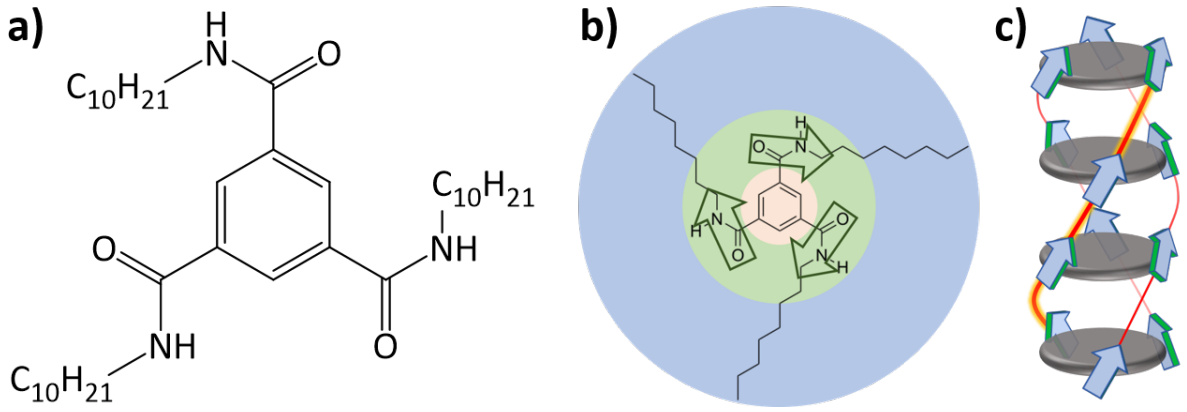

Figure 4.1.1: a) The chemical structure of a BTA-C_{10} molecule. **b)** The primary structure of a BTA-C_8 molecule, with the benzene core, the amide groups, and alkyl tails highlighted in yellow, green, and blue, respectively. Green arrows represent dipole moments. **c)** The secondary structure of a BTA, which is a single BTA column, with indicated dipole moments.

the formation of a triple helix of hydrogen-bonded dipoles that create a macrodipole along the column axis. This enables ferroelectricity in the entire BTA system, as shown in Figure 4.1.1c. This macrodipole makes self-assembly highly cooperative by aligning the amide dipoles. The $30 - 40°$ out-of-plane angle of the dipolar amide groups, the length of the hydrogen bond, and the π-π packing lead to a helical pitch of six BTA molecules [191, 192]. Consequently, each BTA molecule rotates 60° relative to adjacent molecules within a BTA column, aligning with the C_6 symmetry of the benzene core [3].

As the BTA solution transitions to a more solid state, the BTA columns typically organize into a hexagonal structure, driven primarily by steric repulsion between the alkyl tails, which determine the spacing and arrangement of the columns [3]. At lower temperatures, the material crystallizes, and the side tails freeze into a hexagonal lattice [2]. Over a wide range of intermediate temperatures, the material is in a liquid crystalline state. While the tails and amide groups are mobile, the columns remain ordered. At higher temperatures, the material melts into an isotropic liquid without long-range order [3, 174].
Despite their high degree of organization, BTA systems exhibit significant structural disorder due to amorphous regions within the material and defects in the molecular columns, even in the liquid crystalline state. While amorphous regions can be reduced by field annealing, various structural defects occur within BTA columns in the form of translational and rotational offsets. These defects lead to interrupted hydrogen-bonded helices and the formation of subcolumns. The length of these subcolumns depends on the non-defect side tails and serves as a measure of the material's disorder. Furthermore, disorder can occur on a larger scale, leading to more amorphous regions of unorganized molecules.

The ferroelectric properties of BTAs are provided by the dipole moments located in their hydrogen-bonding groups. These dipoles can be reversibly aligned by an external electric field. The amide groups can rotate freely due to the mobility provided by the flexible alkyl tails. The ferroelectricity in BTAs is characterized by the formation of macrodipoles along their columns, which can freely switch between an 'up' or 'down' state [18, 193]. This results in typical hysteresis loop behavior [3]. The ferroelectricity in BTAs is further evidenced by their Curie-Weiss behavior, wherein the dielectric susceptibility diverges at the Curie temperature [93]. Additionally, BTAs exhibit typical butterfly CV-curves [79], are pyroelectric [93], and have a negative piezoelectric coefficient d_{33} due to their disordered microstructure [184].

Theoretical predictions suggest that BTA has promising photovoltaic [194–196] and photochromic [197] properties, making it an intriguing, novel, multifunctional material. Furthermore, the properties of BTAs can be easily tuned by changing the alkyl tail lengths, affecting both the crystallinity of the system and the phase transition temperatures. Typically, longer alkyl tails result in smaller polarization and coercive field values [2, 79]. Additionally, the packing parameters of the liquid crystal, particularly the intercolumnar distances, are impacted [3]. The intercolumnar distance decreases with shorter alkyl tails, leading to a larger dipole density and, consequently, larger polarization values. The actual increase in polarization exceeds the geometrically expected amount because the intercolumnar interaction strength increases and the disorder decreases [3]. This, combined with the lower mobility of the shorter alkyl tails, increases the polarization switching barrier w_b (see Section 2.2.2). Thus, the coercive field and retention time are the highest for the shortest alkyl tail lengths. Additionally, the distances between the BTA columns differ for different alkyl tail lengths, which influences the viscosity of the solution. This plays a role in thin film deposition since larger molecules typically lead to higher solution viscosity due to reduced molecular movement [198]. Lastly, BTA properties can be modified by adding branches to the alkyl chains [3] or by modifying the dipolar moiety [2, 59, 199] and the core [2, 191, 200].

The synthesis of the discotic BTA molecules used standard procedures, in which the core and alkyl tails were synthesized separately and then joined together in the final step before purification. Details on the synthesis can be found in the relevant publications and references [3, 79, 190, 201], and the structure and morphology were verified using standard characterization techniques. Nuclear magnetic resonance (NMR), infrared spectroscopy (IR), and differential scanning calorimetry (DSC) were used to confirm the molecular structure, hydrogen bonding, and phase transition temperatures and enthalpies, respectively. Together with temperature-dependent X-ray diffraction, the phase diagram of the BTAs was constructed [3].
The BTA used in this dissertation was synthesized by Dr. Bart Saes and Dr. Subham Bhattacharjee from the research group of Prof. Dr. Rint P. Sijbesma at Eindhoven University of Technology (Netherlands). The exact synthesis process is described in the supporting information of [79].

This dissertation primarily investigated BTA-C_8. According to DSC, BTA-C_8 is in its liquid crystalline (Col_{hex}) phase at $T \approx 10 - 200$ °C [93, 174]. Furthermore, a single BTA-C_8 molecule exhibits a dipole moment of $\mu = 3 \cdot 4D = 4 \cdot 10^{-29}$ Cm. Assuming BTA-C_8 is packed in a perfect hexagonal lattice, the volume of the unit cell containing one molecule is equal to

$$V_{\mathrm{uc}} = c \cdot a^2 \frac{3\sqrt{3}}{2}, \tag{4.1.1}$$

where $c = 0.34$ nm and $a = 1.72$ nm are the intermolecular and intercolumnar distances of the BTA-C_8 molecules, respectively [3, 79]. Thus, the saturation polarization P_{s} can be obtained from Equation 2.2.1 in Section 2.2.1:

$$P_{\mathrm{s,th}} = \frac{\sum \mu}{V} = \frac{1 \cdot \mu_0}{V_{\mathrm{uc}}} = \frac{2}{3\sqrt{3}} \frac{\mu_0}{c \cdot a^2} \approx 46 \ \frac{\mathrm{mC}}{\mathrm{m}^2}. \tag{4.1.2}$$

Experiments typically yield a remnant polarization of $\approx 45 - 50$ mC m^{-2} at room temperature, as well as a coercive field of ≈ 37 V μm^{-1} at 70 °C with a sweep frequency of 5 Hz [79].

4.1.3 Polymer PVDF

One well-known organic ferroelectric polymer is polyvinylidene fluoride (PVDF), a fluorinated polymer that has been successfully commercialized [2]. It consists of repeated units of vinylidene fluoride (VDF). PVDF polymers are stable, easy to process in solution, and have good mechanical properties. While they are mostly commercialized for their excellent piezoelectric properties, they also demonstrate a decent ferroelectric performance [2, 3, 202].
PVDF units have a dipole moment due to the significant difference in electronegativity between hydrogen and fluorine atoms. The monomer can be found in five different configurations ($\alpha, \beta, \gamma, \delta$, and ϵ), but it prefers to crystallize in the non-polar α-phase, where the subsequent monomer dipoles are oriented antiparallel [203, 204]. Therefore, PVDF must be brought into the ferroelectric phase. This can be achieved by aligning the dipoles with an external electric field so that all difluoro-ethylene (-CH_2-CF_2-) dipoles face the same direction. This results in a full trans configuration of the second most common β-phase [205]. Polarization flipping is achieved by subsequent rotations of the monomers along the flexible polymer backbone [206]. However, reaching the ferroelectric phase with the homopolymer PVDF is cumbersome because it requires the combination of a high electric field, elevated temperatures, and a mechanical stretching force to reach the necessary crystalline β-phase [55].

PVDF is generally used in copolymers because changing their composition allows one to tune their properties for specific applications. Among the various PVDF derivatives, the semi-crystalline copolymer poly(vinylidene fluoride-trifluoroethylene) (P(VDF:TrFE)) has emerged as a promising ferroelectric polymer [199]. The chemical structure of the copolymer P(VDF:TrFE) is shown in Figure 4.1.2.

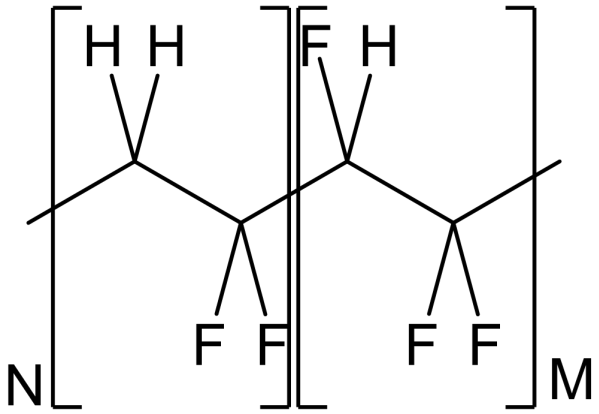

Figure 4.1.2: The chemical structure of a P(VDF:TrFE) copolymer molecule. In this structure, all the hydrogen and fluorine atoms lie in the same plane. This orientation maximizes separation and creates a dipole perpendicular to the polymer backbone chain.

The introduction of trifluoroethylene (-CHF-CF_2-) makes it significantly easier to transition into the ferroelectric β-phase due to the steric hindrance induced between the fluorine atoms. Although this reduces the theoretical saturated polarization because the molecular dipole density of PVDF decreases (by ≈ 15 % in a 30/70 TrFE/VDF mixture), the ease of conditioning outweighs this disadvantage [17]. In general, the intensity of the ferroelectric, pyroelectric, and piezoelectric responses of polymers relies on the polymer film's high level of crystallinity [2, 207]. P(VDF:TrFE) is semi-crystalline, meaning a thin film consists of segments with orderly packed polymer chains (i.e., crystallites) surrounded by amorphous material. The crystallinity of a P(VDF:TrFE) thin film can be enhanced by annealing it above its Curie temperature $T_C \approx 110$ °C, typically at $\approx 130 - 140$ °C for a few hours in an ambient atmosphere [208].

Properly conditioned and electrically poled P(VDF:TrFE) exhibits exemplary room-temperature ferroelectric behavior, demonstrating a remnant polarization of $P_r \approx 60 - 120$ mC m^{-2} and a coercive field of $E_c \approx 50$ V μm^{-1} in a capacitor [2, 111]. The P(VDF:TrFE) (77% : 23% VDF:TrFE) used was commercially supplied by Solvay and used as received.

4.2 Triphenylamines

Triphenylamines (TPAs) are materials containing a core of three phenyl groups connected by a nitrogen atom. Each phenyl group has a peripheral amide group with an aliphatic chain. Three different arrangements of amide group connections were investigated:
N, N', N''-[Nitrilotri(4,1-phenylene)]tritridecanamide (p-TPA-N) with a nitrogen linkage,
N, N', N''-[Nitrilotri(2,1-phenylene)]tritridecanamide (o-TPA-N) with an ortho linkage, and
$4, 4', 4''$-Nitrilotris(N-dodecylbenzamide) (p-TPA-C) with a carbon-linkage.

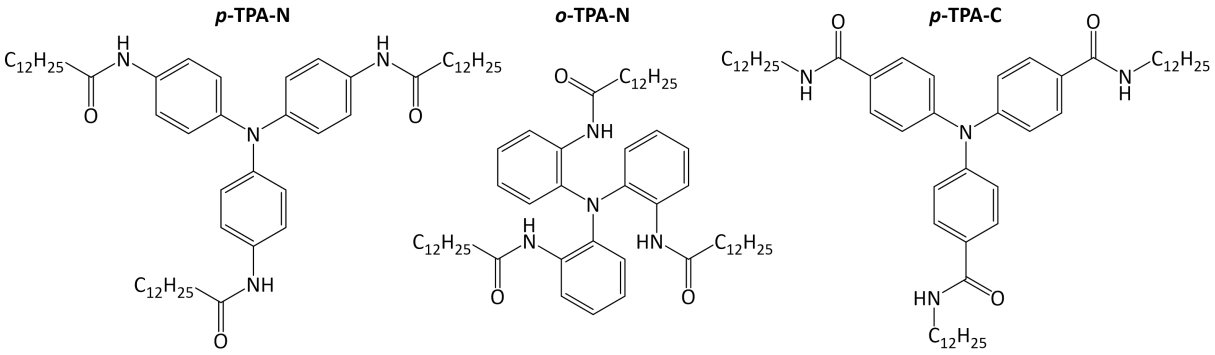

Figure 4.2.1: The chemical structures of the three triphenylamine derivatives p-TPA-N, o-TPA-N, and p-TPA-C, as indicated in the figure.

These arrangements are shown in Figure 4.2.1. The molecular structure of all TPA derivatives generally supports a delocalized π-system that extends over the entire molecule. The HOMO wavefunction is distributed almost equally over the entire TPA scaffold, including the three aromatic lobes and the connecting nitrogen atom [209, 210]. Furthermore, TPA derivatives are well known to be an excellent hole transporting component [210–216].

The synthesis and process and characterization of the TPA derivatives are described in detail in the supporting information of Publication IV. The TPA derivatives used in this dissertation were synthesized by Dr. Ina Michalsky in the research group of Prof. Dr. Milan Kivala at Heidelberg University (Germany).

4.3 Organic semiconducting polymer P3HT

4.3.1 Π-conjugated semiconducting polymers

In organic semiconductors, charge typically moves by hopping between localized states. The electronic coupling between these states is one of the main limiting factors (see Section 2.3.2). In a π-conjugated polymer thin film, charge transport can be either intra- or inter-chain. Intra-chain transport is fast and occurs along the polymer backbone. Inter-chain transport corresponds to long-range charge transport, which is typically assumed to be limited by inter-chain hopping. Generally, transport efficiency (i.e., conductivity and mobility) is highest along the conjugated backbone, followed by overlapping π-orbitals along the π-π stacking direction and lowest along the insulating alkyl side-chain direction. Increasing the structural order of such a system by aligning the conjugated polymer film decreases the average π-π stacking distance and the number of inter-chain hopping events, leading to an increase in charge mobility [217, 218]. Since the degree of polymer alignment is generally recognized as decisive for the charge carrier transport efficiency, aligning and orienting the polymer relative to the substrate and field direction is typically used

to increase order and improve π-π stacking [219].
For semi- and liquid-crystalline polymers, charge transport in macroscopic devices is generally characterized by alternating ordered and disordered phases with varying interconnections and structural defects [218]. This is similar to the structure shown in Figure 2.1.1 in Section 2.1. The amorphous phase exhibits inefficient charge transport due to the lack of π-stacking order. The two types of ordered phases are crystallites and aggregates, which commonly coexist and are typically interconnected. Therefore, charge transport is a multiscale process limited by amorphous regions. It can be improved by forming crystallites and/or aggregates and their interconnections. Charge transport is also influenced by molecular weight, side-chain alignment, and backbone rigidity [218]. Macroscopic charge mobility is controlled by inter-chain jumps resulting from crystalline domains within the generally amorphous films.
The formation of individual polymer chains and their relative orientation often occurs during substrate coating and is influenced by the casting method, substrate, temperature, and solvent. Furthermore, side chain engineering can enhance intermolecular π-π stacking by reducing the stacking distance of adjacent polymer chains and increasing π-π overlap [217, 218]. Π-conjugated polymers can adopt edge-on, face-on, or end-on orientations [217, 218]. Anisotropy within the microstructure of the thin film can improve charge conduction along the polymer backbone and the direction of π-π stacking, thereby improving the general thermoelectric properties.

4.3.2 P3HT properties

Poly(3-hexylthiophene) (P3HT) is a representative π-conjugated polymer and an organic semiconductor. Its chemical structure is shown in Figure 4.3.1a. In this dissertation, P3HT, a low-band-gap polymer donor, was doped with 2,3,4,5-tetrafluoro-7,7,8,9-tetracyanoquinodimethane (F_4TCNQ) and tris(4-bromophenyl) ammoniumyl hexachloroantimonate (Magic Blue, MB). Their chemical structures are shown in Figures 4.3.1b and c, respectively. Both F_4TCNQ and MB exhibit strong electron-accepting abilities and extended π-systems. The HOMO energy level of P3HT ranges from -4.80 to -5.20 eV [220–225], while the LUMO energy levels of F_4TCNQ and MB range from -5.20 to -5.24 [221, 223–226] and from -5.50 to -5.80 eV [225, 227, 228], respectively.
Similar to other π-conjugated polymers, the film structure of P3HT consists of crystalline domains embedded in an amorphous matrix resulting from enhanced aggregation [127]. Charge transport can occur in three directions: along the backbone, π-π stacking, and alkyl stacking. The thermoelectric properties of doped P3HT are usually improved by aligning the polymer chains and increasing the degree of crystallization, resulting in greater structural order. Higher molecular weight and regioregularity of the P3HT polymer chains lead to more aggregates and thus a higher charge carrier mobility within thin films [229].
Generally, the P3HT amorphous phase has a deeper HOMO energy level (by ≈ 0.2 eV) than the crystalline domains [230]. Therefore, F_4TCNQ is likely to dope less of the P3HT amorphous phase than the dopant MB. Thus, the latter is expected to lead to higher charge conductivity [225].

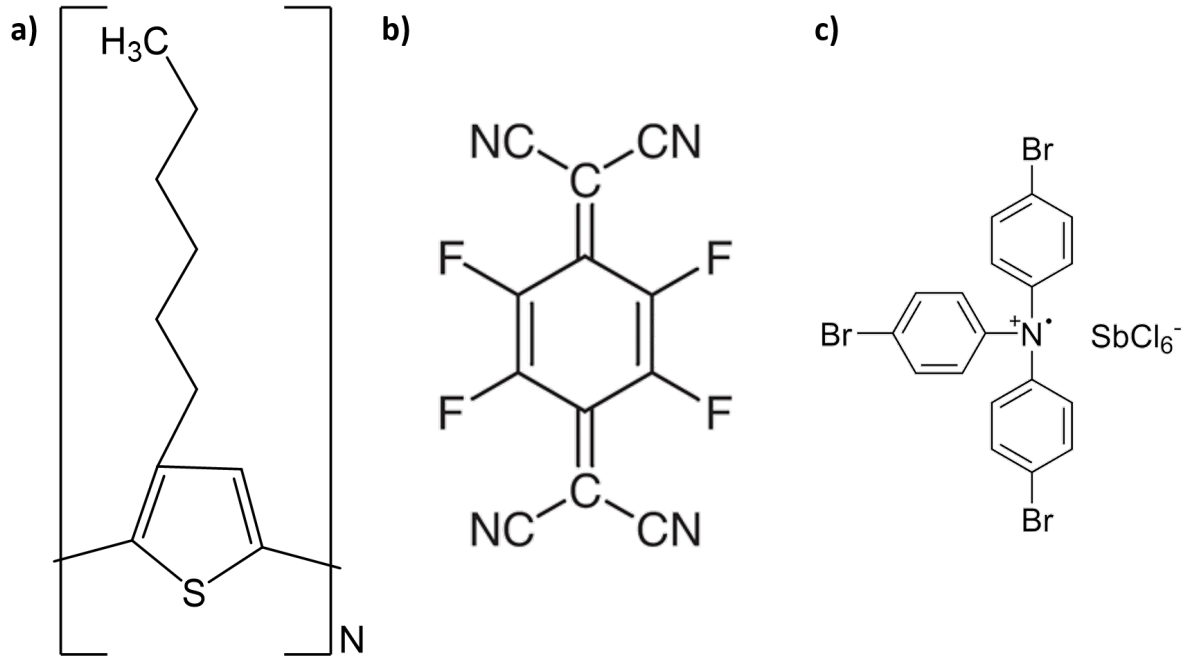

Figure 4.3.1: The chemical structures of **a)** the π-conjugated polymer P3HT, **b)** the dopant F_4TCNQ, and **c)** the dopant MB.

The P3HT used was regioregular (rr) and was supplied commercially by Ossila (M109), with regioregularity of 95.2%, a molecular weight of 36600 g mol^{-1}, and a PDI of 2.0.

Chapter 5

Ferroelectric switching behavior of dip-coated organic ferroelectric BTA

During field annealing, the BTA columns align in the direction of the electric field, thereby enhancing the ferroelectric switching properties of BTA films. Therefore, samples deposited by drop casting or spin coating require extensive post-deposition treatment involving high electric fields and typically elevated temperatures to achieve optimal ferroelectric performance. This chapter aims to experimentally investigate whether the morphology of electrically pre-treated BTA thin films can be altered during deposition to resemble the ferroelectric switching properties of the post-treated, field-annealed thin films. Dip coating was chosen as the coating technique due to its simplicity and availability. The structural and ferroelectric switching properties of thin films dip coated and drop cast from BTA-C_8 in CF solutions were investigated and compared, with and without field annealing. These findings can be generalized to apply to similar supramolecular organic ferroelectrics.

The dip coating theory is provided in Section 3.2.3, and the description of the corresponding samples used for thin film characterization is found in Section 3.1.1. Section 3.3.1 describes the measurement setup and method used to ferroelectrically characterize the fabricated samples (see Section 3.1.2.2). Section 4.1.2.2 introduces BTAs and their properties.

The author completed the entire project, which began as a part of the their master's project. The dip coating experiments, determination of the dip coating speed, structural characterization using PLM and AFM (see Sections 3.3.5.5 and 3.3.5.2), and initial ferroelectric characterization measurements were mostly carried out during the master's project and are also presented in the author's master's thesis. For the sake of completeness, the relevant results are mentioned briefly and marked as such. The structural analysis using XRD (see Section 3.3.5.1) and the extensive ferroelectric characterization of the BTA samples, including preparing new samples, re-measuring, and analyzing the data, were conducted as part of the doctoral project.

Most of the results presented in this chapter are included in Publication I. Much of the text and figures in this chapter originate from Publication I. The original text was written primarily by the author for Publication I and revised and improved by Prof. Dr. Martijn Kemerink. Changes to the text were made to fit this dissertation's argumentation and style. The figures taken from Publication I may have changes to their descriptions.

5.1 Structural characterization

As described in Section 3.2.3, the properties of dip-coated films depend on solution parameters, which are influenced by the solvent and material concentrations. To obtain optimal BTA-C_8 thin films, the material concentration was varied from 5 to 40 mg ml^{-1} and examined using PLM and AFM to analyze thin film and surface alignment, respectively. The author's master's thesis concluded that a visible alignment was achieved within the BTA-C_8 thin films with different BTA-C_8 in CF concentrations, and this alignment was also present on the material surface. Higher BTA-C_8 concentrations appeared to produce better alignment. Thus, the 40 mg ml^{-1} BTA-C_8 in CF solution was selected for further investigation. For reference, Figure A.7.1 in Section A.7 shows a PLM image of a drop-cast 40 mg ml^{-1} BTA-C_8 in CF thin film. The PLM and AFM results for the various BTA-C_8 in CF concentrations are presented in Figures A.7.2, A.7.3, and A.7.4 in Section A.7.

Figure 5.1.1 shows the morphologies of thin films dip coated from a 40 mg ml^{-1} BTA-C_8 in CF solution at dip coating speeds ranging from 0.1 to 150 mm min^{-1}. The monochromatic colors in Figure 5.1.1 indicate the presence of homogeneously aligned molecular clusters, with the columnar alignment axis lying in-plane. Despite the presence of mostly unexplained superstructures, all PLM images show a high degree of in-plane order, which is notably absent in drop-cast films (see Figure A.7.1 in Section A.7).
For dip coating velocities of less than $\approx$ 10 mm min^{-1}, periodic stripes of oriented material are found arranged perpendicular to the dip coating direction. Within these stripes, filament-like structures form with a pronounced alignment along the dip coating direction. This behavior aligns with previous studies on dip coating at similar velocities, suggesting successful macroscopic alignment, albeit with some dispersion [158].
For dip coating velocities between 10 and 60 mm min^{-1}, a periodic line structure that interrupts the crystal morphology emerges parallel to the dip coating direction. These lines are not visible when the surface topography is investigated with a profilometer, indicating that they only reflect variations in in-plane cluster orientation within the dip-coated films. While one cannot draw conclusions about molecular packing based on PLM images alone, BTA's strong tendency to self-organize into supramolecular polymers with a well-defined molecular packing, provided by π-stacking and hydrogen bonding network, renders it unlikely that another, previously unobserved molecular packing occurs in these regions. Further aligned clusters are located between these lines, with an orientation similar to that of lower extraction frequencies. That is, the clusters are aligned parallel to the dip coating direction. There is no definitive explanation for the occurrence of lines parallel to the dip coating direction. Similar lines have been observed before but not reported, so their origin remains unclear. They are speculated to relate to boundaries between coherent domains where the in-plane orientation vector rotates by $\approx 90°$.
For dip coating speeds beyond $\approx$ 70 mm min^{-1}, the morphology changes suddenly, and additional

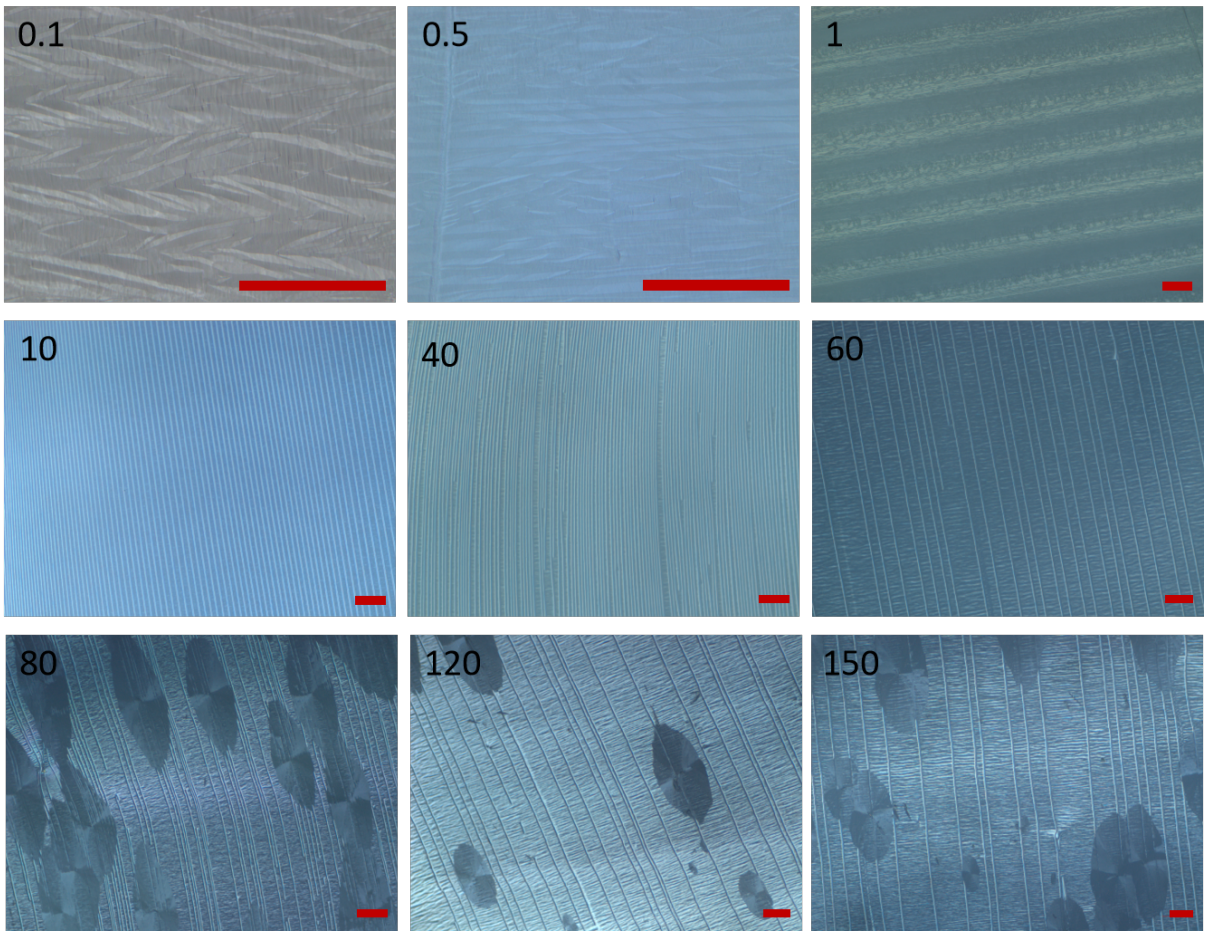

Figure 5.1.1: Reflective PLM images of thin films dip coated from a 40 mg ml^{-1} BTA-C_8 in CF solution at different dip coating speeds, which are presented as numbers in the images in mm min^{-1}. The withdrawal direction is vertical, from top to bottom. All images were taken with 10x magnification, and the scale bars represent 100 μm in all images. This figure was adapted from author's master's thesis.

structures with radial in-plane alignment form. Starting at 80 mm min^{-1}, spherulites clearly develop and persist at all higher dip coating velocities without noticeable further changes. It appears that the spherulite structures overlap with the previously present cluster and line structures. Similar to the line structures, they are exclusively visible under PLM. Similar spherulitic morphologies have been observed in other dip-coated materials at higher dip coating velocities and are usually the result of (radial) growth from a point-like nucleus in an isotropically drying wet film [158].

Based on the change in morphology shown in Figure 5.1.1, it is reasonable to anticipate a change from the evaporation regime to the Landau-Levich regime between 60 and 80 mm min^{-1}.

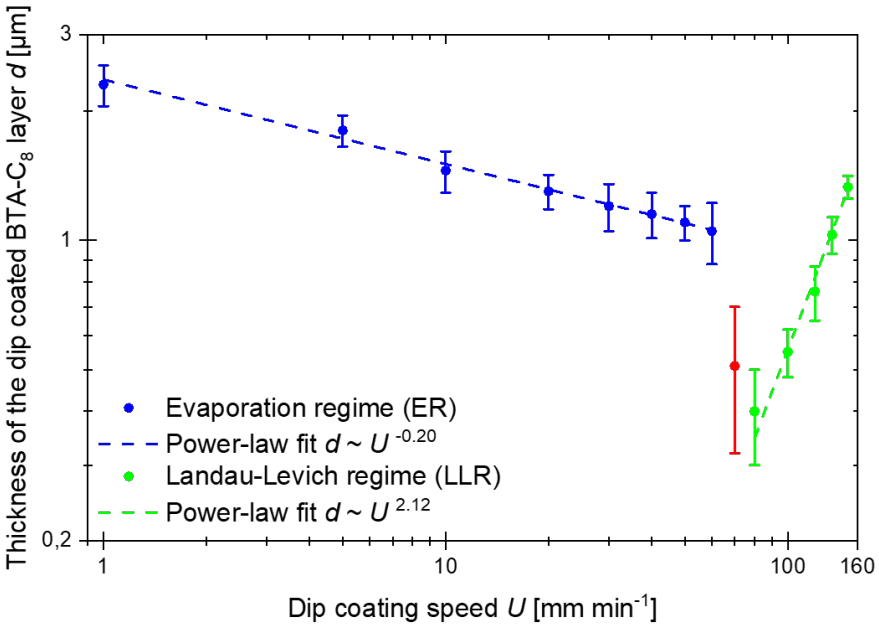

Figure 5.1.2: The film thickness d of samples dip coated from a 40 mg ml^{-1} BTA-C_8 in CF solution as a function of the dip coating speed U. The dashed lines are fits to $d \propto U^{\alpha}$. The blue and green colors correspond to the evaporation and Landau-Levich regimes, respectively. The red data point is excluded from any regime due to its significant deviation from the other data points. This figure was taken and slightly modified from Publication I with permission for usage granted by Advanced Materials Technologies.

Following Rogowski and Darhuber, the film thickness was investigated as a proxy for the total deposited crystal mass as a function of dip coating speed [158], as discussed in detail in Section 3.2.3. Figure 5.1.2 plots the film thickness d of the thin films dip coated with a 40 mg ml^{-1} BTA-C_8 in CF solution on glass substrates against the dip coating velocity U. Two deposition regimes can clearly be distinguished, separated by a characteristic threshold speed U_{th} [158]. The experimental data were fitted with power-law functions $d \propto U^{\alpha}$. For the evaporation and Landau–Levich regimes, the power-law exponents were found to be $\alpha = -0.20$ and $\alpha = 2.12$, respectively. While the absolute values of these exponents differ from those of similar experiments - Rogowski and Darhuber obtained $\alpha = -0.95$ and $\alpha = 2/3$ [158], and Le Berre, Chen, and Baigl obtained $\alpha = -1.14$ and $\alpha = 0.76$ [171], respectively for the evaporation and Landau-Levich regimes - they allow to identify a critical velocity of approximately 70 mm min^{-1}, consistent with the PLM analysis. The differing numbers are attributed to the fact that, unlike BTA, the compounds investigated in the referenced studies do not exhibit supramolecular self-organization [158, 171]. Specifically, gelation through the formation of a supramolecular network in the drying film is expected to have a significantly affect the rheological properties and the final film thicknesses [231–233].

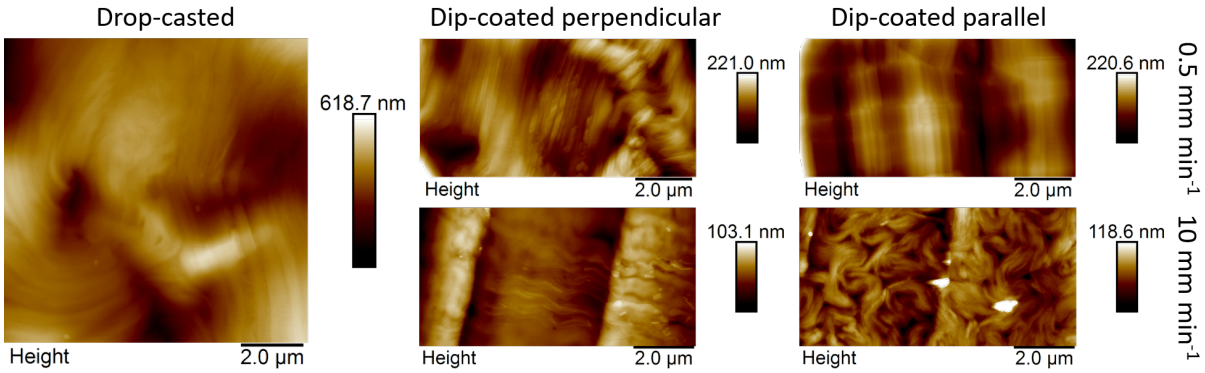

Figure 5.1.3: The AFM topographies of selected in-plane IDE samples coated with a 10 mg ml^{-1} BTA-C_8 in CF solution, as indicated in the figure. The electrodes run vertically in all images but are not always visible due to the relatively large film thicknesses. Consequently, the electric field is horizontal. Perpendicular and parallel coating directions refer to the electrode directions. All images were take with a scan area of either 10 μm $\times$ 10 μm or 10 μm $\times$ 5 μm. The corresponding amplitude images can be found in Figure A.7.5 in Section A.7. This image was taken unmodified from Publication I with permission for usage granted by Advanced Materials Technologies.

Using Equation 3.2.7 in Section 3.2.3, the threshold speed U_{th} can be determined. The evaporation rate of a 40 mg ml^{-1} BTA-C_8 in CF solution was determined to be $\approx 6.8 \cdot 10^{-8}$ kg s^{-1} (see Section 3.2.3). Using the material properties of CF ($\rho = 1489$ kg m^{-3}, $\mu = 0.563 \cdot 10^{-3}$ Pa, and $\sigma = 27.24 \cdot 10^{-3}$ N m^{-1}), the threshold speed could be estimated to be ≈ 160 mm min^{-1} (see Section A.3). However, this value may overestimate the experimental result because evaporation from the contact line is retarded by solution vapor emerging from the liquid reservoir, which is not considered when determining the evaporation rate [158]. Therefore, the experimental observations of the change in morphology and the change in power-law exponent at $\approx 60 - 80$ mm min^{-1} match the estimated threshold speed to an acceptable degree.

Figure 5.1.3 shows the AFM topographies of selected in-plane IDE samples coated with BTA-C_8. Although AFM is a surface-sensitive technique and one cannot assume the measured topographies are representative of the bulk, the large amplitude ($\gg 100$ nm) of the main topographic features in Figure 5.1.3 and the clear correlation between larger and smaller features indicate that decoupling between surface topography and bulk morphology is unlikely in this case. The perpendicular 10 mm min^{-1} sample shows the expected alignment of the supramolecular bundles along the coating direction. In contrast, the 0.5 mm min^{-1} sample has the bundles oriented parallel to the electrodes and perpendicular to the applied electric field and coating direction. At lower speeds, apparently, the IDE structures effectively act as an alignment template. For parallel dip coating at the same (low) speeds, the parallel alignment is even more pronounced. At higher speeds in

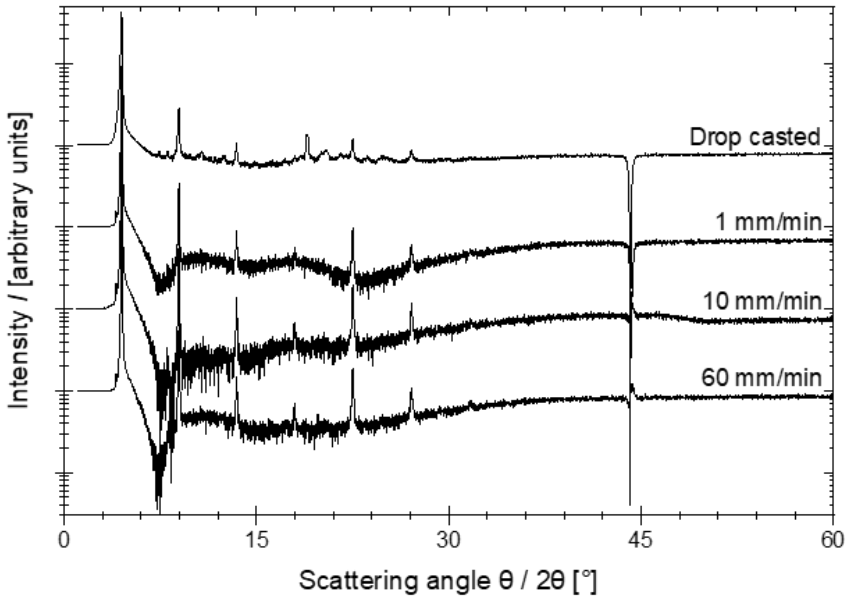

Figure 5.1.4: The relative X-ray scattering intensity I as a function of the scattering angle in a $\theta/2\theta$ measurement. The thin films were either drop cast or dip coated from a 40 mg ml^{-1} BTA-C_8 in CF solution. The data were taken at room temperature. The figure was taken and slightly modified from Publication I with permission for usage granted by Advanced Materials Technologies.

the parallel dip coating direction, a more gyroid morphology is observed.
The morphology of the dip-coated BTA-C_8 thin films was further investigated by XRD. Figure 5.1.4 shows a $\theta/2\theta$ measurement of one drop-cast and multiple dip-coated BTA-C_8 samples. The intensity spectrum of the drop-cast BTA-C_8 is consistent with previous XRD studies of BTA-C_n [2, 79]. Intensity peaks at $2\theta \approx 4.5°$ and their multiples represent the intercolumnar distance. The peaks representing π-π stacking distances are hardly distinguishable since the aligned molecular bundles are in-plane, as will be discussed further below. Some indications of π-π stacking can be seen at $\approx 18 - 20°$. The dip-coated film spectra match the drop-cast film spectra, showing that the same crystal structure is obtained with both techniques. The dip-coated films have a higher noise level and a less pronounced fine structure, which is attributed to smaller film thickness and possibly a reduced long-range order.
Figure 5.1.5 depicts the expected (idealized) morphology of dip-coated samples based on the preceding discussion, as well as the anticipated GIWAXS patterns. The outcomes displayed for different scattering angles stem from the indicated symmetry and morphology considerations. The absolute values of the scattering angles are derived from the spectra shown in Figure 5.1.4. If the BTA stacks were to orient predominantly perpendicular to the dip coating direction, instead of parallel, the GIWAXS patterns for the two relative beam directions would swap.

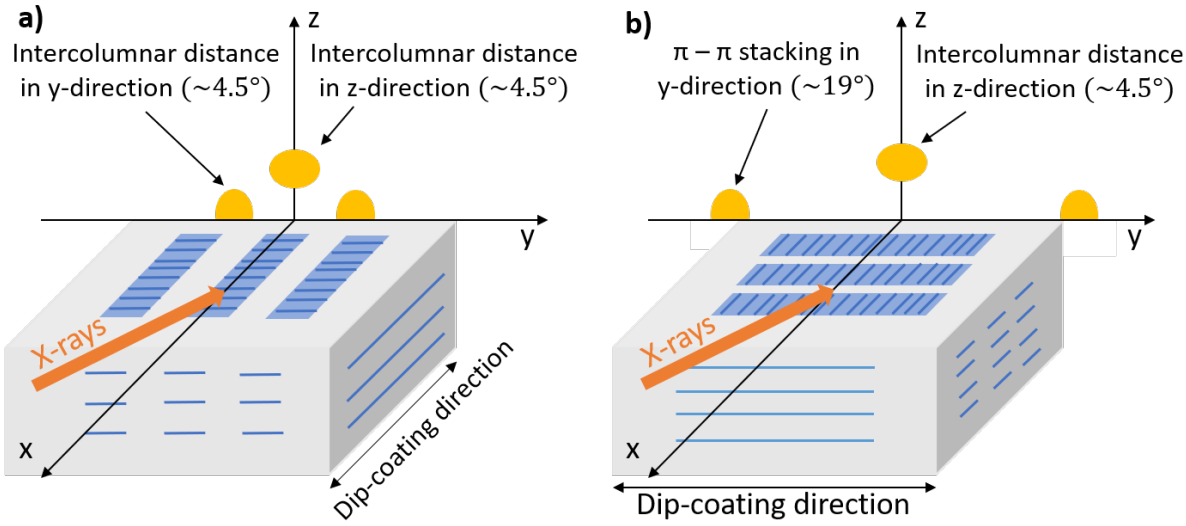

Figure 5.1.5: The anticipated dominant morphology and the resulting first-order GIWAXS maxima of dip-coated thin films for X-rays hitting the thin film **a)** parallel and **b)** perpendicular to the dip coating direction. For edge-on, in-plane oriented bundles of BTA molecules represented by blue rectangles with black lines, no diffraction patterns are anticipated along the z-direction (at $\approx 19°$) associated with π-π stacking. This figure was taken unmodified from Publication I with permission for usage granted by Advanced Materials Technologies.

The angle-averaged intensity spectra of the corresponding GIWAXS measurements are presented in Figure 5.1.6, and the raw 2D spectra are provided in Figure A.7.6 in Section A.7. Figure 5.1.6a shows the intensity integrated along the z-direction (see Figure 5.1.5). The first-order intercolumnar distance peak is clearly visible in all spectra. In line with Figure 5.1.4, second- and third-order peaks are clearly visible at $\approx 9.0°$ and $\approx 13.5°$, respectively. For higher scattering angles, no peaks are visible for parallel dip coated, and very weak, broad peaks are visible for drop cast and perpendicular dip coated. This is is consistent with the prediction in Figure 5.1.5 that only diffraction maxima associated with the intercolumnar stacking distance should appear in bundles that are (almost) entirely edge-on oriented. Differences between the parallel and perpendicular orientations appear in Figure 5.1.6b, which shows the intensity integrated along the y-direction. Particularly, the films measured with the incident beam perpendicular to the dip coating direction exhibit relatively strong peaks associated with π–π stacking, highlighted in red, and relatively weak peaks associated with the intercolumnar stacking, highlighted in green. For parallel illumination, the situation is reversed. Comparison with Figure 5.1.5, therefore, allows the conclusion that significant, yet imperfect, alignment occurs along the dip coating direction. This notion is consistent with the PLM data in Figure 5.1.1, where the alternation of bright and dark regions indicates the presence of domains of different orientations. The origin of the structures

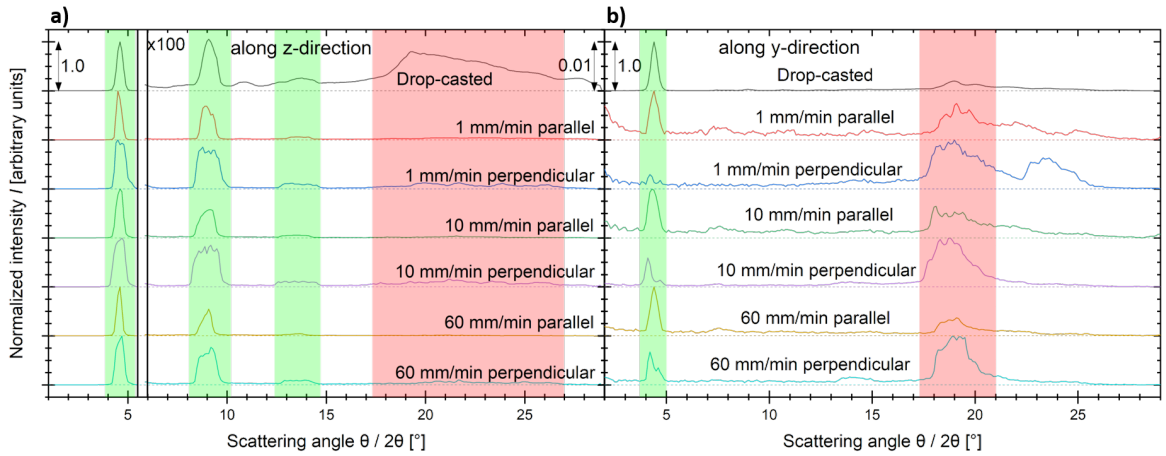

Figure 5.1.6: The normalized intensity I as a function of the scattering angle $\theta/2\theta$ for $2\theta = 1-29°$, as obtained from GIWAXS measurements. The samples shown are the same as in Figure 5.1.4. Dip-coated films were measured with the incoming beam both parallel and perpendicular to the dip coating direction. The intensity I was integrated along **a)** the z-direction (averaged over $75-90°$) with a zoom-in factor of 100 after 6° and **b)** the y-direction (averaged over $0-15°$). These directions refer to the detector and are indicated in Figure 5.1.5 and Figure A.7.6a in Section A.7. The green and red areas show scattering angles associated with the intercolumnar distance and π-π stacking, respectively. This figure was taken unmodified from Publication I with permission for usage granted by Advanced Materials Technologies.

beyond $\approx 22°$ in the spectra for 1 mm min^{-1} is unclear but might be related to (a different packing in) the deviating superstructures that are visible in the PLM images of Figure 5.1.1 for this speed.

5.2 Ferroelectric switching

The effect of aligning BTA-C_8 molecules via dip coating on the ferroelectric behavior was investigated by monitoring polarization charge growth over time at a constant elevated temperature. Figure 5.2.1 shows the corresponding raw (a) and normalized (b) remnant polarization values P_r against the time t, where normalization is used to circumvent the issue that the measured absolute remnant polarization depends on the film thickness, which varies between the samples. The first data point was taken ≈ 6 s after the double wave signal was applied. These measurements effectively probe the extent to which the initial polarizability can be increased by field annealing; that is, they measure the quality of the initial alignment, not the polarization switching time, which is in the ms range for BTA.

Figure 5.2.1a shows measurements of films with different and locally varying thicknesses. A fixed mean value of 2 μm was used to calculate the remnant polarization values. Thus, the variation in

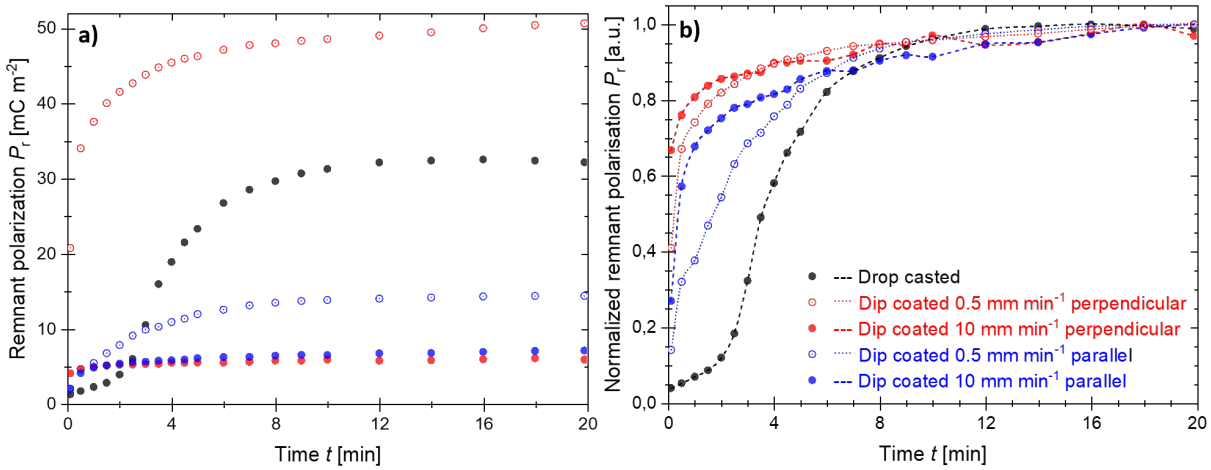

Figure 5.2.1: a) Raw and **b)** normalized remnant polarization P_r as a function of time t, measured at a voltage amplitude $U = 300$ V, frequency $f = 5$ Hz, and temperature $T = 120$ °C. Red and blue correspond to dipping perpendicular or parallel to the in-plane electrodes (see Section 3.1.2.2), respectively, as indicated in the legend (same in both figures). The size of the data points represents the typical error margin of the data. The figure was taken and slightly modified from Publication I with permission for usage granted by Advanced Materials Technologies.

the absolute remnant polarization values of the different films can be attributed to variations in thickness and does not reflect actual differences in the saturated (long-time) values. Although proper normalization of the film thickness was impossible due to film roughness, no evidence was found that the saturated (long-time) remnant polarization depends on the coating speed or direction. By comparing the saturation values in Figure 5.2.1a to the expected nominal remnant polarization of BTA-C_8 ($P_\mathrm{r} \approx 48$ mC m^{-2}), one can estimate an effective film thickness reflecting the amount of material that is present in the rough film. This value should be close to the mean thickness. Focusing on the perpendicular samples, where the differences between 0.5 and 10 mm min^{-1} are largest, one finds an effective thickness of 2 μm for the former and 0.3 μm for the latter. Comparing these values to those obtained on bare glass (see Figure 5.1.2 in Section 5.1) shows that the presence of the electrodes hardly affects the thickness of the 0.5 mm min^{-1} sample, whereas it reduces the thickness by roughly a factor of five at the higher speed of 10 mm min^{-1}. These findings are consistent with the discussion of the AFM data in Figure 5.1.3 in Section 5.1, where it was argued that the presence of the electrodes can significantly impact film formation. Unfortunately, neither PLM nor XRD has sufficient resolution to determine the orientation between the finger electrodes. However, the AFM images in Figure 5.1.3 in Section 5.1 suggest at least an equally good preferential alignment as the GIWAXS data for films on pure glass.

Figure 5.2.1b shows that all dip-coated BTA-C_8 samples exhibit a significantly faster increase in ferroelectric switching than the drop-cast sample and have a higher remnant polarization at short times. While the drop-cast sample starts at around 5% of its maximum remnant polarization, the

	BTA-C_8 dip coated parallel to the electrodes	BTA-C_8 drop casted on top of the electrodes	BTA-C_8 dip coated perpendicular to the electrodes
Orientation of BTA columns Electric field $\vec{E}$ Electrodes	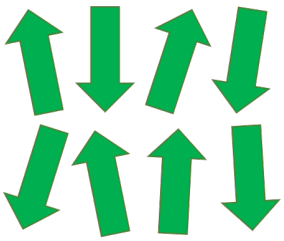	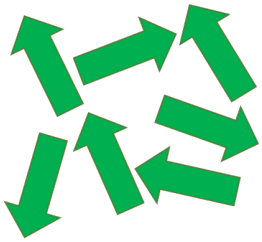	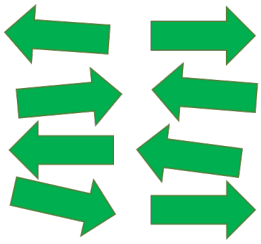
Degree of alignment of BTA columns	~100%	~0%	~100%
BTA columns aligned along electric field	~100%	~50%	~0%

Figure 5.2.2: A schematic overview of the (ideally) expected alignment of the BTA molecules, and thus their dipole moments, for drop casting and dip coating, both parallel and perpendicular to the electrodes, before an electric field is applied. Green arrows represent the BTA molecular columns and indicate possible macrodipoles. The corresponding discussion on the mean alignment of molecular columns in drop casted BTA is presented in Section A.8. This figure was adapted from author's master thesis.

sample dip coated perpendicular to the electrodes at 10 mm min^{-1} starts at roughly 65%. The sample dip coated parallel to the electrodes at the same speed starts at approximately 30%. This is consistent with the preferential but imperfect alignment of the BTA bundles in the direction of dip coating, as seen in Figures 5.1.1 and 5.1.6 in Section 5.1. The faster switching of dip-coated samples is attributed to the presence of macroscopic regions aligned in the field direction, which can nucleate further growth of field-aligned bundles. Figure 5.2.2 shows this schematically, and the mean alignment of molecular columns in drop casted BTA is discussed in Section A.8. Moreover, the reduced long-range order of the dip-coated films, as hypothesized based on Figure 5.1.4 in Section 5.1, might facilitate the molecular motion needed for field alignment, and as such be a practical advantage.

A more detailed understanding of the effect of pre-alignment on ferroelectric switching can be gained by examining the temperature dependence of the remnant polarization, presented in Figure 5.2.3. Specifically, a continuous DW measuring signal was applied while the temperature was increased in steps. For each temperature step, the measurement ran for $10 - 15$ min at a constant temperature to allow for polarization saturation. Then, the remnant polarization was measured before the temperature was increased and the next polarization measurement was performed. The corresponding raw data are presented in Figure A.7.7 in Section A.7.

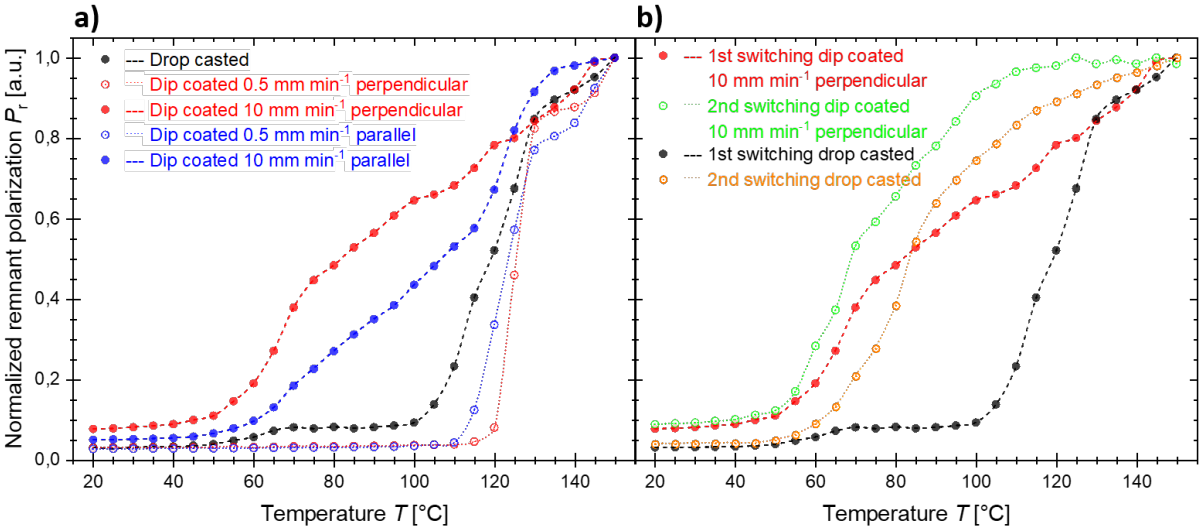

Figure 5.2.3: The normalized remnant polarization P_r as a function of temperature T, measured at a voltage amplitude of $U = 300$ V and a frequency of $f = 5$ Hz. The different colors correspond to different coating parameters, as indicated in the legend. **a)** The first heating run of all samples. **b)** First and second heating runs for drop-cast and dip-coated perpendicular (10 mm min^{-1}) samples. The size of the data points represents the typical error margin of the data. The corresponding raw data are presented in Figure A.7.7 in Section A.7. This figure was taken and slightly modified from Publication I with permission for usage granted by Advanced Materials Technologies.

As shown in Figure 5.2.3a, the non-aligned, drop-cast sample begins ferroelectric switching at ≈ 105 °C, followed by a significant increase in outgoing current and saturation at ≈ 140 °C. The absence of a perfect saturation at high temperatures is attributed to the transport of BTA material from the electrode to the gap regions, which was observed before in in-plane devices [79]. Interestingly, irrespective of the dip coating direction, the 10 mm min^{-1} samples begin switching at much lower temperatures, $\approx 55 - 60$ °C, than the 0.5 mm min^{-1} samples, which only begin switching after the drop-cast sample at temperatures around $115 - 120$ °C. At the same time, the perpendicular 10 mm min^{-1} sample shows a significantly faster onset than the parallel 10 mm min^{-1} sample; for 0.5 mm min^{-1}, the differences are insignificant. In the saturation regime, no significant differences were observed.
The significant difference between the 0.5 and 10 mm min^{-1} perpendicularly coated samples is unexpected based on the results in Figures 5.1.1 and 5.1.6 in Section 5.1, which indicate that both coating speeds should lead to a significant preferential alignment. However, the difference is apparent in the AFM images in Figure 5.1.3 in Section 5.1. At lower speeds, the undesired morphology resulting from the IDE structures must be broken up by a combination of heating and an applied electric field. Note that the temperature of 120 °C used in the experiment in

Figure 5.2.1 is such that this alignment occurs rapidly. For parallel dip coating at low speeds, the pronounced parallel alignment (see Figure 5.2.3) seemingly does not further affect the switching onset in Figure 5.2.1. At higher speeds in the parallel dip coating direction, the observation that this sample behaves intermediately between the optimal 10 mm min^{-1} perpendicular sample and the 0.5 mm min^{-1} samples is consistent with the more gyroid morphology observed in Figure 5.1.3 in Section 5.1.

The temperature dependence of the ferroelectric switching was further investigated by comparing the first and second heating runs of the drop-cast and 10 mm min^{-1} dip-coated perpendicular samples, presented in Figure 5.2.3b. The second heating runs were performed either immediately or a few days after the first heating run. Similar data were obtained from both experiments, allowing us to conclude that long-term morphological changes do not play an important role, which is consistent with the absence of changes observed in AFM and PLM images. The data in Figure 5.2.3b show that, from a functional perspective, the alignment in the best dip-coated sample is equivalent to that in an isotropic (drop-cast) sample after field annealing. As expected, the second heating run of the drop-cast film turns on at a much lower temperature than in the first heating run due to field annealing. However, the device starts switching later than the dip-coated sample in the first run, yet it reaches full saturation slightly earlier. Comparing the first and second heating runs of the dip-coated sample shows that morphological improvement of as- or drop-cast samples is still possible, though most of the material is already available for switching in the as-cast film.

5.3 Conclusion

The effect of dip coating on the ferroelectric switching in BTA molecules was investigated by dip coating BTA thin films and comparing the corresponding in-plane devices to drop-cast ones. A significant change in morphology, specifically the alignment of molecular clusters along the dip coating direction, was observed using PLM, AFM, and XRD. This change was attributed to enhanced crystallization and columnar alignment in the dip-coated thin films. The film thicknesses of the dip-coated BTA thin films were investigated, and both the evaporation and Landau-Levich regimes were established, with a well-defined dip coating threshold speed of $\approx 60 - 80$ mm min^{-1}. Although the corresponding power-law exponents differed from those of similar experiments, the threshold speed values obtained from theoretical predictions were similar to those achieved by the dip coating process and the structural changes observed in PLM.

The ferroelectric switching of in-plane BTA thin films was investigated by monitoring the change in remnant polarization as a function of time and temperature. For the former, all dip-coated samples exhibited a significantly earlier and stronger onset of remnant polarization, attributed to the presence of macroscopic aligned regions acting as nucleation growth centers. The latter showed that samples dip-coated at a speed of 10 mm min^{-1} started switching at significantly

reduced temperatures of ≈ 50 °C compared to drop-cast samples (≈ 100 °C). Conversely, samples with a dip coating speed of 0.5 mm min^{-1} began ferroelectric switching at higher temperatures of ≈ 120 °C, speculated to be due to the electrodes acting as an alignment template and inducing undesired morphology. Comparing the first ferroelectric switching process of a dip-coated sample with the second of a drop-cast sample produced similar results. This allowed to conclude that a dip-coated sample functions the same way as a field-annealed drop-cast sample during ferroelectric switching, meaning that the molecular alignment is equivalent in both cases.

Chapter 6

Simulated Barkhausen noise in organic ferroelectric BTA

Barkhausen noise provides additional insight into the switching process of ferroelectric materials by allowing the progression of switching events to be studied. However, most research has focused on inorganic ferroelectric materials and perovskites. There are hardly any simulations or experimental studies on Barkhausen noise in disordered organic materials. This chapter presents the results of kinetic Monte Carlo (kMC) simulations that investigated self-organized critical behavior in BTA-C_8 ferroelectric switching at various temperatures, driving frequencies, and degrees of disorder. Although unsuccessful, experimental measurements were also performed.

The theory of Barkhausen noise is described in Section 2.2.7. Section 3.3.3 presents the measurement setup used to characterize the samples (see Section 3.1.2). A description of BTA is given in Section 4.1.2. This chapter includes a description of the kMC simulation.

The kinetic Monte Carlo simulations for ferroelectric switching in BTA were initially developed by Dr. Tim Cornelissen, a former member of the research group, as part of his PhD project. M.Sc. Fabian T. Thome expanded the simulations to include investigations of crackling noise during switching for his master's project. M.Sc. Toni Seiler further worked on the simulations during his master's project, fixing code-related issues and providing temperature-dependent power-law exponent simulations. B.Sc. Marcel Hecker attempted to perform experimental measurements as part of his bachelor's project. The author supervised M.Sc. Toni Seiler's and B.Sc. Marcel Hecker's projects. While the author did not work extensively on the code, significant contributions to the analysis procedures and data evaluation were made. Furthermore, the author simulated and evaluated the frequency-dependent power-law exponents and wrote the corresponding manuscript summarizing the present results. Since this was a collaborative project, contributions from different collaborators will be marked as such.

Most of the results presented in this chapter are included in Publication II. Much of the text and figures in this chapter originate from Publication II. The original text was written primarily by the author for Publication II and revised and improved by Prof. Dr. Martijn Kemerink, unless otherwise specified. Changes to the text were made to fit this dissertation's argumentation and style. Some of the figures included in Publication II were initially made by B.Sc. Marcel Hecker for his bachelor's thesis and M.Sc. Fabian T. Thome and M.Sc. Toni Seiler for their master's theses, and will be marked as such. The figures taken from Publication II may have changes to their descriptions.

6.1 Kinetic Monte Carlo model

This section follows closely the corresponding descriptions given in the master's theses of M.Sc. Fabian T. Thome and M.Sc. Toni Seiler, which the author summarized for Publication II.

6.1.1 General simulation structure

To study critical behavior and Barkhausen noise, processes must be considered on both the macroscopic scale and molecular levels. A kinetic Monte Carlo (kMC) simulation was used to achieve this, considering only electrostatic interactions. Other interactions were accounted for by prescribed morphology and dipole rotations. The Matlab-based simulation program allows one to simulate dipole orientation in static systems, such as BTA. Throughout the simulation, the dipoles cannot change their spatial position, but they can flip, thus changing their orientation depending on the applied electric field.
First, the constants for the calculations and the material morphology are defined. Then, the simulation box size is set and the material grid is calculated. The latter considers dipole positions spaced using distances defined by the morphology. Additionally, structural disorder is introduced in the form of spatial offsets. Then, the applied electric field increases over time. For each electric field step, the resulting flipping rates are calculated using classical energy calculations to determine which dipoles may flip. The energy values are updated, and the simulation continues until the electric field reaches its final value. More information is provided in the following sections.

Dr. Tim Cornelissen wrote the initial simulation program to study ferroelectric switching kinetics in BTA. This work resulted in significant contributions to several publications [105, 109, 234]. A description of the simulation program can be found in these publications and Dr. Tim Cornelissen's PhD dissertation [3]. The program was then developed further by other members of the research group. A brief summary of the most important changes can be found in Section A.9. The following subsections describe the simulation steps used in the updated program.

6.1.2 BTA morphology and grid initialization

The BTA morphology in the simulation resembles the one discussed in Section 4.1.2.2. The hydrogen bonds formed between the dipolar amide groups undergo out-of-plane rotation by $30 - 40°$, resulting in a helical pitch of six molecules, with interdiscular and intercolumnar distances of 3.5 Å and 17.2 Å for an alkyl chain with eight carbon atoms (BTA-C_8) [191, 192, 235–237]. The only parts of the BTA structure that appear explicitly are the amide groups in the form of dipole vectors. Other parts are included implicitly in lattice parameters, such as the intercolumnar distance (alkyl chain length) and the distance between the middle of a BTA molecule and the dipoles (size of the benzene core). Unlike molecular dynamics (MD) simulations, all particles remain fixed in position throughout the simulation, and the dipole vectors are the only

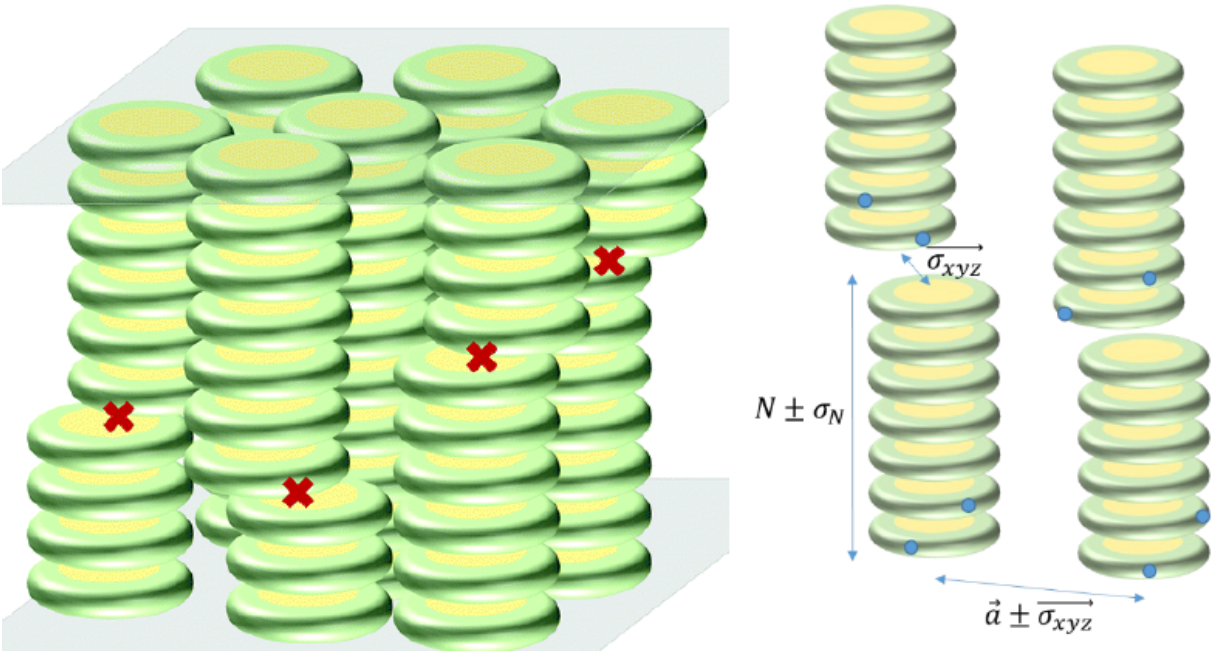

Figure 6.1.1: Columnar structure of BTA showcasing the displacements due to defects (red crosses) and different length scales. In a BTA discotic, the spacing of the benzene core and amide groups is represented in yellow and green, respectively. Defects divide the BTA columns, which span from one electrode to the other, into subcolumns of length N and variance σ_{N}. Each defect consists of a shift in space, σ_{xyz}, with respect to the original position, as defined by the crystal geometry; a rotation around the column axis; and a possible change in helicity. This figure was initially adapted from M.Sc. Toni Seiler's master's thesis and taken unmodified from the supporting information of Publication II with permission for usage granted by Physical Chemistry Chemical Physics.

mobile aspect. Similar to an Ising model, the dipoles can be in one of two states, distinguished only by the z-component of the permanent dipole moment. Since thin films are modeled, periodic boundary conditions are used in x- and y-directions; mirror boundary conditions are applied in the z-direction to account for the metal electrodes. This makes use of the fact that the effect of a conducting plane on a charge Q is equivalent to that of an oppositely charged mirror image $-Q$ on the other side of the electrode.

Disorder is introduced into the system by dividing the BTA columns, which would extend from electrode to electrode under ideal conditions, into subcolumns of various lengths. The general simulated structure is columnar, with benzene cores of the BTA molecules stacking on top of each other until a defined height, n_{z}, is reached. There are $x \cdot y$ columns that are simulated. The length of each subcolumn is drawn from a Gaussian distribution with a mean value of N and a variance of σ_{N}, and only integer values are permitted. The molecules within a column rotate

	Parameter	Value	Unit
Morphology	Helical pitch	6	Number of molecules
	Dipole out-of-plane rotation β	40	Degrees (°)
	Hexagonal packing distance α	1.7	nm
	Columnar interdisc distance c	0.35	nm
	Dipole distance from center L	0.28	nm
Disorder	Subcolumn length N	$2 - 100$	Number of molecules
	Subcolumn length variance σ_{N}	$0 - 50$	Number of molecules
	Positional shift σ_{xyz}	0.01	nm
Simulation box	Driving frequency f	$10^2 - 10^5$	Hz
	Box size in x-direction n_{x}	$4 - 11$	Number of molecules
	Box size in y-direction n_{y}	$4 - 11$	Number of molecules
	Box size in z-direction n_{z}	$40 - 700$	Number of molecules
	Interaction cut-off range r_{c}	30	Number of dipoles
	Total number of dipoles n	$n = 3n_{\mathrm{x}} \cdot n_{\mathrm{y}} \cdot n_{\mathrm{z}}$	Number of dipoles
Material	Permanent dipole moment μ_{per}	4	Debye (D)
	Polarizability α	1	e Å^2 V^{-1}
	Temperature T	$100 - 375$	Kelvin (K)
	Attempt-to-flip frequency ν_0	1	THz
	Effective permittivity ϵ_{r}	2	

Table 6.1: Simulation parameters that were typically used. The subcolumn length N is a measure of the disorder; the higher the value, the less the disorder in the system. Parameters that are given a single value were set to that value for all simulations.

fixedly by an angle of $\alpha = 60°$ with respect to each other. To simulate defects, each subcolumn is separated from the others in the same stack by a shift σ_{xyz}, a randomized rotation around the column axis, and a potential change in helicity. At the start of a simulation run, the grid forming the BTA columns is created using the specified parameters. Figure 6.1.1 illustrates the different defect parameters and the symmetry breaking. Table 6.1 shows the parameters for a typical simulation.

6.1.3 Energy calculations

At its core, the simulation considers the electrostatic interactions between the dipoles, whose positions are defined by the morphology, and calculates the resulting energies. This enables us to obtain the flipping rates that determine the evolution during the kMC simulation. The energy of a dipole i is given by

$$U_{\mathrm{i}} = -\boldsymbol{\mu}_{\mathrm{i}} \cdot \boldsymbol{E}_{\mathrm{i}}, \tag{6.1.1}$$

with the total dipole moment $\boldsymbol{\mu_i}$ and the local electric field $\boldsymbol{E}_\mathrm{i}$. The total dipole moment consists of the permanent and induced contributions, with the latter being determined by the local field $\boldsymbol{E}_\mathrm{i}$ and the polarizability α of the material:

$$\boldsymbol{\mu}_\mathrm{i} = \boldsymbol{\mu}_\mathrm{i}^\mathrm{per} + \boldsymbol{\mu}_\mathrm{i}^\mathrm{ind} = \boldsymbol{\mu}_\mathrm{i}^\mathrm{per} + \alpha \boldsymbol{E}_\mathrm{i}. \tag{6.1.2}$$

To calculate the energy of a dipole i, the local field at its position must first be calculated. Throughout the simulation box, an externally applied electric field $\boldsymbol{E}_\mathrm{app}$ is assumed to be constant, and its x- and y-components are chosen to be zero. Then, the contribution to the electric field induced by a different dipole j is given by

$$\boldsymbol{E}_\mathrm{ij} = \frac{\boldsymbol{\mu}_\mathrm{j} - 3\hat{r}_\mathrm{ij}\left(\boldsymbol{\mu}_\mathrm{j}\hat{r}_\mathrm{ij}\right)}{4\pi\epsilon_0\epsilon_\mathrm{r} r_\mathrm{ij}^3}. \tag{6.1.3}$$

Here, $\epsilon_0\epsilon_\mathrm{r}$ is the material permittivity, and $\hat{r}_\mathrm{ij} = r_\mathrm{ij}\boldsymbol{r}_\mathrm{ij}$ is the real-space vector (distance) separating the dipoles i and j. Due to numerical limitations, the dipole-dipole interactions calculated this way must be confined to a certain number of nearest neighbors. For this purpose, a sphere with a cut off radius of $r_\mathrm{c} = 30$ is defined, inside of which all interactions are considered explicitly. Due to the long-range nature of Coulomb interactions, the contribution of the remaining dipoles is not negligible and is approximated using the reaction field method [238]. Within this framework, it is assumed that all dipoles inside the sphere induce a polarization charge density, denoted by $\boldsymbol{P}_\mathrm{RF} = \sum_{r<r_\mathrm{c}} \boldsymbol{\mu}_\mathrm{i}$, on the sphere surface. This polarization charge density is given by the sum of all dipole moments inside the sphere. This leads to the following reaction-field at the center position:

$$\boldsymbol{E}_\mathrm{RF} = \frac{2\left(\epsilon_\mathrm{r} - 1\right)\boldsymbol{P}_\mathrm{RF}}{2\epsilon_\mathrm{r} + r_\mathrm{c}^3}. \tag{6.1.4}$$

Therefore, the complete local electric field can be written as

$$\boldsymbol{E}_\mathrm{i} = \boldsymbol{E}_\mathrm{app} + \boldsymbol{E}_\mathrm{RF} + \sum_{j, r_\mathrm{ij}<r_\mathrm{c}} \boldsymbol{E}_\mathrm{ij}. \tag{6.1.5}$$

Coupling Equations 6.1.1 and 6.1.5 provides the energy of dipole i. However, a self-consistency problem arises due to the feedback arising from the induced dipoles. The induced dipoles depend on the local field, which, according to Equations 6.1.3 and 6.1.4, depends on the induced dipoles. Thus, the problem cannot be solved exactly, so an iterative approach is chosen. Initially, the permanent dipole moment of the amide groups is taken as the total dipole moment. Although the values yielded for the electric fields are incorrect, they are used to calculate a better approximation of the actual dipole moment. Repeating these steps several times yields converging values of $\boldsymbol{E}_\mathrm{i}$ and $\boldsymbol{\mu}_\mathrm{i}$, which are considered the actual values. Thus, the energies for all dipoles in any given dipole configuration can be obtained.

In particular, the energy difference ΔU_i between a state with the dipole up and a state with the dipole down is an important factor in the flipping rate and is referred to as the flipping energy.

The value of ΔU_i depends on the surrounding environment, which changes significantly during the evolution of a simulation. Rather than solving for the induced dipoles at each kMC step, an approximation of the flipping energy change is obtained in advance. In addition to calculating the flipping energy for a given environment, the flipping energy for a neighboring dipole that has been flipped is also obtained. The difference of these two values yields $d_\mathrm{j}\Delta U_\mathrm{i}$, which measures the effect of a neighboring dipole's reversal on the flipping energy and rate of dipole i. By performing this calculation for all dipoles j in the interaction sphere of dipole i, the energy difference ΔU_i can be kept at an approximately correct value throughout the evolution of one simulation without recalculating the induced dipoles. Expanding this calculation to all dipoles in the simulation box saves a significant amount of computational time.

6.1.4 Flipping rates

The flipping energies are based solely on electrostatic interactions, which depend on the morphology and can be calculated as

$$\nu_\mathrm{i} = \begin{cases} \nu_0 \exp\left(\frac{-\Delta U_\mathrm{i}}{k_\mathrm{B}T}\right), & \text{if } \Delta U_\mathrm{i} > 0 \\ \nu_0, & \text{otherwise.} \end{cases} \tag{6.1.6}$$

Here, ν_0 is the attempt-to-flip frequency, which is taken as a typical vibrational frequency of the material, and $k_\mathrm{B}T$ is the thermal energy in the system. During the kMC simulation, the flipping rates serve as weight factors in determining which dipole flips. The probability that dipole i will be selected for a flip is given by $\nu_\mathrm{i}/\nu_\mathrm{tot}$, with the sum of all flipping rates $\nu_\mathrm{tot} = \sum_i \nu_\mathrm{i}$. At each simulation step, a random number between zero and one is drawn to determine which dipole will flip. A second random number, $r_2 \in [0, 1]$, is used to calculate the time increment associated with the current step:

$$\Delta t_\mathrm{i} = \frac{\log(r_2)}{\nu_\mathrm{tot}}. \tag{6.1.7}$$

This ensures that, in parts of the simulation where many dipoles are volatile and thus ν_tot is large, each flip is, on average, much faster than in a situation where the vast majority of dipoles are stable. After each kMC step, all flipping energies are updated based on the energy calculations performed prior to the simulation. Saving the state of all dipoles at each time step and converting it to physical polarization closely resembles a real experiment. Since the external field is a free parameter, hysteresis loops and switching transients can be recorded in addition to simple (de)polarization studies.

6.2 Simulation and analysis procedure

In all numerical experiments, the BTA system was driven by a slowly varying external field while the polarization was measured. Initially, all dipoles pointed downwards, providing a fully saturated starting condition. The parameter representing the electric field was ramped from -0.8

to +0.8 V nm^{-1} and back again. The entire process took 1 ms, and a total of 120 different field values were used, with each field value representing a sub-simulation and a possibly recalculated induced dipole problem. Table 6.1 in Section 6.1.2 shows typical simulation settings.

Figure 6.2.1a shows a typical result of a simulated switching process over time: the driving field E (blue), the permanent polarization P_P (orange), and the obtained current of a complete loop I (green) - i.e., the concatenation of all sub-simulations - as a function of time t. The current represents the number of flipped dipoles per time bin, which builds up over longer time frames as jerks. Large jumps in permanent polarization and current spikes are observed when the applied electric field is large enough, i.e., when it approaches the coercive field of the simulated system. Some of the spikes are numerical artifacts, as evidenced by their regular occurrence, and are due to the abrupt changes in the applied field and the corresponding recalculation of the linear polarization and flipping rates.
Filtering out those data points yields the total polarization curves shown in Figure 6.2.1b, where most of the current peaks remain, indicating the presence of crackling noise. To identify the individual events, a threshold level was set, as indicated by the horizontal black lines in Figure 6.2.1b. This is necessary because dipole flips are often initiated by thermal fluctuations but reverse shortly afterwards because the local field still points in the opposite direction. Many relatively small events arise this way, but they do not contribute to the switching process and must be filtered out. An event begins when the absolute value of the polarization current first exceeds the threshold level and ends when it falls below the level again. An alternative method is to define events by counting the number of flipped dipoles per time step, which is preferred because it offers an immediate measure of avalanche sizes, whereas the polarization current depends on the sample geometry. However, since these two quantities are linearly proportional, the current is the obvious choice as a proxy for avalanche size in a real experiment.
Setting the threshold level involves a trade-off between missing small crackling events and including events generated by thermal noise. Figure 6.2.1c shows the number of detected events as a function of the threshold level, normalized to the largest measured spike x_{max} of one loop, for both methods. The identical behavior of the curves demonstrates the equivalence of the two approaches. In this case, the threshold value was manually set on the plateau to the right of the thermal noise peak, as this position optimally excludes thermal fluctuations while including irreversible dipole avalanches, which is further confirmed by inspecting Figure 6.2.1b. The threshold value fluctuated at around 15 dipoles per time step. In addition to collecting data from the entire loop, events arising exclusively from switching activity near zero polarization can be analyzed separately. This corresponds to investigating the system at the coercive field only. This approach allows differentiation between field-specific and field-integrated event distributions.
After setting the threshold level, the events were analyzed based on their characteristic properties. The duration of an event was determined by the time difference between the intersection points

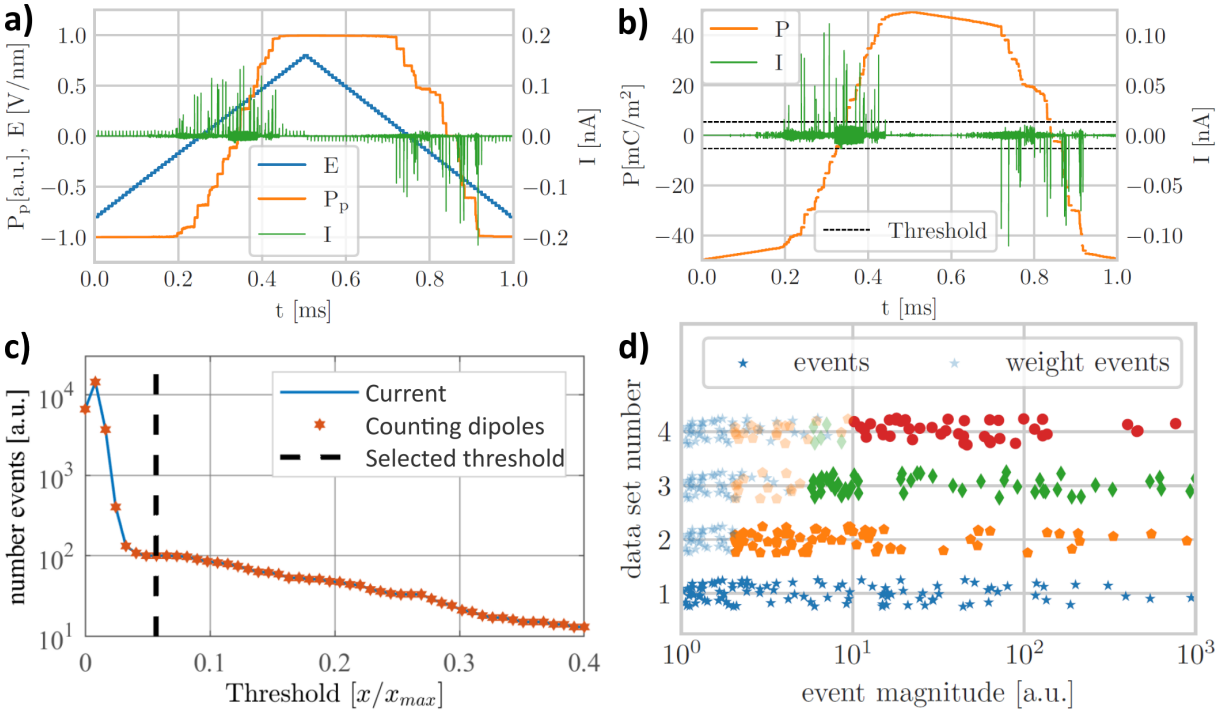

Figure 6.2.1: The typical results of a numerical experiment **a)** before and **b)** after the artifacts arising from the abruptly changing field are filtered. The current shows significant spikes that constitute dipole avalanches. A threshold level represented by black horizontal dotted lines in (b) is applied to identify single events. The threshold level is chosen to be just above the thermal background noise. **c)** Reducing the threshold level increases the number of events detected for a single simulated loop. The optimal threshold level indicated by black vertical line in (c) is set just beyond the kink, as there is an inflated number of small (thermal) events due to thermal fluctuations. **d)** Upon merging multiple individual simulations (denoted by different symbols) with different threshold values, a correction is needed in the regime of small events. This correction was implemented by creating weighted events based on those data sets that extend to this regime. The simulation parameters were $f = 1$ kHz, $n_x = n_y = 4$, $n_z = 300$, $N = 10$, $\sigma_N = 1$, $T = 300$ K. This figure was initially adapted from M.Sc. Fabian T. Thome's master's thesis and taken unmodified from Publication II with permission for usage granted by Physical Chemistry Chemical Physics.

of the threshold and the switched dipoles (or current). In the simulations, events were typically completed within a few bins, rendering a statistical analysis of their width in terms of probability density functions (PDFs) nonsensical. This is attributed to a combination of finite-size effects and the kMC method's tendency toward intrinsic switching [109]. The remaining investigated characteristics generally showed sufficiently broad distributions.

As previously established, distributions of crackling quantities commonly follow power laws. More

precisely, a power-law distribution means that the probability of finding an event with a value of X in the interval $[x, x + \mathrm{d}x]$ is given by

$$p(x)\,\mathrm{d}x = P(x \leq X < x + \mathrm{d}x) = Cx^{-\alpha}\mathrm{d}x \tag{6.2.1}$$

with the normalization constant C. In practice, the power law holds only above a finite minimum cutoff value $x_{\min}$, as otherwise the normalization condition

$$\int_{x_{\min}}^{x_{\max}} p(x)\,\mathrm{d}x = 1 \tag{6.2.2}$$

could not be met. In real systems, a finite upper cutoff $x_{\max}$ is also expected, as events that are truly infinite cannot occur. The range in which the power law would be fitted was determined by visualizing the event data. Bins that increase logarithmically in width along the event axis were used to reduce the effect of significant fluctuations in the tail of the distribution. The computed probability was then divided by the bin width. The complete probability density function was normalized according to Equation 6.2.2. To obtain stable fitting results, the probability density $p(x)$ and the bin positions were log-transformed, and a linear least squares fit was performed. After reversing the transformation, the power-law fit was extracted. This method was compared to the so-called maximum likelihood estimation, which is widely used in crackling noise studies of ferroelectrics [96, 121, 124, 239]. Details on these fitting methods can be found in Section A.10. Since the number of events typically collected from a single loop was generally insufficient for a meaningful statistical analysis, data from multiple single numerical experiments with equal settings was combined. This resulted in the implementation of a correction involving the creation of weighted events. The weighted events replicated the simulation results that reached the lowest limit. This was done to circumvent the issue of merging data sets with potentially different threshold levels, as the combined data featured an artificially reduced probability density for the (summed) size and energy for small events. Figure 6.2.1d illustrates this approach for four synthetic data sets with different threshold levels. A similar correction for inter-event times was unnecessary since they are not correlated with event size or energy.

Figure 6.2.2 shows the results of an exemplary set of simulations and the corresponding probability densities. In these simulations, the size S is defined as the greatest number of flipped dipoles per time step during one avalanche, while the summed size S_Σ is obtained by adding up all dipoles that flipped per time step during one event. The latter was not analyzed further as it is subject to artifacts arising from a large fraction of singular events. The energy of an avalanche U is defined by its proportionality to the integral of the electrical power, and the inter-event time δt is the time-span between events. The PDFs for the sizes and energies exhibit a similar structure, featuring an initial region of small events not captured by the power law, followed by a substantial portion of the distribution displaying power-law behavior. The distribution shows a steep decline for the largest events due to limitations arising from the system size. The size S and summed size

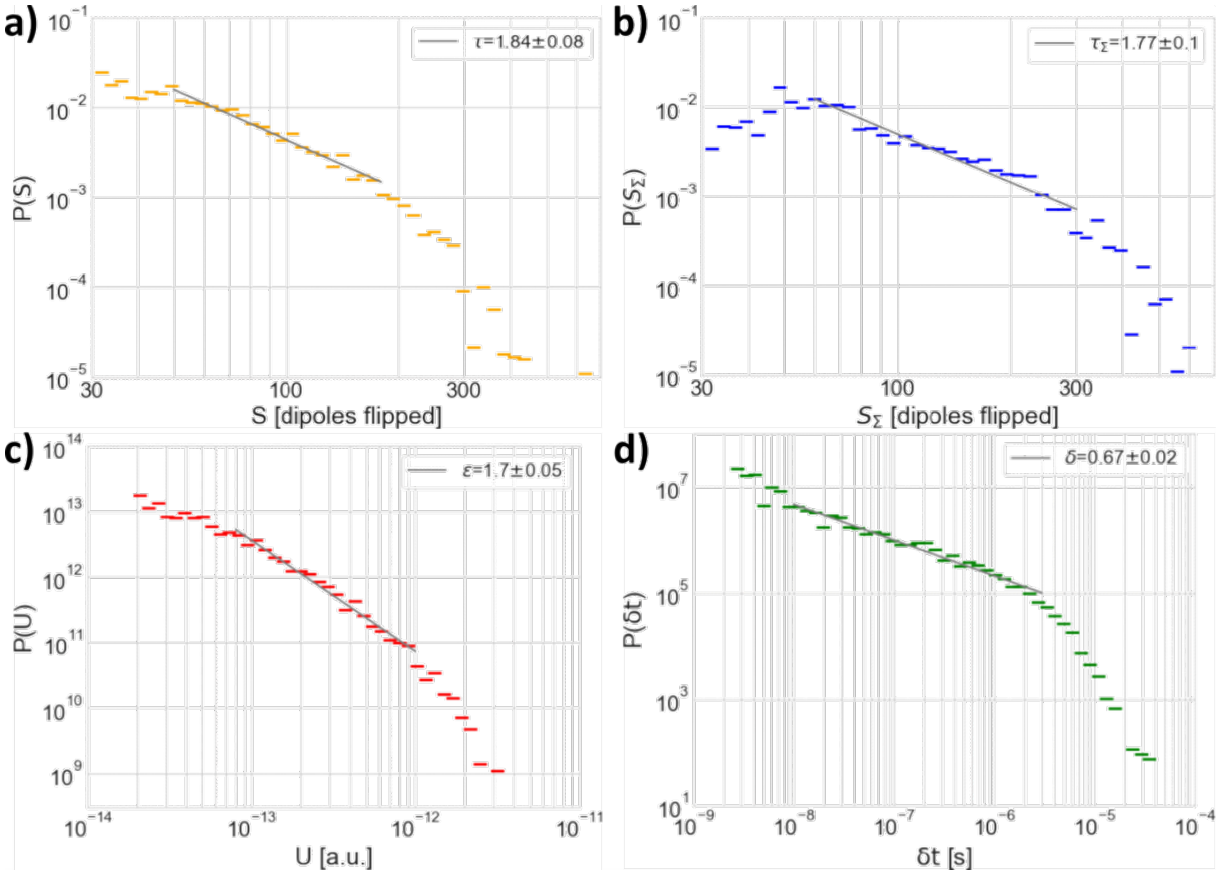

Figure 6.2.2: The probability densities for **a)** size S, **b)** summed size S_Σ, **c)** event energy U, and **d)** inter-event time δt. All distributions exhibit a similar structure, with a region showing a power-law behavior (fitted data), followed by a sudden decline due to system size limitations or, in the case of inter-event time, simulation duration limitations. The simulation parameters were $f = 1$ kHz, $n_\mathrm{x} = n_\mathrm{y} = 4$, $n_\mathrm{z} = 300$, $N = 10$, $\sigma_\mathrm{N} = 1$, $T = 300$ K, number of events = 1911. This figure was initially adapted from M.Sc. Toni Seiler's master's thesis and taken unmodified from Publication II with permission for usage granted by Physical Chemistry Chemical Physics.

S_Σ distributions show a clear shift towards larger events as a result of summing over all points within an event. The energy distribution shows the same trend as the event size distribution, and the proportionality $U \propto I^2 \propto S^2$ is clearly visible in the spread of the values. Inter-event times are directly tied to the time given by the sweeping frequency of the applied electric field. In these simulations, the time was $t = 10^{-3}$ s, and all the events occurred within the time frame of $\delta t \approx 2 \cdot 10^{-4}$ s.

6.3 Simulation results

M.Sc. Fabian T. Thome and M.Sc. Seiler Toni investigated the influence of system size and disorder parameters on the simulation. The findings are described in detail in their respective master's theses. A summary of the conclusions is presented in Publication II. The following contains a brief summary of these results. In this dissertation, the focus is on the influence of the temperature and sweeping frequency on the BTA system behavior.

6.3.1 System size influence

A general concern with the numerical simulation of potentially critical behavior in finite systems is that a relatively higher number of larger events could occur in larger simulation boxes. To ensure that finite-size effects did not affect the results, additional simulations were carried out in which the system size n_z was gradually increased for several sizes ranging from 40 to 700 molecules in the z-direction. It was observed that larger event sizes occurred more frequently as the column length increased until $n_\mathrm{z} \approx 300$. For even larger systems, hardly any effect was found; therefore, the main simulations were carried out with a system size of n_z=300. This corresponds to a film thickness of $\approx$ 105 nm, which is less than the film thicknesses typically investigated experimentally. In summary, the size of the largest avalanche is not limited by the height of the system provided that the system's thickness exceeds $\approx$ 100 nm.
Furthermore, to investigate the effect of column height on event size, the mean of the event size was analyzed for different system sizes. A strong initial increase, which diminished with an increase in system size, was observed. This effect was also examined for systems with a greater number of shorter columns in the x- and y-directions. While the resulting distribution showed smaller events, the effect was rather small. Adding more columns while keeping their length constant barely produced any changes. Unlike when the box height is varied, no limitations due to the geometry were apparent. Thus, one-dimensional avalanche propagation along the column axis was recognized as the dominant mode of switching. This behavior was attributed to the morphology, particularly the significant difference between the hexagonal packing distance and the interdisc distance. The dipoles are more densely packed in the z-direction, so an initial thermal perturbation is more likely to propagate in that direction, leading to needle-like dipole avalanches. In summary, dipole avalanches propagate almost exclusively along the column axis.

6.3.2 Temperature and sweeping frequency influence

Since jerky behavior was observed in the polarization switching of BTA and the power-law distributions of event characteristics were established, the focus was set on specific values of these exponents and how they depends on temperature T, sweeping frequency f, and material characteristics. Since switching in organic ferroelectrics is a thermally activated process, temperature is one of the parameters under investigation. As $k_\mathrm{B}T$ increases, switching becomes more

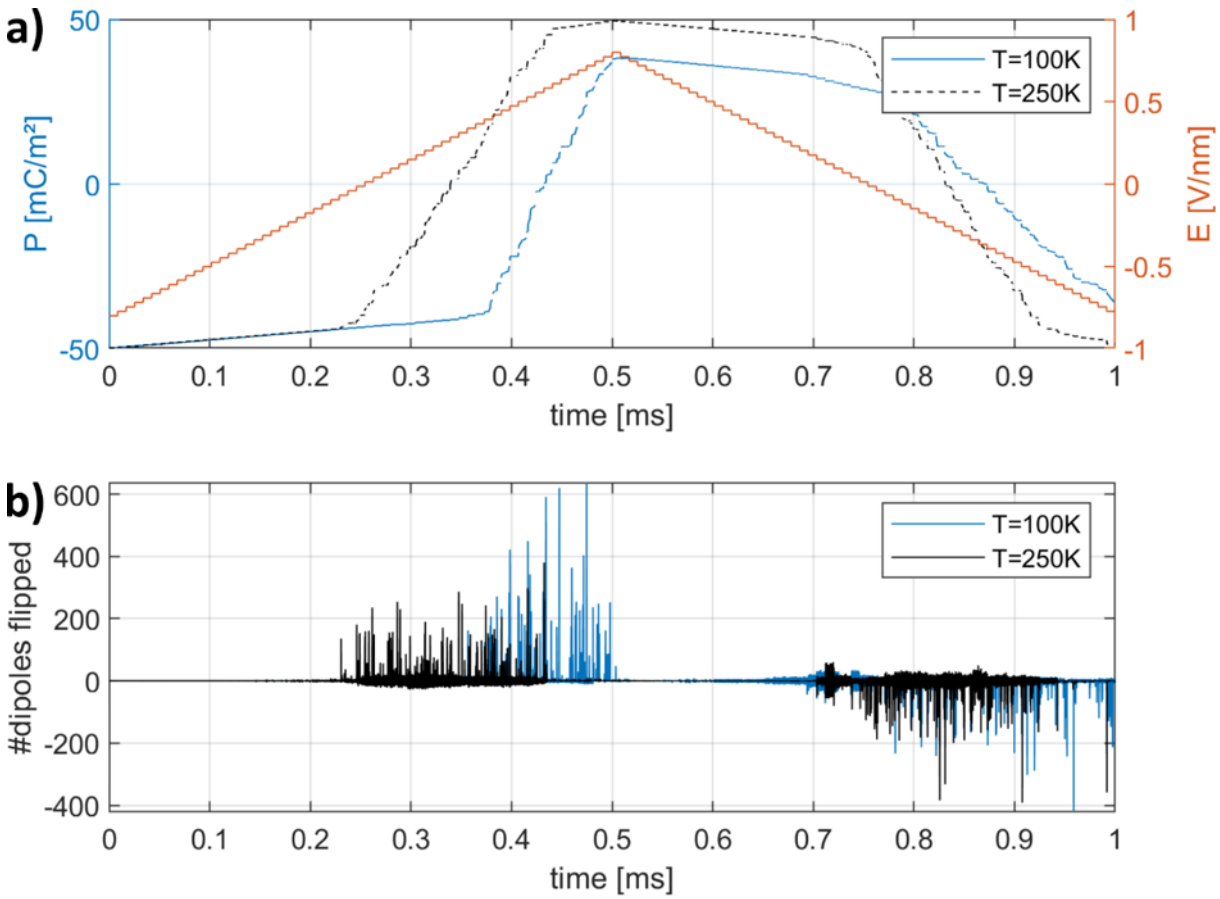

Figure 6.3.1: A comparison of two simulations with different temperatures of 100 and 250 K. **a)** As thermal excitations become less likely, the switching process begins at higher fields, and the system does not fully switch at the lowest temperature. **b)** The event sizes for lower temperatures are generally larger than those for high temperatures. The simulation parameters were $f = 1$ kHz, $n_{\mathrm{x}} = n_{\mathrm{y}} = 4$, $n_{\mathrm{z}} = 300$, $N = 10$, $\sigma_{\mathrm{N}} = 1$. This figure was initially adapted from M.Sc. Toni Seiler's master's thesis and taken unmodified from the supporting information of Publication II with permission for usage granted by Physical Chemistry Chemical Physics.

volatile, and small events in which the system jumps between neighboring meta-stable states occur more frequently. The role of larger avalanches diminishes, and the polarization reversal tends to spread slowly and steadily, a phenomenon known as the creep regime. This regime has been experimentally confirmed to lead to higher power-law exponents [240]. Overall, the values of the critical power-law exponents depend on temperature, which is attributed to the onset of the thermal creep regime. In all observed cases, the critical nature of the switching remained unchanged, as system-spanning avalanches still appeared alongside smaller ones.

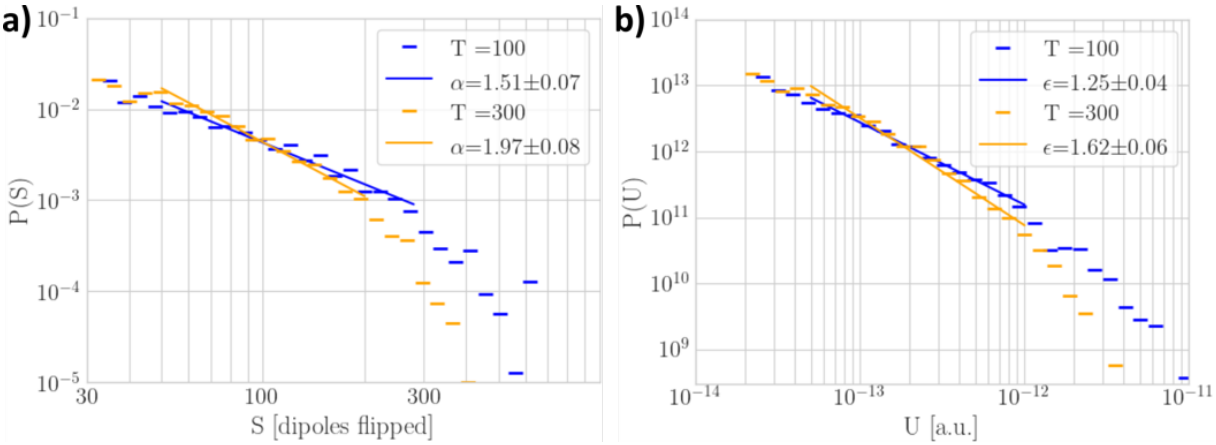

Figure 6.3.2: The probability distribution for **a)** event size and **b)** energy for the same system settings at a lower ($T = 100$ K) and a higher ($T = 300$ K) temperature. The simulation parameters were $f = 1$ kHz, $n_x = n_y = 4$, $n_z = 300$, $N = 10$, $\sigma_N = 1$. This figure was initially adapted from M.Sc. Toni Seiler's master's thesis and taken unmodified from Publication II with permission for usage granted by Physical Chemistry Chemical Physics.

The temperature was swept between 100 and 300 K. As expected for ferroelectric materials, lower temperatures required higher fields to initiate the switching process. Depending on the chosen applied electric field, not the entire simulation box switched at the lowest temperatures. Figure 6.3.1 shows a comparison of typical simulations for 100 and 250 K. Figure 6.3.2 displays a comparison of the corresponding distributions, showing a shift to larger event sizes at lower temperatures in both the size and energy distributions. This shift is expected, as fewer thermal excitations lead to a higher electric field required for switching, making it more probable that one event will cause a larger avalanche. Consequently, the exponents recovered from the power law are significantly smaller for the 100 K simulation.
The results of the systematic temperature sweep are displayed in Figure 6.3.3a, where the power-law exponents for temperatures ranging from 100 to 300 K are shown. For the (experimentally realistic) parameters used, temperatures below 100 K would result in minimal switching throughout the process. Above 300 K, the thermal noise in the system causes significant variation in the datasets, which is evident in the highest temperatures shown. The size and energy distributions exhibit similar trends across the entire temperature range. There is an initial plateau until $T = 160$ K and a clear increase with temperature above that. At low temperatures, the extracted exponents are consistent with mean-field predictions of system-spanning avalanches, indicated by the horizontal lines in Figure 6.3.3a. Higher power-law exponents indicate that switching focuses on smaller events. The agreement of the numerical values with the theoretically predicted values, combined with their relative constancy at lower temperatures, suggests that the field-driven switching process in BTA exhibits self-organized criticality at temperatures below ≈ 170 K.

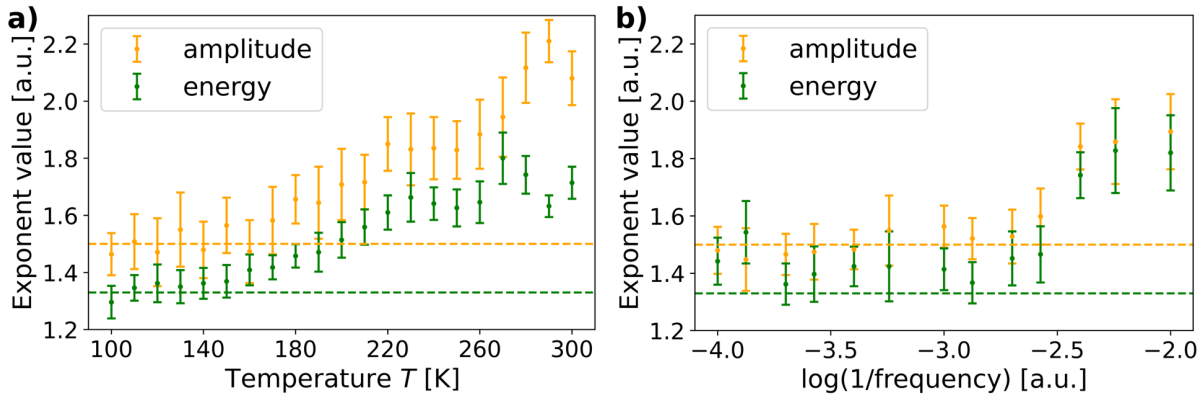

Figure 6.3.3: The size/amplitude (orange) and energy (green) power-law exponents extracted from simulations of larger systems for **a)** various temperatures at $f = 1$ kHz and **b)** various sweeping frequencies at $T = 160$ K. The horizontal lines indicate the exponent values calculated from the MFP model (≈ 1.5 for size and ≈ 1.33 for energy, respectively). The simulation parameters were $n_x = n_y = 4$, $n_z = 300$, $N = 10$, $\sigma_N = 1$. This figure was taken unmodified from Publication II with permission for usage granted by Physical Chemistry Chemical Physics.

As the temperature increases, the exponents also increase. This implies that the system favors smaller, localized events, which leads to a deviation from the mean-field prediction. It also indicates that the system is entering a creep regime. As the thermal energy in the system increases, field-induced events are more likely to be replaced by smaller, partially thermally induced events. In contrast, at lower temperatures, switching occurs at higher electric fields. This increases the probability that flipping one subcolumn will cause further events in one avalanche. Thus, larger events are more probable, ultimately leading to self-organized criticality. Furthermore, the effect of the sweeping frequency f on the power-law exponents was investigated, as shown in Figure 6.3.3b. Since the self-organized criticality in BTA below $T = 170$ K was established, the sweeping frequency was investigated in the range from 10^2 to 10^4 Hz at a temperature of $T = 160$ K. For these simulations, the bin size was fixed at 1 ns. The size and energy exponents are consistent with the mean-field prediction at higher sweeping frequencies and increase as the sweeping frequencies decreases at lower frequencies. The size and energy power-law exponent trends for T and $\log(1/f)$ are similar.

One possible explanation for the similar trends is related to the thermally activated nature of switching processes in organic ferroelectrics. The TA-NLS model (see Section 2.2.4.4) assumes that switching is limited by the activation of pre-existing nucleation sites within small regions of the material [99, 100]. The TA-NLS model yields an expression for the coercive field (see Equation 2.2.14 in Section 2.2.4.4), which states $E_c \propto T \log(1/f)$. A high sweeping frequency in a hysteresis loop measurement results in a large coercive field because the system does not have enough time to equilibrate and relax to its lowest energy state. The coercive field decreases

linearly with temperature, and the logarithm of the inverse frequency has the same effect. Figure 6.3.3 shows a strong similarity between the trends of the power-law exponents as a function of temperature and the logarithm of the inverse frequency. Therefore, the power-law exponents are anti-correlated with the system's coercivity.

6.3.3 Disorder parameter variation

If the chiral columnar BTA system indeed exhibits self-organized criticality upon field-driven polarization reversal at lower temperatures, then the observed exponents should be invariant to modest changes in system parameters. To verify this, further simulations were performed in the low-temperature range, where the critical exponents consistently remained around the predicted mean-field values. The investigated disorder parameters included the variance of the distribution from which the subcolumn sizes were generated, and the chirality of the defects.
Investigating different defect types revealed that a single defect type can lead to either stabilization or destabilization of the system, depending on the defect's geometrical details and the corresponding exponent deviations. Generally, a 'sufficient' variation in defects is needed to obtain universal exponents. Specifically, the introduced disorder must be large enough to prevent entirely intrinsic switching, whereas too much disorder leads to small events dominating the switching process. This behavior is consistent with the Random-Field-Ising model mentioned previously [241]. For the present system, this implies that heterogeneity in both defect type and subcolumn length are necessary conditions to recover the universal exponents.

6.4 Experimental results

To confirm the simulated results, experimental measurements were conducted on both out-of-plane and in-plane BTA samples. The biggest challenge was reducing the noise level of the measurement setup while maintaining sufficient time resolution, as the expected currents associated with single jerks are very small. Despite carrying out noise reduction, measuring Barkhausen noise in the investigated BTA samples was unsuccessful. Figures A.9.1 and A.9.2 in Section A.9 show exemplary response currents and the corresponding probability density distributions with extracted power-law exponents. Given that Barkhausen noise in P(VDF-TrFE) was measured successfully (see Chapter 7), it is suspected that the switching events are too small in BTAs. To verify this, the number of dipoles that flipped within of BTA samples was estimated and compared to both the simulations and the noise level of the setup. The corresponding calculation can be found in Section A.11. According to the findings, the number of regions that would need to be switched simultaneously to achieve a measurable current is far larger than what is plausible based on the weak inter-columnar coupling. In other words, the negative result of the experiments (i.e., Barkhausen noise being below the resolution threshold of the setup used) is consistent with the predictions of the numerical model.

6.5 Conclusion

Barkhausen noise was simulated in BTA using kMC method to study the material's self-organized critical behavior at different temperatures, driving frequencies, and degrees of disorder. The simulation program and the kMC simulation process were described. First, the BTA morphology is initialized. Then, the energy between dipole sites is calculated. Finally, the system is driven by an electric field, which flips the dipoles based on their flipping rates. After each step, the energies and flipping rates are updated. The system was analyzed by isolating the dipoles that flipped due to the electric field change and investigating the probability densities as a function of the number of flipped dipoles. Disorder in the system was varied by changing both the subcolumn size and variation, defect density, and defect type.

Although system size generally matters for simulations, it was determined that selecting a large enough system ($\gtrsim 100$ nm) eliminates finite-size effects. Furthermore, it was found that the ferroelectric switching in the BTA system mostly occurs as a one-dimensional avalanche along the column axis, a phenomenon attributed to the BTA morphology. The influence of both temperature ($100 - 300$ K) and sweeping frequency $\left(10^2 - 10^4 \text{ Hz at } T = 160 \text{ K}\right)$ on the behavior of the BTA system was investigated. Lower temperatures required higher electric fields for ferroelectric switching and typically exhibited larger switching dipole avalanches. The extracted power-law exponents exhibited a plateau at the lower temperatures between 100 and 170 K situated at a value of ≈ 1.5, which is the theoretically predicted value for critically self-organized behavior. For higher temperatures, the power-law exponents increased with temperature because the system favored small events. This is attributed to thermal fluctuations becoming dominant, thus introducing a creep regime. Additionally, the qualitative behavior of the power-law exponents was found to be similar for the logarithm of the inverse of the sweeping frequency and the temperature. The TA-NLS model explains this behavior as expected for a thermally activated switching process in organic ferroelectric materials. Furthermore, the disorder parameters were varied to confirm the self-organized criticality in BTA. Depending on the defect type, variation of the amount of disorder present can lead to either stabilization or destabilization of the system. Universal power-law exponents were observed with a 'sufficient' amount of defect variation, while too little or too much disorder led to intrinsic-like switching or small events dominating the switching process, respectively.

Experimental measurements of the Barkhausen noise in BTA were also performed. However, the switching events in BTA were too small to be resolved with the given setup, even after noise reduction. To experimentally measure Barkhausen noise in such columnar liquid crystalline molecules, stronger intermolecular and, especially, intercolumnar coupling is likely required to increase domain and avalanche sizes. This may be difficult to achieve in liquid crystalline materials. For BTAs, this could be achieved by reducing the system's temperature, introducing shorter alkyl tails, and possibly adding chiral groups, which generally induce more order [79]. However, such materials or conditions would also cause significantly larger coercive fields, potentially rendering them unswitchable.

Chapter 7

Experimentally measured Barkhausen noise in organic ferroelectric copolymer P(VDF:TrFE)

Barkhausen noise provides additional insight into the switching process of ferroelectric materials by allowing the progression of switching events to be studied. However, most research has focused on inorganic ferroelectric materials and perovskites. Although Barkhausen noise was successfully established in BTA systems through kMC simulations, corresponding measurements were unsuccessful (see Chapter 6). To the best of the author's knowledge, the only experimental investigation of Barkhausen noise in disordered organic ferroelectric materials has been performed by Mai and Kliem on P(VDF:TrFE) thin films [242]. In their work, however, the current peaks measured were generated without an applied electric field due to thermally induced reordering of dipoles when crossing the Curie temperature. While this study confirmed Barkhausen noise in the copolymer P(VDF:TrFE), it neither investigated the system through ferroelectric switching nor the power-law behavior. Therefore, this chapter presents the first experimental investigation of Barkhausen noise via ferroelectric switching through field annealing in the organic ferroelectric copolymer P(VDF:TrFE). The values and rise times of the applied electric fields were systematically varied, and the resulting behavior of the system was investigated.

The theory of Barkhausen noise is described in Section 2.2.7. Section 3.3.3 presents the measurement setup used to characterize the samples (see Section 3.1.2.1). A description of P(VDF:TrFE) is given in Section 4.1.3.

The first experiments measuring Barkhausen noise in P(VDF:TrFE) were conducted by M.Sc. Toni Seiler during his master's project. He prepared the samples and proposed a measurement setup. B.Sc. Marcel Hecker improved on the setup and systematically measured the crackling noise behavior of the samples prepared by M.Sc. Toni Seiler as part of his bachelor's project. The author supervised the project, contributing to the data analysis and evaluation while familiarizing himself with the measurement process. Since this project was a collaboration, parts from different contributors will be marked as such.

Most of the results presented in this chapter are included in Publication III. Much of the text and figures in this chapter originate from Publication III. The original text was written primarily by the author for Publication III and revised and improved by Prof. Dr. Martijn Kemerink, unless otherwise specified. Changes to the text were made to fit this dissertation's argumentation and style. Some of the figures included in Publication III were initially made by M.Sc. Toni Seiler and B.Sc. Marcel Hecker for their master's and bachelor's theses, respectively, and will be marked as such. The figures taken from Publication III may have changes to their descriptions.

7.1 Data acquisition and analysis procedure

This section describes the procedure for measuring and evaluating Barkhausen noise. It closely follows the description provided in the bachelor's thesis of B.Sc. Marcel Hecker.

Prior to the noise measurements, the ferroelectric switching of the P(VDF:TrFE) samples was verified. Figures 7.1.1a and b show a typical DW measurement (see Section 3.3.1.2) and the corresponding P-E-hysteresis loop, respectively. The values obtained for the coercive field and the remnant polarization were $E_\mathrm{c} \approx 40 - 50$ V $\mu\mathrm{m}^{-1}$ ($U_\mathrm{c} \approx 20 - 25$ V) and $P_\mathrm{r} \approx 60 - 65$ mC m^{-2}, respectively, depending on frequency, temperature, and applied voltage. These values are in good agreement with those reported in other studies [2, 243].

Each noise measurement, or a single combination of applied voltage and rise time, was repeated multiple times for each sample, and the data were captured in bundles of 100 current waveforms. Since not all measurements exhibited Barkhausen noise, the data were cleaned up before analysis. For each measurement, the slew rate $S(t) = \left(\frac{\mathrm{d}I}{\mathrm{d}t}\right)^2$ was calculated and compared to a threshold based on the maximum applied voltage. Waveforms that did not meet the threshold were rejected. Otherwise, the waveforms were displayed and manually approved to further eliminate spurious signals that appeared semi-randomly but seemed to become more frequent after prolonged measurements, especially at higher fields. Although this will not be pursued further here, the disappearance of Barkhausen noise is tentatively attributed to a gradual decrease in structural disorder due to an effective 'field annealing'. Interestingly and importantly, the appearance or disappearance of the Barkhausen noise signals was not correlated with the overall switching behavior, which continued to correspond with the full polarization reversal around a constant coercive field. An automated (AI) approach was explored but was declined due to a high false-positive rate, as explained in B.Sc. Marcel Hecker's bachelor's thesis.
The sorted datasets were analyzed in multiple steps. An exemplary analysis process is shown in Figure 7.1.2. Figure 7.1.2a shows the current density response to a typical applied square waveform measured in the P(VDF:TrFE) samples. To exclude breakdown phenomena and charge trapping and release as the sources of visible current peaks, the corresponding P-E-hysteresis loop is plotted and discussed in Figure A.12.1 in Section A.12. The corresponding slew rate was calculated, and datasets with $S < 10^{-5}$ A^2 s^{-2} were excluded. This threshold was based on typical measured results, excluding most of the background noise, as shown in Figure 7.1.2b. Next, the baseline was calculated by identifying the local minima of the slew rate and interpolating these data points using a piecewise cubic Hermite interpolating polynomial (PCHIP). The interpolated baseline was then subtracted from the calculated slew rate to account for the underlying slew rate caused by the slope of the switching peak, as shown in Figure 7.1.2c. Using the corrected slew rate, the probability density function (PDF) was calculated. Finally, power laws were fitted on to the PDFs in a double-logarithmic representation of the data to obtain the power-law exponents

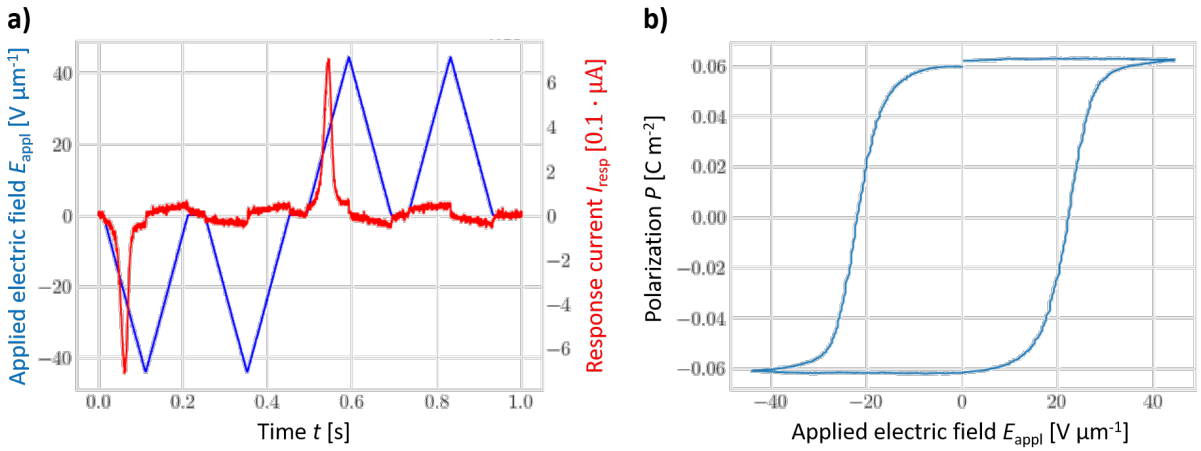

Figure 7.1.1: a) The typical switching current I_{resp} representative of P(VDF:TrFE) samples in correlation with the applied electric field E_{appl} as a function of time t. **b)** The corresponding P-E-hysteresis loop obtained from the background-corrected and integrated switching peaks. This figure was initially adapted from M.Sc. Toni Seiler's master's thesis and taken unmodified from the supporting information of Publication III with permission for usage granted by Physical Chemistry Chemical Physics.

via the slope of the fit, as shown in Figure 7.1.2d. To improve the statistics, two methods were used for the power-law fitting: The maximum likelihood (ML) method and the least squares (LS) method. Details on these fitting methods can be found in Section A.10.

7.2 Experimental results

Based on the previous results measured by M.Sc. Toni Seiler, which are presented in his master's thesis, the effect of both the rise time and the applied voltage on the power-law exponents was expected. Thus, the measurements were taken for three different rise times, while maintaining a constant frequency of the total double-wave waveform pulse. Similarly, the applied voltage was varied from below to well beyond the coercive field. Figure 7.2.1a shows a typical DW measurement, with Figures 7.2.1b and c showing a zoom-in on the current density for two different rising times and applied voltages, respectively.
Three different rise times were systematically investigated: 100, 400 and 800 μs. For each rise time, the applied voltage, and thus the electric field, was gradually increased, typically from 10 to 33 V. The histograms of all the individual measurements, including the power-law exponent fits, are shown in Figures A.12.2, A.12.3, and A.12.4 in Section A.12 for 100, 400, and 800 μs, respectively. A measurement of a dielectric reference capacitor is provided in Figure A.12.5 in Section A.12 for comparison. Some measurements deviate from the expected behavior of a plateau or slow decrease in the probability for lower slew rates followed by a roll-off containing

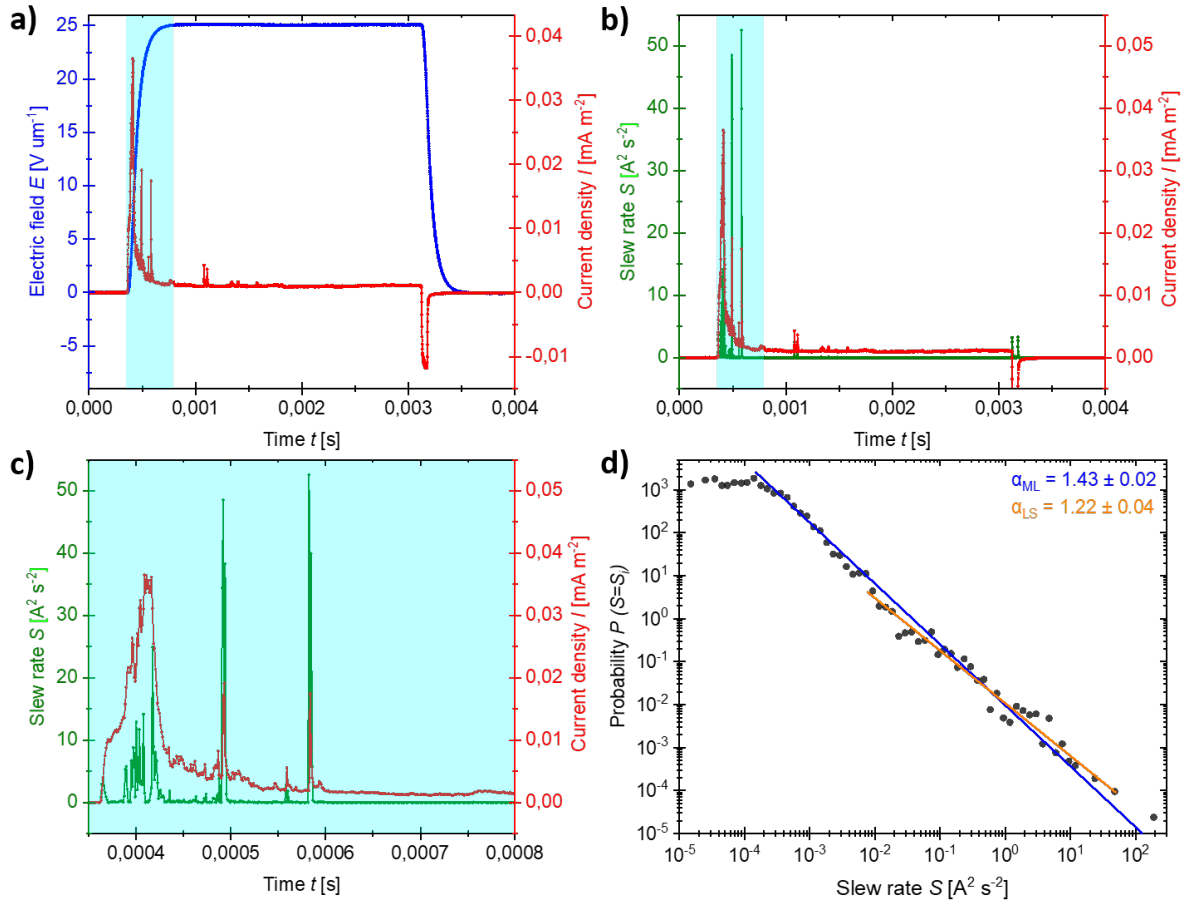

Figure 7.1.2: An example of a typical data analysis for an applied voltage of ≈ 25 V. **a)** The measured current density I (red) of a P(VDF:TrFE) sample as a response to an applied square electric field waveform E (blue) as a function of time t. The waveform's rising slope (marked in cyan) is rounded due to the noise-filtering input circuit. The downward peak in the current density at ≈ 3.2 ms arises from displacement current. Current peaks after the voltage ramp arise because the sample does not fully switch during the ramp since the applied electric field is near the coercive field. The corresponding P-E-hysteresis loop is shown and discussed in Figure A.12.1 in Section A.12. **b)** The slew rate S (green), calculated from the current signal I (red). **c)** The slew rate S (green) and the current signal I (red), zoomed in on the relevant part of the measured spectrum, which extends from the beginning to the end of the slope of the applied voltage waveform, as marked in cyan in (a) and (b). **d)** The fitted power laws with the extracted power-law exponents for measurements using both ML (blue line) and LS (orange line, depicted as linear) fitting methods. This figure was taken unmodified from Publication III with permission for usage granted by Physical Chemistry Chemical Physics.

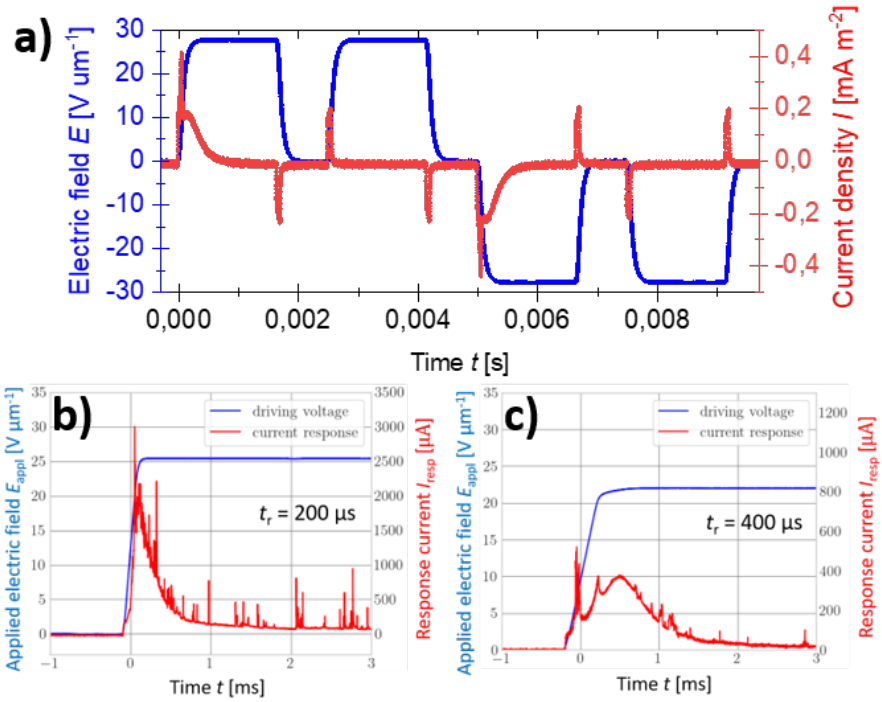

Figure 7.2.1: a) A current density measurement of a P(VDF:TrFE) sample (red) in response to an applied electric field in the form of a squared double wave (blue). One measurement period is shown, and the response current does not exhibit well-developed Barkhausen noise. The applied waveform is a square double wave with variable rise times; therefore, the step-like increase is not instantaneous. The rounding of the applied electric field is due to the noise-filtering input circuit used and does not effect the measured response current from the sample. Similar measurements with Barkhausen noise (sudden increases of the current response) showcasing the changes in the shape of the main switching peak depending on the ramp time of the square waveform are shown for **b)** 200 μs and **c)** 400 μs rising times, respectively. Current peaks after the voltage ramp arise because the sample does not fully switch during the ramp since the applied electric field is near the coercive field. This figure was initially adapted from B.Sc. Marcel Hecker's bachelor's thesis and taken unmodified from the supporting information of Publication III with permission for usage granted by Physical Chemistry Chemical Physics.

the power-law behavior at the beginning, followed by a steeper exponential drop at larger event sizes [241]. For example, 19.8 V for 100 μs shows a second bump, and 27.2 V for 800 μs initiates the power-law fit within the transitional region. Generally, voltages corresponding to electric fields above the coercive field exhibit a more pronounced transition region from the noise plateau (due to thermal fluctuations) at small event sizes to power-law-like behavior. This is attributed to the power law dominating the cutoff region and resulting in a direct transition from the plateau to the power law. Furthermore, it was discovered that the rise times varied slightly within the

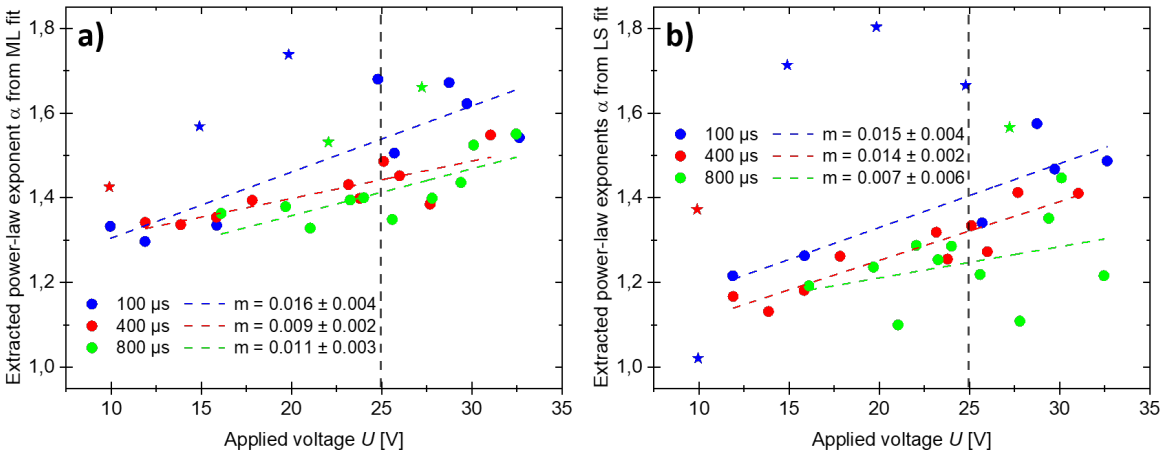

Figure 7.2.2: The power-law exponent α as a function of the applied voltage U for three different rise times: 100 μs (blue), 400 μs (red), and 800 μs (green). These power-law exponent values were extracted from **a)** ML and **b)** LS fits of measured histograms. The extracted power-law exponents were fitted with a linear function to illustrate their trends, as indicated by the colored dashed lines. The corresponding slopes m are included in the plots. Some data points were deemed inconclusive due to difficulty obtaining unique fits to the histograms. These points are marked with stars and excluded from the linear fit. The coercive field of P(VDF:TrFE) is around 25 V, as indicated by the vertical dashed black line. This figure was taken unmodified from the supporting information of Publication III with permission for usage granted by Physical Chemistry Chemical Physics.

measurement series. For example, the 100 μs rise time measurement series encompasses rise times between 100 and 150 μs. The same variability in rise times is present for both 400 and 800 μs. This variation in rise times is attributed to the voltage amplifier's feedback mechanism reacting to changes in the capacitance of the ferroelectric samples under an applied electric field. The variability of the samples during prolonged measurements resulted in a significant proportion of non-ideal probability distributions. This inspired the use of two independent approaches, ML and LS (see Section A.10), to determine the power-law exponents.

Figure 7.2.2 shows the extracted power-law exponent values for different applied voltages and rise times. Higher applied voltages, and thus electric fields, lead to higher power-law exponents with an increase of roughly 0.01 V^{-1} for a fixed rise time, as indicated by the colored dashed lines in Figure 7.2.2. Figure 7.2.3 provides a better representation of the findings. It summarizes the extracted power-law exponents for different rise times and applied voltages in a box plot. Apart from a small offset, the mean exponent values obtained using the ML and LS approaches are similar, falling slightly below the mean field value of 1.5. Additionally, as shown in Figure 7.2.3a,

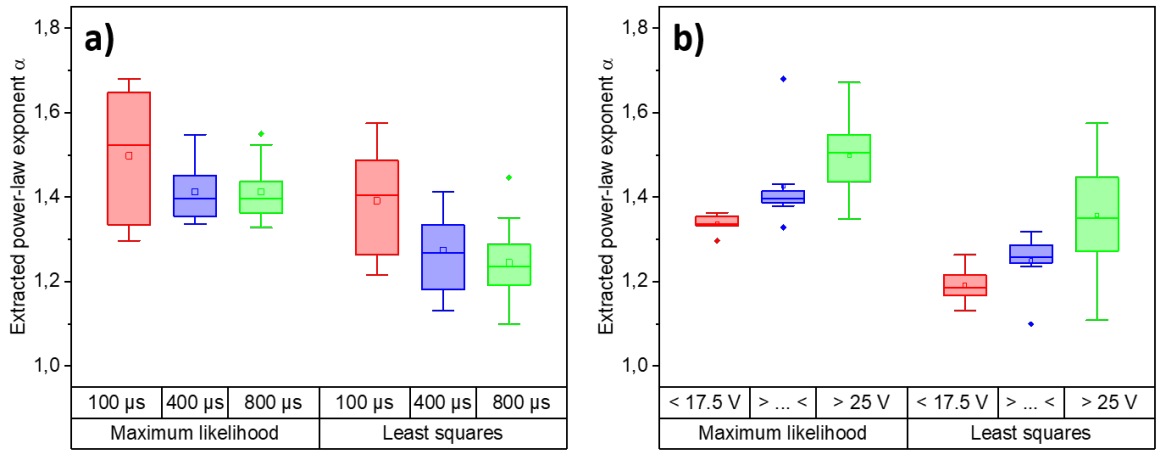

Figure 7.2.3: The box plot of the extracted critical power-law exponents α for **a)** three different rise times, including all applied voltages for each rise time in the analysis, and **b)** three different intervals of applied voltages, including all rise times for each voltage interval in the analysis, for both fitting methods. The shorthand label of the middle panel indicates voltages between 17.5 and 25 V. Some data points were excluded due to difficulty obtaining unique fits to the histograms. A similar box plot including all exponent values can be found in Figure A.12.6 in Section A.12. This figure was taken unmodified from Publication III with permission for usage granted by Physical Chemistry Chemical Physics.

both analysis methods suggest an increasing trend in exponents with higher driving speeds (and thus lower rise times). The 100 μs rise time leads to values close to the expected 1.5 from the MFP model (see Section 2.2.7). The same trend is visible for both fitting methods when plotting the power-law exponents against the applied voltage for the three different rise times, see Figure 7.2.3b.

Trends in the extracted power-law exponents, as a function of both rise time and applied voltage, suggest that the system is not truly critically self-organized, as no universal behavior is present. However, the power-law exponent values for the fastest (100 μs) and strongest (above the coercive field) driving conditions are very close to the mean field value of 1.5, indicating that the system is approaching such behavior. Furthermore, distributions generally become more ideal for shorter rise times and higher fields (see Figures A.12.2, A.12.3, and A.12.4 in Section A.12), consistent with the idea that the system approaches self-organized criticality under these conditions. In contrast, the significant variability of the response curves, and thus the extracted critical power-law exponents, especially at weaker driving, suggests that the behavior is not universally self-organized. Instead, it depends on minor variations in the structural (dis)order that occur, for instance, upon repeated switching at higher fields. This is consistent with our previous observation of an increasing occurrence of spurious signals in prolonged measurements at higher fields.

Furthermore, the observed trends in power-law exponents in Figures 7.2.2 and 7.2.3 and Figure A.12.6 in Section A.12 are consistent with the TA-NLS model (see Section 2.2.4.4) that predicts that increasing rise times and thus reducing the driving speed, results in less coercivity in the system. This yields fewer larger and more smaller events, resulting in generally smaller extracted power-law exponents. These findings align with the other results regarding coercivity and event sizes in a simulated BTA ferroelectric system, as presented in Chapter 6. Below the coercive field in particular, the extracted power-law exponents are lower than expected from the mean-field theory. This agrees with other studies carried out for magnetic systems and can be explained by the fact that the entire system is not fully switched [241]. In that scenario, the less stable parts of the system can switch before reaching the coercive field. This leads to smaller, isolated events that do not progress into larger, system-spanning avalanches. Hence, the power-law exponents are smaller.

As mentioned in Section 2.2.5, the TA-NLS theory has previously been used to investigate the (Preisach) distribution of nucleation sites (hysterons) in P(VDF:TrFE). A typical critical volume V^* of 4 nm^3 has been established for this system, which corresponds to approximately 10^3 switched dipoles [105]. In the present case, the smallest event sizes that can be resolved experimentally correspond to approximately 10^8 dipoles switching simultaneously, as described in Section A.11. Thus, the measured signals must reflect the resulting avalanches and not the nucleation events. The absence of specific data prevents drawing firm conclusions, but a possible connection between the distributions of nucleation sites and switching events can be proposed inspired by the numerical work on BTA (see Chapter 6). In that work, it was found that small hysterons consisting of stacks of approximately ten molecules each that are separated by morphological defects can act as nuclei for polarization reversal and form building blocks for system-spanning avalanches. Whether this leads to universal critical behavior depends on the degree and variation of the coupling between these hysterons. In the case of BTA, a quasi-1D system consisting of hexagonally packed supramolecular stacks, the maximum event size is limited to a few hundred molecules, i.e., the size of a single BTA column. Due to its different morphology, domain growth in P(VDF:TrFE) is expected to exhibit a higher dimensionality, supporting much larger avalanches built from smaller interacting hysterons [93, 105]. Previous findings support this, as they revealed the characteristic geometric dimension for domain growth in P(VDF:TrFE) increases with the driving electric field [244]. While speculative, this may be the underlying mechanism for the observed behavior herein. Avalanches triggered by the small nuclei can apparently give rise to critical behavior close to self-organized criticality. The degree to which this occurs depends on how strongly the system is driven. In view of the significant sample-to-sample variation and the absence of signals after longer operation, this seems to depend on relatively subtle variations in morphology.

7.3 Conclusion

This chapter presented experimental measurements of the Barkhausen noise associated with polarization reversal in thin-film P(VDF:TrFE) samples, taken at various applied voltages and rise times. The data from each noise measurement were averaged over 100 current waveforms, and the corresponding slew rate was calculated. After removing the baseline and the smallest events originating from thermal fluctuations, probability density functions were calculated, and power laws were fitted using ML and LS as two different fitting methods.

Data were collected for three different rise times (100, 400, and 800 μs) and various applied voltages (10 to 33 V), with the voltage gradually increased for each rise time. The ML fitting method consistently yielded slightly higher extracted power-law exponents than the LS fitting method. All power-law exponents were lower than the mean field value of 1.5. For applied voltages above the coercive field (at $\approx$ 25 V), the 100 μs rise time yielded power-law exponents very close to 1.5. Generally, decreasing the rise time and increasing the applied voltage both led to an increase in the extracted power-law exponents, which is consistent with the TA-NLS model. However, the system does not appear to exhibit critically self-organized behavior, although it approaches this behavior for certain parameters. This deviation is attributed to the strong dependence on structural (dis)order variations between the samples, which dominate the weaker and slower driving.

Additionally, the possibility of comparing Barkhausen noise with distribution of nucleation sites in the TA-NLS model, as derived from the Preisach distribution, was investigated. It was concluded that the observed Barkhausen noise must originate from switching avalanches rather than nucleation events, given the insufficient size of the latter. While not strictly proven, it is hypothesized that small interactive hysterons may be responsible for domain growth in P(VDF:TrFE), resulting in larger avalanches based on the morphology. This would imply that small nuclei can lead to a critical behavior close to self-organized criticality.

While the results obtained are coherent, it would be interesting to further investigate whether self-organized critical behavior is experimentally achievable in P(VDF:TrFE) by varying the applied voltage and, especially, the rise time. Temperature is also suspected to be an important parameter. All measurements were performed at room temperature since P(VDF:TrFE) ferroelectrically switches at this temperature, and heating the samples further would introduce more thermal fluctuations. However, kMC simulations of Barkhausen noise in BTA yielded self-organized behavior at temperatures $\lesssim$ 175 K (see Chapter 6), while BTA typically switches ferroelectrically at temperatures at or above $\approx$ 340 K. Therefore, reducing the temperature seems to be an effective way to increase the system's overall stability. Furthermore, performing kMC simulations of Barkhausen noise in PVDF would be interesting. M.Sc. Fabian T. Thome attempted to simulate Barkhausen noise in PVDF using the same kMC program as for BTA but with a different morphology. However, the simulations were deemed as unsuccessful because PVDF has strong van-der-Waals interactions that must be considered [245, 246], which could be disregarded for BTA due to its morphology.

Chapter 8

Electrical properties of organic molecular triphenylamines

Ferroelectricity and other material properties can be predicted based on structural similarity to other compounds, among other factors. This chapter investigates the ferroelectric behavior of three TPA derivatives, which are discotic-like compounds with three amide groups similar to BTA. Ferroelectric characterization measurements were performed using DS and DWM. The thin film structure was investigated using AFM and XRD. No evidence of the ferroelectric behavior was found. Small structural changes were observed after the TPA samples were electrically treated at elevated temperatures, though no long-range ordering along the electric field was evident. However, a distinct electrical conductivity with a temperature hysteretic behavior, attributed to the short-range structural ordering developed at elevated temperatures, was established and investigated further.

Section 3.3.1 describes the measurement setup and method used for the ferroelectric characterization of the samples (see Section 3.1.2.2). The basics of DS are introduced in Section 3.3.2. Section 4.2 describes the TPAs.

The project can be divided into two parts: the ferroelectric part and the conductivity part. The former was completed solely by the author. The author performed the ferroelectric and structural characterization using AFM and XRD (see Sections 3.3.5.2 and 3.3.5.1). The second part of the project investigated the conductivity of the TPA compounds. While the author performed the corresponding conductivity measurements, this part of the project evolved into a subproject of Dr. Heiko Mager's larger project. Dr. Heiko Mager also provided most of the evaluation and explanation. This dissertation focuses on the first part.

Some of the results presented in this chapter are included in Publication IV. All of the text in this chapter is original and was written by the author for this thesis. Some of the conclusions considering the TPA derivatives originate from Publication IV, which was primarily written by Dr. Heiko Mager based on the author's input and revised and improved by Prof. Dr. Martijn Kemerink, unless otherwise specified. All the figures in this chapter are original, with some data also presented in Publication IV.

8.1 Dielectric spectroscopy

DS measurements were performed to check for possible phase transitions. The TPA samples were cooled down to 80 K, then gradually heated to 420 K, cooled back to 80 K, heated to 420 K, and finally cooled to around room temperature. Their capacitance was measured as a function of temperature and frequency during this process. After reaching a temperature value, it was held for ≈ 15 min before measurement to reach thermal equilibrium and thus minimize fluctuations. Then, the frequency was swept from 1 Hz to 1 MHz. These minimum and maximum temperature values values were chosen because 80 K is the lowest temperature that can be reached with the measurement setup, and the materials start to melt at around 440 K. The measurements were performed under high vacuum.

Figure 8.1.1 summarizes the DS measurement results for the three TPA derivatives. The heating trace of o-TPA-N (Figure 8.1.1a) exhibits two small features at ≈ 150 K and $\approx 260 - 270$ K. The former is barely visible and barely changes with frequency; it vanishes in the cooling trace. The latter represents a peak that shifts to higher temperatures with higher frequencies while decreasing in size. It should be noted that these features are relatively small considering the absolute capacitance value. The wide, large feature after ≈ 350 K is attributed to the substrate. The cooling trace shifts this feature to ≈ 280 K and no longer shows the $\approx 260 - 270$ K feature anymore, which is most likely due to water evaporating from the sample at higher temperatures. Neither the heating nor the cooling traces of p-TPA-N (Figure 8.1.1b) show features indicating a phase transition. Though there are minor changes, they are too small to resemble Curie-Weiss behavior. However, the heating trace of p-TPA-C (Figure 8.1.1c) exhibits a large peak at lower frequencies between 260 and 290 K. This peak completely vanishes at larger frequencies and on the cooling trace. This indicates that it may originate from water evaporating from the sample between the measurements, similarly to o-TPA-N. The small jump at 300 K originates from a measurement range change during the measurement. The jump between 300 and 350 K is only visible for the lowest frequency and disappears completely in the cooling trace. The large increase in capacitance above ≈ 400 K originates from the substrate. Therefore, no features that could be attributed to a phase change are observed.

The measurements were repeated, and second heating and cooling traces were obtained. The heating traces did not exhibit water-related peaks, and the cooling traces resembled those shown in Figure 8.1.1. It was concluded that neither of the TPA derivatives showed features indicating a possible para-to-ferroelectric phase transition at the investigated temperatures and frequencies.

8.2 Ferroelectric characterization

Since the DS measurements (see Section 8.1) did not indicate any possible phase transitions, ferroelectric characterization measurements were performed over a wide temperature and frequency range. The ferroelectric characterization was done by the DWM. The applied signal was varied

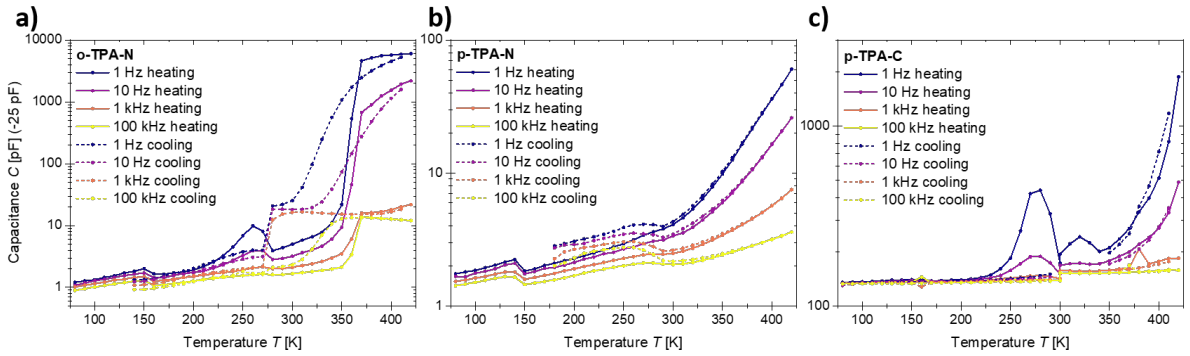

Figure 8.1.1: Dielectric spectroscopy measurements of **a)** o-TPA-N, **b)** p-TPA-N, and **c)** p-TPA-C. All graphs show the capacitance C as a function of temperature T at several frequencies f for each temperature step. The capacitance was corrected by 25 pF, which corresponds to the typically constant background of an empty device up to ≈ 400 K. Measurements started at 80 K, and the samples were heated up to 420 K and then cooled back down to 80 K. Both the heating and cooling traces are shown. The latter had some contacting issues due to the temperature variation, resulting in missing data points.

to achieve different combinations over a large range of the voltage $U = 250 - 350$ V, frequency $f = 0.1 - 100$ Hz, and temperature $T = 100 - 420$ K. None of the measured parameter combinations indicated ferroelectric switching; the corresponding current responses merely showed displacement and leakage currents. Figure A.13.1 in Section A.13 shows an exemplary measurement of the ferroelectric characterization of the o-TPA-N. In addition to the DWM measurements, CV-measurements of the TPA samples were attempted. Unfortunately, no measurements could be performed since all of the TPA samples short-circuited early during the measurements.
The lack of dipolar activity aligns with previous results for similar non-planar C3-symmetric compounds [247]. However, the measurements exhibited significant 'leakage' currents, especially at higher temperatures. Additionally, the high 'leakage' currents persisted after reducing the temperature to room temperature. This phenomenon is examined further in Section 8.3.

8.3 Conductivity measurements

IV(t) measurements were performed to measure the conductivity of the TPA derivatives. A constant DC voltage signal of 100 V was applied, and the temperature was varied. After reaching a temperature value, it was held for ≈ 15 min before measurement to reach thermal equilibrium and thus minimize fluctuations.
Figure 8.3.1 summarizes the findings on temperature-dependent conductivity. The corresponding raw measurement data are presented in Figure A.13.2 in Section A.13. All untreated TPA samples start at a low current of $\approx 10^{-11}$ A at room temperature. The current, and thus the conductivity,

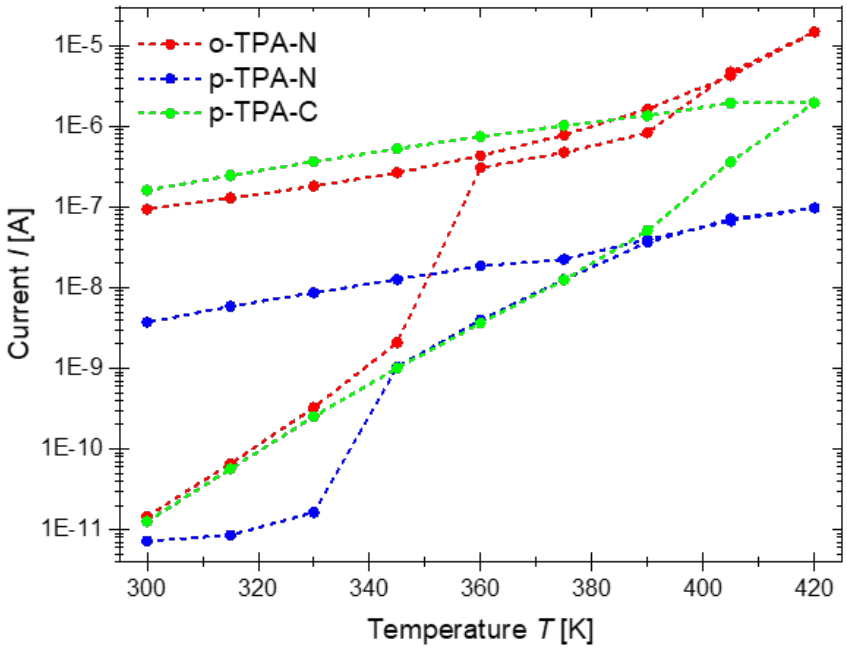

Figure 8.3.1: The logarithmic current I of the three TPA derivatives as a function of temperature T. The currents have been corrected for device background. The corresponding raw measurement data can be found in Figure A.13.2 in Section A.13.

increases with temperature for all three TPA derivatives. However, the rate at which the current increases and the final current values at the highest investigated temperature of 420 K differ. O-TPA-N exhibits a steep jump in current between 345 and 360 K and has the highest current of $\approx 10^{-5}$ A at 420 K. P-TPA-N exhibits a small increase between 330 and 345 K and has the lowest current of $\approx 10^{-7}$ A at 420 K. P-TPA-C increases steadily with temperature, exhibiting a current of $\approx 2 \cdot 10^{-6}$ A at 420 K, which is between the corresponding values of the other two TPAs. During cooling, all currents decrease, albeit significantly more slowly than their increase during heating. All three TPA derivatives finish with a current that is multiple orders of magnitude larger than the initial current at room temperature; o-TPA-N and p-TPA-C reach $I \approx 10^{-7}$ A, while p-TPA-N finishes with $I \approx 3 \cdot 10^{-9}$ A.

Figure 8.3.1 shows that the three TPA derivatives exhibit significantly enhanced electrical conductivity at room temperature after field annealing at elevated temperatures. The most probable cause of this temperature hysteretic behavior in conductivity is a permanent, conductivity-enhancing structural reordering, which is investigated in Section 8.4.

8.4 Structural characterization

Structural characterization was performed using AFM and XRD before and after the TPA thin films were subjected to conductivity measurements (see Section 8.3). The former means that the measurement was performed directly after material deposition. The latter was performed after the deposited material underwent conductivity measurement and was field-annealed at 100 V and up to 420 K. Then, it was measured by AFM and XRD.

Figure 8.4.1 shows selected AFM topographies of the TPA derivatives before and after conductivity measurements. Before treatment, both o-TPA-N and p-TPA-C form clusters of material without preferential alignment. After field annealing, their cluster formation is increased, though no preferred orientation is observed. For p-TPA-N, material bundles form before treatment and are strongly enhanced after treatment. However, since the bundles are perpendicular to the electric field (see Figure 8.4.1), it is suggested that the electric field does not directly align the bundles but instead contributes energy to the system.
Figure 8.4.2 shows the 2D GIWAXS measurements of the three TPA derivatives before and after conductivity measurements. Although no significant differences are observed before and after treatment, the diffraction patterns appear slightly more pronounced (narrower) and have stronger contrast with the background after treatment. This suggests that, although no significant morphological changes occur within the thin films, the crystallinity changes slightly and improves overall, albeit minimally.
The TPA thin films on glass and in-plane devices were also measured by PLM (see Section 3.3.5.5) to investigate alignment. The main problem was that the thin films were extremely uneven on both pure glass and in-plane devices, which prevented focusing on the films. No pronounced structures or other features indicating long-range alignment were observed, which aligns well with the findings of other structural resolution methods that also observed little to no alignment in untreated samples.

8.5 Conclusion

The presence of ferroelectric switching was investigated in the three TPA derivatives using various methods. DS measurements were performed by measuring capacitance as a function of temperature ($80 - 420$ K) at various frequencies (1 Hz $- 1$ MHz). Some minor features were obtained for the three TPA derivatives, but the possibility for them being para-to-ferroelectric phase transitions was ruled out. DWM measurements were also conducted on the TPA derivatives over a wide temperature range of $100 - 420$ K and a frequency range of $0.1 - 100$ Hz. None of the investigated parameter combinations showed ferroelectric switching. CV measurements were also attempted but were unsuccessful.
However, a significant increase in electrical conductivity with temperature was observed in all TPA

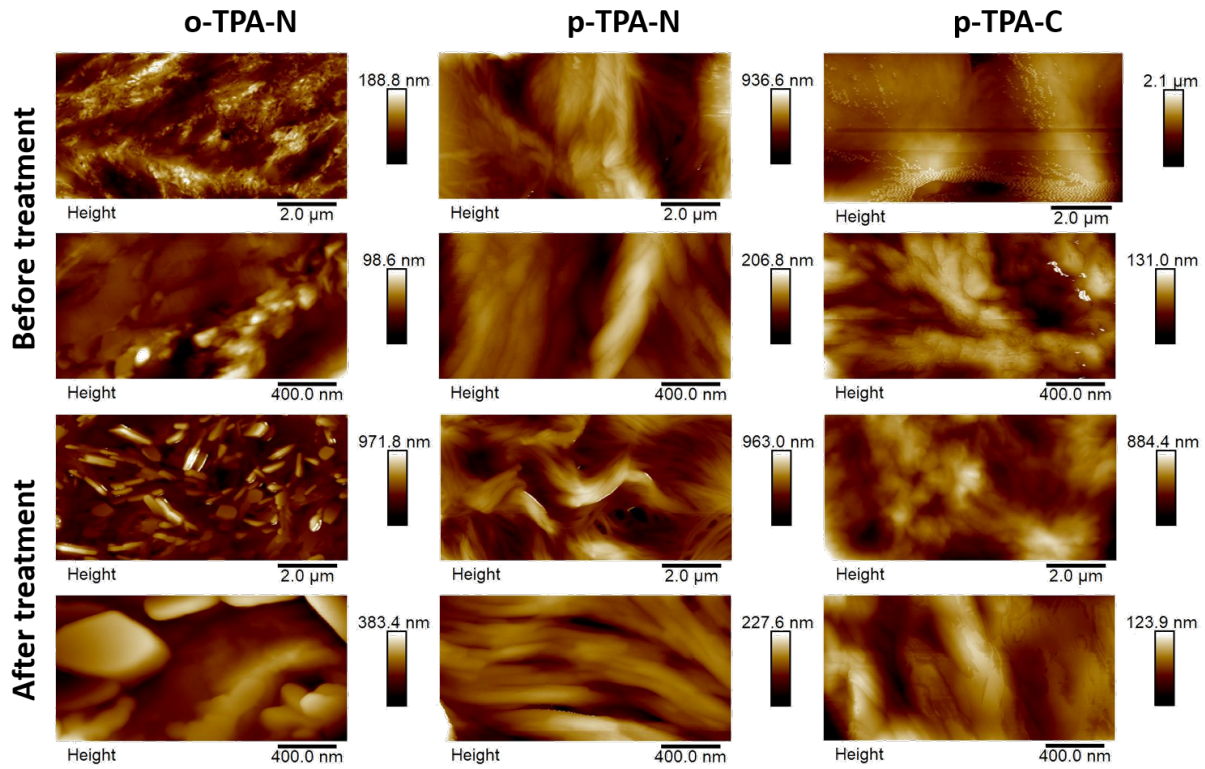

Figure 8.4.1: The AFM topographies of selected o-TPA-N, p-TPA-N, and p-TPA-C on IDEs samples before and after the alignment process. The electrodes run vertically in all images. Consequently, the electric field is horizontal. All images were take with a scan area of either 10 μm $\times$ 5 μm or 2 μm $\times$ 1 μm. The corresponding amplitude images can be found in Figure A.13.3 in Section A.13.

samples. IV(t) measurements were performed to investigate this effect further. All TPA derivatives exhibited a significant increase in electrical conductivity by multiple orders of magnitude at elevated temperatures ($\geq$ 360 K), which remained significantly enhanced upon cooling back to room temperature, thus exhibiting a temperature hysteretic behavior in conductivity. This enhancement in electrical conductivity was attributed to a permanent, conductivity-enhancing structural reordering of the TPA thin films caused by applying an electric field at elevated temperatures. This was confirmed by structural characterization using AFM and XRD, which showed a generally improved crystallinity and ordering without significant morphological changes. The full evaluation and explanation of the mechanism behind the observed conductivity behavior can be found in Dr. Heiko Mager's dissertation and Publication IV. While the author contributed to the above-described measurements, this went beyond the scope of the author's project and this dissertation. As speculated by Dr. Heiko Mager in his dissertation, the tendency of the TPA derivatives to form supramolecular columns and the presence of the dipolar amide groups indicate

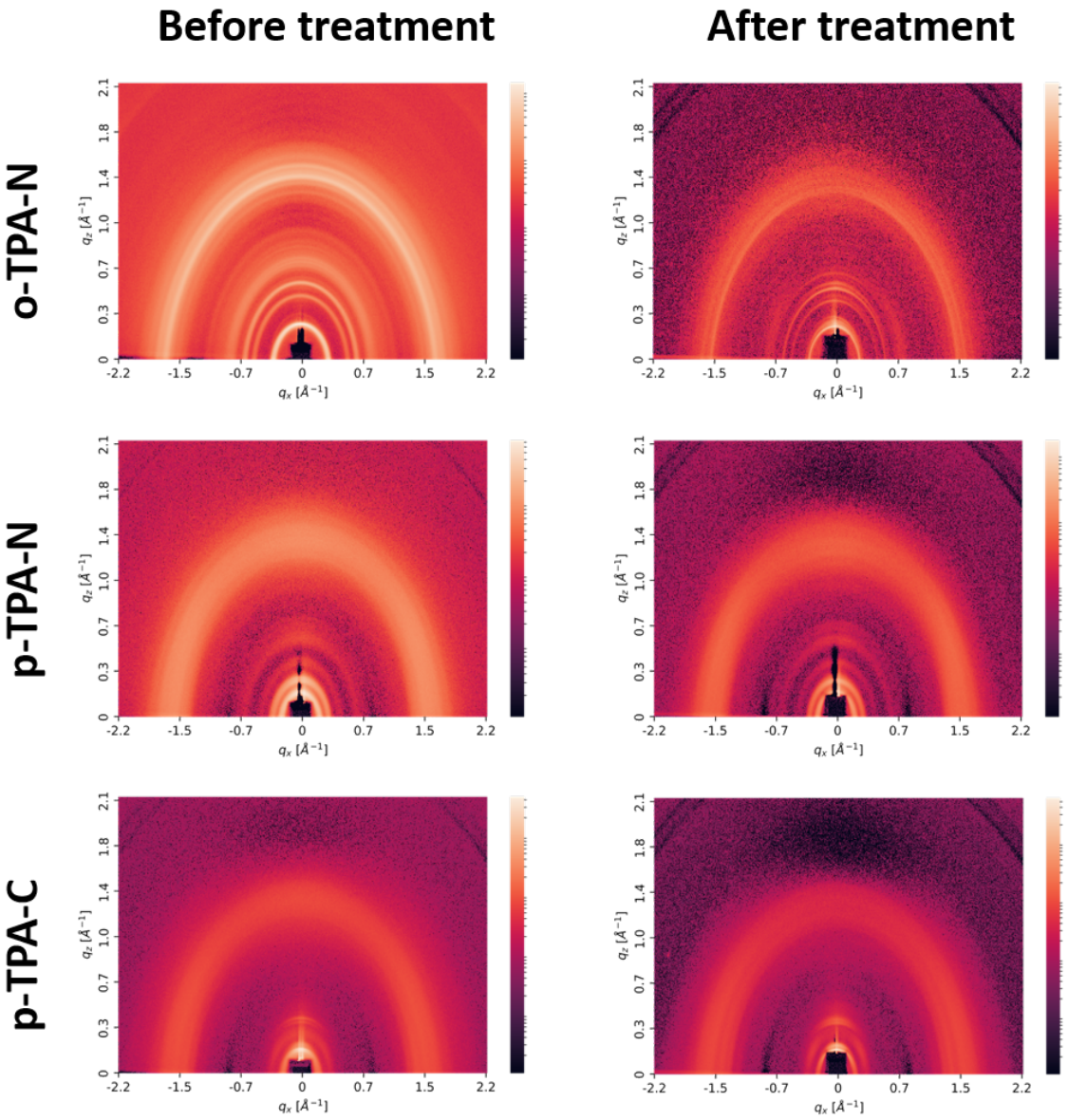

Figure 8.4.2: The 2D GIWAXS measurements of selected o-TPA-N, p-TPA-N, and p-TPA-C on IDEs samples before and after the alignment process. The images were taken perpendicular to the electrodes. Similar measurements were also performed parallel to the electrodes, and no differences were established except for worse resolution for the latter.

the strong possibility of a dipolar interface layer [237], which would reduce the injection barrier without requiring true ferroelectric polarization switching and thus enables charge injection and transport.

Chapter 9

Thermoelectric properties of dip-coated conjugated polymer P3HT

Organic semiconductors typically have low thermal conductivity and a high Seebeck coefficient. However, due to the trade-off between these two parameters, achieving a competitive figure of merit is difficult. One way to improve the figure of merit is to enhance the structural order of the devices. This chapter investigates the effect of dip coating on the structural and thermoelectric properties of P3HT thin films. Dip coating was chosen as the coating and alignment technique due to its simplicity and availability. Dip-coated P3HT thin films were systematically investigated at various dip coating speeds and material concentrations. The structural characterization of pristine (undoped) dip-coated P3HT was performed using UV-vis spectroscopy, AFM, XRD, and PLM. Thermoelectric measurements were performed to obtain the conductivity and Seebeck coefficient on P3HT thin films sequentially doped with F_4TCNQ and MB.

The dip coating theory is provided in Section 3.2.3. Section 3.3.4 describes the measurement setup and background for the thermoelectric characterization of the P3HT samples (see Section 3.1.3). Section 4.3 introduces π-conjugated polymers and summarizes the properties of P3HT and the dopants used.

The project was completed in collaboration with M.Sc. Morteza Shokrani. The author conducted the dip coating experiments and performed all structural characterization of the samples. M.Sc. Morteza Shokrani carried out the thermoelectric characterization and the corresponding data evaluation. Collating and interpreting the results was a joint effort.

Most of the results presented in this chapter are included in Publication V. Much of the text and figures in this chapter originate from Publication V. The original text was written primarily by the author and M.Sc. Morteza Shokrani for Publication V and revised and improved by Prof. Dr. Martijn Kemerink, unless otherwise specified. Changes to the text were made to fit this dissertation's argumentation and style. The figures taken from Publication V may have changes to their descriptions.

9.1 Dip coating of P3HT

To become familiar with P3HT and its dip coating process, dip-coated samples were fabricated using different solvents and P3HT concentrations. Following Rogowski and Darhuber, the film thickness was investigated as a proxy for the total deposited mass as a function of dip coating speed [158], as discussed in detail in Section 3.2.3. Figures 9.1.1a and b show the differences in film thickness between dip-coated 5 and 10 mg ml^{-1} P3HT in CF. Figures 9.1.1b and c show the film thickness of dip-coated 10 mg ml^{-1} P3HT in CF and ODCB, respectively. In all cases, the evaporation and Landau-Levich regimes were established and were clearly separated by a characteristic threshold speed U_{th} [158]. The experimental data were fitted with power-law functions $d \propto U^{\alpha}$. The power-law exponents in the Landau-Levich regime varied significantly between solvents and concentrations, ranging from ≈ 0.3 to 0.9. The power-law exponents in the evaporation regime all lied around -0.7 to -0.8. While the absolute values of these exponents differed from those of similar experiments - Rogowski and Darhuber obtained $\alpha = -0.95$ and $\alpha = 2/3$ [158], and Le Berre, Chen and Baigl obtained $\alpha = -1.14$ and $\alpha = 0.76$ [171], respectively for the evaporation and Landau-Levich regimes - the power-law exponents in the evaporation regime are comparable. Furthermore, the experimental data clearly identify the threshold velocities, as indicated in Figure 9.1.1.

The threshold speed U_{th} can be determined using Equation 3.2.7 in Section 3.2.3. The evaporation rates of the 10 mg ml^{-1} P3HT solutions were found to be $\approx 4.2 \cdot 10^{-7}$ and $\approx 4.3 \cdot 10^{-10}$ kg s^{-1} for CF and ODCB, respectively. Using the material properties of the solvents (CF: $\rho = 1489$ kg m^{-3}, $\mu = 0.563 \cdot 10^{-3}$ Pa, and $\sigma = 27.24 \cdot 10^{-3}$ N m^{-1}; and ODCB: $\rho = 1300$ kg m^{-3}, $\mu = 1.31 \cdot 10^{-3}$ Pa, and $\sigma = 36.61 \cdot 10^{-3}$ N m^{-1}), the threshold velocities were estimated to be ≈ 252 and ≈ 2.3 mm min^{-1} for CF and ODCB, respectively (see Section A.3). However, these values may overestimate the experimental results because evaporation from the contact line is retarded by solution vapor emerging from the liquid reservoir, which is not considered when determining the evaporation rate [158]. For dip coating of BTA (see Chapter 5), an overestimation of about two times was found. Therefore, the experimentally observed threshold velocities of ≈ 110 and ≈ 0.7 mm min^{-1} in Figures 9.1.1b and c are in good agreement with the estimated ones.

Since previous publications have shown that dip coating benefits from the use of more volatile solvents due to their faster evaporation rates, further investigations of the structure and thermoelectric properties were carried out using CF as the solvent of choice [248].

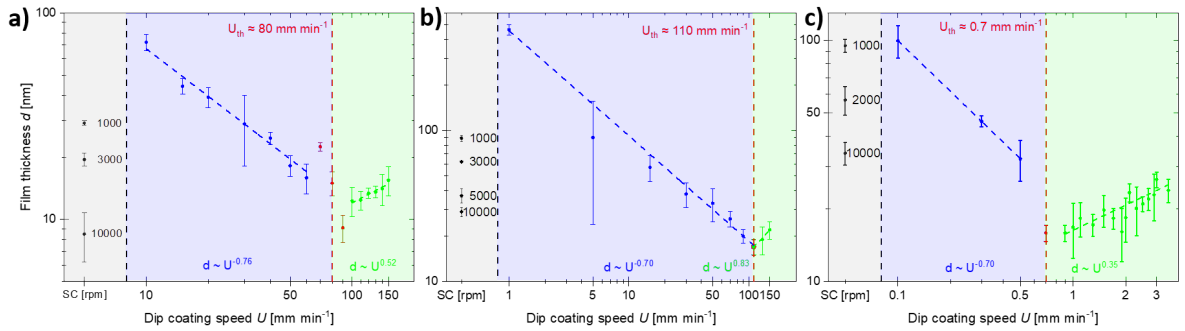

Figure 9.1.1: Film thicknesses d of dip-coated **a)** 5 mg ml^{-1} P3HT in CF, **b)** 10 mg ml^{-1} P3HT in CF, **c)** and 10 mg ml^{-1} P3HT in ODCB, as a function of dip coating speed U on a double-logarithmic scale. The evaporation (blue) and Landau-Levich (green) regimes, along with their corresponding power-law fits (at the bottom), are highlighted, as are the threshold speeds U_{th} (red). The differences in the threshold speeds for the different P3HT concentrations in CF (a and b) are due to changes in the solution properties caused by varying P3HT concentrations within the solutions. Multiple spin coating speeds (marked as 'SC', gray) are included for comparison. The error bars represent the absolute minimum and maximum measured film thicknesses (not standard deviations), and the values themselves are weighted averages of all measured film thicknesses. This figure was taken and slightly modified from Publication V with permission for usage granted by Advanced Electronic Materials.

9.2 Structural characterization

To measure the degree of order in P3HT thin films, the UV-vis absorption spectra (see Section 3.3.5.4) recorded prior to doping (i.e., of pristine films) was analyzed. The degree of polymer backbone alignment can then be quantified using the dichroic ratio, which is the ratio of the maximum absorbance values of the absorbance peaks with the dip coating direction perpendicular to and parallel with the polarizer, respectively [141, 249–251]. Absorbance spectra of P3HT from CF solution are shown in Figure 9.2.1 as a function of the wavelength λ and in Figure A.14.1 in Section A.14 as a function of the energy E. The spectra of all investigated samples show the characteristic features of neat P3HT, albeit with different degrees of structural order [250]. A strong absorption peak appears at $\approx 550 - 555$ nm (≈ 2.24 eV) with two shoulder peaks at $\approx 515 - 520$ nm (≈ 2.40 eV) and $\approx 600 - 605$ nm (≈ 2.06 eV). The appearance of the peaks at $\approx 550 - 555$ nm and $\approx 600 - 605$ nm indicates an ordered structure after self-assembly of the P3HT polymer in the CF solution [252]. For lower withdrawal speeds (1 and 15 mm min^{-1}), the vibronic substructure is more pronounced than in the spin coated sample, indicating increased structural order in the former. For comparison, the measured absorption spectrum of P3HT in CF solution is shown in Figure 9.2.1a (dashed line). This spectrum aligns well with previous results and does not exhibit vibronic substructure, indicating that there is little to no self-organization

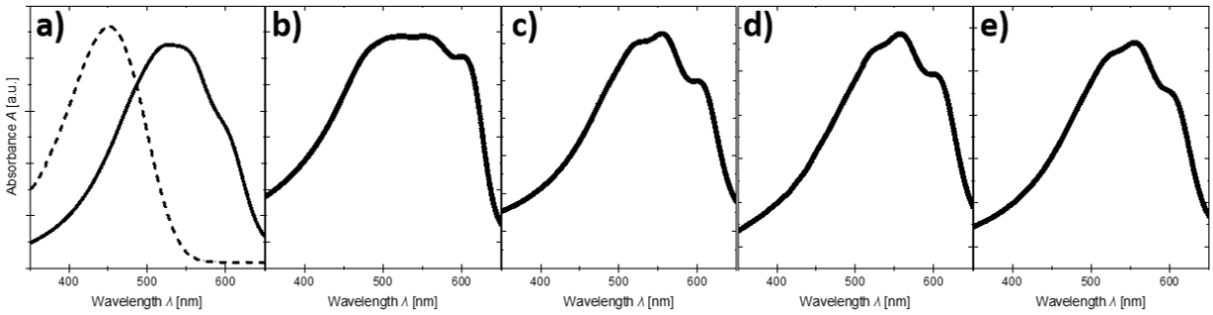

Figure 9.2.1: The UV-vis spectroscopy absorbance spectra of pristine P3HT thin films dip and spin coated from a 10 mg ml^{-1} P3HT in CF solution at different dip coating speeds as a function of the wavelength λ. The samples shown are **a)** spin coated at 3000 rpm (solid line) and spin coated at 3000 rpm from a 0.01 mg ml^{-1} P3HT in CF solution (dashed line), and dip coated at **b)** 1, **c)** 15, **d)** 70, and **e)** 150 mm min^{-1}. The spectra were measured with the polarizer parallel to the dip coating direction. The characteristic $0-0$ and $0-1$ P3HT peaks are visible at $\approx 600-605$ nm and $\approx 550-555$ nm, respectively. The corresponding absorbance spectra as function of energy E are shown in Figure A.14.1 in Section A.14. This figure was taken unmodified from Publication V with permission for usage granted by Advanced Electronic Materials.

of P3HT aggregates present in the solution. Therefore, the increased structural order likely arises during deposition of the thin films, possibly due to pre-aggregation in the solution [253, 254]. Somewhat unexpectedly, given published results, the measured dichroic ratios are close to 1, ranging non-systematically from 0.98 to 1.03 for different dip coating speeds, as shown in Figure 9.2.2. Thus, no anisotropic alignment seems to be present.

Furthermore, the free exciton bandwidth of aggregates W can be calculated from the UV–vis absorbance spectra of the dip-coated samples shown in Figures 9.2.1 and 9.2.2 by fitting the spectra using Spano's method [255]. Generally, a decrease in the free exciton bandwidth is a result of increased aggregation and an increase in the conjugation length of P3HT [250]. Thus, the free exciton bandwidth was calculated from the obtained energy difference dE between the $0-0$ and $0-1$ absorbance peaks and their amplitude ratio A_{0-0}/A_{0-1} using the following expression for the free exciton bandwidth:

$$W \approx \frac{\left(1-\sqrt{A_{0-0}/A_{0-1}}\right)\mathrm{d}E}{0.073\sqrt{A_{0-0}/A_{0-1}}+0.24} \tag{9.2.1}$$

The fit results are shown in Figure 9.2.3 for three dip coating speeds. The obtained values of electrical conductivity ($\sigma \cong 1-6$ S cm^{-1} (see Section 9.3)) and free exciton bandwidth $W \cong 65-85$ meV of the dip-coated samples (from Equation 9.2.1) are, within the error margins, in good agreement with the corresponding trends presented by Hynynen et al. [250] and Kajiya et

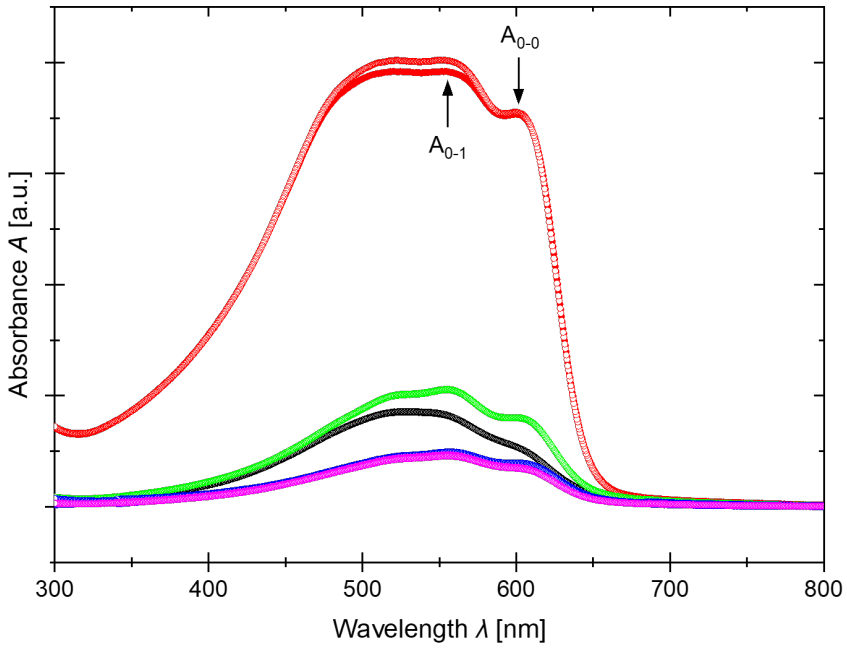

Figure 9.2.2: The UV-vis spectroscopy absorbance spectra of pristine dip and spin coated 10 mg ml^{-1} P3HT in CF thin films as a function of wavelength λ for different dip coating speeds. The characteristic absorbance peaks $0-0$ and $0-1$ are visible at $\approx 600-605$ nm and $\approx 550-555$ nm, respectively. Open and closed symbols represent measurements taken with polarization perpendicular and parallel to the dip coating direction, respectively. The withdrawal speeds are (top to bottom): 1 (red), 15 (green), 70 (blue) and 150 (purple) mm min^{-1}. A 3000 rpm spin-coated sample is shown for comparison (black). This figure was taken unmodified from the supporting information of Publication V with permission for usage granted by Advanced Electronic Materials.

al. [256]. The fit results of spin-coated samples are not included in Figure 9.2.3 since fitting the corresponding spectrum (see Figure 9.2.1) following Spano's method did not produce good fitting results. Hynynen et al. established a clear correlation between increased P3HT aggregation and a higher electrical conductivity. Therefore, since the conductivity of the dip-coated P3HT films is higher than of the spin coated ones (see Section 9.3), the results suggest that the dip-coated films should be generally more aggregated.

Figure 9.2.4 shows the AFM topologies (see Section 3.3.5.2) of three selected dip-coated P3HT samples from the two different dip coating regimes, as well as a spin-coated sample for comparison. Although AFM is a surface-sensitive technique and the measured topographies cannot upfront be assumed to represent the bulk, it has been established that, when present, alignment within a thin

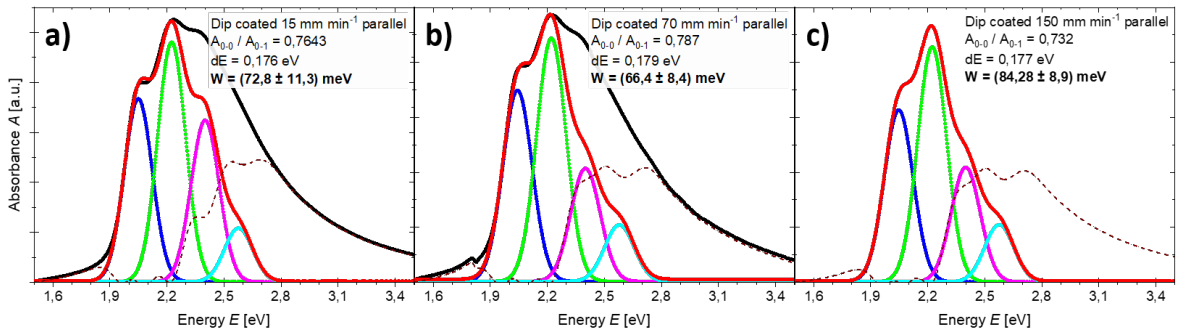

Figure 9.2.3: Fits of absorbance peaks in UV-vis spectroscopy spectra of dip-coated samples with pronounced vibronic structure for **a)** 15, **b)** 70, and **c)** 150 mm min^{-1} dip coating speeds. The fits were performed using Gaussian functions with a constant width and spacing. The colored lines correspond to the fits for the $0-0$ (blue), $0-1$ (green), $0-2$ (magenta), and $0-3$ (cyan) P3HT peaks, respectively. The red line is the sum of the fitted peaks, and the dashed brown line shows the difference between the measured and fitted spectra. The peak height ratio A_{0-0}/A_{0-1} and energy difference dE values are obtained from the shown fits are used to calculate the free exciton bandwidth W. The errors in the free exciton bandwidth values represent the deviation typically observed from the shown values when the fit parameters were varied acceptably during the fitting process. This figure was taken unmodified from the supporting information of Publication V with permission for usage granted by Advanced Electronic Materials.

film is generally clearly observable via AFM due to distinct morphologies forming [257–259]. In our case, no visible uniaxial alignment is present in any of the prepared samples. Different material cluster sizes are present at different dip coating speeds; however, no structures or morphologies suggesting alignment are visible. The RMS roughness values decrease for thinner films and are in the range of several nm, which aligns with expectations for an aggregated, semicrystalline material.

Furthermore, the morphology of the dip-coated P3HT thin films was investigated using XRD (see Section 3.3.5.1). Figure 9.2.5 shows the 2D GIWAXS measurements of a spin-coated sample and three selected dip-coated samples. The spin-coated sample exhibits the characteristic diffraction pattern of an isotropic P3HT thin film. However, the 1 mm min^{-1} dip-coated sample shows two distinct features. First, high-intensity peaks along the z-direction are visible, which may indicate a preferential edge-on alignment [250]. Second, the broad amorphous background feature at ≈ 1.5 Å^{-1} visible in the other samples appears to be separated into multiple diffraction rings. This strongly suggests more ordered structuring within the thin film, which is consistent with the general enhancement of crystalline features and order by dip coating at lower dip coating speeds [141]. At higher dip coating speeds, these features weaken (70 mm min^{-1}) or disappear completely (150 mm min^{-1}). While this indicates that lower dip coating speeds have more order

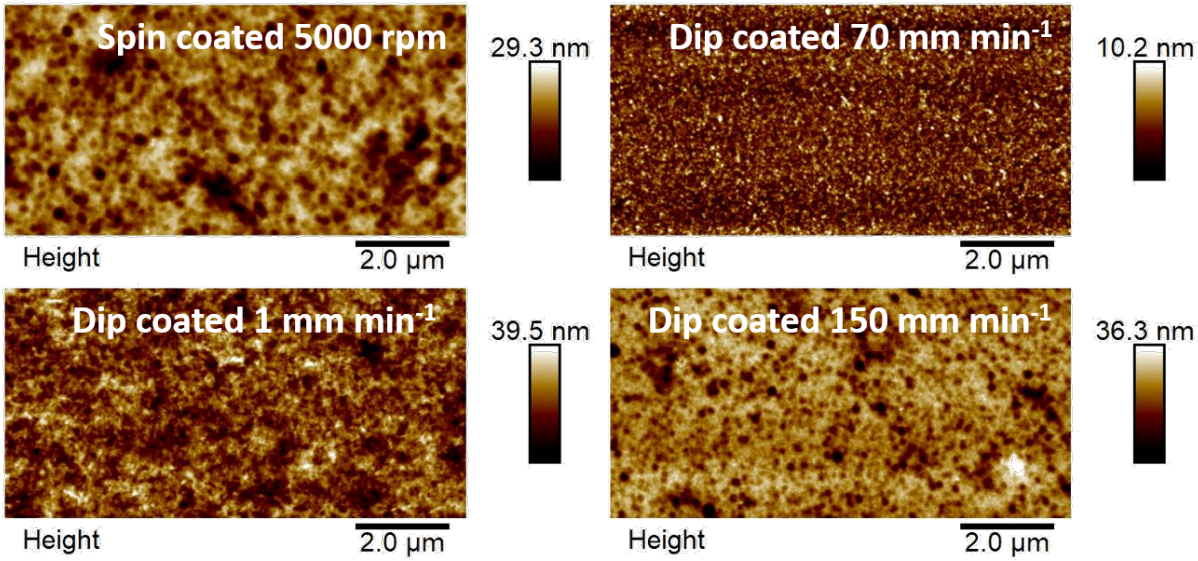

Figure 9.2.4: The AFM topologies of the selected pristine P3HT thin films coated from a 10 mg ml^{-1} P3HT in CF solution. The films were either spin coated with 5000 rpm (RMS: 4.2 nm), or dip coated with 1 (RMS: 6.1 nm), 70 (RMS: 1.8 nm), and 150 mm min^{-1} (RMS: 5.1 nm), as indicated in the figure. All images were take with a scan area of 10 μm $\times$ 5 μm. The corresponding amplitude images can be found in Figure A.14.2 in Section A.14. This figure was taken unmodified from Publication V with permission for usage granted by Advanced Electronic Materials.

than higher dip coating speeds, it should be noted that higher dip coating speeds have much lower film thicknesses, as shown in Figure 9.1.1 in Section 9.1. Hence, they have a worse signal-to-noise ratio than lower dip coating speeds.

Lastly, P3HT thin films were investigated using reflective PLM (see Section 3.3.5.5). Figure 9.2.6 and Figure A.14.3 in Section A.14 show typical results for P3HT in CF and ODCB, respectively. While some small-scale crystallization is visible, no long-range order or larger crystallites were found. The stripe structures perpendicular to the dip coating direction that were observed for both CF and ODCB at lower and intermediate dip coating speeds are height variations, as determined by surface characterization. This type of feature is not uncommon in dip coating; however, its origins remain largely unknown, as discussed in Chapter 5.

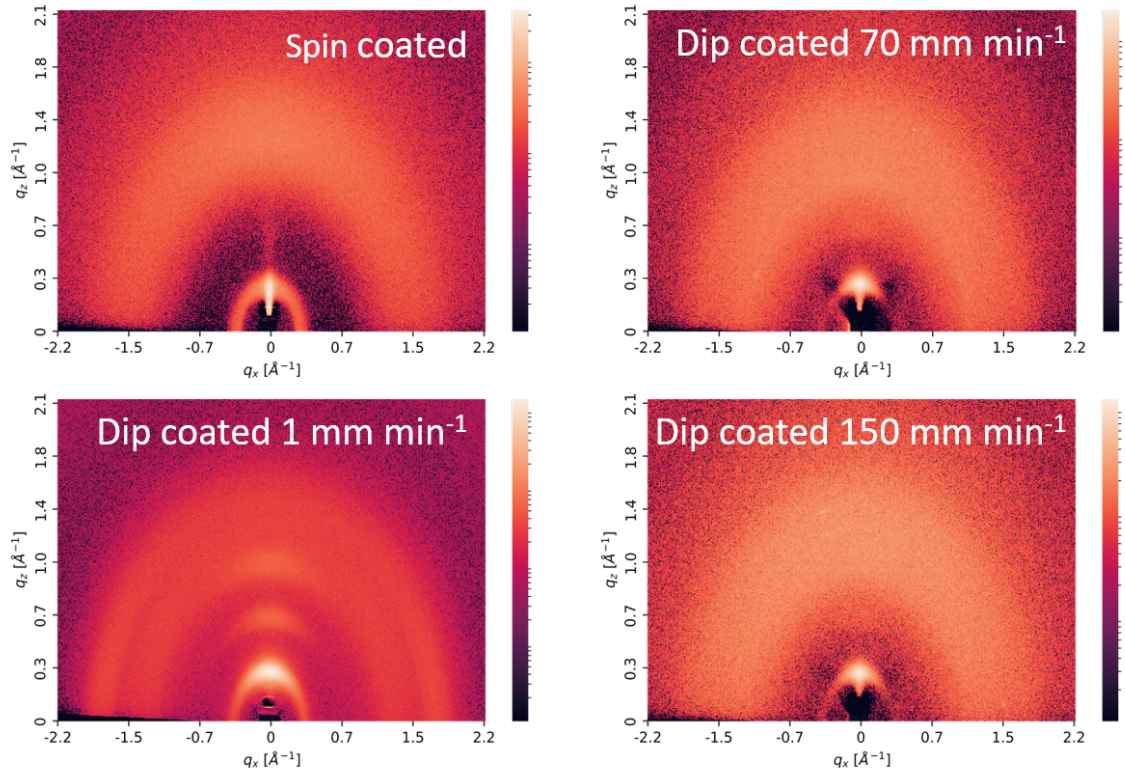

Figure 9.2.5: The 2D GIWAXS diffraction patterns of selected pristine P3HT samples spin and dip coated from a 10 mg ml^{-1} P3HT in CF solution. The films were either spin coated with 5000 rpm, or dip coated with 1, 70, and 150 mm min^{-1}, as indicated in the figure. The P3HT thin films were deposited on pure glass substrates without electrodes. The counts/intensities are on a logarithmic scale. This figure was taken unmodified from Publication V with permission for usage granted by Advanced Electronic Materials.

9.3 Thermoelectric characterization

The thermoelectric characterization of doped P3HT thin films entailed measuring their electrical conductivity and Seebeck coefficient. To optimize the figure of merit, the carrier concentration was varied to maximize the power factor. One general problem is that too little dopant results in under-doped thin films with low conductivity. On the other hand, too large an amount of F_4TCNQ negatively affects the morphology of the P3HT films and leads to F_4TCNQ aggregation. This prevents one from reaching higher conductivity [221, 223, 224]. After the dip coating process and evaporating the electrodes (or vice versa), the films were sequentially doped with F_4TCNQ at systematically varied F_4TCNQ doping concentrations and P3HT film thicknesses, and the electrical conductivity was measured. Figure 9.3.1 summarizes the findings.
Figure 9.3.1a shows the variation in the F_4TCNQ doping concentration for P3HT thin films

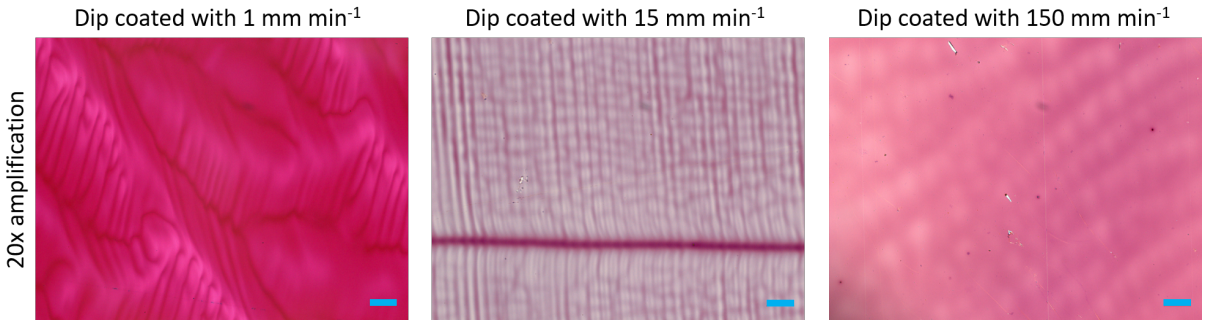

Figure 9.2.6: The reflective PLM images of three pristine P3HT thin film samples dip coated from a 10 mg ml^{-1} P3HT in CF solution. All images were taken with reflective PLM using crossed polarizers. The blue scale bars represent 50 μm. The dip coating direction was horizontal. The 1 mm min^{-1} dip coating speed is representative for films below 10 mm min^{-1}, as these films are relatively uneven. Intermediate dip coating speeds ($\approx 10 - 100$ mm min^{-1}) show two distinct features: hill-like stripe structures, which are significantly higher than the rest of the film and are parallel to the solution surface line, are most likely caused by meniscus defects; and flat film in between, as is visible at 15 mm min^{-1}. Lastly, films dip coated at dip coating speeds above 100 mm min^{-1} do not exhibit any pronounced structure and are relatively flat, as shown here for 150 mm min^{-1}. This figure was taken unmodified from the supporting information of Publication V with permission for usage granted by Advanced Electronic Materials.

spin coated at different speeds. Different spin coating speeds were used as a proxy for film thickness. A drop in electric conductivity was visible in the 5000 rpm and thinnest ($\approx$ 20 nm) spin-coated sample at a F4TCNQ doping concentration of $0.8 - 1.0$ mg ml^{-1}, which indicates over-doping of the P3HT thin film. Figures 9.3.1d-f further investigate the same F_4TCNQ doping concentrations and show the corresponding UV-vis absorption spectra. The thin films are clearly under-doped at concentrations below 0.8 mg ml^{-1} as seen by the continuously decreasing pristine P3HT absorption peak at $\approx$ 550 nm. No significant difference was observed between the 0.8 and 1.0 mg ml^{-1} F_4TCNQ doping concentrations. Additionally, Figure 9.3.1b shows the UV-vis absorbance spectra for the thinnest (5000 rpm) P3HT thin films at various F_4TCNQ doping concentrations. Over-doping of the P3HT thin film is apparent for F_4TCNQ doping concentrations greater than 1 mg ml^{-1}, as seen by the increasing shoulder/peak at $\approx$ 380 nm, which indicates non-ionized F_4TCNQ. Additionally, the influence of time on conductivity was investigated since time passes between sample preparation and electrical characterization. The doped P3HT samples de-dope over time; thus, a slightly higher F_4TCNQ doping concentration could be beneficial for achieving the optimum during thermoelectric measurements. Figure 9.3.1c shows the changes in electrical conductivity of P3HT doped with F_4TCNQ as a function of F_4TCNQ doping concentration over time. For the three time points investigated, the maximum electric conductivity is observed at 1 mg ml^{-1} F_4TCNQ doping concentration. Additionally,

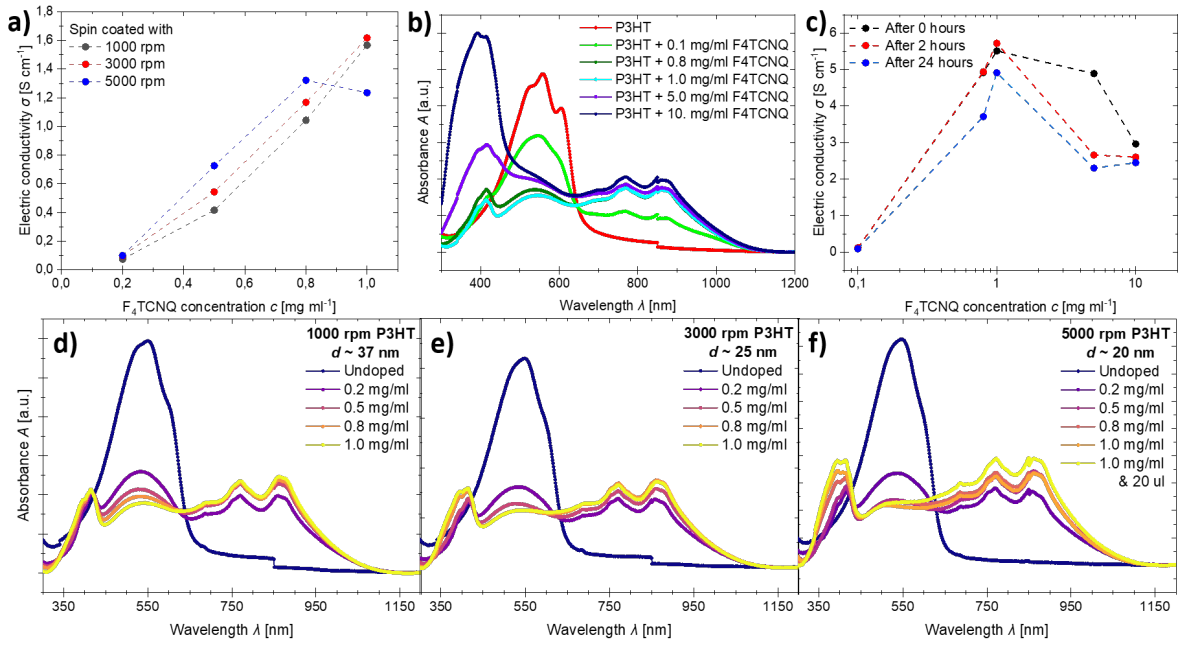

Figure 9.3.1: a) The electric conductivity σ of 1000 ($d \approx 37$ nm), 3000 ($d \approx 25$ nm), and 5000 ($d \approx 20$ nm) rpm spin-coated P3HT in CF samples as a function of F_4TCNQ doping concentration c. The amount of deposited F_4TCNQ solution was 90 μl in all cases. **b)** The UV-vis absorbance spectra of 5000 rpm spin-coated P3HT in ODCB thin films sequentially doped with different concentrations of 90 μl F_4TCNQ. **c)** The electric conductivity of the same samples as in (b), measured directly after sample fabrication, after two hours, and after 24 hours. **d-f)** UV-vis absorbance spectra of 1000 (d), 3000 (e), and 5000 (f) rpm spin-coated P3HT in CF thin films sequentially doped with different concentrations of 90 μl F_4TCNQ, except for one 5000 rpm measurement where 20 μl was used instead. Different spin coating speeds were used as a proxy for film thickness. This figure was taken slightly modified from the supporting information of Publication V with permission for usage granted by Advanced Electronic Materials.

conductivity barely changes during the first two hours after sample preparation for F_4TCNQ doping concentrations below or at 1 mg ml^{-1}.
Therefore, as indicated by the results in Figure 9.3.1, the maximum electrical conductivity is achieved at a doping concentration of $\approx$ 1 mg ml^{-1}, which seems to be the crossover between under- and over-doping for the investigated range of film thicknesses. Thus, a 1 mg ml^{-1} F_4TCNQ doping concentration was chosen for further investigation. In line with the structural characterization results, no significant or systematic anisotropy in conductivity or Seebeck coefficient was found.

Furthermore, the effect of the substrate and sample geometry on the thermoelectric properties was checked. Both silicon and glass substrates with both top and bottom electrodes were

used (see Section 3.1.3). While the measured conductivities and Seebeck coefficients varied among the samples, no trends were observed. Additionally, the variation measured was only slightly larger than that observed between samples with the same substrate and electrode geometry. Thus, no definitive statement could be made. These effects were not investigated further, and glass substrates with bottom electrodes were mostly used for the thermoelectric characterization.

Figure 9.3.2 summarizes the resulting thermoelectric properties of the P3HT thin films sequentially doped with F_4TCNQ as a function of dip coating speed. Only dip coating speeds above 10 mm min^{-1} are shown, as extracting reliable thermoelectric properties at lower dip coating speeds is challenging due to the decreased film flatness (see Figure 9.2.6 in Section 9.2). As the dip coating speed increases, the electrical conductivity decreases, while the Seebeck coefficient increases correspondingly (see Figure 9.3.2a). The resulting power factor (Figure 9.3.2b) shows a downward trend at lower dip coating speeds, dominated by dropping conductivity. There is then a leveling off, or even a slight increase, at dip coating speeds around or beyond the threshold velocity. This can be explained by the increasing Seebeck coefficient of the samples at higher withdrawal speeds. The data on the left side of the dashed lines displays the thermoelectric properties of multiple spin-coated films that serve as reference samples without preferential anisotropy. Varying the spin coating speed (1000, 3000, and 10000 rpm) matches the thickness of these reference samples to that of the dip-coated ones. Higher spin coating speeds lead to a slight improvement in overall thermoelectric efficiency. Figure A.14.4 in Section A.14 provides a direct comparison of the spin-coated samples and their thermoelectric properties.
To explain the modest thickness dependence of the thermoelectric performance of spin-coated thin films, it is assumed that, for P3HT chains, it is energetically favorable for them to adopt a specific orientation (edge-on or face-on) near the substrate surface depending on the substrate, solvent, and casting parameters. As the film's thickness increases, the orientation may transition to a more disordered mixed state [260, 261]. Increasing the spin coating speed reduces the film thickness and could increase the ratio of the oriented to non-oriented regions within the sample. This could explain the slight increase in power factor at higher spin coating speeds. Although spin-coated samples have comparatively high Seebeck coefficients, their low electrical conductivity results in low power factors, which are lower than those of better-performing dip-coated samples. Note that some of the latter films are substantially thicker than the spin-coated films (see Figure 9.1.1b in Section 9.1) and exhibit the opposite trend with thickness; that is, they have a higher power factor for thicker films. This rules out the possibility that the trends in Figure 9.3.2 are due to the same mechanism. One alternative explanation for the dependence of thermoelectric properties on dip coating speed that can be quickly ruled out is that thicker films contain lower dopant concentrations. This could occur, particularly when doping saturation is not reached during sequential doping, since an equal number of dopants is applied to all films. This would lead to lower electrical conductivity and higher Seebeck coefficients for thicker films at lower dip

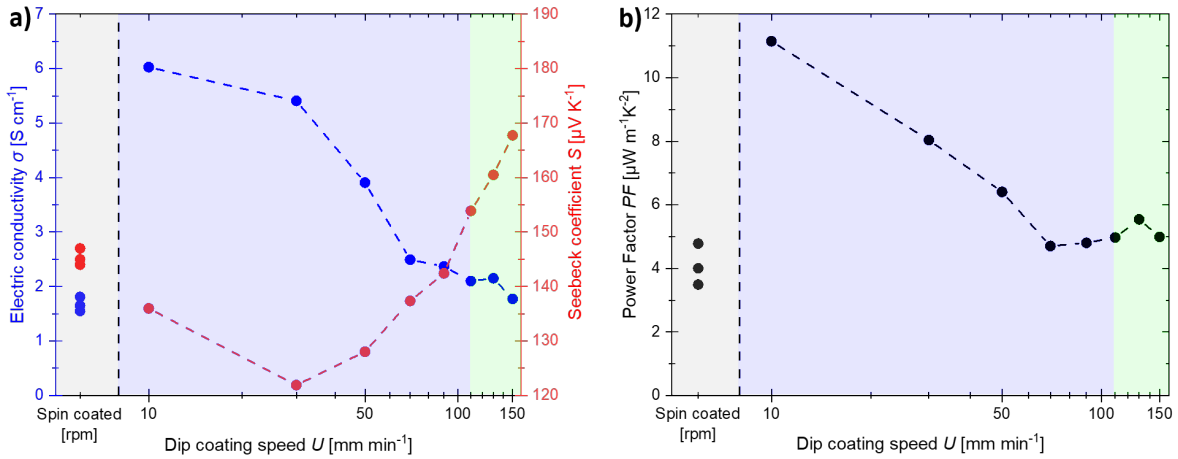

Figure 9.3.2: The thermoelectric properties of dip coated 10 mg ml^{-1} P3HT in CF sequentially doped with 1 mg ml^{-1} F_4TCNQ thin films as a function of dip coating speed U. For comparison, 1000, 3000, and 10000 rpm spin coated samples (gray) are shown. Both the evaporation and Landau-Levich regimes are highlighted in blue and green, respectively, as in Figure 9.1.1 in Section 9.1. **a)** Electric conductivity σ (blue) and Seebeck coefficient S (red); **b)** corresponding power factor PF. This figure was taken unmodified from Publication V with permission for usage granted by Advanced Electronic Materials.

coating speeds. However, the opposite trend is observed. Additionally, repeating the same measurements with several samples from the evaporation regime at higher doping concentrations (see Figure A.14.5 in Section A.14) shows the same pattern observed in Figure 9.3.2. Figure A.14.5 in Section A.14 also suggests that dip coating speeds below 10 mm min^{-1} do not lead to a further increase in power factor.

The monotonous increase in electrical conductivity with decreasing dip coating speed in the evaporation regime is attributed to increased order, as indicated by the UV-vis spectroscopy and GIWAXS data in Figures 9.2.1 and 9.2.5 in Section 9.2. This aligns with the fact that, in the evaporation regime, a withdrawal rate lower than the evaporation rate allows the formation of a well-defined meniscus (see Section 3.2.3). This leads to a film with more structural order due to the larger amount of time available for self-organization. Furthermore, the increase in crystallinity within the thin film due to meniscus behavior is independent of polymer orientation. It is reasonable to assume that a prolonged presence at the meniscus fosters an environment conducive to polymer self-organization. The corresponding decrease in the Seebeck coefficient reflects the common trade-off and can be attributed to fewer hard hops, probably inter-aggregate, in the percolating path. In contrast, no significant improvement in crystallization dependent on withdrawal speed is observed in the Landau-Levich regime because the withdrawal rates are much higher than the evaporation rate. Higher dip coating speeds result in thicker films and longer

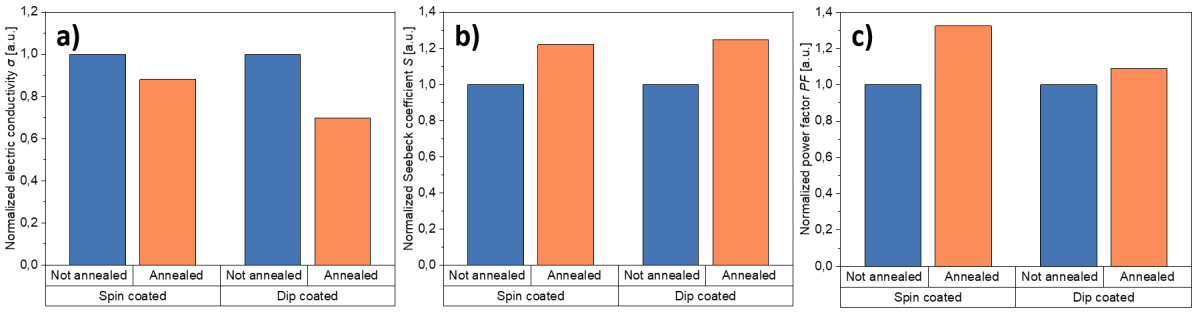

Figure 9.3.3: The **a)** electric conductivity σ, **b)** Seebeck coefficient S, and **c)** power factor PF of P3HT samples before and after annealing. The P3HT samples were either 3000 rpm spin coated or 10 mm min^{-1} dip coated, and sequentially doped with F_4TCNQ, respectively. The values of the thermoelectric parameters are normalized to their non-annealed values.

drying times; however, the associated drying times and the effect on thermoelectric performance are negligible compared to the evaporation regime.
In summary, the experiments suggest that dip coating did not align the P3HT films. Rather, the enhanced crystallinity of both thin and thick P3HT films appears to be the primary reason for the improved thermoelectric performance of dip-coated thin films. This raises the question of whether the same improvement could be achieved through thermal annealing, a process that also allows the P3HT chains to rearrange into a more ordered structure. To this end, the effects of annealing and dip coating on the thermoelectric efficiency of the P3HT films were compared. Figure 9.3.3 summarizes the findings and shows the thermoelectric parameters of both spin- and dip-coated P3HT samples normalized to their non-annealed values. The P3HT samples sequentially doped with F_4TCNQ were measured after sample fabrication. Then, the samples were annealed at 180 °C inside a glove box with a nitrogen atmosphere for ≈ 30 min, and measured again after cooling. In general, annealing the samples resulted in a slight decrease in conductivity and an increase in the Seebeck coefficient. This led to a slight improvement in the power factor for both the spin-coated and dip-coated samples. One possible explanation for this behavior comes from the fact that, in highly ordered organic materials (including P3HT), conductivity is limited by an energy offset (of ≈ 0.2 eV for P3HT) between the crystalline and amorphous phases (see Section 4.3.2). As shown in the unpublished work of M.Sc. Aditya Dash, a member of the research group, the crystallinity of the crystalline phase is expected to improve slightly when annealed, thereby increasing the barrier. Thus, the conductivity decreases and the Seebeck effect increases, which explains both the trends and relative differences shown in Figure 9.3.3.

Additional experiments were conducted to explore the potential for enhancing the thermoelectric performance of dip-coated P3HT films further. These experiments used Magic Blue (MB) as an alternative dopant. Samples that were sequentially doped with F_4TCNQ and MB were compared

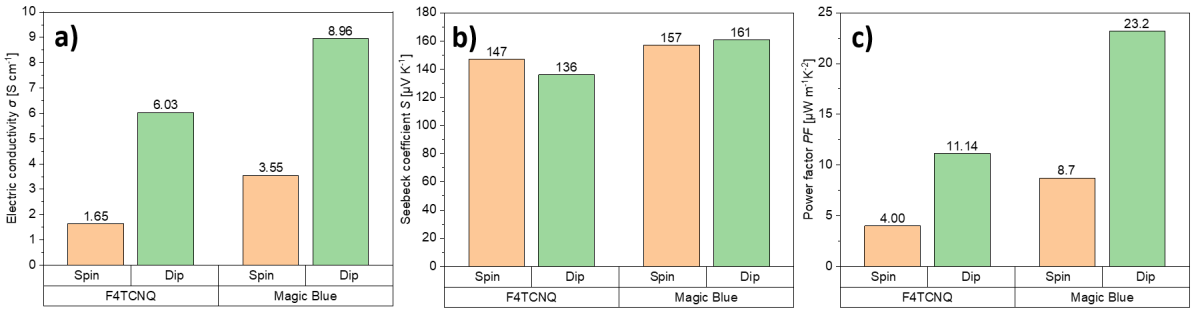

Figure 9.3.4: The **a)** electric conductivity σ, **b)** Seebeck coefficient S, and **c)** power factor PF of 3000 rpm spin-coated and 10 mm min^{-1} dip-coated P3HT samples sequentially doped with F_4TCNQ and MB, respectively. The power factor increases two to threefold with MB doping. This figure was taken unmodified from the supporting information of Publication V with permission for usage granted by Advanced Electronic Materials.

for both spin-coated and dip-coated films. A dip coating speed of 10 mm min^{-1} was chosen as the optimal dip coating speed for thermoelectric performance. As shown in Figure 9.3.4, the Seebeck coefficients remained similar, but the samples doped with MB displayed a significant increase in electrical conductivity. This resulted in power factors that were two to three times higher. While the absolute power factor values are lower than the highest values reported in studies using more elaborate alignment techniques (e.g., rubbing), the enhancement from F_4TCNQ to MB aligns well with previous findings [262, 263].

Compared to the original sequential doping method, in which the dopant solution is spin coated on the polymer film (see Section 3.1.3), sequential doping by dip coating provides greater control and potentially higher thermoelectric performance. Thus, the doping level in the P3HT films was precisely varied by controlling the dwell time in the MB solution. The maximum power factor obtained was ≈ 36 μW m^{-1} K^{-2} at a dwell time of ≈ 2 s, as shown in Figure 9.3.5. This represents a more than threefold enhancement over dip-coated films and is more than eight times higher than the standard spin-coated films sequentially doped with F_4TCNQ.

As discussed in Publication V, comparing the obtained data to literature data in terms of trends and absolute values of electrical conductivity, Seebeck coefficient, and power factor is challenging because dip coating is typically used to improve field effect mobility and on/off current ratios rather than thermoelectric properties. Nevertheless, Wang et al. compared the field effect mobility of dip-coated and spin-coated P3HT films in the same study and reported a two- to tenfold increase in mobility for dip-coated samples [257]. They measured samples at various dip coating speeds (around a few mm min^{-1}), but did not differentiate between different dip coating regimes. It is assumed that the improvement they reported likely occurred within the

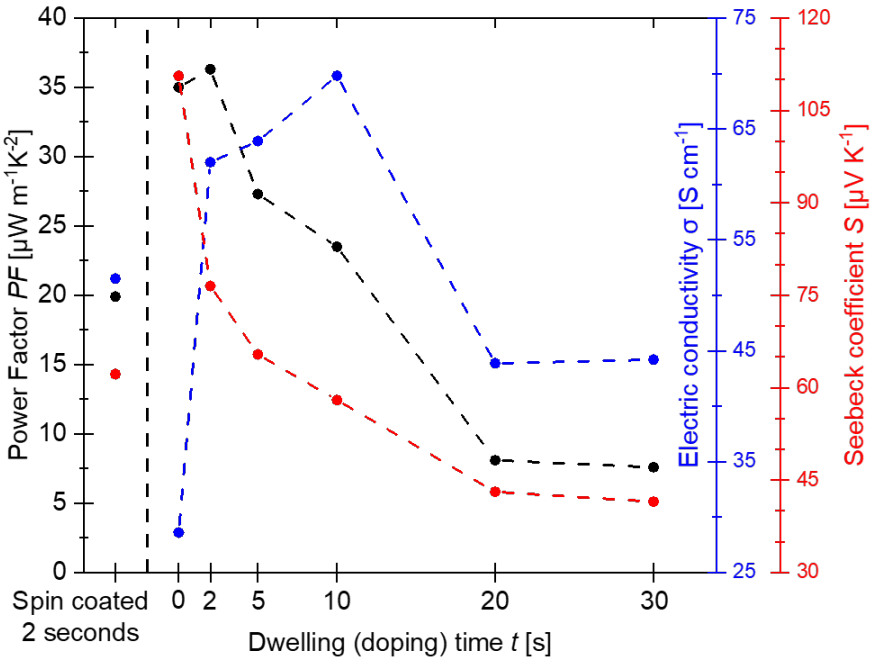

Figure 9.3.5: The thermoelectric properties of a 3000 rpm spin-coated and multiple 10 mm min^{-1} dip-coated P3HT thin films doped with MB as a function of the dwelling time t, which varies the doping concentration and excludes the time taken for immersion and withdrawal. The effective dwelling time of the spin-coated sample was $\approx$ 2 s. This figure was taken unmodified from the supporting information of Publication V with permission for usage granted by Advanced Electronic Materials.

evaporation regime. In this regime, they observed an increase in mobility as the dip coating speed decreased, followed by a drop at the lowest speeds, which aligns with the trends observed for electrical conductivity (see Figure A.14.4 in Section A.14). Moreover, Surin et al. examined the mobility of dip-coated, spin-coated, and drop-cast P3HT films as a function of solvent boiling point [264]. They found that dip-coated films only exhibited improved field effect mobility compared to spin-coated films when low-boiling-point solvents, such as CF, were used. This improvement supports the idea that lower dip coating speeds allow more time for structural order to form, unlike faster film fabrication processes, such as spin coating. While other reports describe improved mobility and crystallinity in dip-coated P3HT films [265, 266], the absence of a standard reference sample makes quantitative comparisons difficult in light of additional factors that may influence the results, including the molecular weight, polydispersity index (PDI), and regioregularity of the P3HT, the type and concentration of the solvent, and the nature of the substrate interface [256, 261].

Although research on improving the thermoelectric efficiency of P3HT films through dip coating is still on-going, the results presented in this section provide a valuable point of comparison with other well-established methods. For example, Hynynen et al. achieved a power factor of 3 μW m^{-1} K^{-2} by mechanically stretching free-standing P3HT films, which is approximately ten times lower than our best results [145]. Hamid-Sakr et al. demonstrated that high-temperature rubbing of spin-coated films can increase the power factor to 8 μW m^{-1} K^{-2} [267]. Similarly, Untilova et al. further improved the power factor to 56 μW m^{-1} K^{-2} by combining doctor blading and high-temperature rubbing [268]. In summary, the thermoelectric characteristics presented in this section, obtained without additional processing steps besides dip coating, surpass those previously obtained for solution-processed P3HT films in the absence of rubbing. This demonstrates the under-explored potential of dip coating as a simple method for producing high-performance thermoelectric thin films.

9.4 Conclusion

This chapter presented the effects of dip coating on the structural and thermoelectric properties of P3HT thin films. The film thickness of the dip-coated P3HT thin films was investigated as a function of the dip coating speed for different concentrations of P3HT. Dip coating speed ranged from 10 to 150 mm min^{-1} or 0.1 to 3.5 mm min^{-1} for CF or ODCB as solvents, respectively. In all cases, both the evaporation and the Landau-Levich were established, separated by a well-defined threshold speed of $\approx$ 110 or $\approx$ 0.7 mm min^{-1} for CF or ODCB, respectively. The threshold speeds were in good agreement between the experimental values and the theoretical predictions. Several pristine P3HT thin films dip-coated from a P3HT in CF solution at different speeds were investigated using UV-vis spectroscopy and compared to spin-coated films. No anisotropic alignment was found from dichroic ratios. Furthermore, the free exciton bandwidth was obtained from the spectra. The obtained values of $\approx 65-85$ meV agreed well with other similar results and suggested that dip coating generally introduces more aggregation into the film than spin coating does. AFM topologies did not reveal any structures or morphologies suggesting alignment. 2D GIWAXS measurements confirmed these findings, although a generally improved order in the film structure was established for the lowest dip coating speed of 10 mm min^{-1}. Additionally, PLM revealed no long-range order or larger crystallites in the dip-coated pristine P3HT thin films.
For thermoelectric characterization, dip-coated P3HT thin films were sequentially doped with either F_4TCNQ or MB. The F_4TCNQ doping concentration was varied to maximize thermoelectric performance, which was achieved at a doping concentration of $\approx$ 1 mg ml^{-1}. Electrical conductivity and Seebeck coefficient were measured for samples dip coated at varying speeds ($10-150$ mm min^{-1}) and sequentially doped with F_4TCNQ, and compared to spin-coated samples. The corresponding power factor was improved roughly threefold for the best sample, which was dip coated with 10 mm min^{-1}. This suggests that a lower dip coating speed leads to increased

order, which is consistent with the results of the structural investigation. Heating the samples only slightly improved the power factor for both spin- and dip-coated samples. Sequentially doping P3HT thin films with 1 mg ml^{-1} MB resulted in a significant increase in conductivity; meanwhile, the Seebeck coefficient remained similar for all samples. These results are similar to those obtained with F_4TCNQ as a dopant and yielded a roughly threefold increase in power factor in both spin- and dip-coated samples. Furthermore, using dip coating instead of sequential doping as a doping technique demonstrated an improvement in the thermoelectric properties by an additional $\approx 50\%$ for MB.

Although the obtained power factor values were smaller than those from sophisticated deposition and alignment methods, such as rubbing, the optimal dip coating speed yielded higher values than those reported in the literature for dip coating. This difference is attributed to the difference in the investigated parameter space (primarily dip coating speed). Therefore, dip coating is a potentially useful simple method for producing high-performance thermoelectric thin films.

Chapter 10

Conclusions

In this dissertation, the effects of structural disorder on electrical properties of molecular organic ferroelectrics and semiconductors were investigated. Structural disorder was introduced as an essential part of organic materials. The ferroelectric liquid crystal BTA, semicrystalline copolymer P(VDF:TrFE), and π-conjugated polymer P3HT were chosen as representatives of their respective organic material class for the investigations. The electrical properties for varied amount of disorder in the systems were measured both experimentally and using kMC simulations. In all systems, direct correlations between the disorder and thin film properties were established.

First, the effect of dip coating on the ferroelectric switching in columnar hexagonal liquid crystalline ferroelectric BTA was investigated. Dip-coated thin films were characterized and pronounced alignment of molecule clusters along the dip coating direction was established. The film thicknesses were investigated as a function of extraction speed and concentration. Although the power-law exponents differed from those reported previously, a clear qualitative change in the dip coating regimes was established, enabling the identification of Landau-Levich and evaporation regimes, which are separated by a well-defined threshold velocity. The ferroelectric switching was investigated for BTA thin films dip coated in the evaporation regime. A significantly earlier onset in ferroelectric switching for dip-coated samples was established compared to drop casting, regardless of dip coating direction or speed. This difference is attributed to the coexistence of macroscopically aligned domains with the orientation axis parallel to or perpendicular to the dip coating direction, occurring in a roughly 2:1 ratio. Comparing the temperature dependence of the ferroelectric switching for different coatings revealed that, for dip coating speed of 10 mm min^{-1} perpendicular to the electrode direction, the molecular alignment of as-cast films is equivalent to that of field-annealed films. This eliminates the need for post-deposition alignment steps. While not the focus of this study, there was no evidence suggesting that device degradation or fatigue depends on deposition conditions, which aligns with previous work on BTA, where degradation was found to be limited by electrode breakdown [79].

The BTA system was further studied by investigating Barkhausen noise during the ferroelectric switching using kMC numerical simulations. The simulations showed that the material exhibits critical behavior over long ranges of the event sizes at temperatures $T \lesssim 175$ K for a wide range of disorder parameters, though a minimum amount of disorder is required. Disorder in the system was varied by changing the subcolumn size and variation, corresponding to defect density, as well as the defect's nature. The resulting behavior is similar to that of a random field Ising model. The behavior of the system and changes in power-law exponents were investigated for a wide range of temperatures. At lower temperatures ($T \lesssim 175$ K) and (equivalently) higher driving frequencies, the extracted power-law exponents were similar to the mean-field predictions for self-organized criticality. Higher temperatures and lower driving frequencies led to larger values, indicating thermal creep: many switching events originated from thermal excitations rather than the driving field. Although the critical power-law exponents were affected to at least some degree by all the examined parameters, the changes were significant only outside the self-organized critical regime. This justifies the assumption of self-organized criticality in the simulated system. Measuring the Barkhausen noise of BTA experimentally was unsuccessful due to the small currents produced by the material during the switching process. This is in agreement with the event sizes expected based on the numerical simulations.

In contrast, Barkhausen noise associated with polarization reversal in thin-film P(VDF:TrFE) samples was successfully measured experimentally for various applied voltages and rise times. The obtained event size histograms were fitted using ML and LS fitting methods, and the power-law exponents were extracted. The exponents were consistently slightly higher with the ML method and were below or at the mean field value of 1.5 with both fitting methods. Decreasing the rise time and increasing the applied voltage both led to an increase in the extracted power-law exponents. These trends are consistent with the TA-NLS model. Based on these trends, it has been concluded that the system is not truly critically self-organized due to the lack of universal behavior. However, since the exponents for the fastest rise times and the highest applied voltages (i.e., voltages above the coercive field) were close to the mean field value, and since the corresponding distributions became more ideal, it seems that the system approached self-organized criticality under those conditions. For weaker and slower driving, however, the behavior is not universally self-organized; instead, it depends on variations in structural (dis)order that vary between samples and even during measurements. Lastly, mapping the measured Barkhausen noise directly onto the distribution of nucleation sites in the TA-NLS model was deemed impossible based on their magnitude. Instead, it is speculated that domain growth in P(VDF:TrFE) occurs through avalanches formed from a greater number of nucleation sites, whose interactions depend strongly on sample morphology and switching history.

Continuing with ferroelectricity, three TPA derivatives were investigated for ferroelectric behavior. Although extensive research using DS and DWM measurements revealed no indications for ferroelectric switching or dipolar activity, a considerable electrical conductivity was found and investigated. All TPA derivatives exhibited a significant increase in electrical conductivity over multiple orders of magnitude with temperature, as well as a permanently enhanced electrical conductivity after cooling back to room temperature. This temperature hysteretic behavior in electrical conductivity was concluded to relate to structural reordering at elevated temperatures. The similar behavior of the three TPA derivatives, which only exhibit quantitative differences, is consistent with the lack of differences found in AFM and XRD analyses. Minor changes in surface topography upon field annealing at elevated temperatures were observed by AFM and minor improvements in crystallinity were visible in 2D GIWAXS XRD measurements for all compounds.

Lastly, as a representative example of a semicrystalline π-conjugated polymer, dip coating of P3HT was systematically investigated, and the presence of both the evaporation and Landau-Levich regimes, as well as their dependence on parameters such as solvent type and concentration, was demonstrated. While previous research has mostly focused on a few low dip coating speeds (possibly in the evaporation regime, depending on the solution concentration chosen), this study specifically investigated the low-to-intermediate dip coating speeds at which the transition between the two dip coating regimes occurs. For optimized sequential doping, this study demonstrated major improvements in electrical conductivity and thermoelectric efficiency at lower withdrawal speeds. Structural and optical analyses indicated that there is little to no alignment in the investigated parameter space. Evidence of a predominant edge-on orientation with improved order comes from 2D GIWAXS diffraction patterns at the lowest investigated dip coating speeds. Overall, the improved thermoelectric performance at lower withdrawal speeds is attributed to improved structural order due to increasing drying time in the evaporation regime, which improves charge carrier transport within the aggregated and crystalline domains of P3HT. This finding is of particular interest for fabricating thicker P3HT films with improved electrical conductivity without elaborate post-deposition processing.

Chapter 11

Acknowledgments

This dissertation is the result of collaborative research conducted from 2022 to 2025 in the research group of Prof. Dr. Martijn Kemerink at the Institute for Molecular Systems Engineering and Advanced Materials (IMSEAM) at Heidelberg University (Germany). I would like to thank everyone who supported my studies and me personally during my promotion in physics. My deepest gratitude goes to

my supervisor, Prof. Dr. Martijn Kemerink, for giving me the opportunity to research organic electronics in his research group. I am grateful for his constant interest in my projects and his many helpful suggestions. His guidance was always helpful, steering me in the right direction while giving me enough freedom to explore on my own. I also appreciate his openness, kindness, and open-door policy.

Prof. Dr. Peer Fischer, for kindly taking over the position of second referee for this dissertation. I would also like to thank Prof. Dr. Tristan Bereau and Prof. Dr. Ulrich Uwer for participating in my defense as examiners of theoretical and experimental physics, respectively.

Dr. Dorothea Scheunemann, for her excellent care of the entire research group, her support, and her dedication to keeping the research group going.

Dr. Clemens Göhler, for his engagement in the research group, the many fruitful discussions, and his help with laboratory work, especially with electronics and Python programs.

all current and former members of AG Kemerink, for the valuable work-related discussions and the familiar research atmosphere. I am also thankful for the great times spent outside the office, no matter the activity. I would particularly like to thank Dr. Heiko Mager, a great SFB-1249 and ferroelectric colleague and my flatmate; M.Sc. Morteza Shokrani and M.Sc. Toni Seiler, with

whom I had great and fruitful collaborations on the joint projects; M.Sc. Anton Kompatscher and M.Sc. Priya Viji, for an amazing time outside of work; M.Sc. Maximilian Litterst, for scientific discussions, especially about ferroelectrics, and for being a nice office neighbor; M.Sc. Constantin Tormann, for his hands-on approach and help with mechanical tasks in the laboratories; Henna Tuikka-Graf, the research group secretary, for her excellent administrative support; Dr. Indre Urbanaviciute, for providing useful information and her valuable contributions to my project, even after her promotion ended; and Dr. Tim Cornelissen, for his helpful introduction when I started.

all current and former staff of IMSEAM, for their general help and organization, especially the administrative head of the IMSEAM core facility Dr. Olaf Skibbe, scientific coordinator and head of administration Fania Geiger, the technical staff including engineer Stefan Kauschke, engineers Lisa and Michael Kutek, Elisabeth Makosch, Anusha Sounder Rajan, and Ksenia Pavlova, IT representative Cornelius Bartosch, institute secretary Henrike Zimmermann, and (former) student assistants M.Sc. Tobias Krebs, B.Sc. Sebastian Klein, and B.Sc. Niclas Hofmann.

Dr. Ina Michalsky from the research group of Prof. Dr. Milan Kivala, for synthesizing the triphenylamines. I would also like to thank Dr. Ina Michalsky and Prof. Dr. Milan Kivala for collaborating with me on the SFB-1249 'N-Heteropolycycles as Functional Materials' project.

Dr. Bart Saes and Dr. Subham Bhattarcharjee from the research group of Prof. Dr. Rint P. Sijbesma at Eindhoven University of Technology (Netherlands), for synthesizing and sending the BTA molecules used in this dissertation.

my friends, especially my dearest friends Marcus Angermann and Benjamin Schmiedel, for their constant support and companionship.

my parents, who gave me continuous and unconditional support, and ultimately, the opportunity to achieve this.

Chapter 12

Author's publications and contributions

Author's publications during the promotion

I A. A. Butkevich, M. Kemerink, "Switching Behavior of Dip-Coated Organic Ferroelectric Trialkylbenzene-1,3,5-tricarboxamide (BTA)", *Advanced Materials Technologies* **2023**, 8, 2200500.

II A. A. Butkevich, F. T. Thome, T. Seiler, M. Hecker, M. Kemerink, "Barkhausen noise in the columnar hexagonal organic ferroelectric BTA", *Physical Chemistry Physical Physics* **2025**, 27, 12837-12847.

III A. A. Butkevich, M. Hecker, T. Seiler, M. Kemerink, "Barkhausen noise in the organic ferroelectric copolymer P(VDF:TrFE)", *Physical Chemistry Chemical Physics* **2025**, 27, 9637-9644.

IV H. Mager, A. A. Butkevich, S. V. Haridas, O. Shyshov, J. Borstelmann, I. Michalsky, M. Garcia-Iglesias, V. Rodriguez, D. Gonzalez-Rodriguez, A. R. A. Palmans, M. Kivala, M. von Delius, M. Kemerink, "Long-range electrical conductivity in non-π-conjugated organic molecular materials", *arXiv* **2025**, 2506.02673.

V M. Shokrani, A. A. Butkevich, M. Kemerink, "Improving the Thermoelectric Properties of Conjugated Polymer Thin Films by Dip Coating – but not through Alignment", *Advanced Electronic Materials* **2024**, 2400695.

Author's contributions to the publications

I Prepared the samples, performed both the structural and ferroelectric characterization, analyzed the data, wrote the manuscript.

II Partially performed and analyzed the simulation results, wrote the manuscript draft and revised it together with the co-authors.

III Supervised the co-authors during their project, helped with data analysis, wrote the manuscript draft and revised it together with the co-authors.

IV Prepared the TPA and BTA samples, performed both structural and ferroelectric characterization and dielectric spectroscopy measurements of the TPA derivatives, evaluated the 2D GIWAXS measurements, and provided the corresponding images for all materials, partly wrote the manuscript draft (only the TPA parts) and revised it together with the co-authors.

V Prepared the samples, performed the dip coating experiments and structural characterization, partly analyzed the data, together with M.Sc. Morteza Shokrani wrote the manuscript draft and revised it together with the co-authors. First co-authorship is shared with M.Sc. Morteza Shokrani.

Bibliography

[1] C. Brabec, U. Scherf, V. Dyakonov, *Organic Photovoltaics: Materials, Device Physics, and Manufacturing Technologies*, John Wiley & Sons, **2011**.

[2] I. Urbanaviciute, *Multifunctional Supramolecular Organic Ferroelectrics*, Linköping University Electronic Press, **2019**.

[3] T. Cornelissen, *Switching Kinetics and Charge Transport in Organic Ferroelectrics*, Linköping University Electronic Press, Linköping, **2020**.

[4] A. Pochettino, *Acad. Lincei Rend* **1906**, *15*, 355.

[5] C. K. Chiang, A. J. Heeger, A. G. Macdiarmid, *Berichte der Bunsengesellschaft für physikalische Chemie* **1979**, *83*, 407–417.

[6] Y.-W. Park, A. J. Heeger, M. A. Druy, A. G. MacDiarmid, *The Journal of Chemical Physics* **1980**, *73*, 946–957.

[7] K. Asadi in *Organic Ferroelectric Materials and Applications*, (Ed.: K. Asadi), Woodhead Publishing Series in Electronic and Optical Materials, Woodhead Publishing, **2022**, pp. xv–xvi.

[8] V. Coropceanu, J. Cornil, D. A. da Silva Filho, Y. Olivier, R. Silbey, J.-L. Brédas, *Chemical Reviews* **2007**, *107*, 926–952.

[9] A. M. Bagher, *International Journal of Sustainable and Green Energy* **2014**, *10*, 53–58.

[10] M. Mariello, K. Kim, K. Wu, S. P. Lacour, Y. Leterrier, *Advanced Materials* **2022**, *34*, 2201129.

[11] O. Ostroverkhova, *Chemical Reviews* **2016**, *116*, 13279–13412.

[12] J. Valasek, *Physical Review* **1921**, *17*, 475–481.

[13] H. Jaffe, *Journal of the American Ceramic Society* **1958**, *41*, 494–498.

[14] D. Damjanovic, *Reports on Progress in Physics* **1998**, *61*, 1267.

[15] G. H. Haertling, *Journal of the American Ceramic Society* **1999**, *82*, 797–818.

[16] M. Acosta, N. Novak, V. Rojas, S. Patel, R. Vaish, J. Koruza, G. A. Rossetti, Jr., J. Rödel, *Applied Physics Reviews* **2017**, *4*, 041305.

[17] J. F. Legrand, *Ferroelectrics* **1989**, *91*, 303–317.

[18] C. F. C. Fitié, W. S. C. Roelofs, M. Kemerink, R. P. Sijbesma, *Journal of the American Chemical Society* **2010**, *132*, 6892–6893.

[19] O. Knopfmacher, M. L. Hammock, A. L. Appleton, G. Schwartz, J. Mei, T. Lei, J. Pei, Z. Bao, *Nature Communications* **2014**, *5*, 2954.

[20] J.-H. Lee, H.-J. Yoon, T. Y. Kim, M. K. Gupta, J. H. Lee, W. Seung, H. Ryu, S.-W. Kim, *Advanced Functional Materials* **2015**, *25*, 3203–3209.

[21] X. Chen, X. Han, Q.-D. Shen, *Advanced Electronic Materials* **2017**, *3*, 1600460.

[22] K. S. Han, S. Lee, M. Kim, P. Park, M. H. Lee, J. Nah, *Advanced Functional Materials* **2019**, *29*, 1903633.

[23] T. Sekine, R. Sugano, T. Tashiro, J. Sato, Y. Takeda, H. Matsui, D. Kumaki, F. Domingues Dos Santos, A. Miyabo, S. Tokito, *Scientific Reports* **2018**, *8*, 4442.

[24] S. Jang, S. Jang, E.-H. Lee, M. Kang, G. Wang, T.-W. Kim, *ACS Applied Materials & Interfaces* **2019**, *11*, 1071–1080.

[25] A. Petritz, E. Karner-Petritz, T. Uemura, P. Schäffner, T. Araki, B. Stadlober, T. Sekitani, *Nature Communications* **2021**, *12*, 2399.

[26] M. A. Parvez Mahmud, N. Huda, S. H. Farjana, M. Asadnia, C. Lang, *Advanced Energy Materials* **2018**, *8*, 1701210.

[27] S. R. Forrest, *Nature* **2004**, *428*, 911–918.

[28] S. Y. Son, Y. Kim, J. Lee, G.-Y. Lee, W.-T. Park, Y.-Y. Noh, C. E. Park, T. Park, *Journal of the American Chemical Society* **2016**, *138*, 8096–8103.

[29] A. Nawaz, A. Kumar, I. A. Hümmelgen, *Organic Electronics* **2017**, *51*, 94–102.

[30] Z. Bao, A. Dodabalapur, A. J. Lovinger, *Applied Physics Letters* **1996**, *69*, 4108–4110.

[31] R. D. McCullough, *Advanced Materials* **1998**, *10*, 93–116.

[32] J.-M. Verilhac, G. LeBlevennec, D. Djurado, F. Rieutord, M. Chouiki, J.-P. Travers, A. Pron, *Synthetic Metals* **2006**, *156*, 815–823.

[33] J. S. J. S. Dugdale, *The Electrical Properties of Disordered Metals*, Cambridge University Press, **1995**.

[34] S. Baranovskii, O. Rubel in *Springer Handbook of Electronic and Photonic Materials*, (Eds.: S. Kasap, P. Capper), Springer International Publishing, Cham, **2017**, pp. 1–1.

[35] C. Kittel, P. McEuen, *Introduction to Solid State Physics*, John Wiley & Sons, **2018**.

[36] P. A. Lee, T. V. Ramakrishnan, *Reviews of Modern Physics* **1985**, *57*, 287–337.

[37] B. Kramer, A. MacKinnon, *Rep. Prog. Phys.* **1993**, *56*, 1469–1564.

[38] P. Sheng, B. van Tiggelen, *Waves in Random and Complex Media* **2007**, *17*, 235–237.

[39] N. Zhang, C. Gao, Y. Xiong, *Journal of Energy Chemistry* **2019**, *37*, 43–57.

[40] Z. Shi, M. Li, J. Sun, Z. Chen, *Advanced Energy Materials* **2021**, *11*, 2100332.

[41] C. A. Angell, K. L. Ngai, G. B. McKenna, P. F. McMillan, S. W. Martin, *Journal of Applied Physics* **2000**, *88*, 3113–3157.

[42] K. Binder, W. Kob, *Glassy Materials and Disordered Solids: An Introduction to Their Statistical Mechanics*, World Scientific, **2011**.

[43] D. Chen, H. Zhuang, M. Chen, P. Huang, V. Vlcek, Y. Jiao, *Disordered Hyperuniform Solid State Materials*, **2022**.

[44] M. Sahimi, *Applications Of Percolation Theory*, CRC Press, London, **1994**.

[45] S. J. Fonash, *Solar Cell Device Physics*, Elsevier, **2012**.

[46] N. R. Tummala, Z. Zheng, S. G. Aziz, V. Coropceanu, J.-L. Brédas, *The Journal of Physical Chemistry Letters* **2015**, *6*, 3657–3662.

[47] Z. Zheng, N. R. Tummala, T. Wang, V. Coropceanu, J.-L. Brédas, *Advanced Energy Materials* **2019**, *9*, 1803926.

[48] G. Kupgan, X.-K. Chen, J.-L. Brédas, *ACS Materials Letters* **2019**, *1*, 350–353.

[49] P. Reiser, M. Konrad, A. Fediai, S. Léon, W. Wenzel, P. Friederich, *Journal of Chemical Theory and Computation* **2021**, *17*, 3750–3759.

[50] T. Vehoff, Y. S. Chung, K. Johnston, A. Troisi, D. Y. Yoon, D. Andrienko, *The Journal of Physical Chemistry C* **2010**, *114*, 10592–10597.

[51] T. Vehoff, B. Baumeier, A. Troisi, D. Andrienko, *Journal of the American Chemical Society* **2010**, *132*, 11702–11708.

[52] J. D. Dunitz, A. Gavezzotti, *Chemical Society Reviews* **2009**, *38*, 2622–2633.

[53] B. Pinter, T. Fievez, F. M. Bickelhaupt, P. Geerlings, F. D. Proft, *Physical Chemistry Chemical Physics* **2012**, *14*, 9846–9854.

[54] T. T. Wang, J. M. Herbert, A. M. A. M. Glass, *The Applications of Ferroelectric Polymers*, Blackie and Chapman and Hall, **1988**.

[55] *Ferroelectric Polymers: Chemistry: Physics, and Applications*, (Ed.: H. S. Nalwa), CRC Press, Boca Raton, **1995**.

[56] K. Asadi, *Organic Ferroelectric Materials and Applications by Elsevier Science - Ebook | Scribd*.

[57] S. Horiuchi, Y. Tokura, *Nature Materials* **2008**, *7*, 357–366.

[58] L. Jin, F. Li, S. Zhang, *Journal of the American Ceramic Society* **2014**, *97*, 1–27.

[59] A. S. Tayi, A. Kaeser, M. Matsumoto, T. Aida, S. I. Stupp, *Nature Chemistry* **2015**, *7*, 281–294.

[60] J. F. Scott, *Ferroelectrics* **2016**, *503*, 117–132.

[61] H. Haken, H. C. Wolf, *Molekülphysik und Quantenchemie: Einführung in die experimentellen und theoretischen Grundlagen*, Dritte, überarbeitete und erweiterte Auflage, Springer, Berlin Heidelberg, **1998**.

[62] M. Trainer, *European Journal of Physics* **2000**, *21*, 459.

[63] M. Alguero, J. M. Gregg, L. Mitoseriu, *Nanoscale Ferroelectrics and Multiferroics: Key Processing and Characterization Issues, and Nanoscale Effects, 2 Volumes*, John Wiley & Sons, **2016**.

[64] K. Asadi in *Organic Ferroelectric Materials and Applications*, (Ed.: K. Asadi), Woodhead Publishing Series in Electronic and Optical Materials, Woodhead Publishing, **2022**, pp. 1–6.

[65] W. J. Merz, *Physical Review* **1953**, *91*, 513–517.

[66] S. Ducharme, A. V. Bune, L. M. Blinov, V. M. Fridkin, S. P. Palto, A. V. Sorokin, S. G. Yudin, *Physical Review B* **1998**, *57*, 25–28.

[67] R. BLINC, *Ferroelectrics* **2004**, *301*, 3–8.

[68] A. Bussmann-Holder, N. Dalal in *Ferro- and Antiferroelectricity: Order/Disorder versus Displacive*, (Eds.: N. S. Dalal, A. Bussmann-Holder), Springer, Berlin, Heidelberg, **2007**, pp. 1–21.

[69] M. E. Lines, A. M. Glass, *Principles and Applications of Ferroelectrics and Related Materials*, OUP Oxford, **2001**.

[70] M. Poulsen, S. Ducharme, *IEEE Transactions on Dielectrics and Electrical Insulation* **2010**, *17*, 1028–1035.

[71] C. Kittel, *Physical Review* **1951**, *82*, 729–732.

[72] S. T. LAGERWALL, *Ferroelectrics* **2004**, *301*, 15–45.

[73] C. F. Pulvari, *Physical Review* **1960**, *120*, 1670–1673.

[74] L. D. Landau, *Phys. Z. Sowjetunion* **1937**, *11*, 26–35.

[75] A. Devonshire, *The London Edinburgh and Dublin Philosophical Magazine and Journal of Science* **1949**, *40*, 1040–1063.

[76] P. Chandra, P. B. Littlewood in *Physics of Ferroelectrics*, *Vol. 105*, Springer Berlin Heidelberg, Berlin, Heidelberg, **2007**, pp. 69–116.

[77] V. M. Fridkin, S. Ducharme, *Physics of the Solid State* **2001**, *43*, 1320–1324.

[78] J. F. Scott, *Advanced Materials* **2010**, *22*, 5315–5317.

[79] I. Urbanaviciute, X. Meng, T. D. Cornelissen, A. V. Gorbunov, S. Bhattacharjee, R. P. Sijbesma, M. Kemerink, *Advanced Electronic Materials* **2017**, *3*, 1600530.

[80] S. Horiuchi, Y. Tokunaga, G. Giovannetti, S. Picozzi, H. Itoh, R. Shimano, R. Kumai, Y. Tokura, *Nature* **2010**, *463*, 789–792.

[81] S. Ducharme, V. M. Fridkin, A. V. Bune, S. P. Palto, L. M. Blinov, N. N. Petukhova, S. G. Yudin, *Physical Review Letters* **2000**, *84*, 175–178.

[82] G. Vizdrik, S. Ducharme, V. M. Fridkin, S. G. Yudin, *Physical Review B* **2003**, *68*, 094113.

[83] P. Wurfel, I. P. Batra, *Ferroelectrics* **1976**, *12*, 55–61.

[84] X. J. Lou, *Journal of Applied Physics* **2009**, *105*, 094107.

[85] T. Cornelissen, M. Kemerink in *Organic Ferroelectric Materials and Applications*, (Ed.: K. Asadi), Woodhead Publishing Series in Electronic and Optical Materials, Woodhead Publishing, **2022**, pp. 185–232.

[86] A. N. Kolmogorov, *Bull Acad Sci URSS (Cl Sci Math Nat)* **1937**, *3*, 335.

[87] M. Avrami, *The Journal of Chemical Physics* **1940**, *8*, 212–224.

[88] Y. Ishibashi, Y. Takagi, *Journal of the Physical Society of Japan* **1971**, *31*, 506–510.

[89] H. Orihara, S. Hashimoto, Y. Ishibashi, *Journal of the Physical Society of Japan* **1994**, *63*, 1031–1035.

[90] S. Hashimoto, H. Orihara, Y. Ishibashi, *Journal of the Physical Society of Japan* **1994**, *63*, 1601–1610.

[91] X. Du, I.-W. Chen, *MRS Online Proceedings Library (OPL)* **1997**, *493*, 311.

[92] S.-M. Nam, Y.-B. Kil, S. Wada, T. Tsurumi, *Japanese Journal of Applied Physics* **2003**, *42*, L1519.

[93] A. V. Gorbunov, T. Putzeys, I. Urbanavičiūtė, R. a. J. Janssen, M. Wübbenhorst, R. P. Sijbesma, M. Kemerink, *Physical Chemistry Chemical Physics* **2016**, *18*, 23663–23672.

[94] B. Alessandro, C. Beatrice, G. Bertotti, A. Montorsi, *Journal of Applied Physics* **1990**, *68*, 2901–2907.

[95] B. Alessandro, C. Beatrice, G. Bertotti, A. Montorsi, *Journal of Applied Physics* **1990**, *68*, 2908–2915.

[96] E. K. H. Salje, D. Xue, X. Ding, K. A. Dahmen, J. F. Scott, *Physical Review Materials* **2019**, *3*, 014415.

[97] F. Colaiori, *Advances in Physics* **2008**, *57*, 287–359.

[98] P. Cizeau, S. Zapperi, G. Durin, H. E. Stanley, *Physical Review Letters* **1997**, *79*, 4669–4672.

[99] M. Vopsaroiu, J. Blackburn, M. G. Cain, P. M. Weaver, *Physical Review B* **2010**, *82*, 024109.

[100] M. Vopsaroiu, P. M. Weaver, M. G. Cain, M. J. Reece, K. B. Chong, *IEEE Transactions on Ultrasonics Ferroelectrics and Frequency Control* **2011**, *58*, 1867–1873.

[101] A. V. Gorbunov, X. Meng, I. Urbanaviciute, T. Putzeys, M. Wübbenhorst, R. P. Sijbesma, M. Kemerink, *Physical Chemistry Chemical Physics* **2017**, *19*, 3192–3200.

[102] F. Preisach, *Zeitschrift für Physik* **1935**, *94*, 277–302.

[103] C. H. Tsang, B. Ploss, B. Ploss, F. G. Shin, *Ferroelectrics* **2001**, *259*, 139–144.

[104] L. Stoleriu, A. Stancu, L. Mitoseriu, D. Piazza, C. Galassi, *Physical Review B* **2006**, *74*, 174107.

[105] I. Urbanavičiūtė, T. D. Cornelissen, X. Meng, R. P. Sijbesma, M. Kemerink, *Nature Communications* **2018**, *9*, 4409.

[106] L. Cima, E. Laboure, P. Muralt, *Review of Scientific Instruments* **2002**, *73*, 3546–3552.

[107] Y. Kim, A. Kumar, O. Ovchinnikov, S. Jesse, H. Han, D. Pantel, I. Vrejoiu, W. Lee, D. Hesse, M. Alexe, S. V. Kalinin, *ACS Nano* **2012**, *6*, 491–500.

[108] Y. Kim, X. Lu, S. Jesse, D. Hesse, M. Alexe, S. V. Kalinin, *Advanced Functional Materials* **2013**, *23*, 3971–3979.

[109] T. D. Cornelissen, M. Biler, I. Urbanaviciute, P. Norman, M. Linares, M. Kemerink, *Physical Chemistry Chemical Physics* **2019**, *21*, 1375–1383.

[110] D. Zhao, I. Katsouras, K. Asadi, W. A. Groen, P. W. M. Blom, D. M. de Leeuw, *Applied Physics Letters* **2016**, *108*, 232907.

[111] V. Khikhlovskyi, A. V. Gorbunov, A. J. J. M. van Breemen, R. A. J. Janssen, G. H. Gelinck, M. Kemerink, *Organic Electronics* **2013**, *14*, 3399–3405.

[112] K. G. Wilson, *Scientific American* **1979**, *241*, 158–179.

[113] D. Sornette, *Critical Phenomena in Natural Sciences: Chaos, Fractals, Selforganization and Disorder: Concepts and Tools*, Springer Science & Business Media, **2006**.

[114] J. P. Sethna, K. A. Dahmen, C. R. Myers, *Nature* **2001**, *410*, 242–250.

[115] K. A. Dahmen, Y. Ben-Zion, J. T. Uhl, *Physical Review Letters* **2009**, *102*, 175501.

[116] K. A. Dahmen in *Avalanches in Functional Materials and Geophysics*, (Eds.: E. K. Salje, A. Saxena, A. Planes), Springer International Publishing, Cham, **2017**, pp. 19–30.

[117] H. J. Williams, W. Shockley, *Physical Review* **1949**, *75*, 178–183.

[118] E. K. Salje, K. A. Dahmen, *Annual Review of Condensed Matter Physics* **2014**, *5*, 233–254.

[119] G. Durin, S. Zapperi, *Journal of Statistical Mechanics: Theory and Experiment* **2006**, *2006*, P01002.

[120] M. Zaiser, B. Marmo, P. Moretti in Proceedings of International Conference on Statistical Mechanics of Plasticity and Related Instabilities — PoS(SMPRI2005), Sissa Medialab, Indian Institute of Science, Bangalore, India, **2006**, p. 053.

[121] P. Tückmantel, *Scanning Probe Studies of Structural and Functional Properties of Ferroelectric Domains and Domain Walls*, Springer Nature, **2021**.

[122] I. S. Baturin, M. V. Konev, A. R. Akhmatkhanov, A. I. Lobov, V. Ya. Shur, *Ferroelectrics* **2008**, *374*, 136–143.

[123] V. Ya. Shur, A. R. Akhmatkhanov, I. S. Baturin, E. V. Shishkina, *Journal of Applied Physics* **2012**, *111*, 014101.

[124] C. D. Tan, C. Flannigan, J. Gardner, F. D. Morrison, E. K. H. Salje, J. F. Scott, *Physical Review Materials* **2019**, *3*, 034402.

[125] B. Casals, G. F. Nataf, E. K. H. Salje, *Nature Communications* **2021**, *12*, 345.

[126] S. M. Sze, M. K. Lee, *Semiconductor Devices, Physics and Technology*, 3rd ed, Wiley, Hoboken, N.J, **2012**.

[127] A. Köhler, H. Bässler in *Electronic Processes in Organic Semiconductors*, John Wiley & Sons, Ltd, **2015**, Chapter 1, pp. 1–86.

[128] *Electronic Processes in Organic Electronics: Bridging Nanostructure, Electronic States and Device Properties*, (Eds.: H. Ishii, K. Kudo, T. Nakayama, N. Ueno), Springer Japan, Tokyo, **2015**.

[129] In *Organic Flexible Electronics*, (Eds.: P. Cosseddu, M. Caironi), Woodhead Publishing Series in Electronic and Optical Materials, Woodhead Publishing, **2021**, pp. i–iii.

[130] Linus. Pauling, *Journal of the American Chemical Society* **1931**, *53*, 1367–1400.

[131] B. A. Fox, M. L. Hartsell, D. M. Malta, H. A. Wynands, G. J. Tessmer, D. L. Dreifus, *MRS Online Proceedings Library* **1995**, *416*, 319–330.

[132] M. Schwoerer, H. C. Wolf, *Organic Molecular Solids*, John Wiley & Sons, **2007**.

[133] H. Bässler, *physica status solidi (b)* **1981**, *107*, 9–54.

[134] H. Baessler, *Physica Status Solidi B (Basic Research); (Germany)* **1993**, *175:1*, DOI `10.1002/pssb.2221750102`.

[135] A. V. Nenashev, J. O. Oelerich, S. D. Baranovskii, *Journal of Physics: Condensed Matter* **2015**, *27*, 093201.

[136] A. Miller, E. Abrahams, *Physical Review* **1960**, *120*, 745–755.

[137] V. Ambegaokar, B. I. Halperin, J. S. Langer, *Physical Review B* **1971**, *4*, 2612–2620.

[138] N. Felekidis, **2018**.

[139] H. Bässler, A. Köhler in *Unimolecular and Supramolecular Electronics I: Chemistry and Physics Meet at Metal-Molecule Interfaces*, (Ed.: R. M. Metzger), Springer, Berlin, Heidelberg, **2012**, pp. 1–65.

[140] R. A. Marcus, N. Sutin, *Biochimica et Biophysica Acta (BBA) - Reviews on Bioenergetics* **1985**, *811*, 265–322.

[141] Q.-Y. Li, Z.-F. Yao, Y. Lu, S. Zhang, Z. Ahmad, J.-Y. Wang, X. Gu, J. Pei, *Advanced Electronic Materials* **2020**, *6*, 2000080.

[142] Y.-H. Chang, S.-R. Tseng, C.-Y. Chen, H.-F. Meng, E.-C. Chen, S.-F. Horng, C.-S. Hsu, *Organic Electronics* **2009**, *10*, 741–746.

[143] E. Pascual-San-José, X. Rodríguez-Martínez, R. Adel-Abdelaleim, M. Stella, E. Martínez-Ferrero, M. Campoy-Quiles, *Journal of Materials Chemistry A* **2019**, *7*, 20369–20382.

[144] L. Biniek, S. Pouget, D. Djurado, E. Gonthier, K. Tremel, N. Kayunkid, E. Zaborova, N. Crespo-Monteiro, O. Boyron, N. Leclerc, S. Ludwigs, M. Brinkmann, *Macromolecules* **2014**, *47*, 3871–3879.

[145] J. Hynynen, E. Järsvall, R. Kroon, Y. Zhang, S. Barlow, S. R. Marder, M. Kemerink, A. Lund, C. Müller, *ACS macro letters* **2019**, *8*, 70–76.

[146] S. Nagamatsu, W. Takashima, K. Kaneto, Y. Yoshida, N. Tanigaki, K. Yase, K. Omote, *Macromolecules* **2003**, *36*, 5252–5257.

[147] M. Brinkmann, J.-C. Wittmann, *Advanced Materials* **2006**, *18*, 860–863.

[148] S. H. Eom, H. Park, S. H. Mujawar, S. C. Yoon, S.-S. Kim, S.-I. Na, S.-J. Kang, D. Khim, D.-Y. Kim, S.-H. Lee, *Organic Electronics* **2010**, *11*, 1516–1522.

[149] H. Zhou, S. Jiang, S. Yan, *The Journal of Physical Chemistry B* **2011**, *115*, 13449–13454.

[150] R. Runser, S. E. Root, D. E. Ober, K. Choudhary, A. X. Chen, C. Dhong, A. D. Urbina, D. J. Lipomi, *Chemistry of Materials* **2019**, *31*, 9078–9086.

[151] S. Hong, J. Lee, H. Kang, K. Lee, *Solar Energy Materials and Solar Cells* **2013**, *112*, 27–35.

[152] D. P. Birnie in *Sol-Gel Technologies for Glass Producers and Users*, (Eds.: M. A. Aegerter, M. Mennig), Springer US, Boston, MA, **2004**, pp. 49–55.

[153] A. G. Emslie, F. T. Bonner, L. G. Peck, *Journal of Applied Physics* **1958**, *29*, 858–862.

[154] D. Meyerhofer, *Journal of Applied Physics* **1978**, *49*, 3993–3997.

[155] M. Aegerter, M. Mennig, *Sol-Gel Technologies for Glass Producers and Users*, Kluwer Academic Publishers, **2004**.

[156] J. Puetz, M. A. Aegerter in *Sol-Gel Technologies for Glass Producers and Users*, (Eds.: M. A. Aegerter, M. Mennig), Springer US, Boston, MA, **2004**, pp. 37–48.

[157] T. Schneller, R. Waser, M. Kosec, D. Payne, *Chemical Solution Deposition of Functional Oxide Thin Films*, Springer, **2013**, p. 796.

[158] R. Z. Rogowski, A. A. Darhuber, *Langmuir* **2010**, *26*, 11485–11493.

[159] R. Z. Rogowski, A. Dzwilewski, M. Kemerink, A. A. Darhuber, *The Journal of Physical Chemistry C* **2011**, *115*, 11758–11762.

[160] E. Rio, F. Boulogne, *Advances in Colloid and Interface Science*, Dominique Langevin Festschrift: Four Decades Opening Gates in Colloid and Interface Science **2017**, *247*, 100–114.

[161] J. Griffin, A. J. Pearson, N. W. Scarratt, T. Wang, A. D. F. Dunbar, H. Yi, A. Iraqi, A. R. Buckley, D. G. Lidzey, *Organic Electronics* **2015**, *21*, 216–222.

[162] L. E. Scriven, *MRS Online Proceedings Library* **1988**, *121*, 717–729.

[163] P. R. Schunk, A. J. Hurd, C. J. Brinker in *Liquid Film Coating: Scientific Principles and Their Technological Implications*, (Eds.: S. F. Kistler, P. M. Schweizer), Springer Netherlands, Dordrecht, **1997**, pp. 673–708.

[164] L. Landau, V. Levich, *Acta Physicochimica U.R.S.S.* **1942**, *Vol. 17*, pp. 42–54.

[165] B. V Derjaguin, T. N Voropayeva, *Journal of Colloid Science* **1964**, *19*, 113–135.

[166] L. F. Coating, Scientific Principles and Their Technological Implications, ; Kistler, SF, Schweizer, PM, Eds, **1997**.

[167] J. M. Davis, S. M. Troian, *Physics of Fluids* **2005**, *17*, 072103.

[168] A. Darhuber, S. Troian, J. Davis, S. Miller, S. Wagner, *Journal of Applied Physics* **2000**, *88*, 5119–5126.

[169] M. Sarkar, M. Hasanuzzaman, F. Gulshan, A. Rashid, **2022**.

[170] M. A. Hubbe, A. A. Koukoulas, *BioResources* **2016**, *11*.

[171] M. Le Berre, Y. Chen, D. Baigl, *Langmuir* **2009**, *25*, 2554–2557.

[172] H. Y. Erbil, *Advances in Colloid and Interface Science* **2012**, *170*, 67–86.

[173] J. F. Scott, *Journal of Physics: Condensed Matter* **2007**, *20*, 021001.

[174] A. Gorbunov, *Ferroelectric Switching Phenomena in Organic Dielectrics and Semiconductors*, Technische Universiteit Eindhoven, **2018**.

[175] T. J. Seebeck, *Annalen der Physik* **1826**, *82*, 253–286.

[176] J. Martin, *Measurement Science and Technology* **2013**, *24*, 085601.

[177] G. Zhang, C. Xie, P. You, S. Li in *Introduction to Organic Electronic Devices*, (Eds.: G. Zhang, C. Xie, P. You, S. Li), Springer Nature, Singapore, **2022**, pp. 235–259.

[178] J. Martin, T. Tritt, C. Uher, *Journal of Applied Physics* **2010**, *108*, 121101.

[179] C. Wang, F. Chen, K. Sun, R. Chen, M. Li, X. Zhou, Y. Sun, D. Chen, G. Wang, *Review of Scientific Instruments* **2018**, *89*, 101501.

[180] H. Wang, J.-H. Hsu, S.-I. Yi, S. L. Kim, K. Choi, G. Yang, C. Yu, *Advanced Materials* **2015**, *27*, 6855–6861.

[181] T. Miao, W. Ma, X. Zhang, *Journal of Vacuum Science & Technology B* **2012**, *30*, 051804.

[182] *Fundamentals of Heat and Mass Transfer*, 7th ed, (Eds.: T. L. Bergman, F. P. Incropera), Wiley, Hoboken, NJ, **2011**.

[183] A. A. Bunaciu, U., Elena gabriela, H. Y. and Aboul-Enein, *Critical Reviews in Analytical Chemistry* **2015**, *45*, 289–299.

[184] I. Urbanaviciute, X. Meng, M. Biler, Y. Wei, T. D. Cornelissen, S. Bhattacharjee, M. Linares, M. Kemerink, *Materials Horizons* **2019**, *6*, 1688–1698.

[185] S. Horiuchi, K. Kobayashi, R. Kumai, S. Ishibashi, *Nature Communications* **2017**, *8*, 14426.

[186] A. S. Tayi, A. K. Shveyd, A. C.-H. Sue, J. M. Szarko, B. S. Rolczynski, D. Cao, T. J. Kennedy, A. A. Sarjeant, C. L. Stern, W. F. Paxton, W. Wu, S. K. Dey, A. C. Fahrenbach, J. R. Guest, H. Mohseni, L. X. Chen, K. L. Wang, J. F. Stoddart, S. I. Stupp, *Nature* **2012**, *488*, 485–489.

[187] R. A. Wiscons, N. R. Goud, J. T. Damron, A. J. Matzger, *Angewandte Chemie* **2018**, *130*, 9182–9185.

[188] E. Priestly, *Introduction to Liquid Crystals*, Springer Science & Business Media, **2012**.

[189] I.-C. Khoo, *Liquid Crystals*, John Wiley & Sons, **2022**.

[190] S. Cantekin, T. F. A. de Greef, A. R. A. Palmans, *Chemical Society Reviews* **2012**, *41*, 6125–6137.

[191] P. J. M. Stals, J. C. Everts, R. de Bruijn, I. A. W. Filot, M. M. J. Smulders, R. Martín-Rapún, E. A. Pidko, T. F. A. de Greef, A. R. A. Palmans, E. W. Meijer, *Chemistry – A European Journal* **2010**, *16*, 810–821.

[192] K. K. Bejagam, G. Fiorin, M. L. Klein, S. Balasubramanian, *The Journal of Physical Chemistry B* **2014**, *118*, 5218–5228.

[193] C. F. C. Fitié, W. S. C. Roelofs, P. C. M. M. Magusin, M. Wübbenhorst, M. Kemerink, R. P. Sijbesma, *The Journal of Physical Chemistry B* **2012**, *116*, 3928–3937.

[194] A. L. Sobolewski, *Physical Chemistry Chemical Physics* **2015**, *17*, 20580–20587.

[195] M. Wawrzyniak-Adamczewska, M. Wierzbowska, *The Journal of Physical Chemistry C* **2016**, *120*, 7748–7756.

[196] P. Masiak, M. Wierzbowska, *Journal of Materials Science* **2017**, *52*, 4378–4388.

[197] T. Li, X. Li, J. Wang, H. Ågren, X. Ma, H. Tian, *Advanced Optical Materials* **2016**, *4*, 840–847.

[198] C. Gillespie, Does Viscosity Increase With The Size Of The Molecule?, https://www.sciencing.com/viscosity increase-size-molecule-13388/, **2018**.

[199] D. Mao, B. Gnade, M. Quevedo-Lopez in **2011**.

[200] A. V. Gorbunov, M. Garcia Iglesias, J. Guilleme, T. D. Cornelissen, W. S. C. Roelofs, T. Torres, D. González-Rodríguez, E. W. Meijer, M. Kemerink, *Science Advances* **2017**, *3*, e1701017.

[201] N. M. Casellas, I. Urbanaviciute, T. D. Cornelissen, J. Augusto Berrocal, T. Torres, M. Kemerink, M. García-Iglesias, *Chemical Communications* **2019**, *55*, 8828–8831.

[202] Y. Liu, H. Aziguli, B. Zhang, W. Xu, W. Lu, J. Bernholc, Q. Wang, *Nature* **2018**, *562*, 96–100.

[203] A. J. Lovinger, *Macromolecules* **1982**, *15*, 40–44.

[204] J. Martín, D. Zhao, T. Lenz, I. Katsouras, D. M. de Leeuw, N. Stingelin, *Materials Horizons* **2017**, *4*, 408–414.

[205] T. Furukawa, M. Date, E. Fukada, *Journal of Applied Physics* **1980**, *51*, 1135–1141.

[206] T. Furukawa, G. E. Johnson, *Applied Physics Letters* **1981**, *38*, 1027–1029.

[207] T. Furukawa, *IEEE Transactions on Electrical Insulation* **1989**, *24*, 375–394.

[208] G. Teyssedre, A. Bernes, C. Lacabanne, *Journal of Polymer Science Part B: Polymer Physics* **1995**, *33*, 879–890.

[209] V. Faramarzi, F. Niess, E. Moulin, M. Maaloum, J.-F. Dayen, J.-B. Beaufrand, S. Zanettini, B. Doudin, N. Giuseppone, *Nature chemistry* **2012**, *4*, 485–490.

[210] A. Akande, S. Bhattacharya, T. Cathcart, S. Sanvito, *The Journal of Chemical Physics* **2014**, *140*, 074301.

[211] D. C. Hoesterey, G. M. Letson, *The Journal of Chemical Physics* **1964**, *41*, 675–679.

[212] Z. Ning, H. Tian, *Chemical Communications* **2009**, 5483–5495.

[213] G. Wu, Y. Zhang, R. Kaneko, Y. Kojima, K. Sugawa, A. Islam, J. Otsuki, S. Liu, *Synthetic Metals* **2020**, *261*, 116323.

[214] F. Rezaei, A. Mohajeri, *Solar Energy* **2021**, *221*, 536–544.

[215] M. Hao, D. Tan, W. Chi, Z.-s. Li, *Physical Chemistry Chemical Physics* **2022**, *24*, 4635–4643.

[216] Q.-M. Koh, N. S. Mazlan, Q.-J. Seah, J.-C. Yang, Y.-J. Chen, R.-Q. Png, P. K. H. Ho, L.-L. Chua, *ACS Applied Materials & Interfaces* **2024**, *16*, 39708–39716.

[217] A. D. Printz, D. J. Lipomi, *Applied Physics Reviews* **2016**, *3*, 021302.

[218] J. Lenz, R. T. Weitz, *APL Materials* **2021**, *9*, 110902.

[219] D. Scheunemann, V. Vijayakumar, H. Zeng, P. Durand, N. Leclerc, M. Brinkmann, M. Kemerink, *Advanced Electronic Materials* **2020**, *6*, 2000218.

[220] J. Wu, G. Yue, Y. Xiao, J. Lin, M. Huang, Z. Lan, Q. Tang, Y. Huang, L. Fan, S. Yin, T. Sato, *Scientific Reports* **2013**, *3*, 1283.

[221] D. T. Duong, C. Wang, E. Antono, M. F. Toney, A. Salleo, *Organic Electronics* **2013**, *14*, 1330–1336.

[222] R. Gironda, L. Miozzo, D. Tondelier, M. Chaigneau, J. Ghabboun, M. Faroun, A. Papagni, M. M. Salamone, R. Ruffo, A. Yassar, *Organic Photonics and Photovoltaics* **2013**, *1*, DOI 10.2478/oph-2013-0004.

[223] G. Zuo, Z. Li, O. Andersson, H. Abdalla, E. Wang, M. Kemerink, *The Journal of Physical Chemistry C* **2017**, *121*, 7767–7775.

[224] G. Zuo, O. Andersson, H. Abdalla, M. Kemerink, *Applied Physics Letters* **2018**, *112*, 083303.

[225] Y. Zhong, V. Untilova, D. Muller, S. Guchait, C. Kiefer, L. Herrmann, N. Zimmermann, M. Brosset, T. Heiser, M. Brinkmann, *Advanced Functional Materials* **2022**, *32*, 2202075.

[226] Z. Molenda, G. Wantz, S. Chambon, D. M. Bassani, L. Hirsch, *Journal of Materials Chemistry C* **2024**, *12*, 16999–17004.

[227] S. Zhang, H. M. Hill, K. Moudgil, C. A. Richter, A. R. Hight Walker, S. Barlow, S. R. Marder, C. A. Hacker, S. J. Pookpanratana, *Advanced Materials* **2018**, *30*, 1802991.

[228] J.-K. Kim, K. Cho, J. Jang, K.-Y. Baek, J. Kim, J. Seo, M. Song, J. Shin, J. Kim, S. S. P. Parkin, J.-H. Lee, K. Kang, T. Lee, *Advanced Materials* **2021**, *33*, 2101598.

[229] A. Köhler, H. Bässler.

[230] V. Untilova, H. Zeng, P. Durand, L. Herrmann, N. Leclerc, M. Brinkmann, *Macromolecules* **2021**, *54*, 6073–6084.

[231] F. Aparicio, F. García, L. Sánchez, *Chemistry – A European Journal* **2013**, *19*, 3239–3248.

[232] M. B. Baker, L. Albertazzi, I. K. Voets, C. M. A. Leenders, A. R. A. Palmans, G. M. Pavan, E. W. Meijer, *Nature Communications* **2015**, *6*, 6234.

[233] M. Garzoni, M. B. Baker, C. M. A. Leenders, I. K. Voets, L. Albertazzi, A. R. A. Palmans, E. W. Meijer, G. M. Pavan, *Journal of the American Chemical Society* **2016**, *138*, 13985–13995.

[234] T. D. Cornelissen, I. Urbanaviciute, M. Kemerink, *Physical Review B* **2020**, *101*, 214301.

[235] M. P. Lightfoot, F. S. Mair, R. G. Pritchard, J. E. Warren, *Chemical Communications* **1999**, *0*, 1945–1946.

[236] P. J. M. Stals, M. M. J. Smulders, R. Martín-Rapún, A. R. A. Palmans, E. W. Meijer, *Chemistry – A European Journal* **2009**, *15*, 2071–2080.

[237] C. Kulkarni, E. W. Meijer, A. R. A. Palmans, *Accounts of Chemical Research* **2017**, *50*, 1928–1936.

[238] B. A. GIL-VILLEGAS, S. C. McGROTHER and GEORGE JACKSON, *Molecular Physics* **1997**, *92*, 723–734.

[239] B. Casals, G. F. Nataf, D. Pesquera, E. K. H. Salje, *APL Materials* **2020**, *8*, 011105.

[240] P. Tückmantel, I. Gaponenko, N. Caballero, J. C. Agar, L. W. Martin, T. Giamarchi, P. Paruch, *Physical Review Letters* **2021**, *126*, 117601.

[241] J. P. Sethna, K. A. Dahmen, O. Perkovic, Random-Field Ising Models of Hysteresis, Comment: For inclusion in a book "The Science of Hysteresis, Vol. II", edited by Giorgio Bertotti and I. Mayergoyz, **2005**.

[242] M. Mai, H. Kliem, *Journal of Applied Physics* **2013**, *114*, 224104.

[243] N. Meng, R. Mao, W. Tu, X. Zhu, R. M. Wilson, E. Bilotti, M. J. Reece, *Polymer* **2016**, *100*, 69–76.

[244] W. J. Hu, D.-M. Juo, L. You, J. Wang, Y.-C. Chen, Y.-H. Chu, T. Wu, *Scientific Reports* **2014**, *4*, 4772.

[245] R. Hasegawa, M. Kobayashi, H. Tadokoro, *Polymer Journal* **1972**, *3*, 591–599.

[246] M. Kühn, H. Kliem, *physica status solidi (b)* **2008**, *245*, 213–223.

[247] S. Akahane, T. Takeda, N. Hoshino, T. Akutagawa, *Crystal Growth & Design* **2018**, *18*, 6284–6292.

[248] D. Qu, E. Ramé, S. Garoff, *Physics of Fluids* **2002**, *14*, 1154–1165.

[249] X. Gao, Y.-c. Han, *Chinese Journal of Polymer Science* **2013**, *31*, 610–619.

[250] J. Hynynen, D. Kiefer, L. Yu, R. Kroon, R. Munir, A. Amassian, M. Kemerink, C. Müller, *Macromolecules* **2017**, *50*, 8140–8148.

[251] X. Wang, Y. Zhu, Z. Liu, Y. Yuan, L. Qiu, *Advanced Electronic Materials* **2021**, *7*, 2100591.

[252] V. Chaudhary, R. K. Pandey, R. Prakash, A. Singh, *Journal of Applied Physics* **2017**, *122*, 225501.

[253] L. Li, G. Lu, X. Yang, *Journal of Materials Chemistry - J MATER CHEM* **2008**, *18*, DOI 10.1039/b719945g.

[254] E. González-Juárez, E. García-Hernández, C. D. Arrieta-González, R. Salgado-Delgado, M. Güizado-Rodríguez, V. Barba, A. Espinosa-Roa, *Polymer Bulletin* **2021**, *78*, 6455–6472.

[255] F. C. Spano, *The Journal of Chemical Physics* **2005**, *122*, 234701.

[256] D. Kajiya, S. Ozawa, T. Koganezawa, K.-i. Saitow, *The Journal of Physical Chemistry C* **2015**, *119*, 7987–7995.

[257] G. Wang, T. Hirasa, D. Moses, A. J. Heeger, *Synthetic Metals* **2004**, *146*, 127–132.

[258] S. Cho, K. Lee, J. Yuen, G. Wang, D. Moses, A. J. Heeger, M. Surin, R. Lazzaroni, *Journal of Applied Physics* **2006**, *100*, 114503.

[259] L. Xue, X. Gao, K. Zhao, J. Liu, X. Yu, Y. Han, *Nanotechnology* **2010**, *21*, 145303.

[260] S. Joshi, S. Grigorian, U. Pietsch, P. Pingel, A. Zen, D. Neher, U. Scherf, *Macromolecules* **2008**, *41*, 6800–6808.

[261] M. Brinkmann, *Journal of Polymer Science Part B: Polymer Physics* **2011**, *49*, 1218–1233.

[262] A. Dash, S. Guchait, D. Scheunemann, V. Vijayakumar, N. Leclerc, M. Brinkmann, M. Kemerink, *Advanced Materials* **2024**, *36*, 2311303.

[263] S. Guchait, A. Dash, A. Lemaire, L. Herrmann, M. Kemerink, M. Brinkmann, *Advanced Functional Materials* **2024**, *34*, 2404411.

[264] M. Surin, P. Leclère, R. Lazzaroni, J. Yuen, G. Wang, D. Moses, A. Heeger, S. Cho, K. Lee, *Journal of Applied Physics* **2006**, *100*, DOI 10.1063/1.2222065.

[265] G. W. Kim, E. H. Kwon, M. Kim, Y. D. Park, *The Journal of Physical Chemistry C* **2019**, *123*, 23255–23263.

[266] K. Ali, U. Pietsch, S. Grigorian, *Journal of Applied Crystallography* **2013**, *46*, 908–911.

[267] A. Hamidi-Sakr, L. Biniek, J.-L. Bantignies, D. Maurin, L. Herrmann, N. Leclerc, P. Lévêque, V. Vijayakumar, N. Zimmermann, M. Brinkmann, *Advanced Functional Materials* **2017**, *27*, 1700173.

[268] V. Untilova, T. Biskup, L. Biniek, V. Vijayakumar, M. Brinkmann, *Macromolecules* **2020**, *53*, 2441–2453.

[269] J. Oberländer, Z. B. Jildeh, P. Kirchner, L. Wendeler, A. Bromm, H. Iken, P. Wagner, M. Keusgen, M. J. Schöning, *Sensors* **2015**, *15*, 26115–26127.

[270] R. Nigon, T. M. Raeder, P. Muralt, *Journal of Applied Physics* **2017**, *121*, 204101.

[271] K. J. Latimer, J. W. Evans, M. A. Cowell, P. K. Wright, *Journal of The Electrochemical Society* **2017**, *164*, A930.

[272] D. S. Viswanath, T. K. Ghosh, D. H. L. Prasad, N. V. K. Dutt, K. Y. Rani, *Viscosity of Liquids: Theory, Estimation, Experiment, and Data*, Springer Science & Business Media, **2007**.

[273] S. Feja, C. Puhl, *Eignungsuntersuchungen Und Thermodynamisches Verhalten von Kältemittel-Öl-Gemischen Für R245fa Anwendungen*, **2013**.

[274] J. Stapf, Bestimmung der dynamischen Oberflächenspannung mit Hilfe der Blasendruckmethode, https://archiv.ub.uni-heidelberg.de/volltextserver/17777/, Master's thesis, **2014**.

[275] M. Cölle, M. Büchel, D. M. de Leeuw, *Organic Electronics* **2006**, *7*, 305–312.

[276] F. Verbakel, S. C. J. Meskers, R. A. J. Janssen, H. L. Gomes, M. Cölle, M. Büchel, D. M. de Leeuw, *Applied Physics Letters* **2007**, *91*, 192103.

[277] T. Furukawa, *Phase Transitions* **1989**, *18*, 143–211.

[278] A. Clauset, C. R. Shalizi, M. E. J. Newman, *SIAM Review* **2009**, *51*, 661–703.

[279] J. Alstott, E. Bullmore, D. Plenz, *PLOS ONE* **2014**, *9*, e85777.

[280] K. Levenberg, *Quarterly of Applied Mathematics* **1944**, *2*, 164–168.

[281] D. W. Marquardt, *Journal of the Society for Industrial and Applied Mathematics* **1963**, *11*, 431–441.

Appendix A

Appendix

A.1 Substrate cleaning

All substrates, both with and without device structures, were cleaned in the same way. They were either washed with soap and rinsed with water, or submerged in a diluted cleaning concentrate (Hellmanex III) for some time. Then, they were spaced out and cleaned in succession with acetone and isopropanol in an ultrasonic bath for 15 minutes at $35 - 40$ °C. Between each cleaning step and after the last one, the substrates were dried with nitrogen.

A.2 Effective material area in electrode structures

When comparing in-plane and out-of-plane devices, it is necessary to discuss the effective electric field seen by the material film. For out-of-plane structures, the effective material area is assumed to equal the overlap of the top and bottom electrodes. In the case of in-plane IDE structures, however, it is more complicated. Here, the thickness of the material layer between the electrodes is known. However, the total capacitor area $A = l \cdot h$ is needed to obtain the polarization values. l is the total length of the electrodes and can be calculated by summing all the electrode interfaces. h is the total height of the material layer affected by the electric field. While calculating the former is straightforward, estimating the latter is significantly more complex. If the material layer is thicker than the electrode height, the electric field lines curve for the upper part of the material layer, reducing the effective electric field. Since the distance between the electrodes is usually larger than or comparable to the film thickness, this effect should be minimal. The materials and thin films investigated in this dissertation were seemingly not strongly influenced by this effect, as indicated by fully polarizable out-of-plane BTA films on Micrux IDEs with film thicknesses of $\approx 1 - 3$ μm, which were typically the highest film thicknesses investigated. Furthermore, simulations performed by M.Sc. Maximilian Litterst, a member of the research group, using COMSOL Multiphysics suggest that, for typical in-plane electrode and ferroelectric thin film geometries and sizes, electric fields can penetrate the entire ferroelectric film with relative homogeneity. Although this dissertation will not further elaborate on the topic of the effective electric field strengths in thin films, the presented polarization values should still be treated as estimates, as the thin films may potentially not be fully polarized, especially near the coercive field [269–271].

A.3 Solution parameters of mixtures

Since all solutions consist of at least two components (a solid material and a solvent), considering only the solvent parameters may not be sufficient, especially at higher solid material concentrations. Assuming that x_1 and x_2 are the specific (molar or volume) fractions of the two mixed components, and that the same indices are assigned to the corresponding parameters, then the total viscosity of the mixture μ_{mix} is given by

$$\mu_{\text{mix}} = x_1\mu_1 + x_2\mu_2 + x_1x_2G_{12}, \tag{A.3.1}$$

with the mixture-dependent mixing parameter G_{12} [272]. For most real mixtures with volume depression, G_{12} is a complicated function of temperature and mole fraction. There is seemingly no coherent theory for G_{12} and it is a purely empirical parameter [272]. However, for mixtures of chemically similar liquids such as benzene, isopropanol, and toluene, it has been empirically shown that G_{12} typically approaches zero [272, 273]. While it does not provide a coherent estimation when mixing a solid material with a solvent, it allows for simplification when mixing several chemically similar solvents. Thus, when using these kinds of solvents, Equation A.3.1 simplifies to

$$\mu_{\text{mix}} \approx x_1\mu_1 + x_2\mu_2. \tag{A.3.2}$$

A similar approach can be used for density and surface tension in mixtures. In most cases, the density ρ_{mix} can be estimated as the following [272]:

$$\rho_{\text{mix}} \approx x_1\rho_1 + x_2\rho_2. \tag{A.3.3}$$

The same can be shown for the surface tension σ_{mix} [274]:

$$\sigma_{\text{mix}} \approx x_1\sigma_1 + x_2\sigma_2. \tag{A.3.4}$$

Therefore, the 'trivial' approximations for the solution parameters are mostly true.
The above considerations are valid when the material parameters are known. While the densities of the materials used in this dissertation are known, it is not possible to determine the exact values of viscosity and surface tension that will result from adding such solids to a solvent. However, Rogowski and Darhuber provided solution parameter values for nicotinamide in isopropanol [158]. A comparison reveals that the solutions used in this dissertation have similar solid fractions and solvents [3, 158, 159]. Thus, the assumption that changes in solution parameters are on a similar scale seems feasible. However, using Equation 3.2.7 in Section 3.2.3 to compare the values shows that the evaporation rate error leads to a larger variation in the threshold speed than the changes in solution density, viscosity, and surface tension. For this reason, only the solvent parameters are used to estimate the threshold speed.

A.4 Dip coating defects

Similar to most coating techniques, visible particles, pinholes, and craters may occur in the microstructure of a thin film due to dust particles in the air, substrate contamination, and agglomerates in the solution. These defects lead to comet-like trails and aggregations on the substrate. Although substrate cleaning (see Section A.1) and solution processing (see Section 3.1) mitigate these effects, the aggregation and crystallization of the solute during the dip coating process also contributes to the formation of such defects, particularly for weakly soluble materials. This issue is typically addressed by (pre)heating the solution. Furthermore, solvent evaporation during drying phase cools the substrate and film, which may lead to complications in subsequent film formation due to the formation of crater-like structures.

Furthermore, the substrate may be coated inhomogeneously or only partially, which usually occurs due to insufficient substrate wetting, inconsistent withdrawal speeds, or turbulent airflow during drying. The first issue arises from the solvent used, while the second is usually a problem with the dip coater. The latter is due to the wet film's sensitivity during the drying phase, when turbulent flow can affect evaporation and drying rates, leading to inhomogeneities. This problem can be counteracted by adjusting the setup. However, a lack of airflow can also cause problems during the drying phase, as solvent vapor may accumulate above the surface of the solution. The best to avoid this problem is to apply a weak, constant laminar airflow during the drying phase to maintain consistent rates.

Additionally, stripe defects can occur as periodic differences in film thickness perpendicular to the withdrawal direction. These defects are especially common at lower withdrawal speeds due to an effect known as the "coffee-ring effect" [155]. The solvent first evaporates at the edges of the meniscus. Due to capillary feeding, more solvent is added to the evaporating solvent, resulting in the deposition of more solute at the edge of the meniscus. This leads to larger film thicknesses. However, these spots separate from the meniscus and capillary feeding upon withdrawal. Since this process repeats, the stripes are periodic. This effect can be reduced by increasing the withdrawal speed or reducing the ambient temperature. Varying the solvent concentration and therefore the viscosity also influences this effect.

Contamination during the wet stages creates weak points in the thin film structure, which can lead to cracking. These cracks usually appear after post-deposition heat treatment due to additional stress in the film. However, a substantial volume change from the initial liquid to solid state can also cause cracks in the thin film.

Lastly, running or curtaining can occur when the the solution runs down the substrate during the drying stage of deposition. This is caused by long drying times due to large wet film thicknesses, and it typically happens with high withdrawal speeds and low-viscosity solutions.

A.5 XRD momentum transfer

In the incident beam coordinate system $(q_\mathrm{x}, q_\mathrm{y}, q_\mathrm{z})$, the incident beam vector is given by $\boldsymbol{k_\mathbf{i}} = \langle 0, -k, 0\rangle$ with $k = \frac{2\pi}{\lambda}$, where λ is the wavelength of the incident beam. In an elastic scattering event, the outgoing momentum vector $\boldsymbol{k_\mathbf{f}}$ has the same magnitude as the incident momentum vector $\boldsymbol{k_\mathbf{i}}$: $|\boldsymbol{k_\mathbf{f}}| = |\boldsymbol{k_\mathbf{i}}| = k$. The resulting momentum transfer $\boldsymbol{q}$ can be expressed as

$$\boldsymbol{q} = \boldsymbol{k_\mathbf{f}} - \boldsymbol{k_\mathbf{i}} \tag{A.5.1}$$

$$= \begin{pmatrix} 0 \\ -k\cos(2\theta_\mathrm{s}) \\ k\cos(2\theta_\mathrm{s}) \end{pmatrix} - \begin{pmatrix} 0 \\ -k \\ 0 \end{pmatrix} \tag{A.5.2}$$

$$= \begin{pmatrix} 0 \\ k\left(1-\cos(2\theta_\mathrm{s})\right) \\ k\sin(2\theta_\mathrm{s}) \end{pmatrix} \tag{A.5.3}$$

$$= \begin{pmatrix} 0 \\ 2k\sin^2(\theta_\mathrm{s}) \\ 2k\sin(\theta_\mathrm{s})\cos(\theta_\mathrm{s}) \end{pmatrix} \tag{A.5.4}$$

Therefore, the magnitude of the momentum transfer q is given by

$$q = |\boldsymbol{q}| \tag{A.5.5}$$

$$= \sqrt{\left[2k\sin^2(\theta_\mathrm{s})\right]^2 + \left[2k\sin(\theta_\mathrm{s})\cos(\theta_\mathrm{s})\right]^2} \tag{A.5.6}$$

$$= 2k\sqrt{\sin^2(\theta_\mathrm{s}) + \sin^2(\theta_\mathrm{s})\cos^2(\theta_\mathrm{s})} \tag{A.5.7}$$

$$= 2k\sqrt{\sin^2(\theta_\mathrm{s})} \tag{A.5.8}$$

$$= 2k\sin(\theta_\mathrm{s}) \tag{A.5.9}$$

$$= \frac{4\pi}{\lambda}\sin(\theta_\mathrm{s}), \tag{A.5.10}$$

where $2\theta_\mathrm{s}$ is the full scattering angle. The Ewald sphere is centered around $(0, -k, 0)$ and has the following equation:

$$q_\mathrm{x}^2 + (q_\mathrm{y} - k)^2 + q_\mathrm{z}^2 - k^2 = 0. \tag{A.5.11}$$

A.6 XRD setup configurations

The Rigaku SmartLab XRD used for all measurements was equipped with a copper source (wavelength $\lambda \approx 0.154$ nm) and a HyPix-3000 detector in horizontal orientation.

$\theta/2\theta$ measurements

The measurement setup consisted of an incident Soller slit of 5°, a length-limiting slit of 10 mm, a receiving Soller slit of 5°, no monochromator, a receiving slit #1 of 20 mm, a receiving slit #2 open, and a detector distance of 300 mm. A flat sample and a K_β filter for copper were used for sample alignment. Measurements were taken using the recommended sequence and conditions with standard settings. Absolute intensity was measured for angles between 1.0° and 70.0° with a step size of 0.01° and speed of $1.5 - 2.0°$.

2D GIWAXS measurements

The measurement setup consisted of an incident collimator, a Pinhole PB of 0.5 mm as the selection slit, incident soller slit open, a 0.5 mm length-limiting slit, and a 65 mm detector distance. The sample was chosen as the standard, with typical dimensions of 1.0 mm thickness and 10.0 mm width. The measurement mode was 2D single exposure with an incident angle of 0.30°, a detector angle of 16°, and an exposure time of 3600 s.

A.7 Dip coated BTA-C_8 thin films

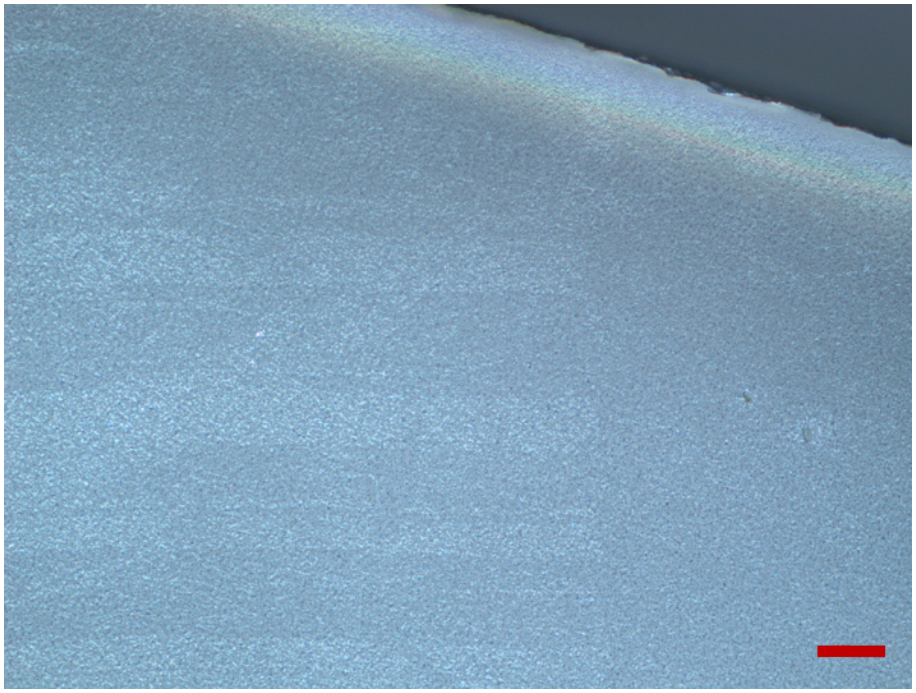

Figure A.7.1: A PLM image of a thin film drop cast from a 40 mg ml^{-1} BTA-C_8 in CF solution. The image was taken with a 10x magnification, and the scale bar represents 100 μm. Many small clusters with random orientation are formed, and there is no directional alignment. This figure was taken from the supporting information of Publication I with permission for usage granted by Advanced Materials Technologies.

Different BTA-C_8 concentration

The dip coated films exhibit clusters with pronounced alignment, as shown in Figure A.7.2. Similar dip coating speeds yield similar structures for 10 and 40 mg ml^{-1} BTA-C_8 in CF solutions, although the higher concentration typically shows larger clusters. The stripes perpendicular and parallel to the withdrawal direction are most likely defects, as discussed in Section A.4.
As depicted in Figures A.7.3 and A.7.4, the AFM images show that the surfaces of the dip-coated thin films are mostly aligned along the dip coating direction.

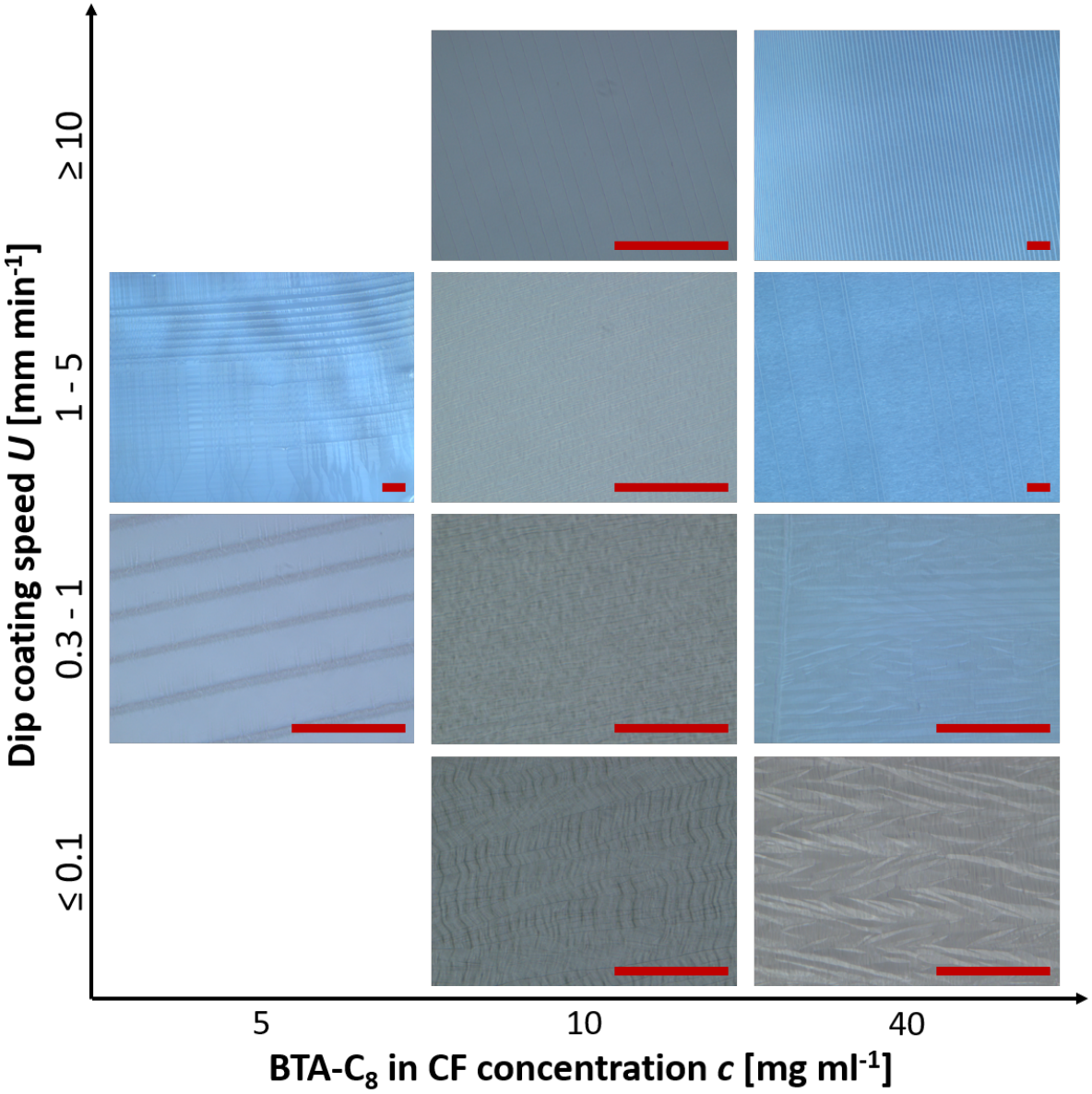

Figure A.7.2: PLM images of thin films dip coated from 5, 10, and 40 mg ml^{-1} BTA-C_8 in CF solutions at different dip coating speeds U. The empty spaces represent samples for which a usable PLM image could not be obtained due to film thickness or roughness. These films were seemingly not aligned. The withdrawal direction is along the vertical direction from top to bottom. All images were taken with reflective or transmission PLM at either 10x or 50x magnification. The scale bars represent 100 μm in all images. The corresponding AFM images can be found in Figures A.7.3 and A.7.4. The figure was adapted from author's master thesis.

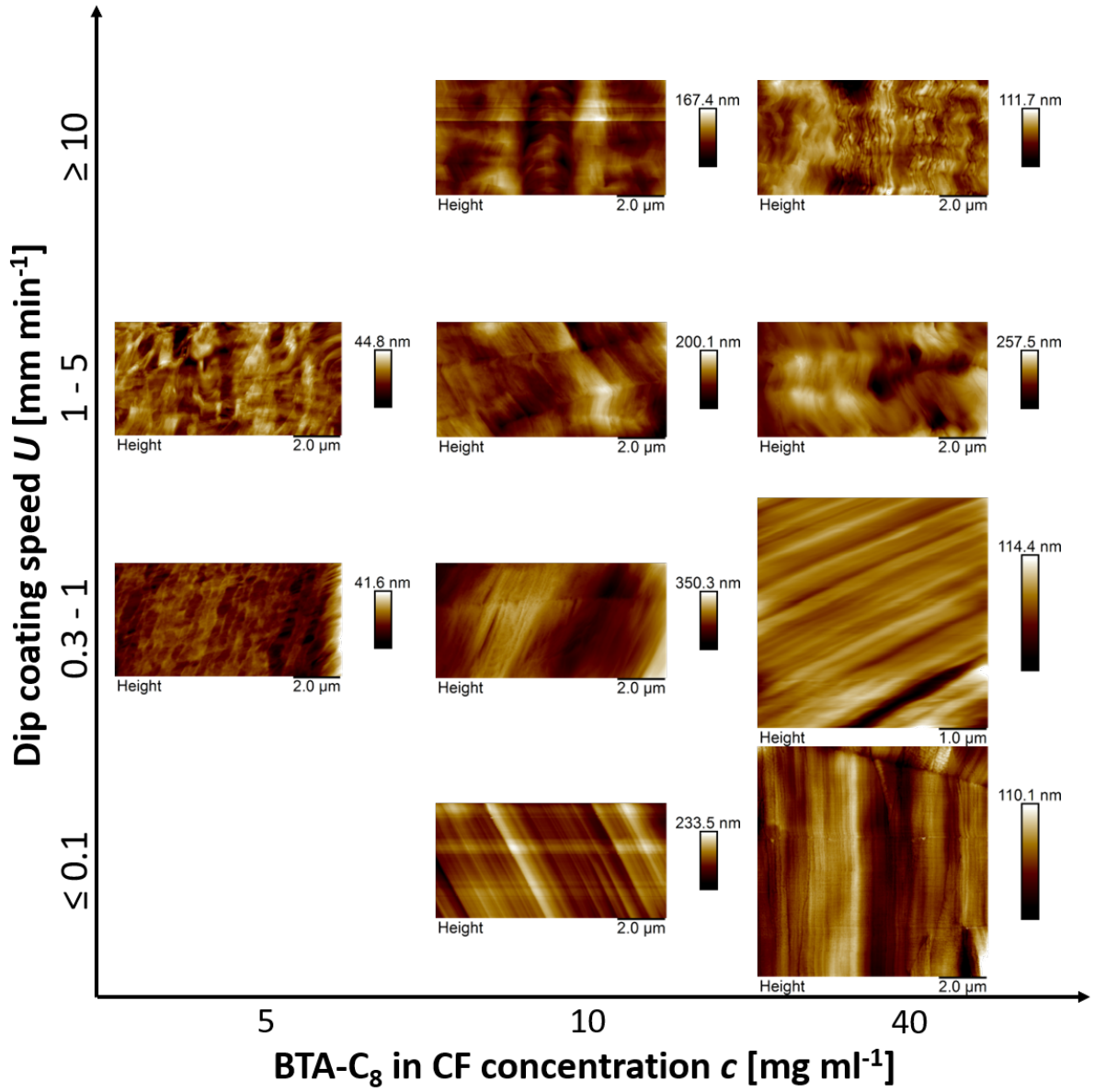

Figure A.7.3: AFM height images of thin films dip coated from 5, 10, and 40 mg ml^{-1} BTA-C_8 in CF solutions at different dip coating speeds U. The empty spaces represent samples for which a usable PLM image could not be obtained due to film thickness or roughness. These films were seemingly not aligned. The withdrawal direction is vertical, from top to bottom. The corresponding amplitude images can be found in Figure A.7.4. The figure was adapted from author's master thesis.

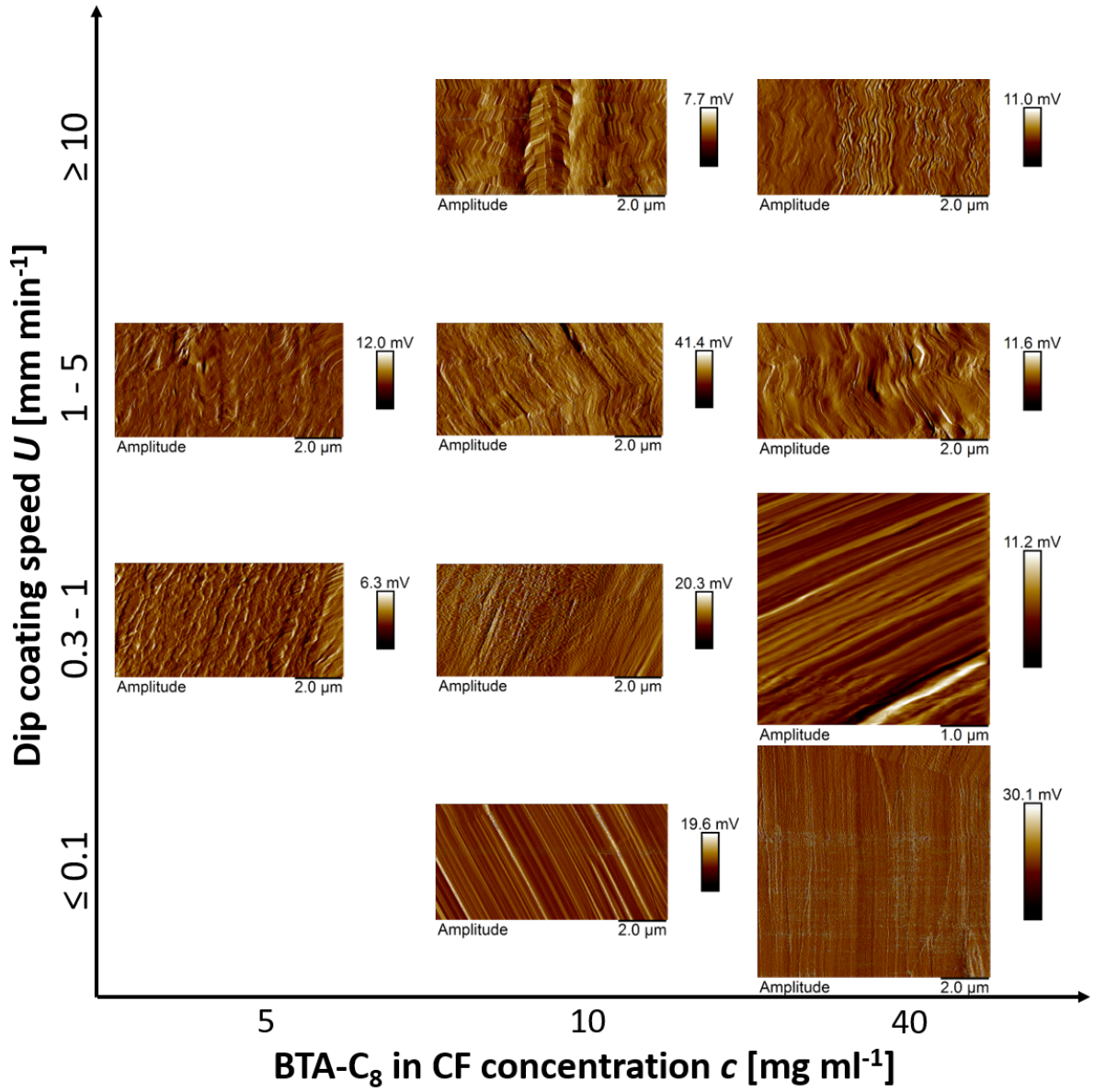

Figure A.7.4: AFM amplitude images of thin films dip coated from 5, 10, and 40 mg ml^{-1} BTA-C_8 in CF solutions at different dip coating speeds U. The empty spaces represent samples for which a usable PLM image could not be obtained due to film thickness or roughness. These films were seemingly not aligned. The withdrawal direction is vertical, from top to bottom. The corresponding height images can be found in Figure A.7.3. The figure was adapted from author's master thesis.

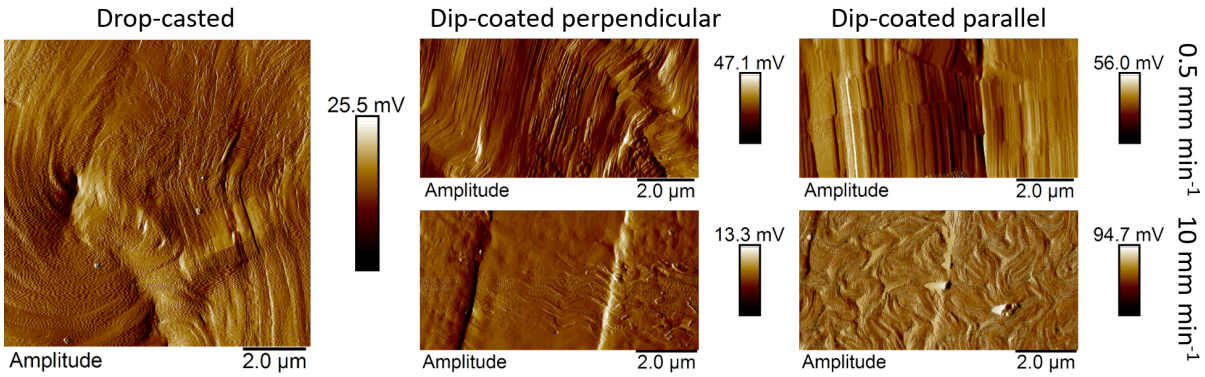

Figure A.7.5: The AFM amplitudes of selected in-plane IDE samples coated with a 10 mg ml^{-1} BTA-C_8 in CF solution, as indicated in the figure. The electrodes run vertically in all images but are not always visible due to the relatively large film thicknesses. Consequently, the electric field is horizontal. Perpendicular and parallel coating directions refer to the electrode directions. All images were take with a scan area of either 10 μm $\times$ 10 μm or 10 μm $\times$ 5 μm. The corresponding height images can be found in Figure 5.1.3 in Section 5.2.

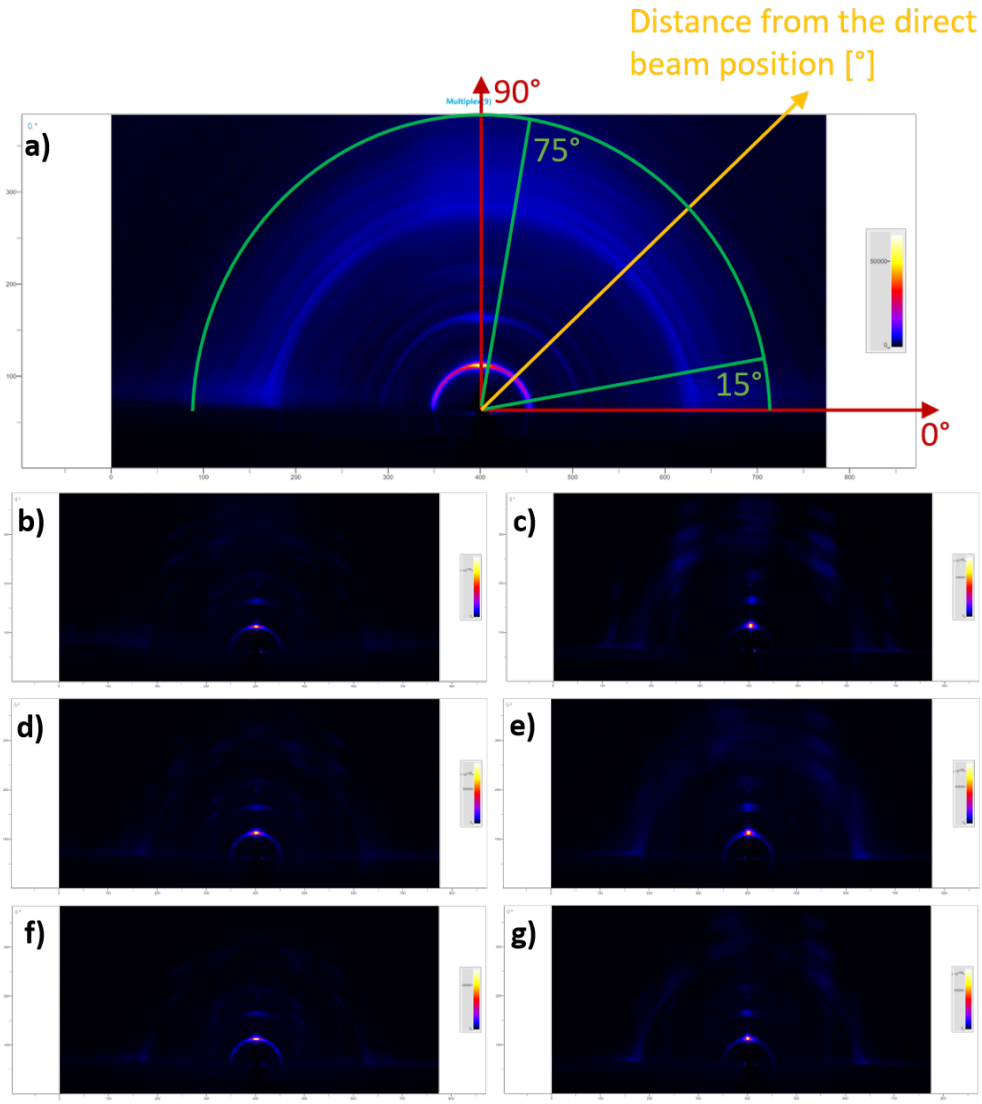

Figure A.7.6: The 2D diffraction data of drop-cast and dip-coated BTA-C_8 thin films. The integrated intensities presented in Figure 5.1.6 in Section 5.1 were obtained by converting the counts of parts of these images into intensity spectra. Intensities integrated along the z- and y-axes were averaged over $75 - 105°$ and $0 - 15°$ in these images, respectively, as indicated in the first image. The diffraction images shown are: **a)** drop-cast film; **b)** dip coated with 1 mm min^{-1} and measured parallel to dip coating direction; **c)** dip coated with 1 mm min^{-1} and measured perpendicular to dip coating direction; **d)** dip coated with 10 mm min^{-1} and measured parallel to dip coating direction; **e)** dip coated with 10 mm min^{-1} and measured perpendicular to dip coating direction; **f)** dip coated with 60 mm min^{-1} and measured parallel to dip coating direction; and **g)** dip coated with 60 mm min^{-1} and measured perpendicular to dip coating direction. This figure was taken and slightly modified from the supporting information of Publication I with permission for usage granted by Advanced Materials Technologies.

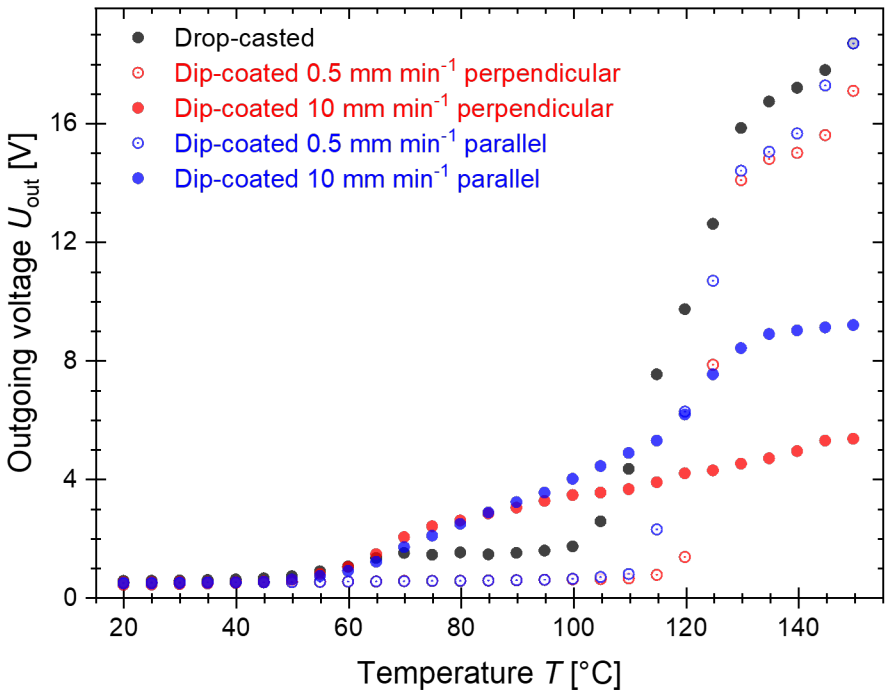

Figure A.7.7: The outgoing voltage maximum U_{out} over the 1 MΩ measurement resistor as a function of temperature T, measured at a voltage amplitude of $U = 300$ V and a frequency of $f = 5$ Hz. The different colors correspond to different coating parameters, as indicated in the legend. The first heating run of all samples is shown. The size of the data points represents the typical error margin of the data. Note that the measured films have different film thicknesses, which explains the variation in the outgoing voltage's absolute values and, consequently, the remnant polarization. This is the same data shown in Figure 5.2.3 in Section 5.2. This figure was taken and slightly modified from Publication I with permission for usage granted by Advanced Materials Technologies.

A.8 Mean alignment of molecular columns in drop-cast BTA

Assuming the situation shown in Fig. 5.2.2 in Section 5.2, considering a 3D case with isotropic and parallel electric field lines between the electrodes, taking the direction of the electric field as the positive direction of the z-axis, and introducing spherical polar coordinates (ϕ, θ) with the angle θ reckoned from this direction, an element of solid angle in such coordinate system is given as $\mathrm{d}\omega = \sin\theta \mathrm{d}\theta \mathrm{d}\phi$. The orientation of some direction in space with respect to the electric field is given by $\cos\theta$. To find the mean alignment, it must be averaged over all directions. It is sufficient to consider the upper hemisphere, $0 \leq \theta \leq \pi/2$, since "upward" and "downward" orientations are equivalent for molecular columns when the orientation of the dipole moments is not taken into consideration. The isotropically distributed directions are given as

$$\frac{1}{2\pi} \int \int \cos\theta \mathrm{d}\omega = \frac{1}{2\pi} \int_0^{2\pi} \mathrm{d}\phi \int_0^{\pi/2} \cos\theta \sin\theta \mathrm{d}\theta = -\frac{1}{4} \left[\cos 2\theta\right]_0^{\pi/2} = \frac{1}{2}. \tag{A.8.1}$$

Thus, the mean alignment along the electric field for randomly oriented molecular columns is 50%.

A.9 Barkhausen noise in BTA

Simulation program changes

After Dr. Tim Cornelissen, the program was developed further by M.Sc. Fabian T. Thome. Two changes were introduced. First, the induced dipoles are updated when a significant change in polarization is detected. Previously, the induced dipole problem was solved once, and the induced dipole moments were assumed to remain constant throughout a simulation. However, if a significant fraction of dipoles reverses, the induced dipoles must be recalculated, which is now included when the relative polarization changes above a set threshold. Second, time binning was modified to enable analysis of polarization changes in the context of Barkhausen noise. Bins are created at the beginning of a simulation, and new values are assigned to a bin according to the time steps taken. Ultimately, the points in a bin are averaged, and empty bins are assigned the value of the previous bins. The simulation structure was changed from a 'for' loop to a 'while' loop to account for the changes. Finally, M.Sc. Toni Seiler also contributed to the program code. The 'jumps' problem, in which a flip is ignored if a time step exceeds the electric field value time limit, was fixed. Several small code adjustments were also made, mostly for optimization. This version of the program was used for the main temperature- and frequency-dependent power-law exponent simulation results presented in Section 6.3.2.

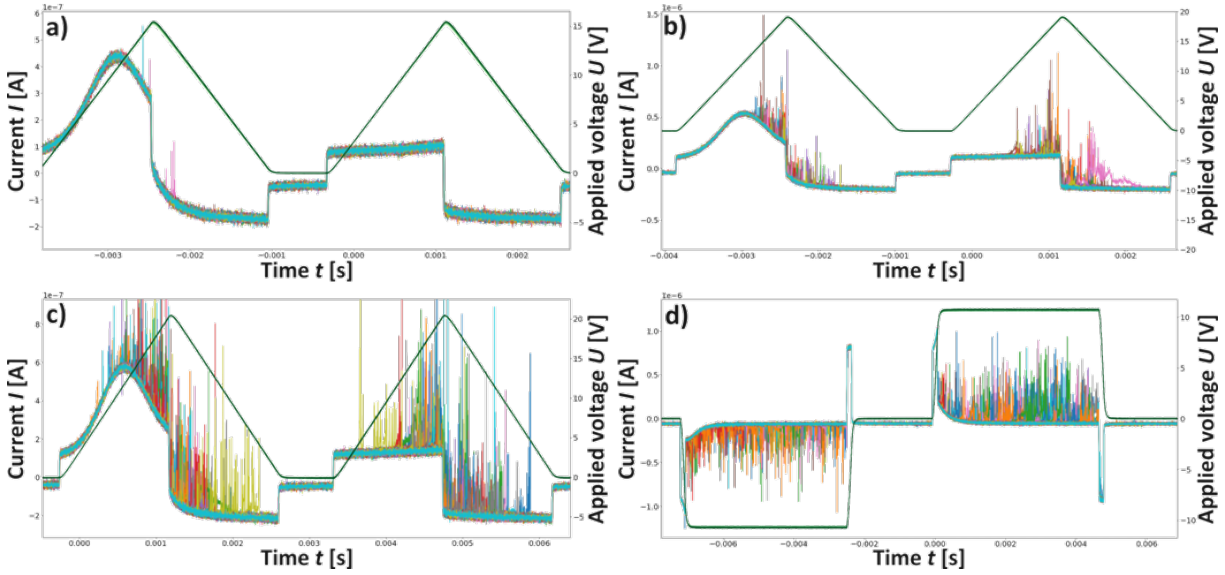

Figure A.9.1: The applied voltage (dark green line) and the resulting currents (multiple colors) of BTA samples with aluminum and silver electrodes measured at 363 K showing **a)** almost only background noise and **b-d)** artifact spikes for different applied voltages and different waveforms. The applied voltage was either a double triangular signal (a-c) or a double square signal (d) as part of a DW measurement. The different colors correspond to different sub-measurements and a total of 100 sub-measurements were made in each measurement. The absence of signal (a) is most commonly measured, signals as in (b-d) were occasionally observed. All appeared above a threshold voltage of around 12 V and were identical in both up- and down-sweeping signals and for both waves, which is not what should be observed in Barkhausen noise signals for ferroelectric switching that only happens in the up sweep of the first wave and should be centered around the coercive field. Higher applied voltages typically led to both more often occurring and generally stronger signals, as is indicated by the amount of the peaks. We attribute these peaks to the formation of unstable conductive filaments, which is a general phenomenon in thin film MIM devices [275, 276]. This figure was initially adapted from B.Sc. Marcel Hecker's bachelor's thesis and taken unmodified from the supporting information of Publication II with permission for usage granted by Physical Chemistry Chemical Physics.

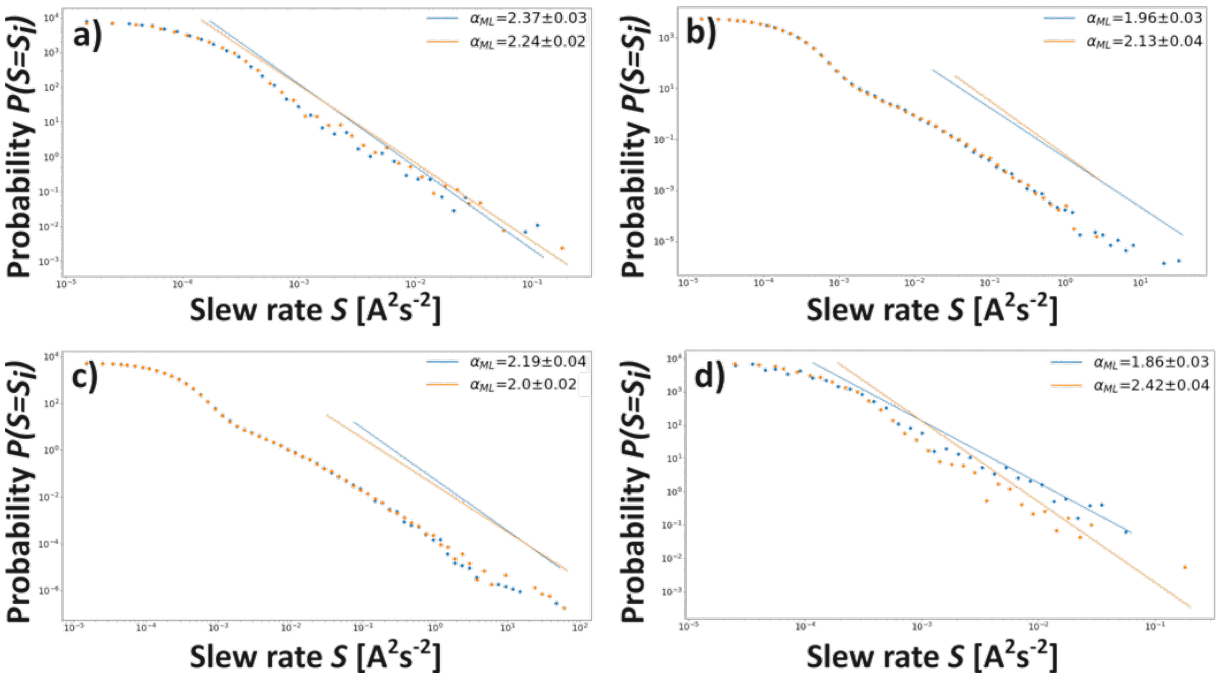

Figure A.9.2: Probability density distributions and the corresponding exponents of the measurements shown in Figure A.9.1. The exponents were fitted by the maximum likelihood method for two different threshold settings, which are indicated in blue and orange. No significant differences between the measurements done for a lower (in blue) and a larger (in orange) threshold setting were observed. Moreover, the shape of the distributions and the corresponding power-law exponents ($\approx 1.9 - 2.5$) are not characteristic for Barkhausen noise. This figure was initially adapted from B.Sc. Marcel Hecker's bachelor's thesis and taken unmodified from the supporting information of Publication II with permission for usage granted by Physical Chemistry Chemical Physics.

A.10 Power-law fitting methods

Least squares (linear) fitting method

This commonly used method used for fitting models to data minimizes the sum of squared residuals S:

$$S = \sum_{i=1}^{N} r_{\mathrm{i}}^2 = \sum_{i=1}^{N} \left(y_{\mathrm{i}} - f\left(x_{\mathrm{i}}\right)\right)^2, \tag{A.10.1}$$

where y_{i} and $f\left(x_{\mathrm{i}}\right)$ are the observed values and the fitted model function with an independent variable x_{i}, respectively. While the minimization can be done analytically for simple functions, the approach is typically non-trivial for non-linear functions. Many different algorithms exist to solve this problem. Within of this publication, the Levenberg-Marquardt algorithm was used [280, 281]. A linear function $f\left(x\right) = mx + b$ is fitted to the measured data in double-logarithmic representation. Thus, the exponential of the fit function is plotted, which results in $f\left(x\right) = x^m e^b$, so that m is associated with the exponent α and e^b is just a constant.

Maximum likelihood fitting method

For a power-law starting at a value x_{min} and having an exponent α, the probability $p\left(x\right)$ can be obtained via

$$p\left(x\right) = \frac{\alpha - 1}{x_{\mathrm{min}}} \left(\frac{x}{x_{\mathrm{min}}}\right)^{-\alpha}. \tag{A.10.2}$$

If there are N observations with $x_{\mathrm{i}} \geq x_{\mathrm{min}}$, the probability of the data fitting the model is proportional to

$$p\left(x|\alpha\right) = \prod_{i=1}^{N} \frac{\alpha - 1}{x_{\mathrm{min}}} \left(\frac{x}{x_{\mathrm{min}}}\right)^{-\alpha}. \tag{A.10.3}$$

The probability $p\left(x|\alpha\right)$ is the so-called likelihood. Maximizing the likelihood yields a better fit. Instead of the likelihood, the log-likelihood $\mathcal{L}$ - the logarithm of the likelihood - is commonly used. Considering the condition $\frac{\partial \mathcal{L}}{\partial \alpha} = 0$, the maximum likelihood estimator $\hat{\alpha}$ is obtained [278]:

$$\hat{\alpha} = 1 + N \left[\sum_{i=1}^{N} \ln\left(\frac{x}{x_{\mathrm{min}}}\right)\right]^{-1}. \tag{A.10.4}$$

The corresponding calculations were implemented into a python package by Alstott et al. in 2014 and were used in this dissertation for analysis and evaluation [279].

A.11 Estimation of the number of switched dipoles

BTA

From sample geometry, the total number of switchable dipoles N_t within a material can be expressed as

$$N_\mathrm{t} = \frac{P_\mathrm{s} A_\mathrm{s} D}{qd}, \tag{A.11.1}$$

where P_s is the saturation polarization, A_s the area and D the thickness of the sample, q the charge and d the size of a microscopic dipole. Thus, the number of dipoles in the material that are switched by a change in charge N_s are given by

$$N_\mathrm{s} = \frac{QD}{qd}, \tag{A.11.2}$$

with the total charge Q, so that QD is the macroscopic dipole moment. The total charge can be obtained from the switching current $I(t)$ via $Q = \int I(t)\,\mathrm{d}t$.
Taking a typical out-of-plane device with an active area of $0.2\ \mathrm{mm} \times 0.25\ \mathrm{mm}$ and a film thickness of 400 nm, assuming 0.34 nm as π-stacking and 1.94 nm as intermolecular distances [79], results in a maximum column height of around 1180 BTA molecules between the top and bottom electrodes. Further assuming a simple hexagonal 2D Bravais lattice, the total number of dipoles in the BTA sample can be calculated via

$$N_\mathrm{t}^\mathrm{g} = n_\mathrm{d} N_\mathrm{ch} c \frac{A_\mathrm{s}}{A_\mathrm{uc}} = n_\mathrm{d} N_\mathrm{ch} N_\mathrm{c}, \tag{A.11.3}$$

with $n_\mathrm{d} = 3$ as the number of dipoles per molecule, $N_\mathrm{ch} \approx 1180$ as the number of molecules in a column, $c = 4$ as the coordination number, A_s as the area and $A_\mathrm{uc} = \left(3\sqrt{3}/2\right) a^2$ the area of the hexagonal unit cell with $a = 1.94$ nm as the intermolecular distance. This results in $\approx 3 \cdot 10^{13}$ BTA molecules and hence a total of $\approx 9 \cdot 10^{13}$ dipoles.
Alternatively, using that BTA has a remnant polarization of around $45 - 50\ \mathrm{mC\ m^{-2}}$ at the measured temperature [101], Equation A.11.1 yields a total of $\approx 8.4 \cdot 10^{13}$ dipoles, which is in good agreement with the previous estimation.

In the kMC simulation, it was concluded that, assuming a constant number of dipoles, the average size of dipole avalanches flipping mainly depends on the column length, which indicates that the columns are only weakly coupled. It was established that for 700 BTA molecules in a column and a width of four columns in both x- and y-directions, 500 dipoles per event were the maximal event size and the power-law onset occurred between 100 and 200 dipoles (see Section 6.3.1). Assuming an event size of 200 dipoles and that the experimentally measured sample consists of multiple such simulated regions, a rough estimate indicates that the measured BTA sample consists of $\approx 1.6 \cdot 10^9$ regions.

In order to achieve a measurable current (in our case ≈ 4 nA for 1 μs time resolution; 938 kHz sampling rate), a total of $\approx 6 \cdot 10^5$ regions have to simultaneously provide a switching event. Due to the weak coupling between the columns and avalanches only occurring within a column, this is very unlikely to happen, implying that the actually occurring switching events will be far below the resolution threshold of the used setup.

P(VDF:TrFE)

From sample geometry, the total number of switchable dipoles N_t within a material can be expressed as

$$N_t = \frac{P_s A_s D}{qd} \tag{A.11.4}$$

Assuming a saturation polarization of $P_s = 110$ mC m^{-2} [17], a typical out-of-plane device with an active area of $A_s = 0.25$ mm $\times$ 0.25 mm, a dipole moment of $D = 1.8$ Debye [277], the elementary charge q, and the size of a macroscopic dipole d, Equation A.11.4 leads to a total of $N_t \approx 4.6 \cdot 10^{14}$ dipoles contributing to the switching of a typical out-of-plane P(VDF:TrFE) device. The minimal resolvable peak for P(VDF-TrFE) assuming a minimal detectable current of 4 nA for the optimal required sampling time of 1 μs (938 kHz sampling rate) results in $\approx 2.8 \cdot 10^8$ dipoles as the minimal number of simultaneously switching dipoles required for detection. Meanwhile, a critical volume of 4 nm^3 obtained from TA-NLS theory yields a magnitude of $\approx 10^3$ dipoles, not allowing a direct experimental observation in noise spectroscopy.

A.12 Barkhausen noise in P(VDF:TrFE)

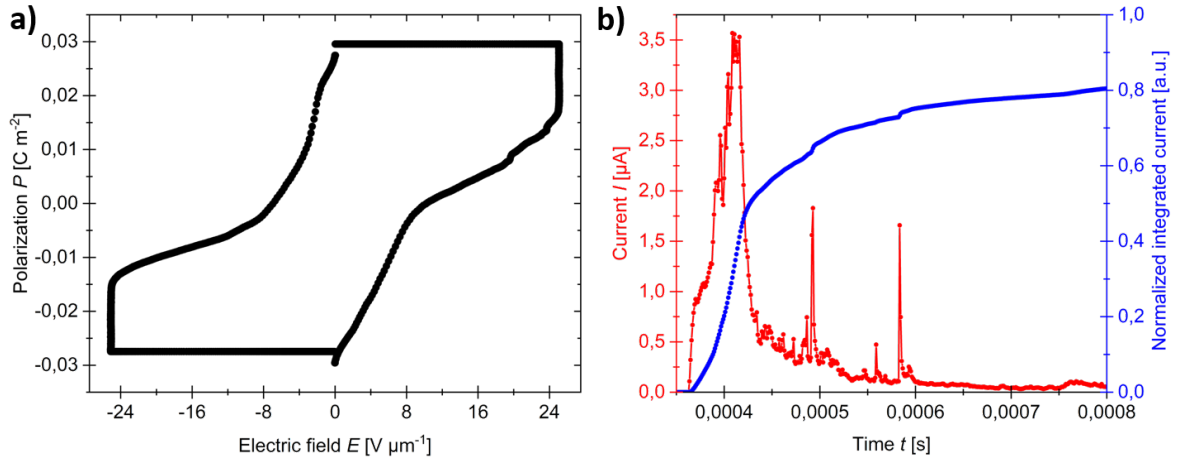

Figure A.12.1: a) The P-E-hysteresis loop obtained by integrating the current measurement depicted in Figure 7.1.2a in Section 7.1, where only the up-peak is shown. The odd shape can be explained by the used waveform and the fact that the measurement was carried out at a maximum electric field value close to the coercive field. The latter makes that the sample is not fully switched once the maximum field is reached, giving rise to the increasing polarization at the maximum applied electric field and to a polarization value of about half the saturated total remnant polarization value. Note also that the square waveform does not allow to determine the coercive field, as opposed to the triangular waveform, as shown in Figure 7.1.1 in Section 7.1. **b)** The normalized polarization zoomed-in on the part before the electric field ramp reaches its maximum value, similar to Figure 7.1.2c in Section 7.1. Around 80% of the total polarization value is reached before the maximum electric field is applied. During the switching peak, no polarization jumps due to the signal spikes are apparent. While the integration of the two large signal spikes between 0.45 and 0.6 ms provides a visible increase in polarization, the latter is within the values expected from larger domain wall movement. Furthermore, signals produced by fully short-circuited samples typically produce different signals that exhibit significantly larger amplitudes, whose integration yields 'polarization' values that are larger than expected for P(VDF:TrFE) and show significant jumps in polarization at the short positions. Importantly, switching spikes vanish for waiting times beyond those shown here. This figure was taken unmodified from the supporting information of Publication III with permission for usage granted by Physical Chemistry Chemical Physics.

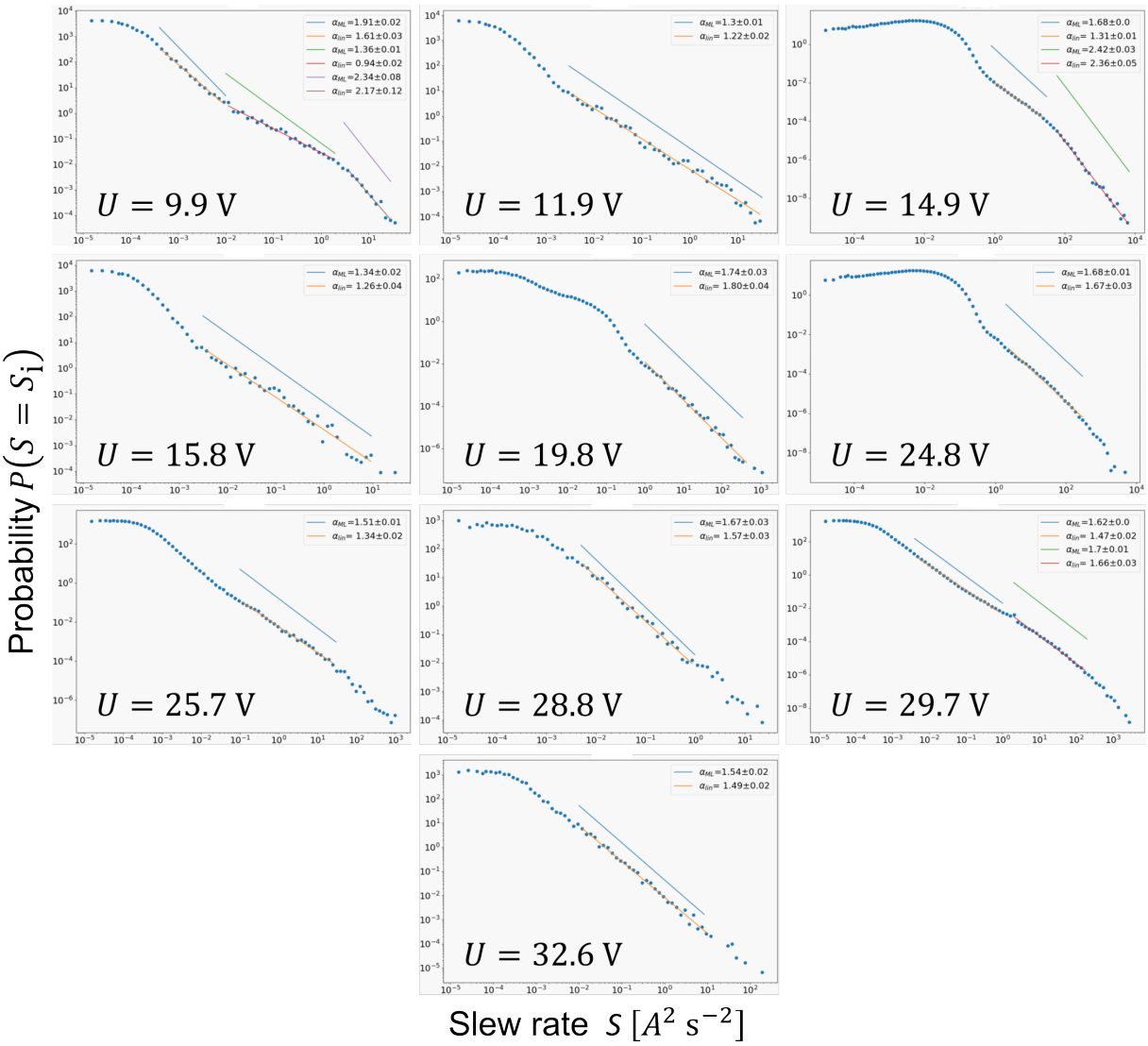

Figure A.12.2: Measured histograms of the 100 μs P(VDF:TrFE) measurements at different applied electric fields with their extracted power-law exponents. Blue and orange lines are the fitted power-laws using the ML and LS (depicted as 'lin' here) fitting methods. The appearance of multiple sets of fits is due to the distribution seemingly showing multiple regions which may be identified as linear on the double-logarithmic scale. The final fit was chosen based on a combination of manual decision and minimizing the fit error. This figure was initially adapted from B.Sc. Marcel Hecker's bachelor's thesis and taken slightly modified from the supporting information of Publication III with permission for usage granted by Physical Chemistry Chemical Physics.

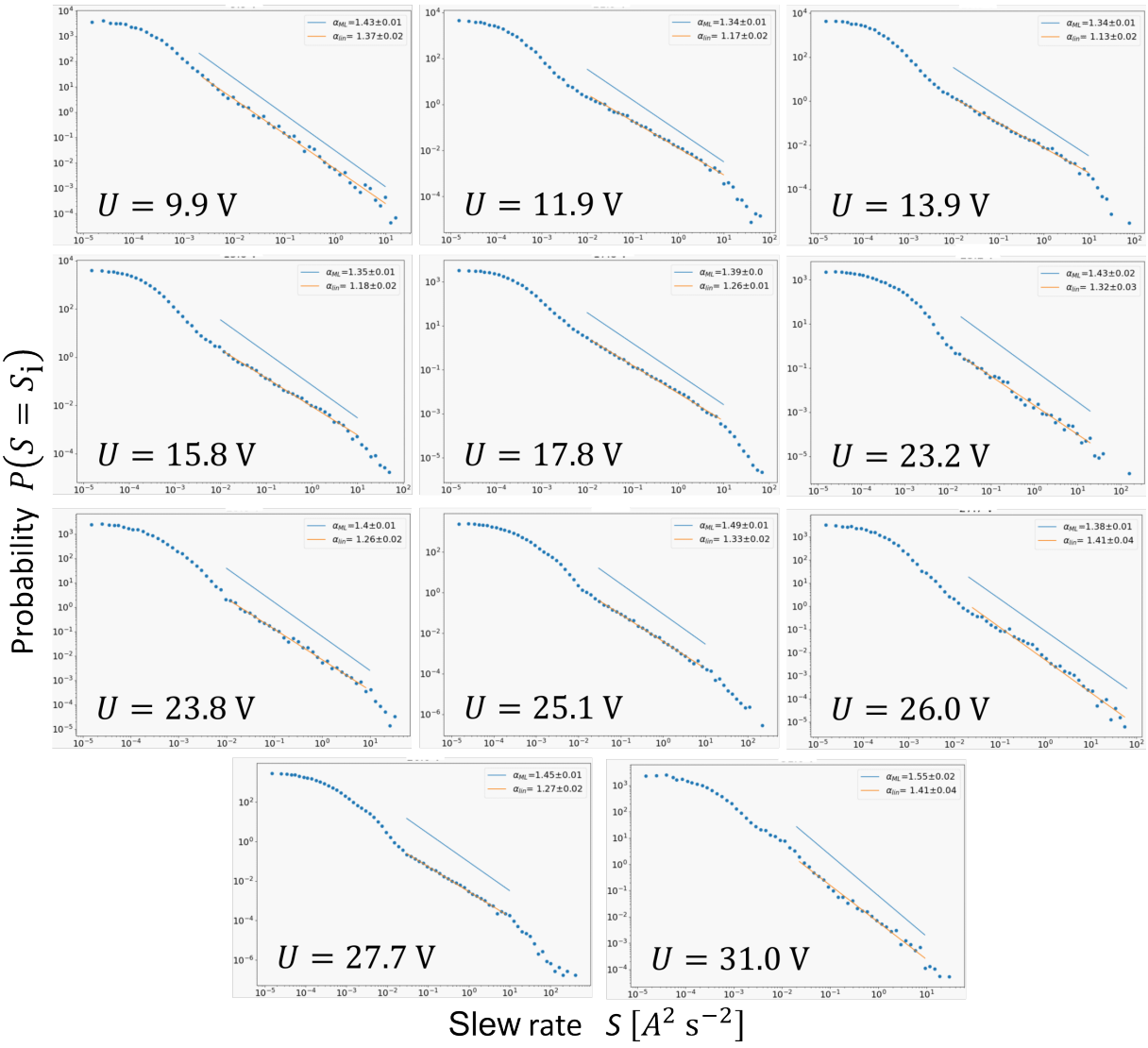

Figure A.12.3: Measured histograms of the 400 μs P(VDF:TrFE) measurements at different applied electric fields with their extracted power-law exponents. Blue and orange lines are the fitted power-laws using the ML and LS (depicted as 'lin' here) fitting methods. This figure was initially adapted from B.Sc. Marcel Hecker's bachelor's thesis and taken slightly modified from the supporting information of Publication III with permission for usage granted by Physical Chemistry Chemical Physics.

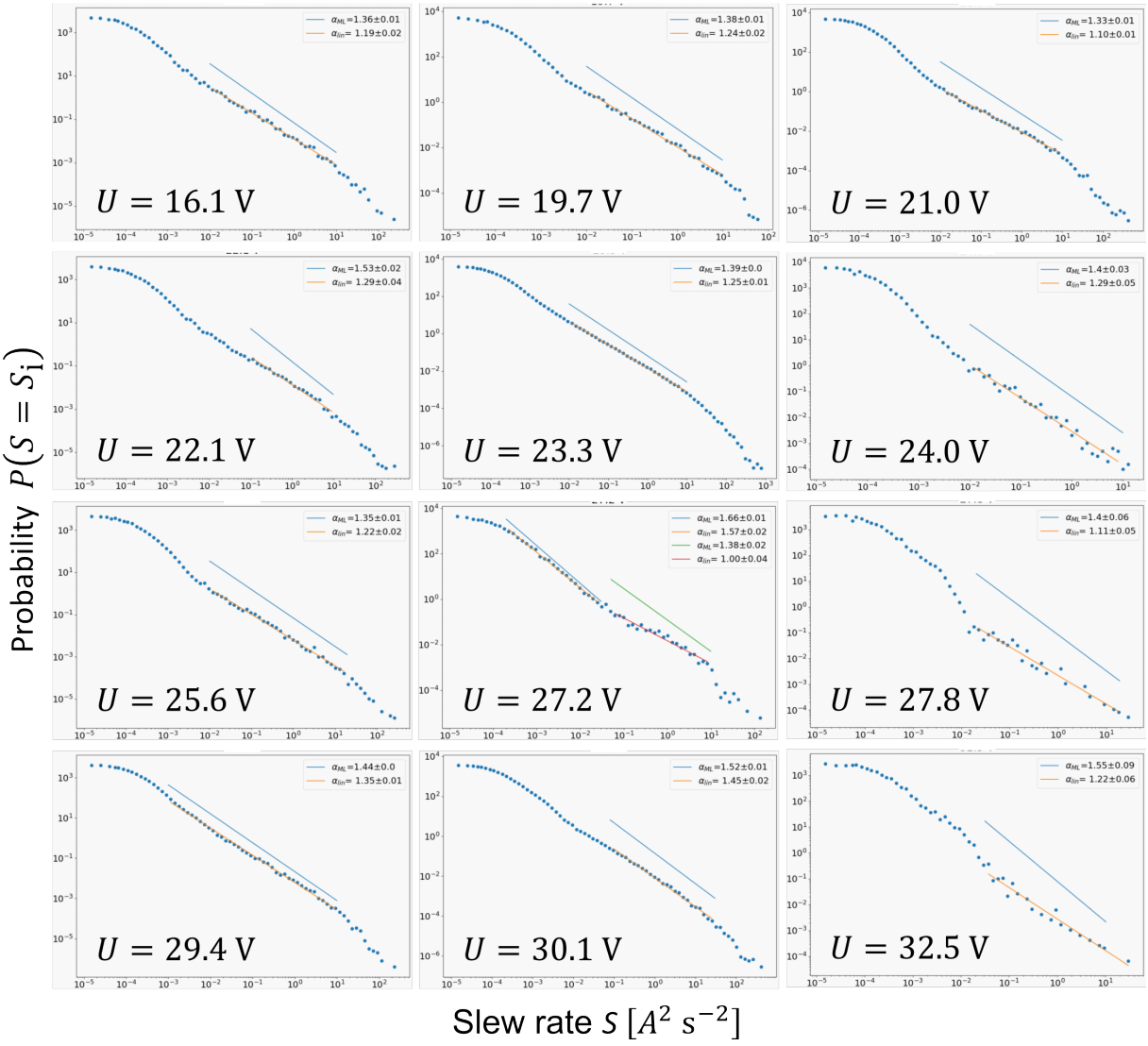

Figure A.12.4: Measured histograms of the 800 μs P(VDF:TrFE) measurements at different applied electric fields with their extracted power-law exponents. Blue and orange lines are the fitted power-laws using the ML and LS (depicted as 'lin' here) fitting methods. This figure was initially adapted from B.Sc. Marcel Hecker's bachelor's thesis and taken slightly modified from the supporting information of Publication III with permission for usage granted by Physical Chemistry Chemical Physics.

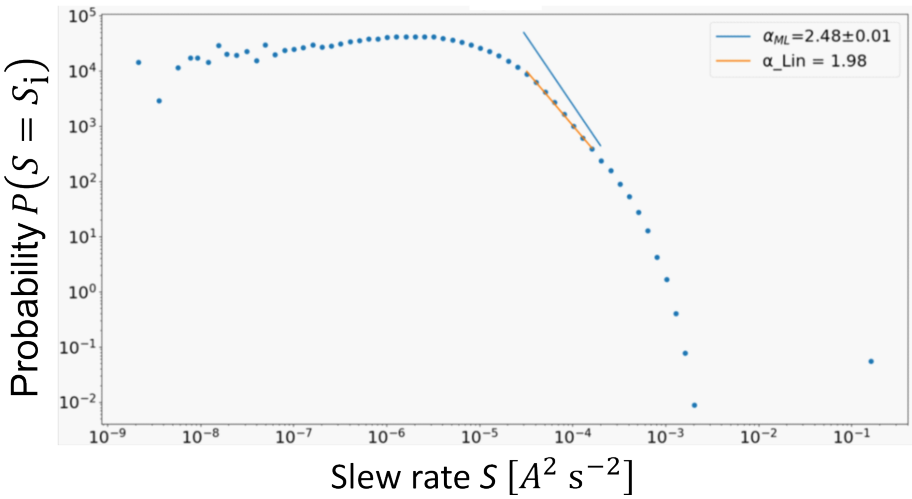

Figure A.12.5: A histogram of the noise spectrum measured for a dielectric reference capacitor at $U = 9.9$ V. The reference capacitor was put into the setup instead of a ferroelectric sample. No power-law behavior is observed over an extended range of slew rates. Instead, a plateau at lower slew rates is apparent, followed by a steep decline appearing as an exponential drop at a slew rate of $\approx 10^{-4} - 10^{-3}$ A^2 s^{-2}. Furthermore, a peak at ≈ 0.4 A^2 s^{-2} caused by the displacement current of the capacitor is visible. This reference measurement was used to rule out the possibility that only random noise was measured and was treated as a lower estimate for the noise floor. This figure was initially adapted from B.Sc. Marcel Hecker's bachelor's thesis and taken unmodified from the supporting information of Publication III with permission for usage granted by Physical Chemistry Chemical Physics.

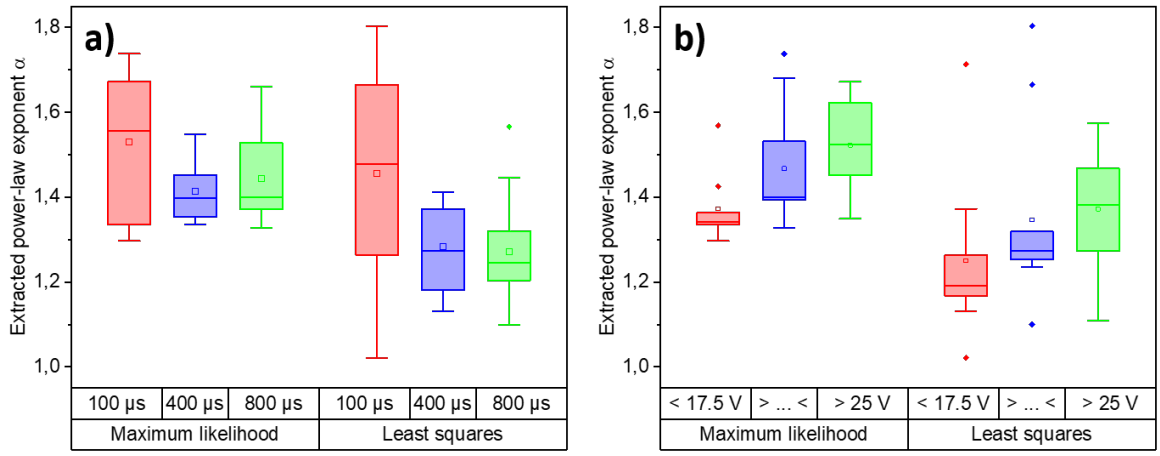

Figure A.12.6: Box plot of the extracted critical power-law exponents α for **a)** the three different rise times and **b)** three different intervals of applied voltage for both fitting methods including all exponent values obtained from the histograms. The shorthand label of the middle panel indicates voltages between 17.5 and 25 V. The values obtained from ML fitting are slightly larger than from LS fitting for all three rise times, although here the difference between the values for 100 μs is minimal. The trend of increasing exponents with applied voltage is clearly visible. This figure was taken unmodified from the supporting information of Publication III with permission for usage granted by Physical Chemistry Chemical Physics.

A.13 Properties of triphenylamines

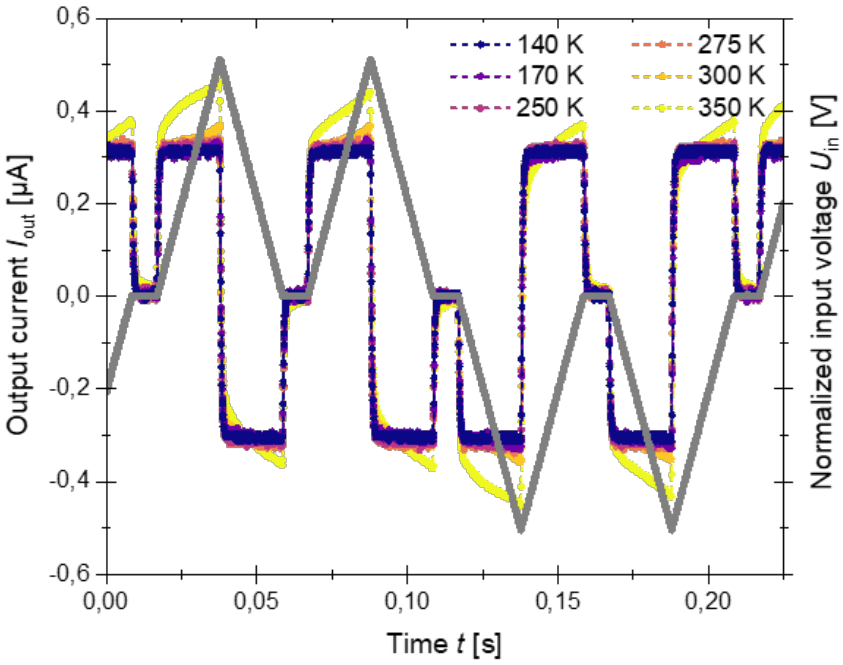

Figure A.13.1: An exemplary ferroelectric characterization measurement performed on the o-TPA-N. A DW signal is applied and the corresponding current response I is measured as a function of time t for different temperatures at a frequency of $f = 5$ Hz. For lower temperatures, mostly displacement currents are measured. With increasing temperatures, the leakage current starts to dominate. The slight difference between first and second peaks is attributed to ionic contributions. Measurements for different applied voltages and at different frequencies were also performed and turned out to be similar for all three TPA derivatives.

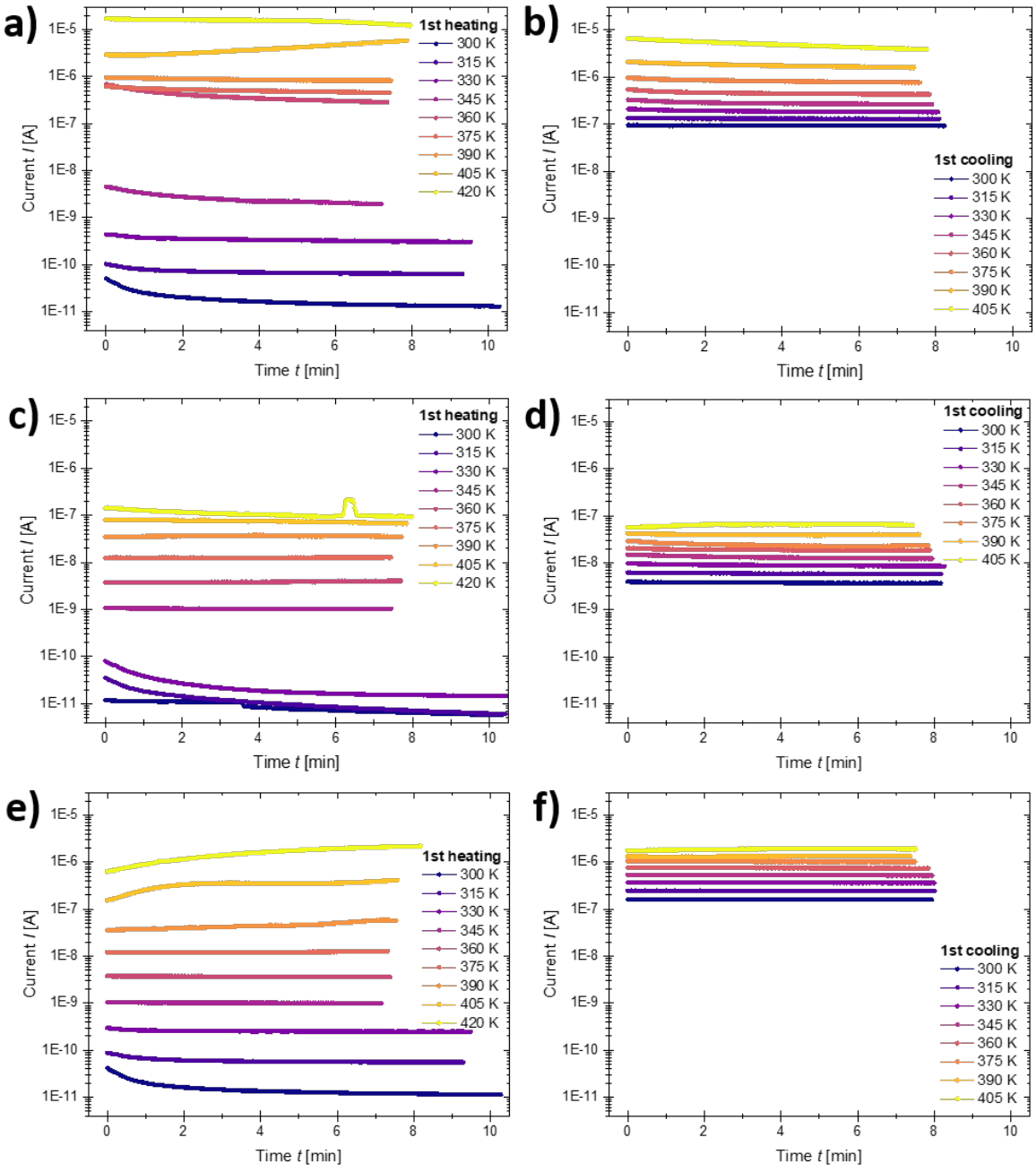

Figure A.13.2: The logarithmic current I for different temperatures T as a function of temperature T of o-TPA-N (a,b), p-TPA-N (c,d), and p-TPA-C (e,f). The first heating (a,c,e) and first cooling (b,d,f) traces are shown for all three TPA derivatives. The currents have been corrected by the device background. Figure 8.3.1 in Section 8.3 shows the current values at time $t = 6$ min.

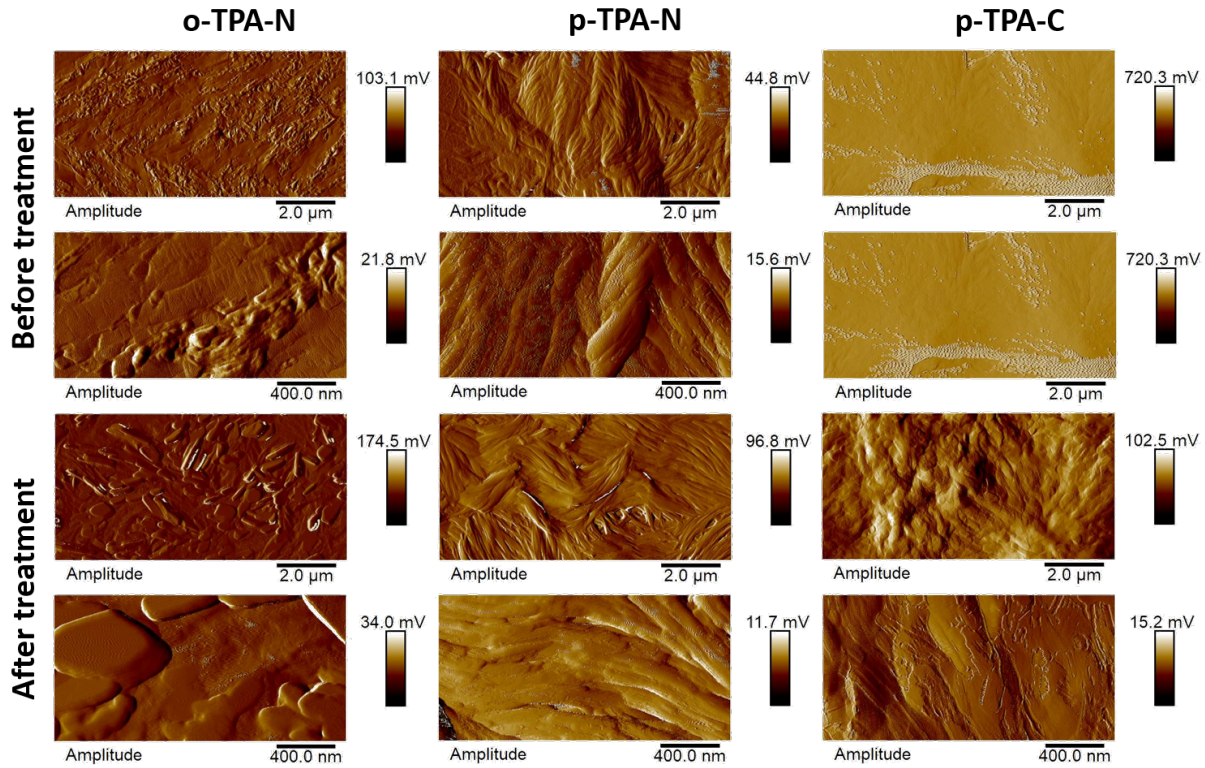

Figure A.13.3: The AFM amplitudes of selected o-TPA-N, p-TPA-N, and p-TPA-C on IDEs samples before and after the alignment process. The electrodes run vertically in all images. Consequently, the electric field is horizontal. All images were take with a scan area of either 10 μm $\times$ 5 μm or 2 μm $\times$ 1 μm. The corresponding height images can be found in Figure 8.4.1 in Section 8.4.

A.14 Dip coating of P3HT

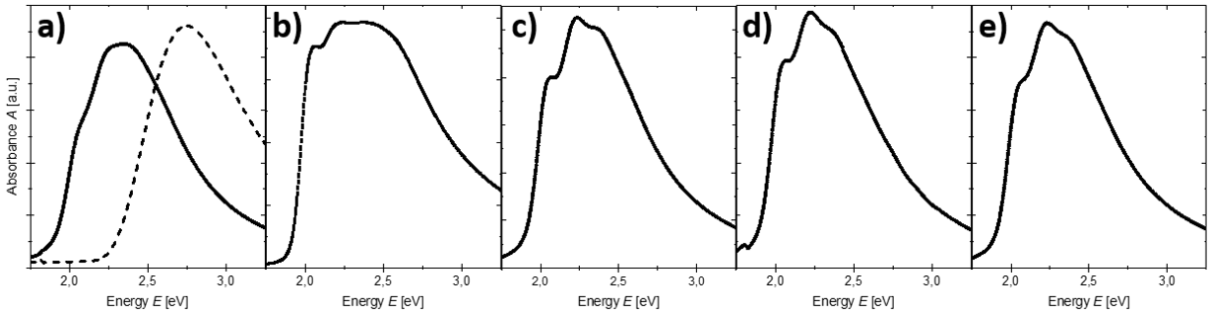

Figure A.14.1: Absorbance UV-vis spectroscopy spetra of pristine P3HT thin films, dip and spin coated from a 10 mg ml^{-1} P3HT in CF solution for different dip coating speeds as a function of the energy E. The shown samples are **a)** spin coated at 3000 rpm (continous line) and spin coated at 3000 rpm from a 0.01 mg ml^{-1} P3HT in CF solution (dashed line), and dip coated at **b)** 1, **c)** 15, **d)** 70, and **e)** 150 mm min^{-1}. The spectra were measured with the polarizer parallel to the dip coating direction. The characteristic $0-0$ and $0-1$ P3HT peaks are visible at $\approx 600-605$ nm and $\approx 550-555$ nm, respectively. The corresponding absorbance spectra as function of wavelength λ are shown in Figure 9.2.1 in Section 9.2. This figure was taken unmodified from the supporting information of Publication V with permission for usage granted by Advanced Electronic Materials.

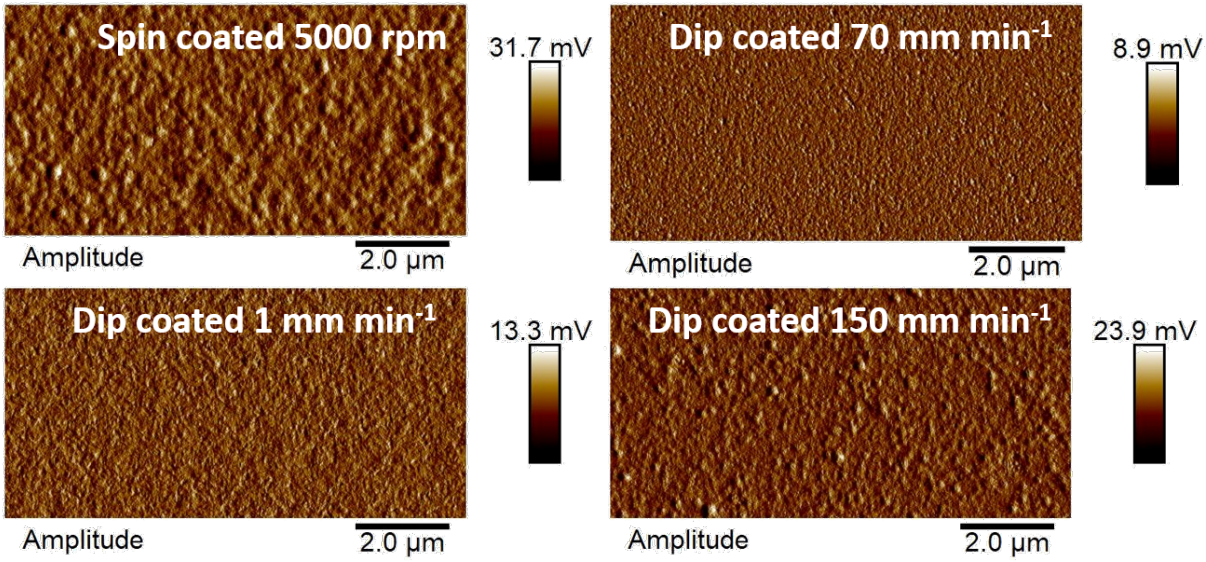

Figure A.14.2: The AFM amplitudes of the selected pristine P3HT thin films coated from a 10 mg ml^{-1} P3HT in CF solution. The films were either spin coated with 5000 rpm (RMS: 4.2 nm), or dip coated with 1 (RMS: 6.1 nm), 70 (RMS: 1.8 nm), and 150 mm min^{-1} (RMS: 5.1 nm), as indicated in the figure. All images were take with a scan area of 10 μm $\times$ 5 μm. The corresponding height images can be found in Figure 9.2.4 in Section 9.2. This figure was taken unmodified from the supporting information of Publication V with permission for usage granted by Advanced Electronic Materials.

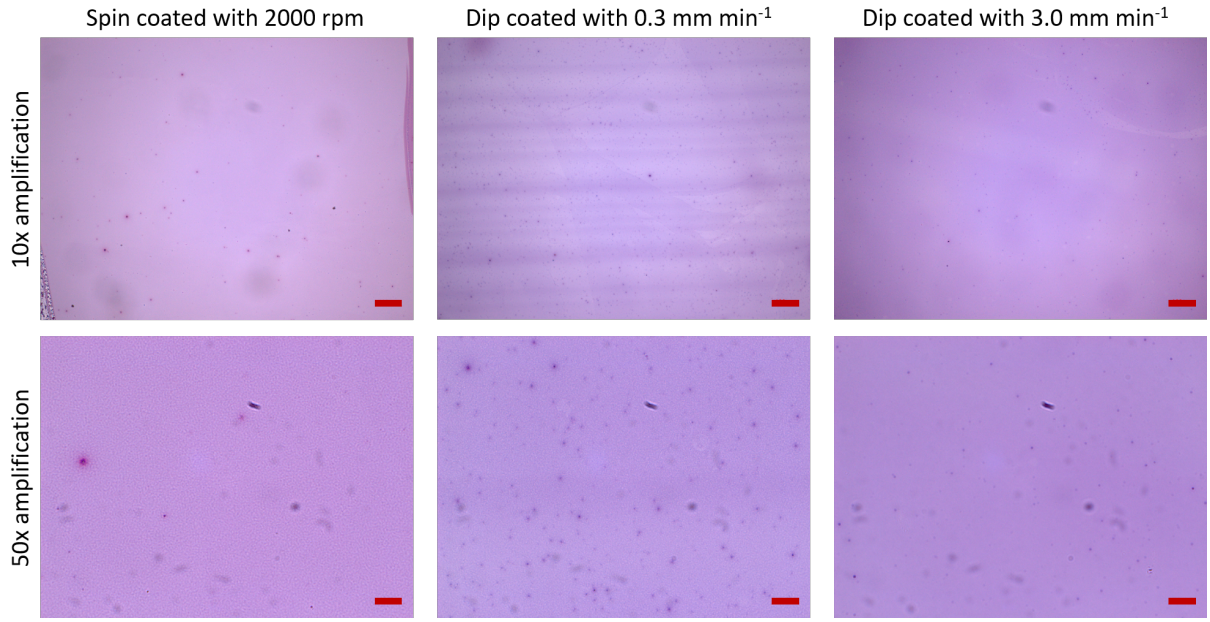

Figure A.14.3: The reflective PLM images of pristine P3HT thin film samples either spin coated (2000 rpm) or dip coated (0.3 and 3.0 mm min^{-1}) from a 10 mg ml^{-1} P3HT in ODCB solution, as indicated in the figure. All images were taken with reflective polarization optical microscopy using crossed polarizers. The red scale bars represent 100 and 20 μm in 10x and 50x amplification images, respectively. The dip coating direction was vertical. This figure was taken unmodified from the supporting information of Publication V with permission for usage granted by Advanced Electronic Materials.

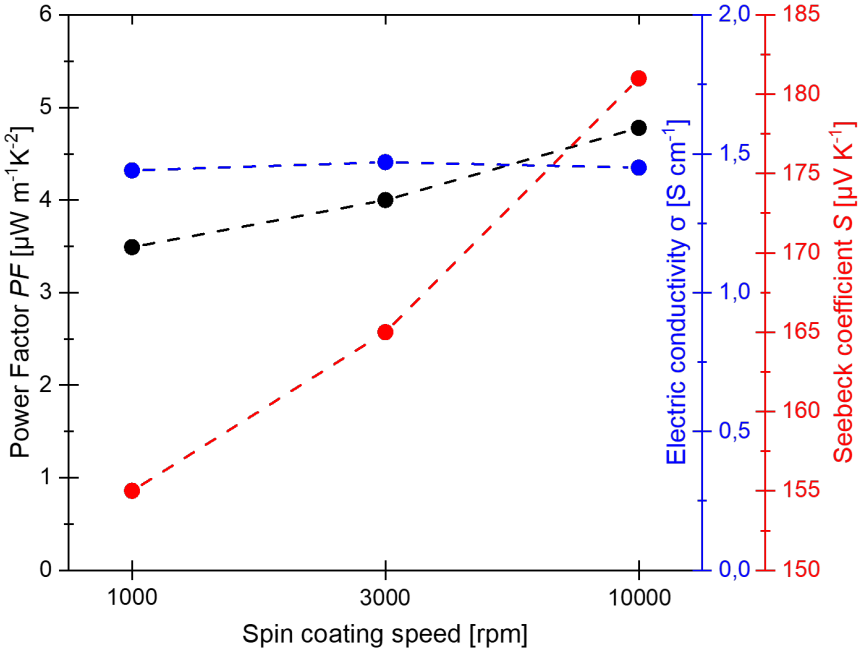

Figure A.14.4: The thermoelectric properties of spin-coated 10 mg ml^{-1} P3HT in CF samples sequentially doped with 1 mg ml^{-1} F_4TCNQ for 1000, 3000 and 10000 rpm spin coating speed. This figure was taken unmodified from the supporting information of Publication V with permission for usage granted by Advanced Electronic Materials.

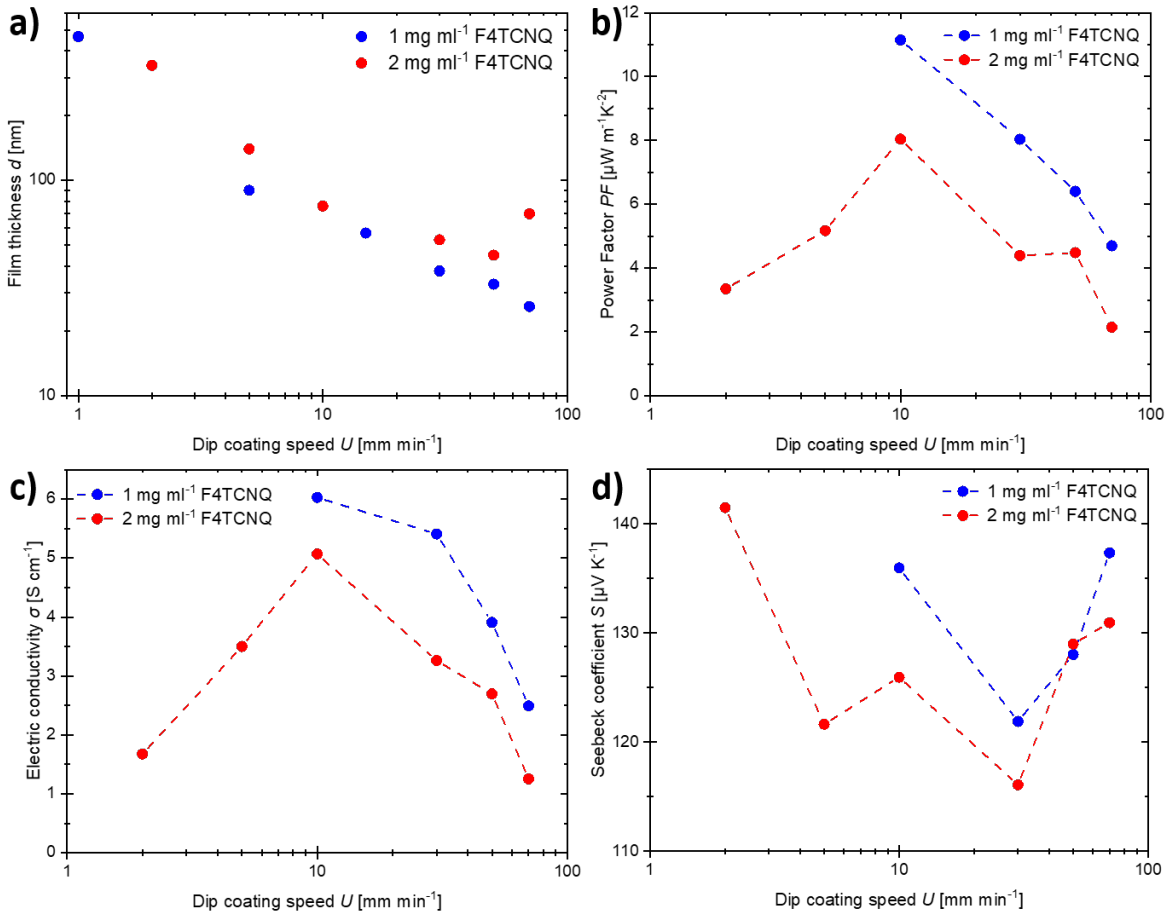

Figure A.14.5: The **a)** film thickness d and **b-d)** thermoelectric properties of P3HT thin films dip coated from a 10 mg ml^{-1} P3HT in CF solution and sequentially doped with 2 mg ml^{-1} F_4TCNQ for lower dip coating speeds U. The 1 mg ml^{-1} F_4TCNQ doping concentration is shown for comparison. This figure was taken unmodified from the supporting information of Publication V with permission for usage granted by Advanced Electronic Materials.